



HAL
open science

Simulation of pulsar magnetospheres : detailed study of some radiative mechanisms

Guillaume Voisin

► **To cite this version:**

Guillaume Voisin. Simulation of pulsar magnetospheres : detailed study of some radiative mechanisms. Solar and Stellar Astrophysics [astro-ph.SR]. Université de recherche Paris Sciences et Lettres, 2017. English. NNT: . tel-01677325v2

HAL Id: tel-01677325

<https://hal.science/tel-01677325v2>

Submitted on 25 Feb 2018

HAL is a multi-disciplinary open access archive for the deposit and dissemination of scientific research documents, whether they are published or not. The documents may come from teaching and research institutions in France or abroad, or from public or private research centers.

L'archive ouverte pluridisciplinaire **HAL**, est destinée au dépôt et à la diffusion de documents scientifiques de niveau recherche, publiés ou non, émanant des établissements d'enseignement et de recherche français ou étrangers, des laboratoires publics ou privés.

THÈSE DE DOCTORAT

de l'Université de recherche Paris Sciences et Lettres
PSL Research University

Préparée à l'Observatoire de Paris

Simulation des magnétosphères de pulsars : étude de phénomènes radiatifs

École doctorale n°127

ASTRONOMIE ET ASTROPHYSIQUE

Spécialité ASTROPHYSIQUE

Soutenue par **Guillaume VOISIN**
le 23 octobre 2017

Dirigée par **Fabrice MOTTEZ**

COMPOSITION DU JURY :

M Jérôme Novak
Observatoire de Paris - CNRS,
Président

Mme Alice Harding
NASA Goddard Space Flight Center,
Rapporteuse

M Alexandre Marcowith
LUPM, CNRS,
Rapporteur

M Benoit Cerutti
IPAG, CNRS
Membre du jury

M Ismaël Cognard
LPC2E, CNRS,
Membre du jury

M Paulo Freire
Max Planck Institute for Radio Astronomy,
Membre du jury

Remerciements / Acknowledgement

Je voudrais remercier mon directeur de thèse, Fabrice Mottez, pour avoir habilement su composer avec mes digressions et, parfois aussi, avec mes caprices. Plus que d'avoir dirigé ma thèse, il m'a accompagné, montré les limites et les écueils avec beaucoup de bienveillance, de patience et, je dois dire, de sang froid. Je crois pouvoir dire qu'aucun d'entre nous n'avait anticipé le résultat de cette thèse, et il n'aurait certainement pas été possible d'en arriver là sans la grande souplesse et l'intelligence humaine dont Fabrice a fait preuve. Pour tout cela, merci.

Silvano Bonazzola, dont la gentillesse et la patience n'ont d'égal que l'étendue et la profondeur de son savoir, est sans doute l'autre pilier de cette thèse. Partager un bureau avec lui a aussi été une des expériences mémorables de ces trois années. J'espère que nous aurons de nouveau l'occasion de déguster un peu de ce Krupnik qui veille en haut de l'étagère.

Bien entendu, je remercie sincèrement tous les collègues du LUTh et d'ailleurs avec qui j'ai pu avoir des discussions amicales et intéressantes et qui ont contribué à enrichir ces trois années. Si, en lisant ces lignes, vous vous sentez concerné à un quelconque degré, sachez que c'est certainement justifié¹ ! Sans exhaustivité aucune je dirais tout de même que chocolats, cafés, thés réguliers avec Christiane, Suzy, Didier, Olivier, Maialen, Miguel, Alexandre, Matthieu, Nathalie... vont me manquer!

Une petite mention spéciale pour Cyril Plou, grâce à qui le peu de savoir que j'ai pu acquérir durant cette thèse à pu être partagé au moins 1934 fois plus².

Enfin, il y a les personnes qui ont permis la réussite de cette thèse et plus généralement qui ont fait en sorte que, dans le peu de choix que la vie offre réellement à chacun, il y ait quelques choix qui me satisfassent profondément et me mènent à taper ces

¹On suppose ici que l'environnement du LUTh est suffisamment sain pour que la réciprocité des relations humaines puissent s'appliquer.

²Nombre de vues de la vidéo réalisée par Cyril pour son site above-earth.fr au 22 janvier 2018. Voir à l'adresse <https://youtu.be/9Tukgswynl4>.

lignes aujourd'hui. Il y a naturellement ma mère qui m'a toujours soutenu avec bienveillance et dévotion et une énergie indiscible, et qui m'a fait confiance sans hésiter le jour où il m'est venu de devenir astrophysicien. Il y a mon père, qui a sans aucun doute fixé une direction sans le savoir le jour où il a rapporté à la maison une lunette astronomique qu'il avait empruntée. Il y a aussi mon frère, avec qui les discussions sont toujours plus enrichissantes. Et il y a Yvette et Marc, sans qui mon passage à Paris aurait sans doute été un peu moins chaleureux (et accessoirement moins gastronomique). Je n'oublie pas moje Żarłok Pimko, qui a sans aucun doute soutenu ce projet par son inexplicable endurance à m'écouter longuement parler de mes projets et difficultés.

Contents

1	Introduction	1
1.1	Pulsars at a glance	1
1.2	Pulsars in radio	7
1.3	Pulsars in x rays	12
1.4	Pulsars in gamma rays	16
1.5	Neutron stars	22
2	Pulsar electrodynamics	27
2.1	The global electrodynamical problem in vacuum	27
2.1.1	The canonical model of electromagnetic field inside the star	27
2.1.2	The Poisson equation with corotation charge density	29
2.1.3	The vacuum field outside the star for the aligned rotator	30
2.1.4	Basic dipolar field geometry : last open field lines, polar cap, curvature radius	31
2.2	Plasma filling and high-energy mechanisms	35
2.2.1	Plasma from the crust	35
2.2.2	Photon radiation mechanisms	37
2.2.3	Lepton creation processes	49
2.3	Active regions	56
2.3.1	The corotating magnetosphere	56
2.3.2	Some general properties of gaps	58
2.3.3	Polar cap	71
2.3.4	Slot gap	86
2.3.5	Outer gap	91
2.4	Global solutions with matter	96
2.4.1	The force-free magnetosphere	96
2.4.2	Electrosphere	100
2.4.3	Kinetic solutions	102
3	Quantum synchrocurvature radiation	107
3.1	The necessity of QED	107
3.1.1	Consistency of the classical theory of curvature radiation	108
3.1.2	Limit of the classical theory	110
3.2	Quantum toy model of radiation	111

3.2.1	States of a toy electron	112
3.2.2	Radiation of the toy electron	115
3.3	Article: Proper states of the electron	118
3.3.1	Introduction	118
3.3.2	Symmetries	120
3.3.3	Second order and Klein-Gordon solutions	120
3.3.4	Dirac's equation solutions	129
3.3.5	Interpretation of the quantum numbers	134
3.3.6	Conclusion	138
3.4	Article: Quantum synchrocurvature radiation	139
3.4.1	Introduction	140
3.4.2	Radiation of confined particles in quantum electrodynamics .	142
3.4.3	Classical curvature radiation from quantum electrodynamics	143
3.4.4	General calculation of synchro-curvature including quantum corrections	149
3.4.5	Power spectrum	154
3.4.6	Discussion and conclusion	157
Appendix 3.A	Toroidal coordinates toolbox	161
Appendix 3.B	Dirac equation in toroidal coordinates	164
Appendix 3.C	Resolution of the radial differential equation	167
Appendix 3.D	Classical Hamilton-Jacobi electron	169
Appendix 3.E	Integration of squared Airy integrals	173
4	Rate and distribution of $\gamma\gamma$ pairs	187
4.1	Accounting for photon anisotropy and pair spectrum	187
4.2	Introduction to the computation of pair spectra	188
4.3	Article: Pairs from anisotropic background	189
4.3.1	Introduction	190
4.3.2	The two-photon-quantum-electrodynamics reaction	192
4.3.3	Probability of reaction for a given photon distribution	196
4.3.4	General solution	199
4.3.5	Applications	204
4.3.6	Discussion	215
4.3.7	Conclusion	216
Appendix 4.A	Derivation of the general result	217
4.A.1	Parametrization of L_- by the three-momentum of the weak photons	218
4.A.2	Integration	223
Appendix 4.B	Formula Compendium	226
5	Pulsar timing model of J0337+1715	229
5.1	Introduction	229

5.1.1	Pulsar timing	229
5.1.2	On the triple system J0337 + 1715	229
5.2	The pulsar timing formula	230
5.2.1	The timing formula in the PSB reference frame	232
5.2.2	Connection between the PSB and the SSB reference frames	234
5.3	The three-body orbits	236
5.3.1	Bi-Keplerian model and parametrization of the orbits	236
5.3.2	Equations of motion at Newtonian order	241
5.3.3	Equations of motion at first post-Newtonian order (1PN)	242
5.3.4	Numerical integration of the equations of motion	244
5.4	Timing delays	247
5.4.1	The geometric delay Δ_G	247
5.4.2	The Einstein delay Δ_E	250
5.4.3	The Shapiro delay Δ_S	253
5.4.4	The aberration delay Δ_A	255
5.5	Validation and preliminary results	258
5.6	Outlook	262
6	Conclusion	265
	Bibliography	271
	Appendix A Constants and notations	285
	Appendix B Landau levels as a solution of the Klein-Gordon equation	287

Introduction

1.1 Pulsars at a glance

The term « pulsar » designates a class of astrophysical objects distinguished by a pulsed signal of short periodicity, from $P_* \sim 1$ ms to $P_* \sim 10$ s. The origin of the pulsation lies in a simple lighthouse effect, light being emitted in a narrow beam that crosses the line of sight of the observer at each rotation. The source is a neutron star, namely a supernova remnant resisting collapse into a black hole only thanks to neutron degeneracy pressure and strong interaction forces. Its typical size is about $2R_* \sim 20$ km in diameter for a typical mass of $M_* = 1.4M_\odot$ where $M_\odot \simeq 2 \cdot 10^{30}$ kg is the mass of the Sun. Additionally, we consider here that pulsars are those stars that are rotation powered, namely the energy they radiate is converted from their rotation energy, which results in a gradual slowdown of the star, corresponding to a period derivative in the range $\dot{P}_* \sim 10^{-22} - 10^{-10}$ s/s (see figure 1.1). The magnetic field of the star plays a major role in this conversion. The magnetic field is very intense, in the range $B_* \sim 10^4 - 10^{10}$ Teslas, and corotates with the star, producing an electromagnetic wave at the period of the star carrying an important part of the slowdown power, or playing a major role in converting this energy into higher-frequency electromagnetic radiation from radio (MHz) to gamma rays. If the magnetic field is usually assumed to be dipolar, which should be a good first approximation at some distance from the star (multipoles having a sharper decay with distance), then radiating regions are on magnetic field lines connected to the magnetic poles. A pulsar can then have up to two rotating beams (see figure 1.2). A pulsar is to be understood in the following as a high-magnetic-field rotation-powered neutron star.

The formation of such stars results from the collapse of massive stars ($> 8M_\odot$) in supernovae. While the envelope of the star is ejected in the supernova process, the matter at the core collapses under the effect of gravity until it can be balanced by the strong nuclear forces and neutron degeneracy pressure. The very intense magnetic field can be naturally explained by conservation of the magnetic flux frozen in the plasma of the progenitor star during the collapse (Pacini, 1967). The neutron star is then cooling down, mostly through neutrino emission for the first $\sim 10^5$ years, and also (and mostly for older stars) from thermal surface radiation in x rays at typically $T_* \sim 10^6$ Kelvins.

Figure 1.1 shows the period derivative versus period $P_* - \dot{P}_*$ diagram with all the neutron stars referenced in the ATNF pulsar catalog (Manchester et al., 2005)¹, which currently gathers 2109 stars with measured and positive \dot{P}_* ². This kind of diagram is to pulsars what the Hertzsprung-Russell diagram is to traditional stars (where gravity is balanced by thermal pressure from thermonuclear origin). It embodies at leading order the main properties of pulsars that can be inferred from the observation of the period and its derivative. In particular, lines of constant spindown power L_{sd} , magnetic field at the surface of the magnetic pole B_* , and spindown age t_{sd} are represented.

Assuming a fiducial momentum of inertia of the star $I_* \sim M_* R_*^2 \sim 10^{39} \text{kg m}^2$ one obtains the spindown power $L_{sd} = 4\pi^2 I_* \dot{P}_* P_*^{-3}$. Assuming a dipolar magnetic field in vacuum, the only source of braking torque is radiation by the rotating field with luminosity $L = \mu_0 c^{-3} 4\pi^2 B_*^2 R_*^6 \Omega_*^4 \sin^2 \chi$ where $\Omega_* = 2\pi/P_*$ is the pulsation of the star and χ is the angle between the rotation axis and the dipolar axis. The spindown age of the star is obtained by equating the spindown power with the luminosity radiated $L_{sd} = L$ and solving for the differential equation obtained. If the luminosity is only that of a vacuum dipolar magnetic field one obtains $t_{sd} = P_*/2\dot{P}_*$. It is interesting to note here that by assuming a general relation $\dot{\Omega}_* = k\Omega_*^n$, where $\dot{\Omega}_*$ is the temporal derivative of Ω_* and k is a constant and n the so-called breaking index, one can obtain a direct measurement of the breaking index n by measuring the second derivative of Ω_* . Indeed, differentiating the slowdown equation above one obtains $n = \Omega_* \ddot{\Omega}_* / \dot{\Omega}_*^2$. In the case of a dipolar magnetic field exposed here $n = 3$, however in the few cases where the second derivative has been measured the breaking index is usually between one and three (Marshall et al. (2016) and references therein).

Four groups of stars appear on figure 1.1 : the normal pulsars, the millisecond pulsars, the young pulsars and what we call here the anomalous pulsars. **Normal pulsars** represent the bulk of the detected pulsars around $P_* = 1\text{s}$, $\dot{P}_* = 10^{-15}$ with a magnetic field of 10^8 Teslas, and spindown age between 10^5 and 10^9 years. Most of them are isolated radio pulsars, meaning that they were not detected at higher frequencies, and do not possess detectable companions. Their normality is also reinforced by the fact that the first detected pulsar, J1921+2153 (Hewish et al., 1968), is part of this class. As they evolve, pulsars are moving towards the lower-right corner of the diagram. It is noteworthy that beyond a certain line of constant spindown power, say between 10^{21} and 10^{23} W, there are no more pulsars. Such a line, whose definition can vary between studies, is called the pulsar deathline, beyond which pulsars turn off.

¹Data from the ATNF pulsar catalog can be accessed at : <http://www.atnf.csiro.au/research/pulsar/psrcat/expert.html>

²Database version of August 2017

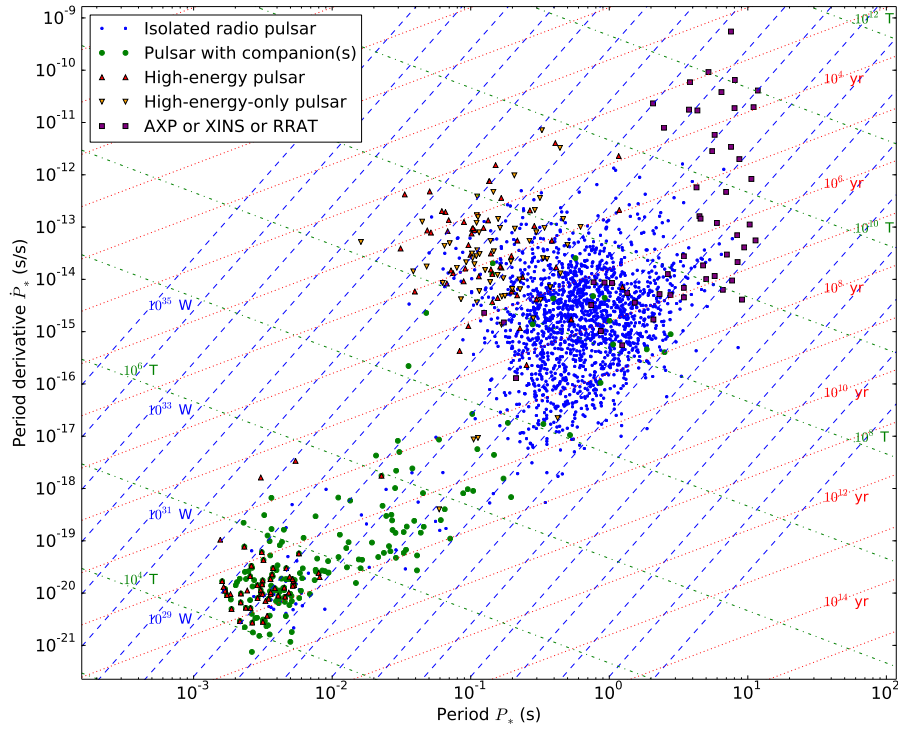


Fig. 1.1.: Diagram period-period-derivative made from the ATNF pulsar catalog (Manchester et al. (2005) and *online catalog*), showing 2109 pulsars of the database with measured period and positive period derivative. Blue dashed lines show lines of constant spindown power, red dotted lines represent constant spindown age, and green dashed-dotted lines represent constant surface magnetic field at the pole (assuming a dipolar magnetic field). See the text and table 1.1 for the associated formulas. AXP stands for anomalous x-ray repeaters, XINS for x-ray isolated neutron stars, and RRAT for rotating radio transients.

Young pulsars are stars of small spindown age, typically $\sim 10^4$ years and less than 10^5 years. In some cases, their association with supernova remnants allows a more precise estimate of the age of the star. The most famous and the most studied pulsar of this class (and probably of all classes) is certainly the Crab pulsar, J0534+2200, whose association with the Crab nebula and the supernova observed in 1054AD is well established. Therefore this star is less than a thousand years old. The period of the Crab is about 33 ms and its period derivative is $4 \cdot 10^{-13}$. Such stars are on average spinning faster than the normal pulsars, with a higher \dot{P}_* but comparable magnetic fields which gives them a high spindown power. The Crab, for example, has the highest spindown power of all radio-loud pulsars with $L_{\text{sd}} \simeq 4.5 \cdot 10^{31}$ W and the second highest of all known pulsars (the highest being the radio-quiet J0537-6910 with $4.9 \cdot 10^{31}$ W). A related consequence is the fact that young pulsars are more prone to radiate at high energies, in particular in gamma rays, which explains the high concentration of radio-quiet and radio-loud high energy pulsars in this region of the diagram.

Millisecond pulsars can be defined as pulsars with period $\dot{P}_* < 20$ ms and period derivative $\dot{P}_* < 10^{-19}$ (Özel and Freire, 2016), with a typical $P_* \sim$ a few ms, $\dot{P}_* \sim 10^{-20}$. The current ATNF pulsar catalog gives 190 objects matching this definition. These objects are characterized by the fact that most of them possess companions (137), often white dwarfs, but also non-degenerate companions in some cases (called redbacks and black widows, see e.g. Roberts (2012)), and a very large spindown age $> 10^8$ years. They also have much lower magnetic fields than other pulsars, typically on the order of a few 10^4 Teslas. A very interesting point is the high number of high-energy pulsars among them compared to the population of normal pulsars. The detection of millisecond pulsars is much harder: on the one hand the flux per pulsation is much weaker and on the other hand the instrumentation able to follow such a rapid pulsating signal was not available until quite recently (see section 1.2 below).

The formation process of millisecond pulsars is called recycling. Two traditional stars orbit each other, one massive enough ($> 8M_{\odot}$) to end in a supernova and the other of lower mass. When the most massive explodes as a supernova, the other one is still at a much earlier stage, forming a pulsar-traditional-star binary. When the companion reaches the last stages of its life its radius becomes much larger (giant phase) and may fill the Roche lobe of the neutron star. When this happens, the neutron star starts accreting matter, and the transfer of orbital momentum spins up the neutron star to millisecond periods. During this phase the system can be observed as a low-mass-x-ray binary. Eventually the pulsar turns on again and its companion turns into a white dwarf. It can also happen with two massive stars in which case the recycling phase is shorter and the system ends up as two neutron stars, one partially recycled and another normal one. This scenario was confirmed by the

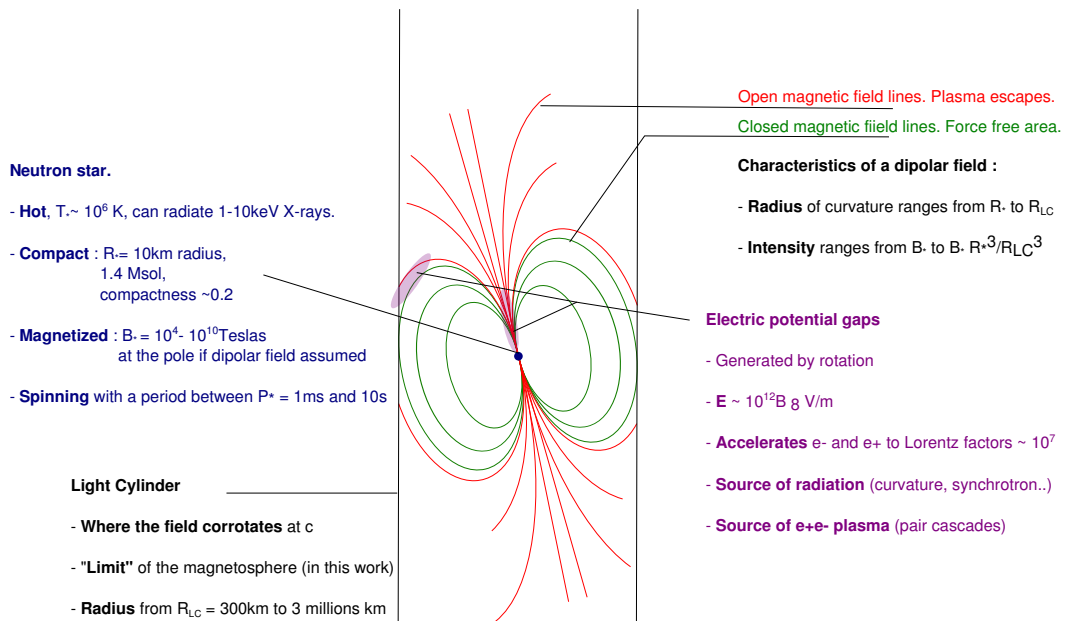


Fig. 1.2.: Sketch of a pulsar with a dipolar magnetic field and the main quantities discussed in the text.

discovery of the double pulsar J0737-3039A/B where A has a period of 22.8 ms and B a period of 2.8 s, as well as by the observation that neutron stars in LMXBs often have millisecond periods (Ritter and Kolb, 2003; Ritter and Kolb, 2004). There are 14 double-neutron-star systems (only one is a double pulsar) and most of them are in the region of the $P_* - \dot{P}_*$ diagram bridging the normal pulsars to the millisecond pulsars, hint of this shorter recycling phase.

Anomalous pulsars regroup the anomalous x-ray repeaters (AXP), the x-ray isolated neutron stars (XINS) and the rotating radio transients (RRAT). Part or totality of the AXPss may belong to the class of magnetars, where the energy source of the observable radiation is the magnetic field itself. The radio emission is irregular or totally absent from these sources, and the magnetic field can be very intense, above the critical field of quantum electrodynamics $B_c = 4.4 \cdot 10^9$ T, above which some phenomena such as photon splitting or resonant scattering become particularly important. Thus, these sources are anomalous from the point of view of normal pulsars, and we shall not comment further on them.

The approach with a vacuum magnetosphere used on figure 1.1 and shortly described above is further developed in chapter 2. Although this gives useful orders of magnitude, this kind of magnetosphere was shown to be inconsistent by Goldreich and Julian (1969) : a vacuum magnetosphere develops very large potential drops of the order of $\sim 10^{16} B_{*8} P_{*1}^{-1} R_{*4}^2 V^3$ (see equation (2.17)) able to pull up plasma from

³Here and in all this work the notation $A_n = A/10^n$. See also appendix A.

the surface and/or trigger pair-creation cascades (see below) such that eventually plasma must fill the magnetosphere. In this work, the magnetosphere is understood as the region within the so-called light cylinder. This is a cylinder the axis of which is centered on the rotation axis of the star with a radius of $R_{LC} = c/\Omega_*$ corresponding to the distance within which corotation with the star is possible without exceeding the speed of light c . Number of critical phenomena are expected to take place within this fiducial limit, in particular related to the strength of the magnetic field which is higher inside. It is the object of chapter 2 to expose some of the main models and achievements in the understanding of the magnetosphere. Once the principle of a plasma-filled magnetosphere is accepted come the problems of species composing the plasma, their dynamics, and their radiations.

The common picture of the plasma-filled magnetosphere is a plasma made of electrons and positrons, with a density everywhere adjusted to create an electric field trailing the plasma in corotation with the star. This corotation density, $\rho_c \simeq -2\epsilon_0\vec{\Omega}_* \cdot \vec{B}$ with \vec{B} the local magnetic field and ϵ_0 the vacuum dielectric constant, is often called the Goldreich-Julian density after the authors of the seminal article that introduced it (Goldreich and Julian, 1969). It gives a typical density of 10^{17}m^{-3} near the magnetic pole of the star. Such a magnetosphere is a particular case of the class of models called force-free, in the sense that the electric field does not work on the plasma which translates into the Lorentz-invariant condition $\vec{E} \cdot \vec{B} = 0$, where \vec{E} is the local electric field. Large-scale force-free simulations have been intensively developed in the past decade. However, even this global picture is not consistent with the observation of non-thermal radiations at all wavelengths, which require acceleration. Such acceleration is thought to occur in localized places where plasma flows along field lines. In particular, these places are expected along the open field lines emerging from the magnetic poles and where plasma can flow to infinity guided by the intense magnetic field. The acceleration regions are called gaps, in the broad sense that some electric potential drop arises along the magnetic field in these regions. In addition to being the source of acceleration, these regions are also probable sources of matter for the magnetosphere. Indeed, electrons and positrons are accelerated in potential drops exceeding 1 TV, enough to produce photons with energies exceeding the rest-mass energy of an electron-positron pair. Quantum electrodynamics mechanisms such as pair production by interaction of the gamma photon with an intense background magnetic field or interaction with another photon can then create pairs, which in turn are accelerated and radiate photons that make pairs etc... Such cascades can possibly provide the plasma needed to fill up the magnetosphere.

One of the main radiation mechanisms, thought to play a central role in most cascade models, is the so-called curvature radiation and its extension synchrocurvature radiation. It consists in the radiation of a charged particle moving relativistically

within a curved intense magnetic field. The magnetic field is so intense that the synchrotron motion is entirely (curvature) or almost entirely (synchrocurvature) quenched by radiation losses. In this thesis we have studied this radiation from quantum-electrodynamics first principles (chapter 3) and found that possibly important corrections arise from the quantification of energy levels due to the background magnetic field.

Pair creation by collision of two photons is a mechanism that is expected to play an important role in the outer magnetosphere and possibly also near the star itself in low-magnetic-field millisecond pulsars. Although the basic physics of this interaction is well-known, the integration over a large number of two-photon encounters is difficult to carry efficiently, in particular in cases where the distribution of photons is broadly anisotropic as one expects in pulsar magnetospheres. In this thesis, we worked out an approximated formulation to deal with such anisotropies that we expose in chapter 4.

One extremely fruitful property of pulsars is their regularity. Indeed, the pulsed signal once averaged over a large number of pulses and corrected for the slowdown displays a period that can be timed as accurately as 100 ns in the best cases. During that time, light crosses a few tens of meters, much less than the size of the star itself. This allows to use pulsars as clocks sending to us a timing signal from locations kiloparsecs away from the Earth. This is particularly interesting for pulsars in binary (or more) systems. Then, the motion of the pulsar in the system and relativistic (special and general) delays due to the companion can be accurately measured giving the possibility to characterize with high accuracy the orbits and the masses. Moreover, it allows to validate the hypothesis that general relativity is correct in strong fields, namely in regimes where one of the orbiting body (the neutron star) is strongly self-gravitating with a large compactness parameter $\Theta = GM_*/(R_*c^2) \simeq 0.2$. In chapter 5, we develop a timing model for a pulsar in a triple system (the pulsar and two white dwarfs) J0337+1715 (Ransom et al., 2014). Such triple configuration is unique to date, and it is hoped that it will eventually make possible unprecedented tests of general relativity in strong fields.

1.2 Pulsars in radio

Pulsars are originally « rapidly pulsating radio sources » (Hewish et al., 1968) and, fifty years later, radio still provides most of pulsar observations. This is due also to the availability of several first-class radio-telescope : Parkes, Jodrell Bank, Green Bank, Arecibo, Effelsberg, Nançay, or the low-frequency LOFAR network. High-energy observations, the other important provider of data, are limited by the need to observe outside the Earth atmosphere, and further technological complications.

Name	Symbol, Expression	Value
Mass	M_*	$1.4M_\odot$
Radius	R_*	10 km
Momentum of inertia	$I_* \sim M_*R_*^2$	10^{39}kg m^2
Period	P_*	1s (np), 10 ms (msp)
Period derivative	\dot{P}_*	10^{-15} (np), 10^{-20} (msp)
Temperature	T_*	10^6 K
Rotational pulsation	$\Omega_* = \frac{2\pi}{P_*}$	$6.3P_{*1}^{-1}\text{rad/s}$
Spindown power	$L_{\text{sd}} = I_*\Omega_*\dot{\Omega}_*$	$3.9 \cdot 10^{25}P_{*1}^{-3}\dot{P}_{*-15}$ W
Corotation density	$\rho_c \simeq -2\epsilon_0\vec{\Omega}_* \cdot \vec{B}$	$10^{17}e\left(\frac{R_*}{r}\right)^3\dot{P}_{*-15}^{1/2}\text{C m}^{-3}$
Magnetic field (dipolar at pole)	$B_* = \frac{P_*^{1/2}\dot{P}_*^{1/2}(I_*c^3\mu_0)^{1/2}}{(4\pi^2R_*^3)}$	$1.5 \cdot 10^8P_{*1}^{1/2}\dot{P}_{*-15}^{1/2}$ T
Light cylinder radius	$R_{\text{LC}} = \frac{cP_*}{2\pi}$	$4.7 \cdot 10^4P_{*1}$ km
Spindown age	$t_{\text{sd}} = P_*/(2\dot{P}_*)$	$1.6 \cdot 10^7P_{*1}\dot{P}_{*-15}^{-1}$ years

Tab. 1.1.

Summary of the quantities presented in this section. For the first six lines fiducial quantities are given, with (np) standing for normal pulsar, and (msp) standing for millisecond pulsar. The expression of the corotation density is the leading non-relativistic order of the complete expression given in equation (2.10). The value of the corotation density is an order of magnitude that does not take into account the angle between the local field and the rotation axis or local sign of charge, and $-e$ is the charge of the electron. A dipolar field is assumed. The last three lines are represented on figure 1.1, and numerical values are given for fiducial normal pulsar values.

However, radio observations of pulsars are not as obvious as it may seem, and several caveats drastically limit the detection of the pulsation : mainly the very low signal per pulsation and the effects of interstellar scattering. In particular the dispersion delay, a scattering effect of the interstellar electron density, can smear the signal in time to the point where it becomes impossible to detect the pulsed nature of the source. This can fortunately be overcome thanks to dedispersion techniques, which have the inconvenience of being computationally expensive. Hence, at least until the beginning of the 1990s when the computing power became sufficient to detect the fainter millisecond pulsars efficiently (only some of the brightest had been found before), the development of pulsar radioastronomy is directly related to the development of computers and the number of pulsars detected to date owes probably more to Moore's law than to improvements in antennas and collection areas⁴.

Pulsar radio observations are impinged by several phenomena, in particular interstellar scattering, the radio background luminosity of the interstellar medium, and Earth-bound interferences. The scattering of the radio signal by electrons on the path of the radio signal provokes several phenomena : delay due to the so-called dispersion measure, pulse broadening, and scintillation. Ironically, it is while studying the latter that the first pulsar was discovered by Hewish et al. (1968), for the study needed a trigger faster than usual. Scintillation results from multiple scattering by the ionized interstellar gas, resulting in a variety of possible paths for the radio waves which in the end may interfere and produce a twinkling of the signal, similar to that of the stars at night due to local variations of refractive index within the Earth atmosphere. Another consequence is that a short pulse such as those of pulsars, following multiple paths with slightly different propagation times, arrives broadened to the observer. This broadening is heavily frequency dependent, ν^{-4} , and prevents observation at low frequencies. The dispersion measure delay is the average extra delay due to the density of electrons along the line of sight. It is proportional to the density of electrons integrated along the line of sight, the so-called dispersion measure (DM) and scales like ν^{-2} . As mentioned above, this delay can be efficiently inverted. Besides, it also allows to determine the approximate distance of the pulsar, provided one has a model of the electron density along the line of sight. The radio background results from the synchrotron radiation of electrons in the galactic magnetic field. It diminishes like $\nu^{-2.8}$ and is significantly suppressed above a few hundred MHz. It remains all the human radio emissions, either from Earthbound devices or from satellites. These can be limited by reserving frequencies for radioastronomy and locating observatories in preserved spaces. It is also possible, to a certain extent, to filter the human emissions. The previous reasons, together

⁴Moore's law predicts a doubling of the number of transistors in CPUs every two years. Most of the largest radiotelescopes still in service were built in the 1960's. However it should not be forgotten that the receivers, as well as instrumentation in general improved during that time.

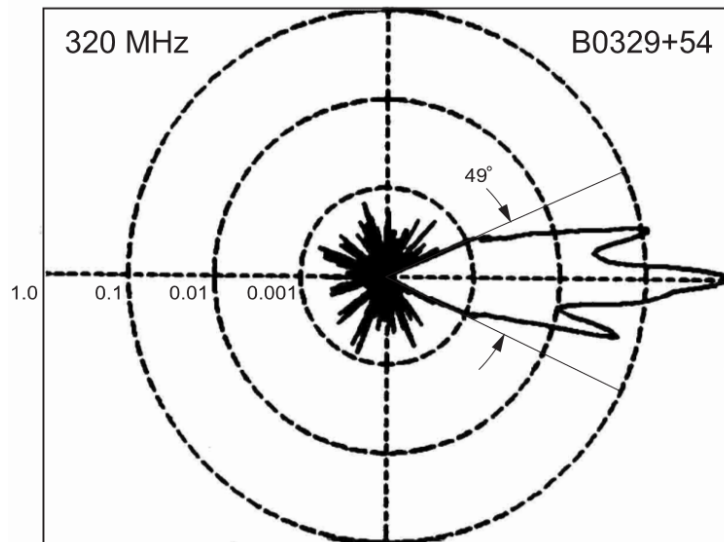


Fig. 1.3.: From Kijak and Gil (2003). A pulsar profile B0329+54 at 320 MHz in log-scale and polar coordinates. The data come from Jodrell Bank Observatory (Gould and Lyne, 1998).

with the interest for a larger bandwidth pushed the observations to frequencies often around 1.4 GHz for timing applications, compared to the first observations that were at a few hundred MHz, with the notable exception of LOFAR specially designed for low frequencies.

Pulse luminosities⁵ range from 0.05mJy kpc² to 23800mJy kpc² at 400MHz and from 0.005mJy kpc² to 6000mJy kpc² at 1400MHz according to the ATNF pulsar catalogue⁶ (Manchester et al., 2005). The bulk of the luminosities is in the range $\sim 10 - 1000\text{mJy kpc}^2$ at 400MHz and on average the luminosity is ~ 10 times less at 1400MHz. Hence the radio spectrum is decreasing with frequency. The maximum of the spectrum, if any, is usually around a few tens of MHz. The pulse width at 50% of the peak luminosity is approximately $2^\circ P_*^{-1/2} / \sin \chi$ of the pulsar rotation at $\sim 1\text{GHz}$ (Rankin, 1990; Lyne and Graham-Smith, 2012), where χ is the angle between the magnetic pole and the rotation axis. This width is fairly independent of the chosen cutoff level, as the signal falls extremely sharply on the edges (see figure 1.3). The polarization is often very linear and varies across the pulse in a way that can often be explained in the frame of the rotating vector model (see below), with a characteristic S-shape. Individual pulses are usually very faint and important random pulse-to-pulse variation occur. However, the integrated pulse profile averaged over a large number of pulses is very stable.

⁵1 Jansky = $10^{-26}\text{W m}^{-2}\text{Hz}^{-1}$

⁶<http://www.atnf.csiro.au/research/pulsar/psrcat/>

The radio emission mechanisms are poorly understood despite significant efforts (see Beskin et al. (2015) for a review). It is however clear that the mechanism(s) must be coherent as otherwise the plasma densities required exceed by far any reasonable density in the magnetosphere. The location of the emission region is consistent with the region above the polar cap with the notable exception of the Crab pulsar (PSR J0534+2200) which seems to emit radio waves from the outer magnetosphere (see e.g. Eilek and Hankins (2016)). Indeed, Radhakrishnan and Cooke (1969) showed that a simple geometrical model called the rotating vector model can explain many observations of the polarization sweep by considering the region above the polar cap. In this model the polarization angle is determined by the local direction of the dipolar magnetic field at the point of emission. Further, the emission is consistent with radius-to-frequency mapping, namely that there exists a one-to-one relationship between the altitude of emission and the frequency of emission, with the general trend that frequency rises as altitude lowers (see e.g. Cordes (1978) and Kijak and Gil (2003)). The integrated pulse profiles often show two main components with distinct characteristic width, polarization and spectral properties. They are not always both present and can be separately identified in different pulsars. This led to the development of an empirical core+cone model of emission (Rankin, 1983; Rankin, 1990; Rankin, 1993) where the core emission comes from a region above the center of the polar cap and the cone emission arises from the magnetic field lines forming the limit of the polar cap. Two examples are given on figure 1.4⁷.

It is to be noted that the radio emission of pulsars presents a wealth of particular cases, such as drifting subpulses, nullings, mode changings or giant pulses. The drifting subpulses are pulse feature that drift in phase at a regular pace. Nullings are the ability of the pulse of some pulsars to stop (or at least become undetectable) while the mode changings are changes in the pulse shape and polarization. Whether the two phenomena are the same thing is an open question, as well as knowing if they are related to the so-called rotating radio transients, which are believed to be associated with radio-quiet rotating neutron stars showing spontaneous emissions at random times (but always at the same phase, hence the deduction that the source is rotating). Giant pulses are exceptionally bright and narrow random pulses observed notably from the Crab pulsar. Their duration is much shorter than the regular pulse, from nanoseconds to microseconds (the Crab has a period of 33 ms) and intensity can be taken from 10 times to more than a thousand times the average pulse intensity (Karuppusamy et al., 2010). The question of knowing if they are related to rotating radio transients, nullings or mode changings is also open.

⁷Both profiles were accessed through the EPN database of pulsar profiles, <http://www.epta.eu.org/epndb/>.

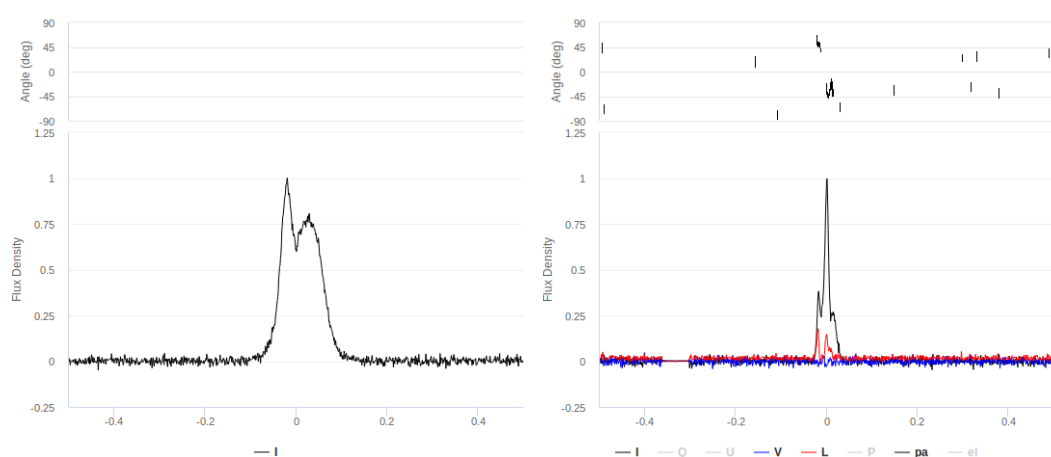


Fig. 1.4.: Left-hand side panel : typical pure core-component (Rankin, 1983) average pulse profile of PSR J0814 + 7929 at 63.8 MHz (Pilia et al., 2016). Core components are characterized among other things by such double-peak at low frequency. Right-hand side panel : typical pure conal (Rankin, 1983) average pulse profile of PSR J1645 – 0317 at 4800 MHz with polarization angle above and polarization Stokes parameters in red and blue (Hoensbroech and Xilouris, 1997). A sharp peak with two lower side peaks, « outriders », is a characteristic of conal profiles at high frequencies. Note the typical S-shape of the polarization angle across the pulse. This is a common feature of integrated pulse profiles (not only of conal pulses) well explained by the rotating vector model (see text).

1.3 Pusars in x rays

X-ray observations constitute a rather recent chapter of astronomy⁸. This owes to the fact that the atmosphere is opaque (fortunately for life) to x-ray radiation until an altitude of ~ 100 km. Therefore the first measurements were made at the dawn of space age: in 1949 a team led by Herbert Friedman fired a V-2 rocket, captured to the Germans at the end of World War II, equipped with photon counters sensitive in different bands from ultraviolet to x-rays (Friedman et al., 1951). After recovering the apparatus, they discovered a clear x-ray detection from the sun above 87km. In 1963 was detected the Crab nebulae with a counter flown on an Aerobee rocket. In parallel, the idea that such nebulae could be powered by a central neutron star emitting x-rays was developing, however the sensitivity and resolution was still too low to detect them. It is only after the discovery of the first pulsar and the subsequent discovery of the Crab and Vela pulsars that the x-ray detections of the two latter objects were possible in the early seventies. Since then, the development of satellite-flown detectors, and in particular the two most recent ones Chandra and XMM-Newton launched in the 2000s, has provided a wealth of data with at least 89 pulsars detected in x-rays (Becker, 2009).

⁸The current section draws largely from Becker (2009). The reader can refer to it and references therein when no other reference is indicated in the text.

From the point of view of the science of pulsars and neutron stars in general, x rays provide a unique window on the star itself, as well as on its magnetosphere. Indeed, neutron stars are believed to be born at temperatures of $10^9 - 10^{11}$ K and to cool down in ~ 100 years to temperatures around $\sim 10^6 - 10^7$ K which correspond to black-body emission in the soft x-ray band, 0.1 – 1 keV. The temperature evolution of an isolated star can be summarized by the equation

$$C(T_i) \frac{dT_i}{dt} = -L_\nu(T_i) - L_x(T_*) + H, \quad (1.1)$$

where T_i is the inner temperature of the star (defined as the region in which the density is above $\sim 10^{10} \text{ g cm}^{-3}$), T_* the surface temperature, C is the heat capacity. The star cools through neutrino emission L_ν and black-body radiation L_x but can be heated back, H , by a flow of radiation and matter from the magnetosphere. Thus, it is clear that the cooling dynamics is directly related to the equation of state of the star, through C , and the nuclear reactions inside the star, through L_ν . Moreover, the radius of the star can in principle be probed through $L_x = 4\pi R_*^2 \sigma T_s^4$ (for a uniform black-body, σ being the Stefan-Boltzmann constant) which gives a direct constraint on the equation of state. At last, the heating term H gives a constraint on the magnetospheric model which has to account for the right energy back-flow. In particular, this term is thought to come mostly from hotspots formed around the polar cap by the returning plasma.

On top of that, x-ray observations can provide a direct measurement of the magnetic field intensity in the case of accreting binary pulsars. In this case, a neutron star accretes from a main sequence star and a hot plasma column radiating in x rays is formed above the magnetic pole (see figure 1.5). The most famous case is certainly that of Hercule X-1 (Truemper et al., 1978), an x-ray binary in the spectrum of which was for the first time recognized an x-ray cyclotron line (figure 1.6). Indeed, if the accreting plasma is assumed to be made of electrons and positrons and at rest in the frame of the star, the transition between Landau levels (see appendix B) corresponds to the emission of photons of energy

$$\hbar\omega \simeq n \frac{B}{B_c} mc^2 \simeq 12n B_8 \text{keV}, \quad (1.2)$$

where n is the harmonic number, $B_c = 4.4 \cdot 10^9 \text{ T}$ is the critical quantum-electrodynamics field intensity, and mc^2 the mass energy of the electron. In the case of Her X-1, the measurement gave a field intensity of $\sim 5 \cdot 10^8 \text{ T}$, compatible with the intensities usually inferred from magnetic spindown power of other pulsars.

The basic modeling of the pulsar x-ray emissions appeals to a three-component model : one cool black-body thought to represent the temperature of the crust, one hot black-body thought to represent one or several hotspots, and a power-law tail

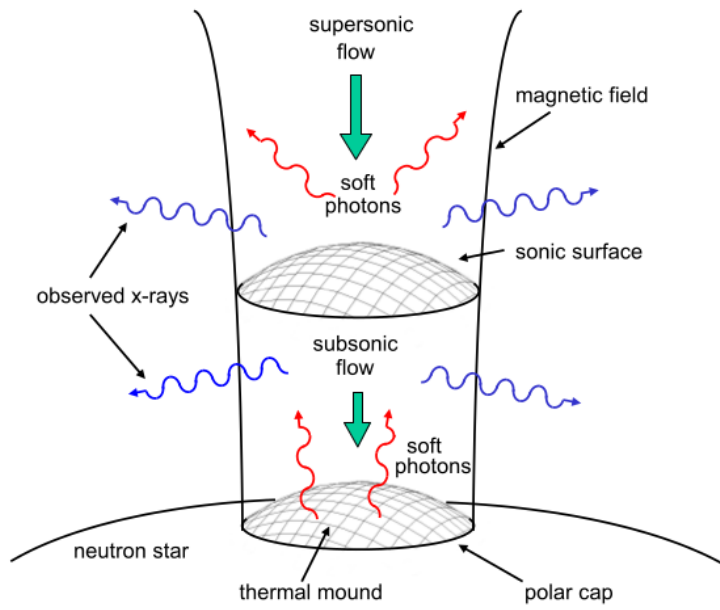


Fig. 1.5.: Schematic x-ray spectra from various types of pulsars, from Becker (2009)

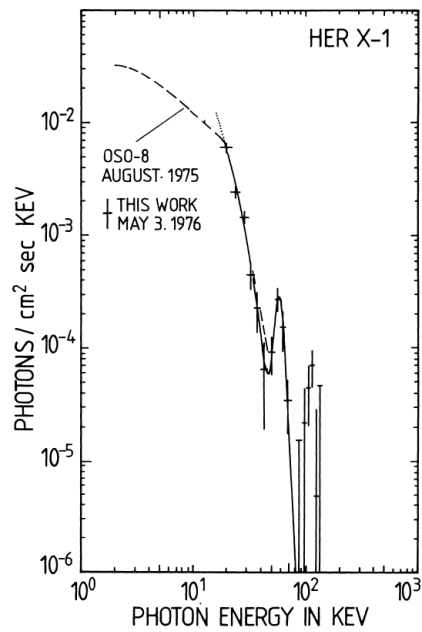


Fig. 1.6.: First cyclotron line in a x-ray binary spectrum, Her X-1, from Truemper et al. (1978)

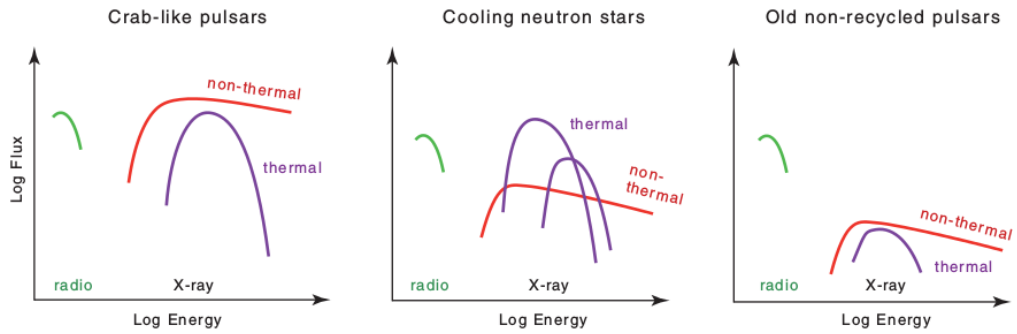


Fig. 1.7.: From Becker (2009). Schematic x-ray spectra from various types of pulsars. See text for millisecond pulsars.

at higher energies ($> 2\text{keV}$) thought to come from magnetospheric synchrotron or curvature radiations. The behavior is qualitatively different between the three types of pulsars. Young pulsars are dominated by the power-law, non-thermal emission with a pulsed fraction close to 100% ; field pulsars have a pulsed fraction usually lower than 50%, when they are mid-aged ($10^4 - 10^5$ years) they are dominated by the two components of thermal emission, a typical example is Geminga's spectrum on figure 1.8, and when they are old (non-recycled) and close to the death line ($10^5 - 10^7$ years) the power-law dominates ; millisecond pulsars with high spindown power ($> 10^{27}$ W) are dominated by an almost entirely pulsed power law while the less energetic ones tend to show the two black bodies as well. Figure 1.7 summarizes these categories, except for the millisecond pulsars. Overall, the orders of magnitude obtained are in line with what can be reasonably expected : cool black-body are a few 10^5 K and with radius $\sim 8 - 20$ km, hotspots are typically around $\sim 2 \cdot 10^6$ K with radii ranging from 50 m to a few kilometers, the power-law photon indexes⁹ range in $\sim 1. - 2.$

If this simple model gives a general picture it is far from solving the full problem. Particular cases are numerous, and the interpretation of the fitted model is not always obvious. A more complete model would allow for atmospheric absorption of the black bodies which yields a fairly deformed spectrum. The size of the hotspots do not always fit with the theoretical expectation of the polar cap size, being either fairly too big or fairly too small.

The three musketeers, called this way for their similarities, are three mid-aged pulsars : Geminga (PSRJ0633+1746), PSRB0656+14 and PSRB1055-52. They are an example of these caveats, and the observation of the evolution of the spectrum with the rotational phase of the pulsar (phase-resolved spectroscopy) that was

⁹The photon index Γ is defined as : $\frac{dN}{dt} = E^{-\Gamma}$. N the number of emitted photons, E the energy of the photons.

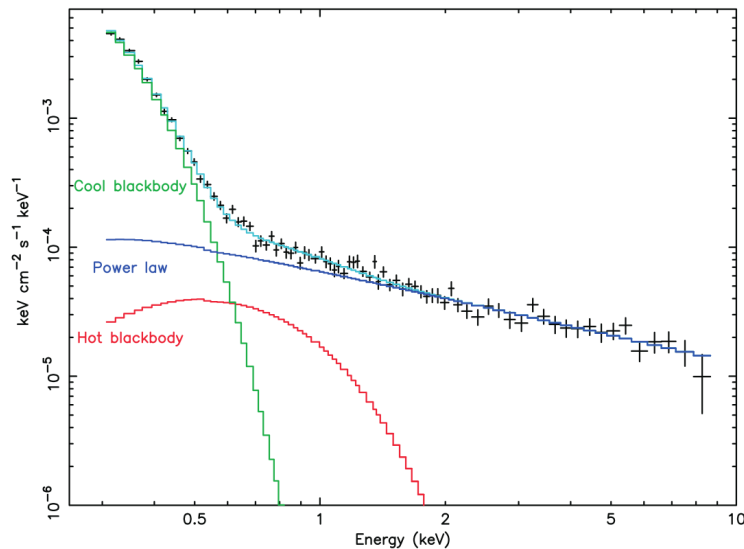


Fig. 1.8.: From Luca (2005) and Caraveo et al. (2004). Unfolded phase-integrated spectrum of Geminga. The best fitting spectral model is represented by the light blue line. It is the sum of a cool blackbody component (green), a hot blackbody component (red) and a power law (blue).

performed on them (Luca, 2005) does not improve the picture. Their hotspots are 100% pulsed as one might expect, except for PSRB0656+14 which varies only by 10%, and the correlation between the peak of the cool-black-body intensity and the peak of the hotspot intensity goes from quasi-correlated to almost anti-correlated. The same kind of variations happen for the power-law component. We see here that in the light of x-ray phase-resolved spectroscopy these three pulsars are no longer really three musketeers.

X rays show us other types of sources that would take other sections to describe. Apart from the already mentioned x-ray binaries, one may mention the central compact objects (CCOs) which are unpulsed x-ray sources in the center of some nebulae, the anomalous x-ray pulsars that turned out to be magnetars at least in a number of cases, or the low mass x-ray binaries which are possibly the progenitors of some millisecond pulsars still at the recycling stage. One should also mention the study of the associated nebulae, when existing, which provides a wealth of information on pulsar winds.

1.4 Pulsars in gamma rays

Gamma-ray observations of pulsars, that is observations at and beyond MeV photon energies exploded recently with the launch of the Fermi (ex-GLAST) space observatory in 2008 and in particular its Large Area Telescope (LAT). Indeed, gamma rays cannot penetrate the Earth's atmosphere and a direct detection is therefore

impossible at ground level. Besides, the detection of high-energy photons suffers from several caveats: photons have to be discriminated against the other high-energy particles coming from space and which are orders of magnitude more numerous, and the absolute flux of photon is very small to the point that the photons are detected one by one. For example, the young Crab pulsar, one of the brightest sources, sends barely one photon per day per square centimeter in the range 0.1 – 100 GeV, corresponding to the range of the LAT. This translates in less than 6 photons per minute on average in the 8000cm² of the LAT. As a result, by the time Fermi was launched, only 7 gamma-ray emitting pulsars had been seen by its predecessor the Compton Gamma Ray Observatory (CGRO) and its instrument EGRET. At the time of writing these lines, 9 years later, the public list of LAT-detected pulsars indicates 205 detections¹⁰, including the seven previously known. Probably the main advantage of gamma-ray telescopes is that they allow to cover large portions of the sky at the same time, ideally close to 2π steradians. For instance, the LAT covers almost the full sky every 3 hours. This arises from the fact that there is no such thing as focus but just a bare detector without lenses or mirrors. The difference with a more conventional telescope is that the detector is not only able to detect the power received but also the direction in which each photon is arriving. In a conventional telescope, this role goes to lenses and mirrors that transform the angular direction of arrival in a two-dimensional mapping on the focal surface. In the case of the LAT, the detector is made of the converters that transform the photon in a pair of electron and positron which path can be tracked using layers of semi-conductors, thus obtaining the direction of the original photon. Finally, a calorimeter helps to determine the energy.

Above 100 GeV, space-based telescopes have too small a surface to efficiently detect a significant number of photons. Fortunately, the Earth atmosphere behaves like a huge converter for these photons which are converted into a shower of electrons and positrons which radiate Tcherenkov light that can be detected in optical/ultraviolet by networks of ground-based telescopes such as HESS, VERITAS or MAGIC. From the properties of the light and in particular the shape of the Cerenkov cone one can deduce the direction and energy of the incident photon. Similarly to space-based telescopes, photons have to be discriminated from a much larger flux of cosmic rays, which fortunately produce distinguishable showers. One usually refers to energies above 100 GeV as very-high energies while energies in the LAT range are high energies.

Detecting a pulsar does not only amount to detect photons, but also to detect pulsations from the star. This makes the task much harder for the photons are very sparsely distributed : with six photons per minute, the Crab undergoes about

¹⁰<https://confluence.slac.stanford.edu/display/GLAMCOG/Public+List+of+LAT-Detected+Gamma-Ray+Pulsars>

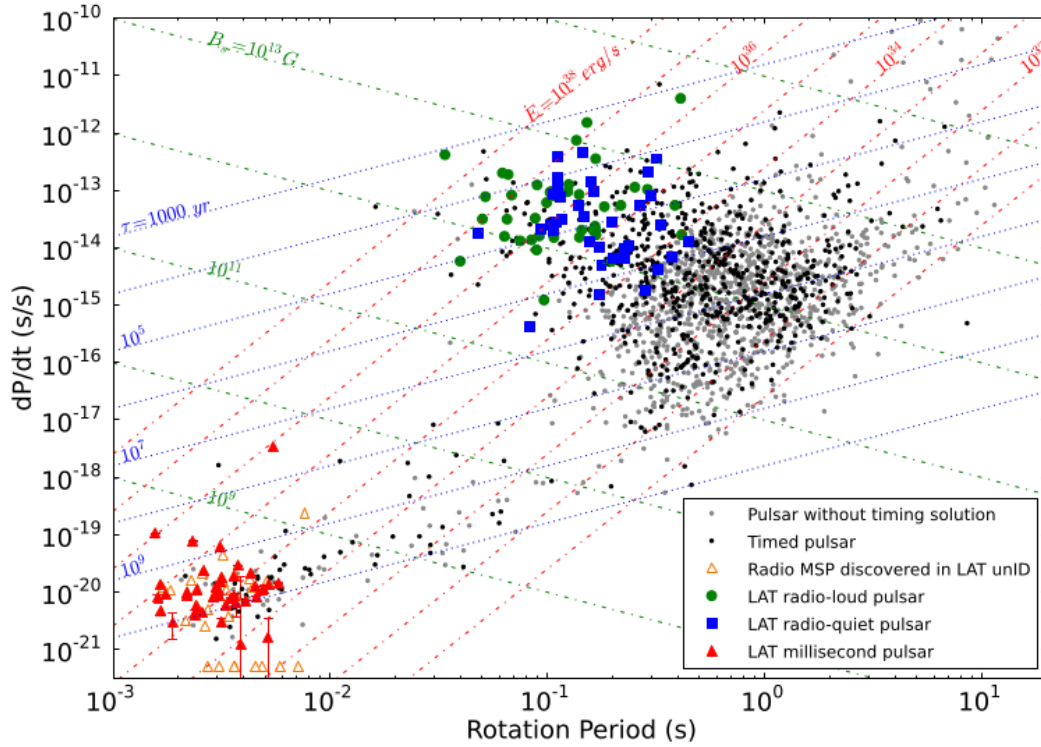


Fig. 1.9.: From The Fermi-LAT collaboration (2013). Pulsar spindown rate \dot{P}_* , vs. the rotation period P_* . Green dots indicate the 42 young, radio-loud gamma-ray pulsars and blue squares show the 35 young, « radio-quiet » pulsar, defined as S_{1400} is the radio flux density at 1400 MHz. The more recent *public list of LAT-detected gamma-ray pulsars* now claims the detection of 93 millisecond pulsars and 112 young pulsars. Red triangles are the 40 millisecond gamma-ray pulsars. The 710 black dots indicate pulsars phase-folded in gamma rays using rotation models provided by the « Pulsar Timing consortium » for which no significant pulsations were observed. Phase-folding was not performed for the 1337 pulsars outside of globular clusters indicated by gray dots. Orange open triangles indicate ratio millisecond pulsars discovered at the positions of previously unassociated LAT sources for which the LAT had not yet seen gamma pulsations at the time of writing The Fermi-LAT collaboration (2013). They are plotted at $\dot{P}_* = 5 \cdot 10^{-22}$ when \dot{P}_* is not available. Shklovskii corrections to P_* have been applied to the pulsars with proper motion measurements. For clarity, error bars are shown only for the gamma-detected pulsars.

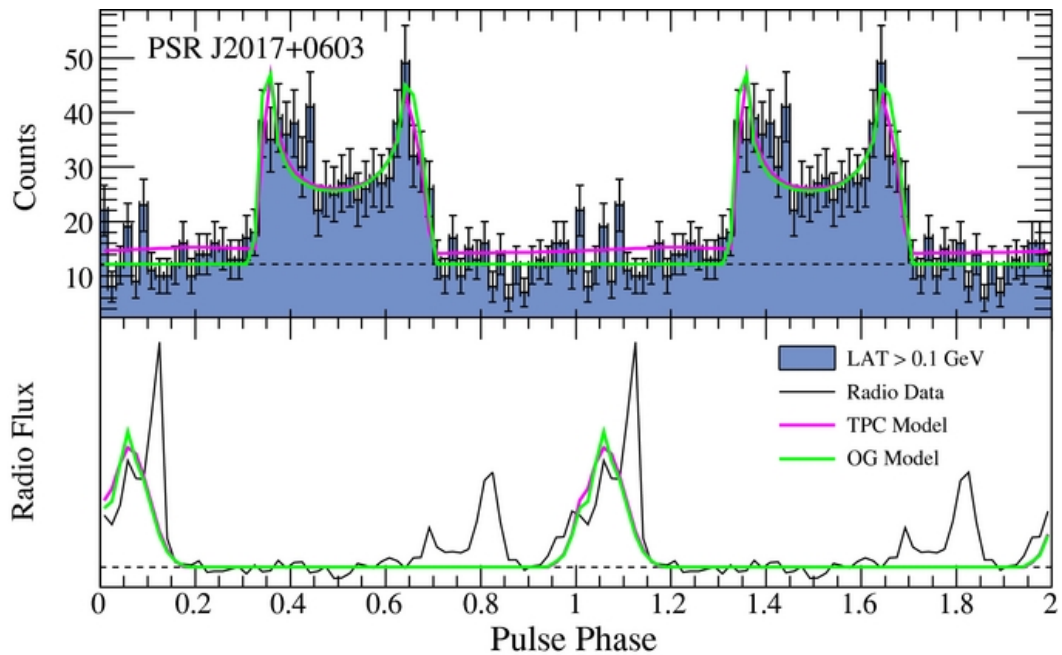


Fig. 1.10.: From Cognard et al. (2011). Top : gamma-ray data and modeled light curves for PSR J2017+0603 with 60 bins per rotation. Bottom : Nançay 1.4 GHz radio profile and modeled light curves. Modeled light curves were made using $\chi = 16^\circ, \zeta = 68^\circ$ and an infinitely thin gap for the two-pole-caustic model, and $\chi = 17^\circ, \zeta = 68^\circ$ and an infinitely thin gap for the outer gap geometry (see sections 2.3.4 and 2.3.5 and Cognard et al. (2011) for details on the models). The angle χ is the angle between the magnetic pole and the spin axis, the angle ζ is the angle made by the line of sight with the spin axis. The dashed horizontal line sets the background level.

300 rotations between each received photon, and some millisecond pulsars have single-pulse fluxes four orders of magnitude lower. Therefore, pulsation detection must be treated statistically. One tests the hypothesis that the events (the photons) result from a distribution against the hypothesis of a uniform random distribution, the so-called H test (Jager et al., 1989). Moreover, the discovery of pulsations owes a lot to radio, and to a lesser extent X-ray observations that provide ephemeris that greatly reduce the parameter space in the search for pulsations. Either the LAT detects gamma rays in directions coincident with known radio or x-ray pulsars, or radiotelescopes are pointed to unidentified LAT sources and sometimes discover a pulsar. In some cases, the pulsar is radio-quiet but sufficiently bright (young pulsars in particular) such that the ephemeris can be determined directly from the gamma observation (see the LAT radio-quiet pulsars on figure 1.9). The population of gamma-ray pulsars thus detected can so far be essentially divided into young pulsars and millisecond pulsars (figure 1.9). The latter category was quite a surprise and Fermi so far made possible the detections of dozens of new millisecond pulsars. As can be seen on figure 1.9, gamma-ray pulsars are preferentially high spindown power pulsars, with an observational death line around 10^{33} erg/s.

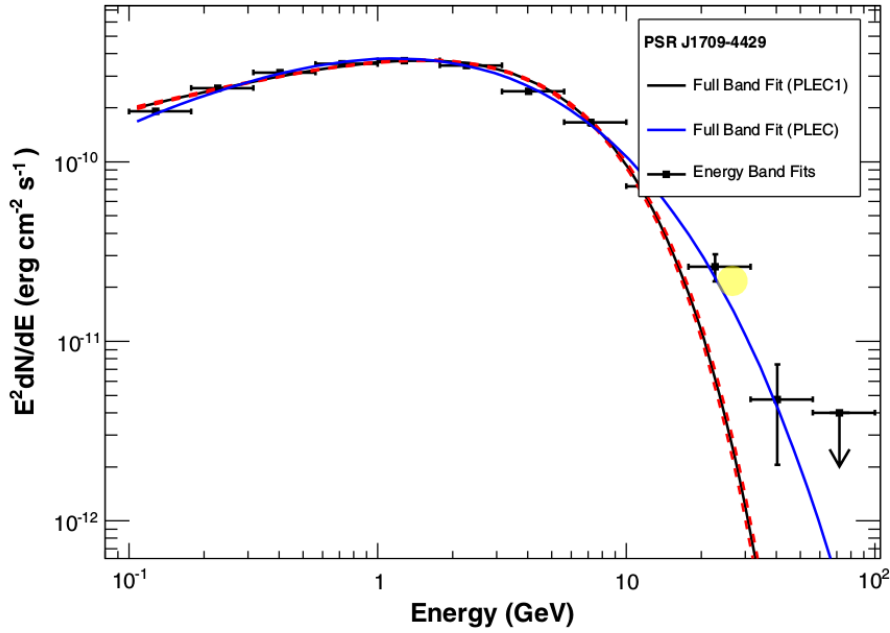


Fig. 1.11.: From The Fermi-LAT collaboration (2013). LAT spectrum of the young pulsar PSR J1709-4429. The black solid line curve shows the best fit with an exponential cutoff, $b = 1$ in equation (1.3) and the dashed red lines the 1σ confidence interval (very small in this figure). The blue solid line shows the result of the fit with free exponential cutoff parameter, which favors $b < 1$ in this case.

Gamma-ray light curves often show two peaks, with a significant bridge emission in between (see figure 1.10), although some pulsars also exhibit only one peak. This structure is usually explained geometrically by an emission originating from large regions of the outer part of the magnetosphere, and undergoing aberration and propagation delays that lead to the formation of caustics, namely phases at which gamma rays from different parts of the magnetosphere arrive at the observer at the same time, thus causing the peaks. Figure 1.10 shows fits of the gamma-ray light curve of PSR J2017+0603 (Cognard et al., 2011) by two popular models, the two-pole-caustic and outer gap models (see sections 2.3.4 and 2.3.5). These models are, in this case, unable to fit perfectly the gamma-ray light curve although they correctly account for the presence of two peaks, a bridge emission, and the correct separation between the two peaks. Besides, within the simple geometrical model of radio emission used by authors, the radio lag between the leading gamma-ray peak and the main radio peak is correctly accounted for. The radio lag and the phase difference between the two peaks appear to be correlated on large samples of pulsars and is a feature that can help discriminate between emission models (The Fermi-LAT collaboration, 2013).

Estimates of the gamma-ray luminosity are in the range $10^{-3} - 1L_{sd}$, where L_{sd} is the spindown luminosity (see table 1.1) making the gamma ray emission the main

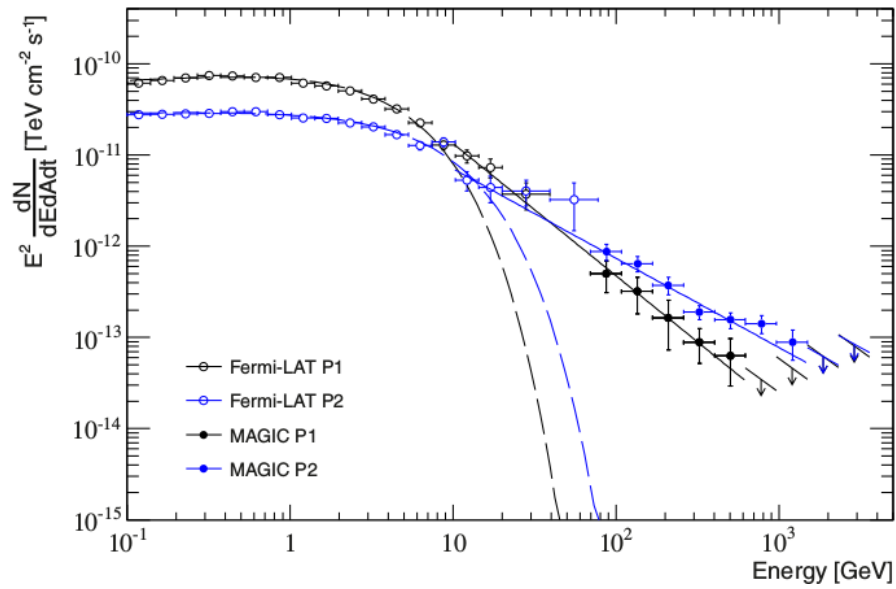


Fig. 1.12.: From Ansoldi et al. (2016). Phase-folded spectral energy distribution (SED) of the Crab first peak (P1, black circles) and second peak (P2, blue circles) at high energy and very high energy (open and filled circles). The results of the power law with exponential cutoff fits to the Fermi-LAT points are shown by dashed lines (Aleksić et al., 2014), whereas the joint Fermi-LAT/MAGIC fits to power-law functions above 10 GeV are shown by solid lines. The upper limits to the differential flux at 95% confidence level are computed under the assumption of the power-law spectrum found in Ansoldi et al. (2016), as represented by the slope of the arrows.

pulsed source of dissipation of spindown power before x-ray emissions and radio emissions. The distribution of gamma luminosities is peaked around $0.1L_{\text{sd}}$ (The Fermi-LAT collaboration, 2013). Note that estimating the gamma luminosity (or any other) suffers from systematic biases, in particular the poor knowledge of the angular distribution of the luminosity outside of the line of sight.

Gamma-ray photon emission spectra are usually fitted by expressions of the form (The Fermi-LAT collaboration, 2013)

$$\frac{dN}{dE} = K \left(\frac{E}{E_0} \right)^{-\Gamma} \exp \left(- \frac{E}{E_{\text{cut}}} \right)^b, \quad (1.3)$$

where N is the number of photons, E is the energy of the photon, E_0 and K are constants to be adjusted arbitrarily, Γ is the so-called photon index of the power-law part, E_{cut} sets the position of the exponential cutoff and b is the sharpness of the cutoff: $b = 1$ exponential cutoff, $b < 1$ subexponential and $b > 1$ super-exponential. The highest energy emission from the outer magnetosphere is usually expected to result from curvature radiation in the radiation reaction regime (see sections 2.2.2 and 2.3.2), with which the cutoff is exponential. However, a number of LAT pulsars such as the one the spectrum of which is presented on figure 1.11 show subexponential cutoffs. This can be due to a superposition of different regions of the magnetosphere each with a different exponential cutoff energy seen simultaneously, or can mean that some other mechanism has to be considered. Phase resolved spectroscopy can help solving this puzzle. The main and probably most studied such pulsar is probably the Crab for which phase resolved spectroscopy up to 400GeV was performed using data from the LAT and from the MAGIC Tcherenkov telescope (Aleksić et al., 2012). More recently, MAGIC also detected pulsed emission from the Crab up to 1.5 TeV, discarding exponential cutoff and preferring a broken power-law spectrum, figure 1.12. These discoveries discard the emission models based on pure curvature radiation and favor Compton scattering (see section 2.2.2). More generally, these findings are setting a stringent constraint on gamma-ray emission models (see the discussion section in Ansoldi et al. (2016) and section 2.3).

1.5 Neutron stars

¹¹ The concept of neutron stars appeared in the years 1930 as a purely theoretical answer to the question of the fate of massive stars after all thermonuclear source of energy has become exhausted. In particular Baade and Zwicky (1934) suggested

¹¹The present section draws largely from Özel and Freire (2016) for the current state of research in probing neutron star matter through observation, and from Lattimer and Prakash (2004) concerning the inferred properties of neutron star interiors. The reader can refer to these two reviews and references therein when no other reference is indicated in the text.

that supernovae could be the transition from a normal star to a body of much smaller mass. Although white-dwarf stars were known to be supported against gravity by the degenerate pressure of an electron condensate, it was not clear what happens to the matter beyond the maximum sustainable mass of a white dwarf, the so-called Chandrasekhar mass, $1.44M_{\odot}$. It had been suggested that a dense neutron core could be formed in the massive star residuals (in particular by Lev Landau and George Gamow, see references in Oppenheimer and Volkoff (1939)), the equilibrium of such a star was computed by Tolman (1939) and Oppenheimer and Volkoff (1939) assuming that the pressure results only from neutron degeneracy. However, such an equation of state results in a maximum mass of only $0.7M_{\odot}$, and the authors even concluded that « it seems unlikely that any neutron cores can play any great part in stellar evolution ».

The general scheme of calculation of Tolman (1939) and Oppenheimer and Volkoff (1939) was correct. The idea is to solve the equations of general relativity for the equilibrium of a self-gravitating fluid which microphysics (and so internal pressure) is characterized by an equation of state (EoS) relating the pressure P to the density of matter ρ . The effects of temperature are neglected in neutron-star EoS, and has to be taken into account only for proto-neutron stars during the supernova process when the matter is still very hot (up to tens of MeV). It turned out that equations of state must take into account strong interactions between nucleons that are believed to result from quantum chromodynamics. It is still an open problem to know what the correct theory of the strong interaction is, and probing the structure of neutron stars is a constraint on this way. Nowadays, experiments on heavy nuclei give strong constraints on the nature of the equation of state in laboratory conditions, namely for nuclei with a density corresponding to nuclear saturation density $\rho_0 = 2.8 \cdot 10^{14} \text{g cm}^{-3}$ and a proton/neutron ratio $x \sim 1/2$. For higher densities and small ratios, as is expected to be the case in astrophysical neutron stars, the nature of the equation of state is an open problem. Since no experiment under such conditions can be performed on Earth, the development on this question relies mostly on astrophysical observations and intense theoretical developments. It results in a broad variety of equations of state having been proposed (see figure 1.13 (b) and Özel and Freire (2016)).

Qualitatively, astrophysical neutron stars are made of a superfluid core and a crust, with masses in the range $1 - 2M_{\odot}$, radii in the range $10 - 20\text{km}$, and average density $\sim 2\rho_0$. In the core, the density can reach $5 - 10\rho_0$ and matter is composed of a mix of nucleons, electrons and muons with a small x ratio. This core contains 99% of the mass of the star, owing to its super-nuclear density. The crust surrounds the core and is around $\sim 1 - 2\text{km}$ thick. It undergoes a sequence of phase transitions from a nuclear density “Swiss cheese” (packed nucleons with voids) at the interface with the core to a usual ${}^{56}\text{Fe}$ iron lattice on the surface of the star. The nucleon ratio

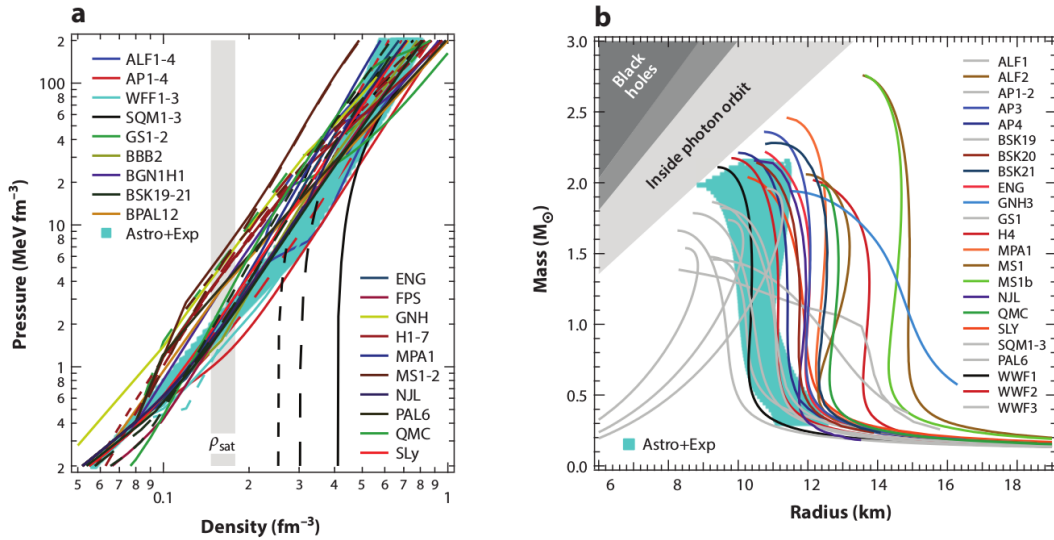


Fig. 1.13.: From Özel and Freire (2016). The astrophysically inferred (a) EoS and (b) mass-radius (M-R) relation corresponding to the most likely triplet of pressures that agree with all of the neutron-star radius and low-energy nucleon-nucleon scattering data and allow for an $M > 1.97M_{\odot}$ neutron-star mass. The light blue bands show the range of pressures and the M-R relations that correspond to the region of the parameter space in which the likelihood is within e^{-1} of its highest value. Around $1.5M_{\odot}$, this inferred EoS predicts radii in the range of 9.9 – 11.2km.

also rises from the inside to the outside. The neutrons form a superfluid loosely bound to the crust. As a result a differential rotation can develop between the crust and the neutron superfluid that can be suddenly caught up. This is believed to be the mechanism behind the observed glitches of some pulsars which are sudden decreases of the rotation period of the pulsar.

It has been shown that there is a one-to-one correspondence between the EoS and the relation between mass and radius. Thus, measuring these two quantities for observed neutron stars gives a direct window on the physics of matter at supernuclear densities. A noticeable characteristic of the mass-radius relation is that the radius of the star diminishes when the mass increases in most equations of state. Further, the radius is fairly constant on the astrophysical range of masses (see figure 1.13 (b)). The maximum mass reachable by a given equation of state must cope with observations. Currently, the most massive neutron-star mass measured with precision is $2M_{\odot}$, thus putting aside a number of incompatible EoS (assuming that all neutron stars have the same EoS). Moreover, EoS have to be compatible with the observed fast rotation of millisecond pulsars (up to 700Hz observed). This implies that the radii cannot be too large, or otherwise centrifugal forces may overcome gravity and the star starts to shed mass away. A good order of magnitude is given by the keplerian rate $\sqrt{GM_*/R_*^3}/(2\pi) = 1833(M_*/M_{\odot})^{1/2}R_{*4}^{-3/2}\text{Hz}$, and Lattimer and Prakash (2004) have shown that once general relativity and deformation of the star

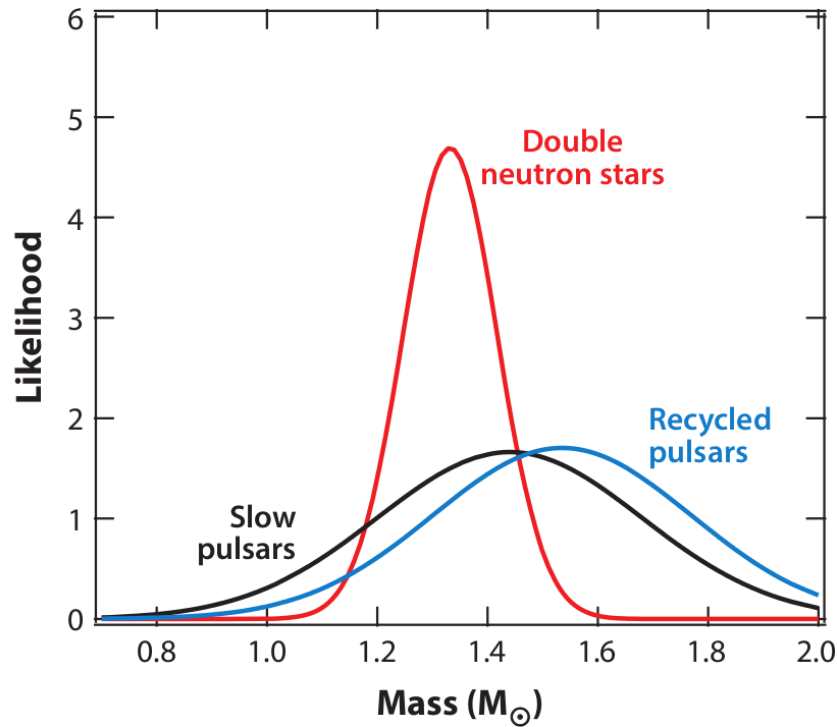


Fig. 1.14.: From Özel and Freire (2016). Mass distribution of the different types of neutron stars, inferred from the available set of measurements assuming a Gaussian distribution.

are taken into account this turns into approximately $1045(M_*/M_{\odot})^{1/2}R_{*4}^{-3/2}$ Hz plus small variations due to the EoS. Further, using bayesian techniques to sample the most likely equations of states based on the measured masses and radii, one can define the area of most likely EoS given the data currently available (blue areas on figure 1.13).

The measurement of the neutron-star masses is fortunately available for a few of them, > 60 at present, and pulsar timing yields precise measurements in ~ 30 cases. One can distribute neutron stars into three kinds, slow, recycled, double, and assume that the statistical distribution of each kind is well represented by a Gaussian. Figure 1.14 shows that each resulting distribution is consistent with the assumed accretion history of each kind: slow pulsars were not recycled and are thus probably closer to the mass at birth of neutron stars, recycled pulsars had a lengthy accretion phase which gives them a larger average mass, and stars in a double neutron-star system display a lighter average mass and narrower dispersion probably related to a specific evolution history. Assuming that each kind of neutron star follows its own Gaussian distribution of masses one can infer these distributions from the available measurements, figure 1.14. The measurement of neutron-star radii is more difficult, as it requires observing the direct thermal x-ray emission from the star. Owing to the extreme smallness of the star, this radiation is not always detectable, and even if it

is, it is not straightforward to interpret since complex-radiation-transfer mechanisms occur in the atmosphere that significantly distort the spectrum and the light curve. Overall, the dozen of known radii fall in the 10 – 11.5 km range.

The name neutron star might eventually have to be replaced by the term strange-quark-matter stars (SQM stars). Indeed, it has been conjectured that the ground state of matter could be quark matter with up, down and strange quarks, having greater binding energy at zero pressure than iron nuclei. In such case, the binding energy of matter is sufficiently strong to avoid the need of gravity to keep the star together. A striking consequence is visible on the mass-radius diagram as the fact that the radius grows with mass along most of the curve except at the highest masses (see SQM1-3 EoS curves on figure 1.13 b).

Pulsar electrodynamics

2.1 The global electrodynamical problem in vacuum

2.1.1 The canonical model of electromagnetic field inside the star

In order to determine the electromagnetic field in the magnetosphere, it is necessary to determine the boundary conditions applicable on the surface of the star and far away from the star. At a large distance from the star ($\gg R_{LC}$), the boundary conditions may be determined by the presence of a nebula, or by the interstellar fields otherwise. For simplicity, we shall consider that the system is isolated and the electromagnetic field cancels at infinity.

Knowing the conditions at the surface of the star supposes to have at least rudimentary model of the field inside the star. Since the earlier work of Pacini, 1967 (so even before the actual discovery of pulsars), the model of a very strong dipolar magnetic field in the magnetosphere has become almost canonical. Presumably, the magnetization of the matter of the star is very low compared to the intensity of the magnetospheric dipolar field, and therefore it makes sense to assume a dipolar field (which is a vacuum solution) inside the star as well. A uniform magnetization of the star is also a common assumption (Michel and Li, 1999). Moreover, the star is approximated as an excellent conductor. The shape of the star must be very close to axial symmetry around the rotation axis, as otherwise intense gravitational radiation would ensue (Shklovskii, 1970) and slow the pulsar down. Besides, spherical symmetry is a reasonable approximation in particular for slow pulsars, probably less for millisecond pulsars which may be deformed by centrifugal forces. Thus, the problem we tackle here is that of a rotating spherical perfect conductor with a strong dipolar magnetic field, problem very similar to that of Faraday disks (also called unipolar inductors).

The very slow decay of the rotation period compared to the period itself, of the order of 10^{-15}s^{-1} in our typical case, allows to consider that the charged fluid inside the star (say electrons) is corotating with the star. If we neglect any other forces, such

as gravity or centrifugal forces, infinite conductivity results in a null electric field in the instantaneous inertial frame of an element of the fluid

$$\vec{E}'_i = 0. \quad (2.1)$$

Corotation of a fluid at position \vec{r} inside the star results in a speed $\vec{v} = \vec{\Omega}_* \times \vec{r}$. It follows that the electric field \vec{E} in the frame of an observer whose frame is attached to the center of inertia of the star is defined by

$$\vec{E}'_i = \vec{E}_i + (\vec{\Omega}_* \times \vec{r}) \times \vec{B} = 0 \quad (2.2)$$

inside the star, with \vec{B} the magnetic field in the frame of the observer.

In what follows we consider that \vec{B} is a dipolar magnetic field localized at the center of the star, and to simplify calculations consider that the magnetic momentum \vec{m} is aligned with the spin of the star $\vec{\Omega}_*$ with $\vec{m} \cdot \vec{\Omega}_* > 0$. Besides, any general relativity effect is neglected. This case is common in the literature from the very first pulsar theories (e.g. Ostriker and Gunn, 1969, Goldreich and Julian, 1969). We present it here for its relative mathematical simplicity, considering that it contains most of the general procedure for deriving electromagnetic fields around pulsars and already some of the key physical elements of more general theories, as we shall see. However, it is clear that such an "aligned pulsar" would in fact not pulse and so this treatment is necessarily incomplete. This problem can be treated in different manners that give the same result (Michel and Li, 1999). The magnetic field reads

$$\vec{B} = B_* \frac{R_*^3}{r^3} \left(\cos \theta \vec{e}_r + \frac{1}{2} \sin \theta \vec{e}_\theta \right), \quad (2.3)$$

where $B_p = \mu_0 |\vec{m}_*| / (4\pi R_*^3)$ is the intensity of the field at the north pole, R_* the radius of the star, and $(\vec{e}_r, \vec{e}_\theta, \vec{e}_\phi)$ is the right-hand-side oriented base vectors in spherical coordinates. The electric field inside the star is directly obtained from (2.2)

$$\vec{E}_i = B_* \frac{R_*^3}{r^3} \Omega_* r \sin \theta \left(\frac{1}{2} \sin \theta \vec{e}_r - \cos \theta \vec{e}_\theta \right). \quad (2.4)$$

The ratio between electromagnetic forces and gravitational forces can be estimated to be

$$\frac{|e| B_* R_* \Omega_*}{GM_* m_e / R_*^2} = 6 \cdot 10^{11} B_{p8} P_{*1} R_{*4}^3 \left(\frac{M_*}{1.4 M_\odot} \right)^{-1}, \quad (2.5)$$

where m is the mass of the electron. This justifies neglecting of non-electromagnetic forces.

From the electric field (2.4), we derive the potential on the surface

$$\phi(R_*, \theta) = -\frac{1}{2} B_* R_*^2 \Omega_* \sin^2 \theta. \quad (2.6)$$

The charge inside the star can be calculated using Gauss's theorem,

$$Q_i = \frac{4\pi}{3} \epsilon_0 B_* R_*^3 \Omega_*. \quad (2.7)$$

This is not the net charge of the star. Indeed, a surface charge appears depending on the conditions outside the star that can compensate for Q_i . We will see an example in the next section.

2.1.2 The Poisson equation with corotation charge density

Another way of considering the previous results is through the Poisson equation, considering that owing to cylindrical symmetry this amounts to an electrostatic problem. In the observer's reference frame, the total electrostatic potential ϕ_T is equal to the particular solution corresponding to (2.6) on the surface of the star plus a homogeneous solution ϕ_0 ,

$$\phi_T = \phi + \phi_0. \quad (2.8)$$

Applying Laplace's operator to equation (2.8) one obtains

$$\Delta \phi_0 = -\frac{\rho_T - \rho_c}{\epsilon_0} = 0, \quad (2.9)$$

where $\rho_T = -\epsilon_0 \Delta \phi_T$ is the total charge density and $\rho_c = -\epsilon_0 \Delta \phi$ is the corotation charge density

$$\rho_c = \epsilon_0 \vec{\nabla} \cdot \vec{E}_i = -2\epsilon_0 \frac{\vec{\Omega}_* \cdot \vec{B}}{1 - (\vec{\Omega}_* \times \vec{r})^2 / c^2}. \quad (2.10)$$

Notice that this density is well approximated by $\rho_c \simeq -2\epsilon_0 \vec{\Omega}_* \cdot \vec{B} + \circ(\Omega_* r / c)$ as long as the corotation speed is small compared to the speed of light.

The charge density ρ_c is the charge density necessary to sustain the corotation electric field (2.4). Besides, we will see in section 2.3.2 that when $\rho_T \neq \rho_c$, equation (2.9) for ϕ_0 gives the solution of the electrostatic potential in the rotating frame while ρ_c is the effective charge density arising from the change of frame to the non-inertial rotating frame. Said differently, an observer in the corotating reference frame sees a charge density $\rho_T - \rho_c$ while an observer in the inertial frame of the star sees ρ_T . If $\rho_T = \rho_c$ as is the case in the present section, the total potential in the corotating frame is that of a vacuum electrostatic boundary problem.

On the surface of the star, the homogeneous solution satisfies $-\nabla \phi_0(r = R_*, \theta) = 0$ since $-\nabla \phi_T = \vec{E}_i(r = R_*, \theta)$, and from equation (2.9) $\Delta \phi_0 = 0$. It follows that the

homogeneous solution is a constant ϕ_0 (see also equation (2.12) for the general form of the homogenous-Poisson-equation solution in cylindrical symmetry),

$$\phi_T(R_*, \theta) = \phi_0 - \frac{1}{2}B_*R_*^2\Omega_* \sin^2 \theta. \quad (2.11)$$

2.1.3 The vacuum field outside the star for the aligned rotator

We now assume vacuum outside the star. The electric potential is therefore a solution of Laplace's equation $\Delta\phi = 0$. For axial symmetry in spherical coordinates it has the form

$$\phi(r > R_*, \theta) = \sum_{l=0}^{\infty} \left(\frac{A_l}{r^{l+1}} + B_l r^l \right) P_l(\cos \theta), \quad (2.12)$$

where A_l, B_l are constants depending on the limit conditions, and $P_l(x)$ are Legendre polynomials. Boundary conditions are set by (2.11) on the surface of the star and by 0 at $r \rightarrow \infty$. It follows that the electric potential outside the star is given by a monopole ($l = 0, B_l = 0$) and a quadrupole ($l = 2, B_l = 0$)

$$\phi(r > R_*, \theta) = \phi_0 \frac{R_*}{r} - \frac{1}{3}B_*R_*^2\Omega_* \frac{R_*^3}{r^3} P_2(\cos \theta), \quad (2.13)$$

where $P_2(x) = \frac{1}{2}(3x^2 - 1)$.

This solution implies surface charge on the star which shields the outer side from the inner side

$$\sigma = \epsilon_0 \left(\vec{E}(R_*^+) - \vec{E}(R_*^-) \right) \cdot \vec{e}_r = \underbrace{\epsilon_0 \frac{\phi_0}{R_*}}_{\sigma_1} - \underbrace{\epsilon_0 B_* \Omega_* R_* \cos^2 \theta}_{\sigma_2}, \quad (2.14)$$

where $\vec{E}(R_*^+)$ is the electric field for $r \rightarrow R_*^+$ and $\vec{E}(R_*^-) = \vec{E}_i(R_*)$ for $r \rightarrow R_*^-$. The total monopolar charge on the surface is given by

$$Q_1 = \int \sigma_1 dS = 4\pi\epsilon_0\phi_0, \quad (2.15)$$

and the total quadrupolar charge on the surface is given by

$$Q_2 = \int \sigma_2 dS = -Q_i, \quad (2.16)$$

Therefore, the net charge of the star is given by $Q_1 + Q_2 + Q_i = Q_1$.

The general vacuum solution (2.13) can then be written as a function of the net charge Q_1

$$\phi(r > R_*, \theta) = -\frac{Q_1}{4\pi\epsilon_0 R_*} \frac{R_*}{r} - \frac{1}{3} B_* R_*^2 \Omega_* \frac{R_*^3}{r^3} P_2(\cos \theta). \quad (2.17)$$

With this model, the electromagnetic field outside the star is entirely determined by the dipolar magnetic-field strength at the pole B_* , the radius of the star R_* , the pulsation Ω_* and the net charge of the star Q_1 . Note that there is no discontinuity of the magnetic field from surface currents between the inside and the outside of the star since we implicitly assumed that the inner magnetic properties of the star are that of vacuum (a dipolar field being a vacuum solution).

Contrary to inside the star, the electric field outside is partly aligned with the magnetic field: $\vec{E} \cdot \vec{B} \neq 0$. Moreover, its amplitude is given by

$$E \sim B_* \Omega_* R_* \simeq 6 \cdot 10^{12} P_1^{-1} B_{*8} R_{*4} \text{V/m} \quad (2.18)$$

just above the surface.

2.1.4 Basic dipolar field geometry : last open field lines, polar cap, curvature radius

In the next sections we will often need a few geometrical concepts, namely the last open field lines, the polar cap, and the curvature radius. In a general rotating plasma-filled magnetosphere I am not aware that these concepts have any simple expression. However, one can find simple order-of-magnitude expressions by considering a pure magnetic dipole, which physically corresponds to the case of a vacuum aligned rotator.

The magnetic (static) dipole of magnetic moment \vec{m} at point \vec{x} reads

$$\vec{B} = \frac{\mu_0}{4\pi} \frac{3\vec{n}(\vec{n} \cdot \vec{m}) - \vec{m}}{\|\vec{x}\|^3} \quad (2.19)$$

where $\vec{n} = \vec{x} / \|\vec{x}\|$.

It is axisymmetric around \vec{m} and can be expressed in polar coordinates

$$\vec{B} = \frac{\mu_0 m}{4\pi \|\vec{x}\|^3} (2 \cos \theta \vec{e}_r + \sin \theta \vec{e}_\theta) \quad (2.20)$$

where θ is taken with respect to the magnetic moment, and $m = \|\vec{m}\|$. In the case of a star of radius R_* , the magnetic moment can be expressed as a function of the magnetic field intensity at the pole B_* or at the equator B_{*e} by

$$m = M_* = \frac{4\pi}{\mu_0} B_{*e} R_*^3 = \frac{2\pi}{\mu_0} B_* R_*^3. \quad (2.21)$$

Magnetic field lines \vec{l} along a curvilinear abscissa s are defined by $d\vec{l}/ds \propto \vec{B}(\vec{l})$. In polar coordinates, $\vec{l} = r(\theta)\vec{e}_r(\theta)$ we obtain the system

$$\frac{dr}{ds} = \frac{2 \cos \theta}{r^3}, \quad (2.22)$$

$$r \frac{d\theta}{ds} = \frac{\sin \theta}{r^3}, \quad (2.23)$$

where we dropped the prefactor $\frac{\mu_0}{4\pi}$. By dividing equation (2.22) by (2.23) and separating the variables one finds that the field lines are defined by

$$\frac{r}{r_0} = \frac{\sin^2 \theta}{\sin^2 \theta_0}. \quad (2.24)$$

Open magnetic-field lines exist when the line path is not causally connected to itself. In rotating magnetospheres, this happens when a line goes out of the light cylinder, in which case the information about the location of the foot of the line would have to propagate faster than light for the line to close. Instead, it extends, “closes”, at infinity. In the case of a vacuum dipole magnetosphere, open field lines exist only if the dipole is not aligned because of the cylindrical symmetry of the aligned case. However, one can contemplate a plasma-filled corotating magnetosphere with a background aligned magnetic dipole (Goldreich and Julian, 1969). In this case matter trails the magnetic field that becomes toroidal near the light cylinder and open magnetic-field lines form. In both cases, the locus of the feet of the open field lines defines the polar cap.

The boundary of the polar cap is defined by the crossing of the field lines tangent to the light cylinder with the surface of the star, also called last open field lines. In the case of an aligned rotator, although there is strictly speaking no open field lines (in vacuum), this “boundary” is defined by $(r_0 = R_{\text{LC}}, \theta_0 = \pi/2)$ in equation (2.24) which gives the opening angle of the polar cap (putting $r = R_*$)

$$\theta_c = \arcsin \left(\frac{R_*}{R_{\text{LC}}} \right)^{1/2} \simeq \left(\frac{R_*}{R_{\text{LC}}} \right)^{1/2}, \quad (2.25)$$

where $R_{\text{LC}} = c/\Omega_*$ is the light cylinder radius, and we used the fact that in general $R_*/R_{\text{LC}} \ll 1$. Equation (2.25) gives a good estimate at a few tens of percent of the polar caps sizes in the aligned filled case or in the inclined dipole case (see below).

It is also useful to know the radius of curvature of the field lines, which is given for a curve in polar coordinates by

$$\rho = \frac{(r'^2 + r^2)^{3/2}}{2r'^2 + r^2 - rr''}, \quad (2.26)$$

with $r' = dr/d\theta$, $r'' = d^2r/d\theta^2$. In the present case this gives

$$\frac{\rho}{R_{\text{LC}}} = \sqrt{\frac{r}{R_{\text{LC}}}} \frac{(4 - 3r/R_{\text{LC}})^{3/2}}{3r/R_{\text{LC}} - 6}, \quad (2.27)$$

and in particular at the surface of the star the radius of curvature of the last open magnetic field is given by

$$\frac{\rho_c}{R_{\text{LC}}} = \frac{4}{3} \left(\frac{R_*}{R_{\text{LC}}} \right)^{1/2} + \mathcal{O} \left(\frac{R_*}{R_{\text{LC}}} \right)^{3/2} \simeq \frac{4}{3} \theta_c. \quad (2.28)$$

The case of an inclined dipole can be studied numerically (see e.g. (Arendt and Eilek, 1998; Cheng et al., 2000)) and is of prime importance for some models, in particular outer-gap models (see section 2.3.5). The most affected field lines are those which go close or beyond the light cylinder since a toroidal component adds up to the field until it forms the so-called Parker's spiral at distances much larger than the light cylinder. It results in the shape and size of the polar cap being affected, however by a limited amount. Its size changes by $\sim 30\%$ maximum, depending on dipole inclination, and its shape becomes non-circular. One even notices the appearance of a dip on the leading edge of the cap, particularly visible in the perpendicular rotator case shown on figure 2.1. On this figure is also shown the bundle of last open field lines in the perpendicular case. Its most noticeable property is probably the fact that the whole bundle is gathered into two wings that sweep the light cylinder. It was realized using the solution of Bonazzola et al. (2015) (see Pétri (2015) for another derivations), numerically solving the field lines using the python library Numpy¹, and solving by dichotomy at each magnetic azimuth for the angle of the foot from the magnetic pole.

¹See www.numpy.org.

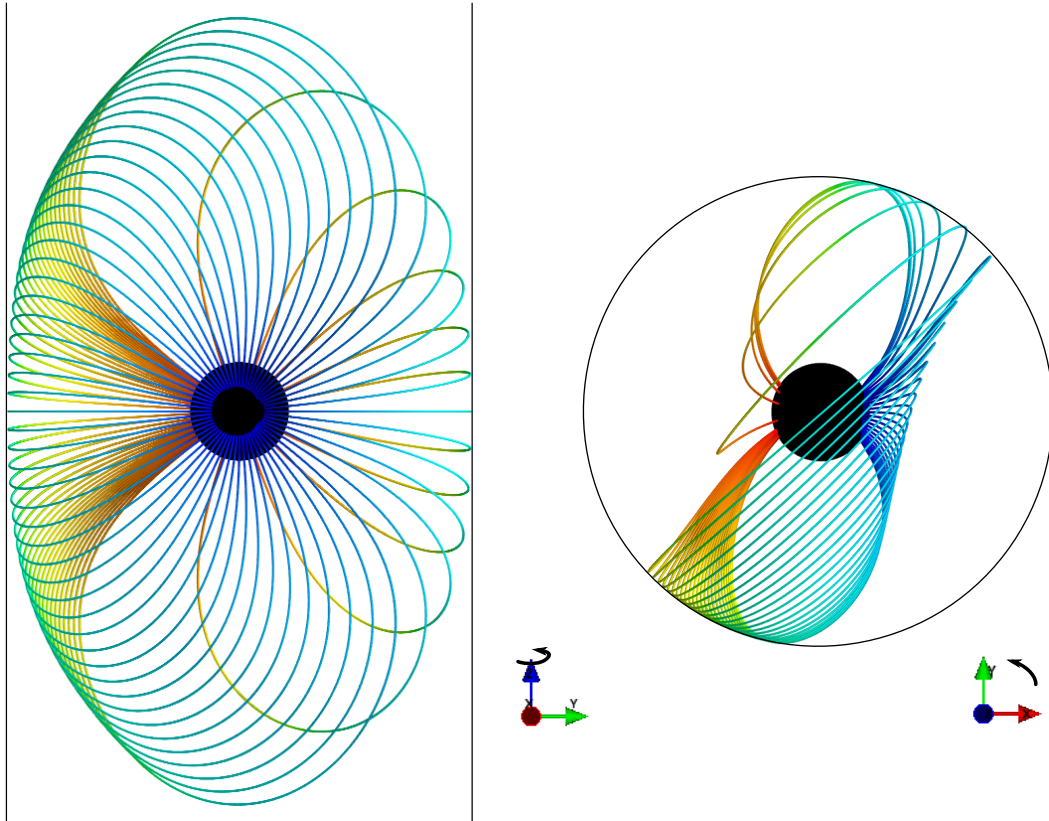


Fig. 2.1.: Last open field lines of a perpendicular vacuum dipole rotating with a period of 1 millisecond giving a small $R_{LC}/R_* \simeq 4.8R_{*4}^{-1}$. The spin axis is z and the magnetic axis is x , the star rotates anti-clockwise, from x to y . The field lines go from blue to red as they go from the north pole (x) to the south pole ($-x$). Sixty lines are plotted with their foot evenly spaced in azimuth around the north pole. The star is the black disk, and the light cylinder is delimited by black solid lines. The direction of rotation is shown black arrows next to the orientation landmark. *Left-hand side panel* : View facing the magnetic pole (x towards the reader). The polar cap is clearly visible at the base of the field lines, with a dip on the leading edge. *Right-hand side panel* : View facing the spin axis (z towards the reader).

2.2 Plasma filling and high-energy mechanisms

The problem becomes more delicate when one starts to consider the sources of matter. Indeed, it is an open problem to determine what kind of particles are making the plasma, and where they come from. It is usually considered that three particles may be present : ions (mostly iron), electrons and positrons. Medlin and Lai 2007 show that for typical pulsar parameters a gaseous atmosphere of ions and electrons forms above the star (if $T_* > T_c = 6 \cdot 10^5 \text{K}$ for $B = 10^8 \text{T}$) therefore filling the magnetosphere. Their results validate the early assumptions of Ruderman (1974). On the other hand, in the case of a condensed and rather cold surface, the electron work function ($\sim 100 \text{eV}$ for $B = 10^8 \text{T}$) may be too high to provide plasma to the magnetosphere.

2.2.1 Plasma from the crust

The possibility of filling the magnetosphere directly from the crust depends essentially on four parameters : the temperature of the crust, the work functions of electrons, the cohesive energy of the atoms, and the energy barrier of ions. The work function is defined as the energy necessary to pull out an electron from the material to infinity. The cohesive energy gives the energy necessary to pull out an atom out of the bulk condensed matter at zero pressure. The energy barrier can be defined as the energy necessary to eject a neutral atom from the surface, ionize it and gain back energy by returning the electrons to the surface. It is related to the cohesive energy, the ionization energy, the electron work function and the number of charges.

If ions or electrons can be extracted from the crust, it is not by the electric field (e.g. (2.18)), which by definition does not penetrate inside a perfect conductor (assumption for the crust). Therefore extraction is mostly a thermal process, and the electric field picks up the charges once they are out until it is eventually short out if too many charges are present. This leads to a space-charge limited flow above the star (section 2.3.3). In this case an equilibrium is reached and the plasma outside the star nearly satisfies the corotation current. In normal pulsars, with $\vec{\Omega}_* \cdot \vec{B} > 0$, the electric field above open field lines take electrons away. In antipulsars, $\vec{\Omega}_* \cdot \vec{B} < 0$, ions are taken away.

If the temperature is high enough, one expects (Medin and Lai, 2007) that the surface of the star vaporizes and forms an atmosphere of heavy ions (carbon, oxygen, iron..) and electrons. One can consider the work function to be virtually zero, and as many charges as necessary can be extracted until the corotation condition is achieved (see next section). In this case the low-altitude part of the magnetosphere

is the direct continuation of the plasma inside the star (in the corotating model of section 2.1.1).

If the temperature is below the sublimation temperature, then electrons and ions inside the crust have to overcome their work function. Again, this can be done if the temperature is high enough (but lower than the sublimation temperature) such that thermal excitation is able to provide enough charges with the right amount of energy to escape the material.

Unfortunately, it is impossible to obtain experimental data on the properties of matter in such intense magnetic fields, high temperature and gravitational field. However theoretical predictions are possible. As Ruderman, 1974 puts it in one of the early papers about the theory of matter in intense magnetic fields : « The nature of such matter seems reasonably susceptible to detailed analysis, if worth the effort. » however noting that « Any possible effects on observations or electrodynamics is much less clear. ». The basic idea of such calculations has remained the same since the early days : in a very intense magnetic field such that the magnetic length scale $\lambda = \sqrt{2\hbar/(eB)}$ (giving the minimal extent of the electron wavefunction) be much smaller than the Bohr radius of atoms, which happens for $B_0 = 10^5$ Teslas, the matter can be treated as lying on Landau states (quantized cyclotron orbits) of the magnetic field, only perturbed by the electric field of the atoms. This applies well at the surface of the neutron star, but the increasing density inside the star makes the contribution of magnetic field to the equation of state inside the star small (Lai, 2001).

Recent results (Medin and Lai, 2007) give the following orders of magnitude :

- An iron surface under $5 \cdot 10^8$ T vaporizes at $T_{Fe} \simeq 6 \cdot 10^5$ K, carbon at $T_C \simeq 2 \cdot 10^5$ K, and helium at $T_{He} \simeq 10^5$ K.
- If the matter is in a condensed state the electron work function has to satisfy $\phi \lesssim 3T_6$ keV where $T_6 = T/(10^6$ K) to furnish the corotation current. At $B = 10^8$ T, $\phi \sim 100$ eV. Therefore, an abundant flow of electrons can be extracted in most pulsars.
- If the matter is in a condensed state, the ion energy barrier has to satisfy $\phi_B \lesssim 3T_6$ keV to furnish the corotation current. Ion energy barriers can be higher or lower, as shown on figure 2.2.

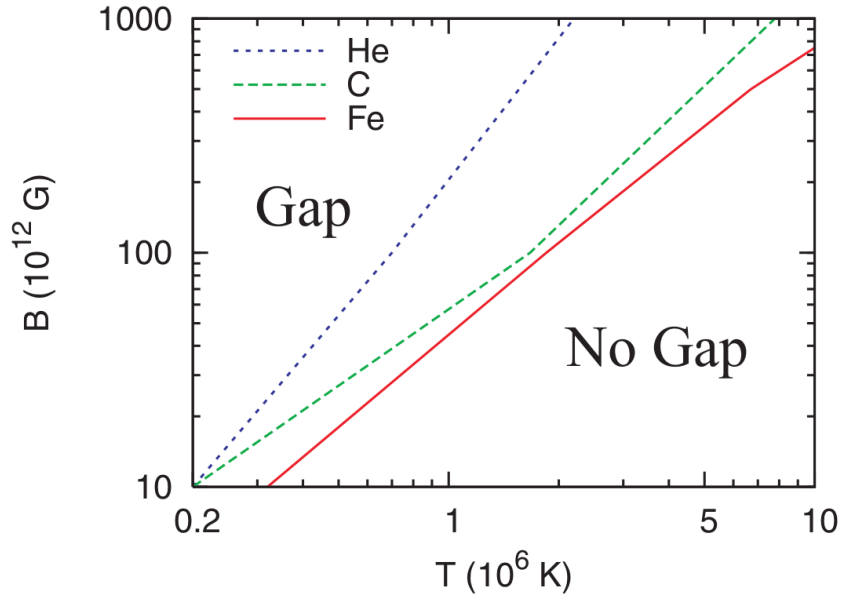


Fig. 2.2.: Domain of parameter in magnetic field intensity and temperature where a gap may form above the surface of an antipulsar for different types of surface material, from Medin and Lai (2007). No gap forms if the thermal emission of ions is strong enough to provide the corotation current.

2.2.2 Photon radiation mechanisms

We overview here the main radiation mechanisms that take place in pulsar magnetospheres. The mechanism of photon splitting (Harding et al., 1997), in which a photon interacts with the strong magnetic field of the pulsar, is not considered. It is really important for magnetic field above the critical value $B_c = 4.4 \cdot 10^9$ T and starts to become important for magnetic field strength $\gtrsim 10^9$ T, which is fairly above the values inferred for most pulsars.

Curvature, synchrotron and synchrocurvature radiations

Within classical electrodynamics curvature, synchrotron, or synchrocurvature radiations all result from the same paradigm : “an accelerated charged particle radiates.”. If one adds the approximation “radiation does not backreact on the motion of the particle” then the classical problem amounts to choose, arbitrarily or not, a trajectory for the particle and to compute the outgoing radiation. Curvature and synchrotron radiation result from a circular trajectory. In the case of synchrotron, this trajectory corresponds to the motion of the particle in a constant, uniform, magnetic field. In the case of curvature, one assumes the motion of the gyrocenter of the particle in a circular (at least locally) magnetic field, thus assuming the gyro-motion is completely negligible. The synchrocurvature takes into account the two components assuming

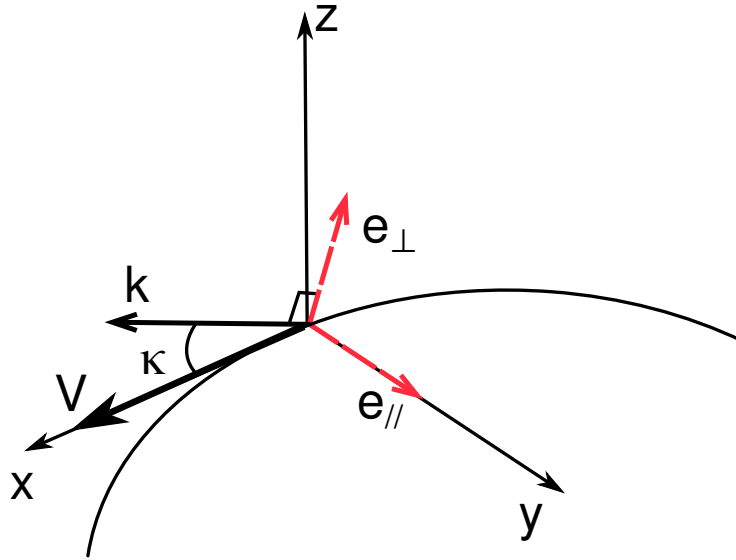


Fig. 2.3.: Polarization basis for radiation from a charge moving along a locally circular trajectory. The electromagnetic radiation has a wave vector \vec{k} . The base vector x is along the instantaneous velocity V , y points towards the instantaneous center of the trajectory, and z completes the direct basis (x, y, z) . The radiation has a wave vector \vec{k} making an angle κ with the velocity in the plane (x, z) . The polarization basis (red dashed) is made of the parallel polarization \vec{e}_{\parallel} along the y vector and of the perpendicular polarization that completes the direct basis $(k, \vec{e}_{\parallel}, \vec{e}_{\perp})$.

the full solution of the motion in a circular magnetic field, within the limit that the perpendicular momentum p_{\perp} (relative to the direction of the local field) be small compared to the longitudinal component p_{\parallel} , that is

$$p_{\perp} \ll p_{\parallel}. \quad (2.29)$$

The theory is carried out from the Liénard-Wiechert retarded potential (see e.g. Jackson (1998)) and has been carried out in particular in Schwinger (1949). The Liénard-Wiechert potentials generalize the usual electric and magnetic potentials of electrostatics to the case of a particle moving with at relativistic speed by taking into account the propagation delays : namely the fact that the fields an observer at a distance d from the particle can measure at a time t was radiated by the particle at $t' = t - d(t')/c$. With these potentials, one computes the Poynting flux at large distances $\vec{S} = \vec{E} \times \vec{B}/\mu_0$. Its Fourier transform then gives the power spectrum.

If one assumes that the trajectory is circular, then one can compute the radiation only for wave vectors in the plane perpendicular to the instantaneous radius of curvature

without any loss of generality (see figure 2.3). The polarization basis is then defined by a parallel and a perpendicular polarization, namely

$$\begin{aligned}\vec{e}_{\parallel} &= (0, 1, 0)_{xyz}, \\ \vec{e}_{\perp} &= \frac{\vec{k}}{k} \wedge \vec{e}_{\parallel} = (-\cos \kappa, 0, \sin \kappa)_{xyz},\end{aligned}\quad (2.30)$$

where κ is the angle from the instantaneous velocity vector in the plane perpendicular to the local curvature radius, and the basis xyz is defined on figure 2.3.

After lengthy calculations one can show that in the ultra-relativistic limit (in which we are interested for pulsars) the intensities of the parallel (to the radius of the trajectory) and perpendicular polarizations per unit pulsation per unit solid angle at an angle κ from the instantaneous velocity vector of the particle are given by

$$\frac{d^2 I^{\parallel}}{d\omega d\Omega} = \frac{1}{2\pi\Omega} \frac{e^2 \omega^2}{12\pi^3 \epsilon_0 c} \left(\kappa^2 + \frac{1}{\gamma^2} \right)^2 K_{2/3}^2(\xi), \quad (2.31)$$

$$\frac{d^2 I^{\perp}}{d\omega d\Omega} = \frac{1}{2\pi\Omega} \frac{e^2 \omega^2}{12\pi^3 \epsilon_0 c} \kappa^2 \left(\kappa^2 + \frac{1}{\gamma^2} \right) K_{1/3}^2(\xi), \quad (2.32)$$

where $\xi = \frac{\omega}{3\Omega} \left| \kappa^2 + \frac{1}{\gamma^2} \right|^{3/2}$. In the case of synchrotron, $\Omega = \omega_B = eB/(\gamma m)$ the synchrotron frequency, while in the case of curvature $\Omega = \Omega_C = c/\rho$ where ρ is the radius of curvature of the field line. The functions K_{ν} are modified Bessel functions (Olver and National Institute of Standards and Technology (U.S.), 2010). Upon integration over solid angles one obtains

$$\frac{dI^{\parallel}}{d\omega} = \frac{1}{2\pi\Omega} \frac{e^2 \Omega \omega}{\gamma^2 \sqrt{3} 4\pi \epsilon_0 c} \left(\int_{\omega/\omega_c}^{\infty} K_{5/3}(x) dx + K_{2/3}(\omega/\omega_c) \right), \quad (2.33)$$

$$\frac{dI^{\perp}}{d\omega} = \frac{1}{2\pi\Omega} \frac{e^2 \Omega \omega}{\gamma^2 \sqrt{3} 4\pi \epsilon_0 c} \int_{\omega/\omega_c}^{\infty} K_{1/3}(x) dx. \quad (2.34)$$

These spectra are peaked around the characteristic frequency

$$\omega_c(\Omega) = \frac{3}{2} \Omega \gamma^3. \quad (2.35)$$

The total power radiated in each polarization is

$$I^{\parallel} = \frac{e^2}{4\pi \epsilon_0 c / \Omega} \frac{7\Omega}{12} \gamma^4, \quad (2.36)$$

$$I^{\perp} = \frac{e^2}{4\pi \epsilon_0 c / \Omega} \frac{\Omega}{12} \gamma^4. \quad (2.37)$$

Finally, one notices that the polarization ratio is exactly 7 at leading ultra-relativistic order. The total spectrum and power summed over polarizations are

$$\frac{dI}{d\omega} = \frac{e^2}{4\pi\epsilon_0 c/\Omega} \frac{\sqrt{3}}{2\pi} \gamma \frac{\omega}{\omega_c} \int_{\omega/\omega_c}^{\infty} K_{5/3}(x) dx \quad (2.38)$$

$$I = \frac{2}{3} \frac{e^2}{4\pi\epsilon_0 c/\Omega} \Omega \gamma^4 \quad (2.39)$$

In the context of pulsars, the super intense magnetic fields and high energies of the leptons often put synchrotron radiation in the quantum regime: the leading effects of the discretization of the orbit of the electron in Landau levels (see appendix B) have to be taken into account. This regime is characterized by the parameter $\xi = \hbar\omega_c(\omega_B)/E$ where E is the energy of the particle. In the classical regime $\xi \ll 1$, and in the ultra-quantum regime $\xi \gg 1$. Said differently, quantum mechanics by considering light as photons, forbids these to have an energy larger than the energy of the particle emitting them, which results from energy conservation. Besides, the cutoff of the spectrum after its peak decays super-exponentially when $\omega_c > E/\hbar$, making E/\hbar a good approximation of the critical pulsation in such cases. Therefore, a generalization of equation (2.35) taking into account quantum effects is

$$\omega_c^{(\text{qu})}(\Omega) = \max\left(\omega_c(\Omega), \frac{E}{\hbar}\right). \quad (2.40)$$

Note that this is not only valid for synchrotron, but also for curvature and synchrocurvature radiation as we show in chapter 3. The total spectrum averaged over the spin of particles and summed over polarizations in the ultra-relativistic limit is given by (Sokolov and Ternov, 1968)

$$\frac{dI^{(\text{qu})}}{d\omega} = I \frac{9\sqrt{3}}{8\pi} \frac{y}{(1+\xi y)^3} \left[\int_y^{\infty} dx K_{5/3}(x) + \frac{\xi^2 y^2}{1+\xi y} K_{2/3}(y) \right] \quad (2.41)$$

where the first term between the brackets corresponds to the case of spinless particles (Schwinger, 1954), and

$$y = \frac{\omega}{\omega_c \left(1 - \frac{\hbar\omega}{E}\right)}. \quad (2.42)$$

The total power reads (Sokolov and Ternov, 1968)

$$I^{(\text{qu})} = I \left(1 - \frac{55\sqrt{3}}{24}\xi\right) \text{ for } \xi \ll 1, \quad (2.43)$$

$$I^{(\text{qu})} = I \frac{2^{8/3} \Gamma(2/3)}{9 \xi^{4/3}} \text{ for } \xi \gg 1, \quad (2.44)$$

where $\Gamma(2/3) \simeq 1.35$ is the gamma function (Olver and National Institute of Standards and Technology (U.S.), 2010). Spin effects arise at second order in ξ for $\xi \ll 1$.

In the ultra-quantum case they play a very important role. For spin and polarization dependent expressions, refer to Sokolov and Ternov (1968).

For all the previous spectra, useful asymptotic expressions can be found using (Olver and National Institute of Standards and Technology (U.S.), 2010)

$$K_\nu(x) \underset{x \rightarrow 0}{\sim} \frac{\Gamma(\nu)2^{\nu-1}}{x^\nu}, \quad (2.45)$$

$$\underset{x \rightarrow \infty}{\sim} \sqrt{\frac{\pi}{2}} \frac{e^{-x}}{\sqrt{x}}, \quad (2.46)$$

and

$$y \int_y^\infty K_\nu(x) dx \underset{y \rightarrow 0}{\sim} \Gamma(\nu - 1)2^{\nu-1}y^{2-\nu} + \frac{\pi}{2 \cos \frac{\pi\nu}{2}} y, \quad (2.47)$$

$$\underset{y \rightarrow \infty}{\sim} \sqrt{\frac{\pi}{2}} \sqrt{y} e^{-y}. \quad (2.48)$$

The synchrocurvature radiation has been obtained by several authors. We outline here the version developed in Kelner et al. (2015) (see references therein or chapter 3 for the other approaches). The authors use the Hamiltonian formalism to derive the motion of a relativistic charged particle in a magnetic field with a cylindrical symmetry : magnetic field lines are circles generating the cylinder. Assuming that approximation (2.29) is satisfied they find that the instantaneous curvature radius is

$$R_c(t) = \rho \left(1 - 2\eta \cos(\omega_B t) + \eta^2 \right)^{-1/2}, \quad (2.49)$$

and

$$\eta = \frac{\beta_\perp}{\beta_D} \text{ with } \beta_D = \frac{\Omega_C}{\omega_B} \beta_\parallel, \quad (2.50)$$

where β_D is the drift velocity along the cylinder that results from inertial terms in the motion of the particle, $\beta_\parallel \lesssim 1$ is the motion parallel to the field, and β_\perp is the velocity perpendicular to the drift trajectory (all in unit of c). Within the approximation

$$\frac{\omega_{\text{cyclo}}}{\Omega_C} \ll \gamma^2 \ll \frac{mc^2}{\hbar\Omega_C}, \quad (2.51)$$

the authors show that the photon-emission time scale is much shorter than the curvature evolution time scale or the energy-loss time scale, and therefore at leading order the radiation spectrum is just obtained by putting in equations (2.31)- (2.34), and (2.36)-(2.37) $\Omega = \Omega_{\text{SC}} = c/Rc(t)$.

One can then average over a synchrotron period $2\pi/\omega_B$. If calculations of the averaged spectra can be fairly cumbersome, the total averaged intensity radiated $\langle I_{SC} \rangle$ can be found to be related to the curvature intensity I_C by

$$\langle I_{SC} \rangle = I_C(1 + \eta^2). \quad (2.52)$$

Notice here that η is not necessarily small.

Cyclotron emission

Cyclotron emission can be seen as the lower end of synchrotron radiation energy spectrum : when the Landau level of an electron, or positron, is too low for the orbital decay to be reasonably taken in the continuous limit. It can also be seen as a purely discrete process, producing emission lines similar to those of ions in optically-thin hot plasmas. Indeed, emission lines corresponding to the cyclotron resonance were observed in some low-mass-x-ray binaries (see section 1.3).

Given an initial Landau state of energy ϵ_i with main number n_i (see equation (B.14)), an electron radiates photons corresponding to quantum transitions to a state of energy ϵ_f and number n_f . The kinematics of the reaction then gives

$$\epsilon_i - \epsilon_f = \omega, \quad (2.53)$$

$$p_i^{\parallel} - p_f^{\parallel} = \omega \cos \theta, \quad (2.54)$$

where ω is the energy of the emitted photon, and θ is the angle made by the direction of the photon with the direction of the magnetic field. There is no conservation of the perpendicular momentum which is “absorbed” by the magnetic field (see also section 2.2.3 below). Inserting (2.54) into (2.53) and using (B.14), one obtains a biunivoque relation between the emission angle and the energy of the emitted photon

$$\omega = \frac{1}{\sin^2 \theta} \left((\epsilon_i - p_i^{\parallel} \cos \theta) - \sqrt{(\epsilon_i - p_i^{\parallel} \cos \theta)^2 - 2m^2 \frac{B}{B_c} (n_i - n_f) \sin^2 \theta} \right). \quad (2.55)$$

Note that there is no divergence in $\sin \theta$ when $\theta \rightarrow 90^\circ$ as may appear at first sight. At leading order, one obtains

$$\omega = \frac{m^2}{\epsilon_i - p_i^{\parallel} \cos \theta} \frac{B}{B_c} (n_i - n_f), \quad (2.56)$$

such that in the frame of perpendicular motion, where $p_i^{\parallel} = 0$, the angular dependence of the energy of the radiated photon is weak (it appears at first order in $(m/\epsilon_i)(B/B_c)$).

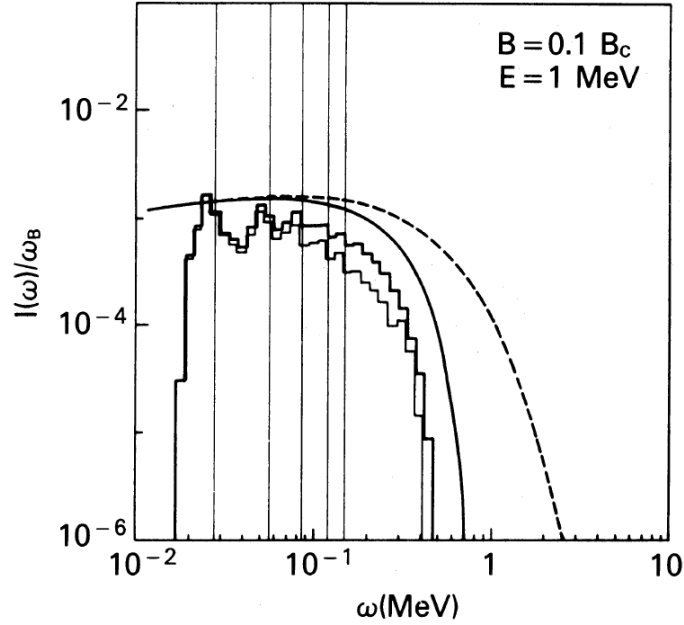


Fig. 2.4.: From Harding and Preece (1987). Single-particle synchrotron emissivity (in units of the cyclotron frequency $\omega_B = eB/m$) for electrons with initial spin-up (light line histogram and spin-down (dark line histogram). Light vertical lines are the energies of the first five harmonics ($n_i = 1..5$ to $n_f = 0$). Solid curve is the quantum asymptotic emissivity ($(dI^{(qu)}/d\omega)/\omega$ with $dI^{(qu)}/d\omega$ from equation (2.41)); dashed curve is the classical emissivity ($(dI^{(qu)}/d\omega)/\omega$ with $dI/d\omega$ from equation (2.38)).

As was shown by several authors (see Latal (1986) and Harding and Preece (1987) and references therein), the reaction rates tend to favor a desexcitation directly to the ground state when the particle energy is very relativistic and the magnetic field very high ($\gtrsim 0.25B_c$). This corresponds to the fact that the synchrotron peak energy saturates at ϵ_i , equation (2.40). More generally, the only way of knowing the exact average relaxation path is to perform a Monte carlo simulation with all the possible transitions n_f from a given starting point n_i . We show an example in figure 2.4 of such spectrum from Harding and Preece (1987). In this case the initial quantum number is already quite high, $n_i = 500$, and the main differences with respect to the synchrotron corrected spectrum (2.41) are the low-energy cut-off due to the minimum photon energy obtained for $n_i - n_f = 1$ in equation (2.55), and the overestimation of the emissivity by the quantum corrected spectrum.

For transitions to the ground state, complete analytical formulas for the transition rates are given by Baring et al. (2005), with asymptotic formulas (Latal, 1986; Baring et al., 2005)

$$\Gamma_{n_i 0}^{\zeta} = \frac{\alpha_{\text{fs}} c}{\lambda_C} \left(1 - \frac{\zeta}{\sqrt{1 + 2n_i \frac{B}{B_c}}} \right) \begin{cases} (2n_i^2)^{n_i} \frac{(n_i+1)!}{(2n_i+1)!} \left(\frac{B}{B_c} \right)^{n+1} & n_i B/B_c \ll 1 \\ \sqrt{\frac{B/B_c}{2n_i}} \left[\frac{\gamma(n_i, n_i)}{(n_i-1)!} - \frac{n_i^{n_i} e^{-n_i} \ln 2n_i B/B_c}{(n_i-1)! \cdot 2n_i B/B_c} \right] & n_i B/B_c \gg 1 \end{cases}, \quad (2.57)$$

where $\alpha_{\text{fs}} \simeq 1/137$ is the fine structure constant and $\lambda_C = \hbar/(mc)$ is the reduced Compton wavelength (see also appendix A). Here spin dependence is included in $\zeta = \pm 1$, and the spin-state basis is that of « transverse polarization » of Sokolov and Ternov (1968) (see also Baring et al. (2005) for a discussion of the choice of spin basis). Spin orientations are important in cyclotron decay and other related problems, because the ground state $n = 0$ is the only non-degenerate state with respect to spin orientation and corresponds to $\zeta = -1$. It results that transitions to the ground state, but also to low states (Harding and Preece, 1987) favor transitions to states with $\zeta = -1$. This effect can easily be seen from the prefactor of (2.57). In particular for a transition from $n_i = 1$,

$$\Gamma_{10}^{\zeta} \simeq 5.7 \cdot 10^{16} (1 - 0.9\zeta) \text{s}^{-1}. \quad (2.58)$$

Besides emission rates, absorption rates can also be important. For example, Lyubarskii and Petrova (1998), consider the absorption of radio photons that increase the pitch angle (i.e. the main quantum number) of electrons and positrons, such that they can then radiate more synchrocurvature and synchrotron radiation. Such rates are very similar to the emission rates (see e.g. Latal (1986)).

Cherenkov radiation

The Cherenkov radiation of a charged particle in a medium, named after the physicist who observed it first in 1934, was explained a couple years later in a seminal paper (Frank and Tamm, 1937) : it results from the propagation of a particle of charge q at a speed v faster than the speed of light in the medium

$$c_{\text{medium}} = \frac{c}{\sqrt{\epsilon(\omega)/\epsilon_0}} \quad (2.59)$$

where ϵ is the dielectric constant of the medium, and $\sqrt{\epsilon/\epsilon_0}$ is the refractive index. For simplicity, it is here assumed a dense homogeneous transparent dielectric medium, that is a medium the response of which is linear and described by a real ϵ independent of the location of the particle. A more complete treatment can be found in textbooks such as Jackson (1998) or Ginzburg and Cytovič (1990).

More qualitatively, the information on the charge q propagates in the medium at the speed $c_{\text{medium}} < v$ and is therefore concealed outside of a cone of angle $\theta = \cos^{-1} c_{\text{medium}(\omega)/v$ with the direction of the particle that describes the wavefront originating from the particle. This cone results from purely kinematic arguments concerning the propagation of waves, and it is therefore normal to find in other shock problems, such as the Mach cone formed by a supersonic object. Overall, Cherenkov radiation should be seen as the reaction of a continuous medium to a shock.

The radiated energy per unit length is given by

$$\frac{dE}{dx} = \frac{1}{4\pi\epsilon_0} \frac{q^2}{c^2} \int_{v^2 > c_{\text{medium}}^2} d\omega \omega \left(1 - \frac{c_{\text{medium}}^2(\omega)}{v^2} \right). \quad (2.60)$$

The polarization is linear and in the plane common to the velocity of the particle and the line of sight of the observer. The frequencies of the radiated electromagnetic waves lie in bands which are bounded by the frequencies solution of $c_{\text{medium}}(\omega) = v$.

In pulsar magnetospheres, Cherenkov radiation was originally invoked by Ginzburg (see also Michel (1982)) as an alternative to curvature and synchrotron radiation

Compton scattering

In this section, we will use units with $\hbar = c = 1$ except otherwise specified.

In a general manner, a relativistic two-particle phenomenon of invariant cross-section $\frac{d^2\sigma}{d\Omega} d\Omega$ has an invariant probability per unit time per unit volume that a particle reacts with a distribution f of the other kind of particle

$$w = \int d\Omega \int d^3\vec{k} \left(V f(\vec{k}) \right) \frac{d^2\sigma}{d\Omega}(\vec{k}, \Omega) j(\vec{k}), \quad (2.61)$$

where Ω is the solid angle of the outgoing particle, $V f(\vec{k})$ is the distribution of ingoing particles of momentum \vec{k} per unit momentum in the volume of interaction V , and j is the ingoing flux. The boundaries of integration can be more or less complex as they have to respect conservation laws. Often, these conservation laws are embodied into the cross section under the form of Dirac delta functions.

In the case of Compton scattering of a free photon of four-momentum $K = (k, \vec{k})$ by a free electron (or positron) of momentum $P = (P^0 = \gamma m, \vec{p})$ the flux j is defined by

$$j = c \frac{K \cdot P}{V k P^0}, \quad (2.62)$$

where V is the volume of interaction.

The Lorentz-invariant cross-section in a non-magnetized medium is given by (Berestetskii et al., 1982)

$$d\sigma = \frac{r_e^2 8\pi dt}{(s - m^2)^2} \left[\left(\frac{m^2}{s - m^2} + \frac{m^2}{u - m^2} \right)^2 + \left(\frac{m^2}{s - m^2} + \frac{m^2}{u - m^2} \right) - \frac{1}{4} \left(\frac{s - m^2}{u - m^2} + \frac{u - m^2}{s - m^2} \right) \right], \quad (2.63)$$

where s, t, u are the relativistic invariants

$$s = (P + K)^2 = (P_s + K_s)^2, \quad (2.64)$$

$$t = (K - K_s)^2 = (P - P_s)^2, \quad (2.65)$$

$$u = (P - K_s)^2 = (K - P_s)^2, \quad (2.66)$$

$$s + t + u = 2m^2, \quad (2.67)$$

where $K_s = (k_s, \vec{k}_s)$ and $P_s = (P_s^0, \vec{p}_s)$ are the four momenta of the scattered photon and electron, respectively. Note that in cross-section (2.63) the differential element $dt = -2k_s k d \cos \theta$ with $\theta = (\vec{k}_s, \vec{k})$, and the cross section is averaged over 2π around the axis defined by \vec{k} .

For free particles, the conservation of four momentum reads

$$P + K = P_s + K_s. \quad (2.68)$$

Specifying this relation in the frame of the electron and squaring $P' + K' - K_s'^2$ one gets

$$k_s' = k' \frac{1}{1 + \frac{k'}{m} (1 - \cos \theta')} \quad (2.69)$$

where θ' is the scattering angle. From this purely kinematic argument, one sees that in the limit $k' \ll m$, one has $k_s' \simeq k'$. This nonrelativistic limit is called the Thomson regime, and the Thomson cross section integrated over scattering angles gives

$$\sigma_T \underset{x \ll 1}{=} \frac{8\pi r_e^2}{3} (1 - x), \quad (2.70)$$

²Primed quantities stand in the frame of the electron, bare quantities stand in the frame of the observer.

where $x = (s - m^2)/m^2$. On the other hand, when $k' \gg m$ there is no dependence of k'_s on k' , rather only on the angle θ , and the cross-section integrated over scattering angles is in the so-called Klein-Nishina regime. It is given by

$$\sigma_{KN} \underset{x \gg 1}{=} \frac{2\pi r_e^2}{x} \left(\ln x + \frac{1}{2} \right). \quad (2.71)$$

If we consider the interesting astrophysical case where the electrons are ultrarelativistic with a Lorentz factor $\gamma \gg 1$ with respect to the observer, then $k' \sim k\gamma$. It results that in the Thomson case the observer will see photons at $k_s \sim \gamma^2 k$ while in the Klein-Nishina regime the energy of the observed photons saturates at $k_s \lesssim \gamma m$.

In the case of pulsar magnetospheres the scattered photons are often assumed to be thermal x rays from the hot surface of the star. In this case, scattering is most efficient close to the surface of the star, namely where the magnetic field is the most intense. The scattering of the photon can be seen as an infinitely short back-and-forth transition of the electron between two states : the photon is absorbed and the electron is excited to a different state and then relaxes reemitting the photon. However, in such intense magnetic fields, electron states are quantized in the so-called Landau levels with an energy step $\simeq \epsilon_B = mB/B_c \simeq 12B_8 \text{keV}$ (see appendix B equation (B.15)) falling in the hard x-ray range. Although at a higher energy than the typical black-body temperature $\sim 1 \text{keV}$, the resonance can be easily reached by photons once Doppler shifting from the reference frame of the star to the reference frame of the electron is taken into account. Therefore, the scattering is resonant at energies commensurate with ϵ_B .

The cross-section of such magnetic Compton scattering was derived by Bussard et al. (1986) and Daugherty and Harding (1986). It turns out to be made of highly complex expressions which comment is beyond the scope of the present section. Authors working on resonant scattering in pulsar magnetospheres usually refer to approximate expressions developed by Dermer (1990), and specifically developed by (Sturmer, 1995; Harding and Muslimov, 1998) in the context of pulsar polar caps. The approach of Dermer (1990) is to consider the (magnetic) Thomson limit $k \ll \epsilon_B \ll m$, and that only the first Landau level participates (particles are in their ground state). Therefore this approximation does not apply to magnetars and more generally to stars with $B \gtrsim B_c$. The cross-section in the frame of the scattering electron with Dermer's approximations is given by

$$\frac{d^2\sigma'_D}{d\epsilon'_s d\mu'_s} = \frac{1}{2} \sigma_T \delta(\epsilon'_s - \epsilon') \left[\underbrace{\frac{3}{4}(1 - \mu'^2)(1 - \mu_s'^2)}_{\text{Angular}} + \underbrace{g_1}_{\text{Nonresonant}} + \underbrace{\frac{1}{2}(g_2 - g_1)}_{\text{Resonant}} \right], \quad (2.72)$$

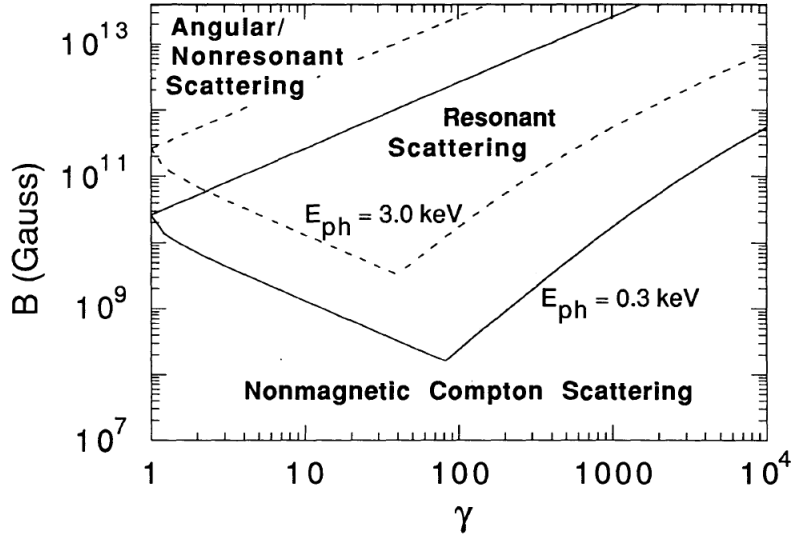


Fig. 2.5.: Reproduced from Dermer (1990). Shows the different regimes as a function of the Lorentz factor γ of the electron and the magnetic field intensity B . The scattered photons are assumed to be monochromatic. Two areas are shown where depending on the energy of the scattered photons E_{ph} . The nonmagnetic Compton scattering area shows where assuming scattering by a free electron is accurate. The angular scattering corresponds to a term in the magnetic cross-section that depends only on the scattering angle.

where

$$g_1 = \frac{u^2}{(u+1)^2}, g_2 = \frac{u^2}{(u-1)^2 + (\epsilon_\Gamma/(2\epsilon_B))^2}, \quad (2.73)$$

with $\epsilon = \hbar k$, $u = \epsilon'/\epsilon_B$ and $\epsilon_\Gamma = 4\alpha_s f \epsilon_B^2/3$ is the resonant width. The cosine of the angles with the direction of the electron are denoted μ' for the incident angle and μ'_s for the scattering angle. As before, primes denote quantities in the frame of the electron. This cross section is polarization-averaged and integrated over azimuthal angles. The resonant and nonresonant terms have almost no dependence on the incidence angle μ' if one assumes that the electron has an ultrarelativistic motion, and the dependence on the scattering angle μ'_s is smooth and relatively small compared to the angular part. Therefore these two terms have been averaged over the scattering angle. Far from the resonance, $u \ll 1$ or $u \gg 1$, the cross section reduces to the field-free Compton cross section in the Thomson regime. For incident photons with energies $\epsilon' \gg m \gg \epsilon_B$, the free-field Klein-Nishina approximation should be used. Figure 2.5 shows an estimate of the domains of application of resonant scattering. It shows that, apart for some recycled millisecond pulsars, resonant scattering should generally be taken into account near the surface of the star, and maybe in the outer magnetosphere of some young pulsars.

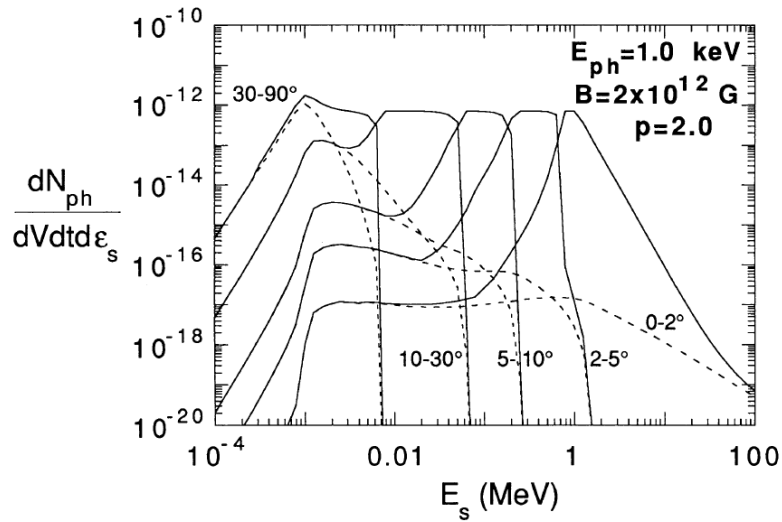


Fig. 2.6.: From Dermer (1990). Angle dependent thin-target spectra in the observer's frame from the Comptonization of 1keV photons by a one-dimensional distribution of electrons with energy spectrum $n_e(\gamma) = \gamma^{-2}$. The scattered photon energy $E_s = \epsilon_s$. The magnetic field is $B = 2 \cdot 10^{12}$ Gauss ($2 \cdot 10^8$ Teslas). The photons are uniformly emitted into the forward hemisphere about the electron beaming axis. The total Comptonized spectra are shown by the solid curves, and the Comptonized spectra with the resonant part omitted are shown by the dashed curves, showing well the importance of the resonance. The curves are labeled by the range of observing angles over which the emitted spectra were calculated.

At resonance, photons are scattered at ϵ_B in the frame of the electron³ and are therefore seen at a typical energy $\gamma\epsilon_B$ by the observer.

The angular dependance of Compton scattering in the Thomson regime (magnetic or not) can be approximated to an average scattering angle of $\theta_s \sim 2/\gamma$ in the frame of the observer (Dermer, 1990), figure 2.6. This can have important consequences in pair cascades (section 2.3.3 and Harding and Muslimov (1998)), since the outgoing photon will produce pairs more easily if its incidence angle on the magnetic field is larger.

2.2.3 Lepton creation processes

A way of filling the magnetosphere with plasma is through creation of electron-positron pairs from the quantum vacuum. In the case of pulsars, one expects the radiation of very strong gamma rays in vacuum gaps, bearing many times the rest mass energy mc^2 of an electron or a positron . The source of these photons is

³Since $\epsilon_B \propto B$ and we assume here electrons and positrons which are flowing along the field lines in pulsar magnetic fields, the Lorentz transforms to and from the frame of the electron are parallel to the magnetic field and therefore do not change its intensity. It results that for all practical purpose $\epsilon_B = \epsilon'_B$. However the Lorentz-boost affects the longitudinal part of the energy of the electron, such that the electron does not have the same energy in both reference frames.

the curvature radiation, the synchrotron radiation, or the Compton scattering from ultrarelativistic electrons and positrons. There are several phenomena through which these photons can transform into pairs, in this text we will focus on the photon-magnetic-field reaction and the photon-photon reaction. Formally one writes respectively

$$\gamma + B \rightarrow e_+ + e_-, \quad (2.74)$$

$$\gamma + \gamma \rightarrow e_+ + e_-. \quad (2.75)$$

Other mechanisms are possible, in particular the creation of pairs by interaction of a gamma ray with the Coulomb field of charged particles such as electrons, positrons or ions (Cheng and Ruderman, 1977), or the creation of positroniums (a pair in a bound state) instead of free pairs (Usov and Melrose, 1995).

Photon-magnetic-field pairs

In this section, we will use units with $\hbar = c = 1$ except otherwise specified.

We consider a gamma photon of energy ω propagating at an angle θ to a uniform magnetic field of intensity B , and converting into an electron-positron pair characterized by the energies ϵ_{\pm} of the leptons and their momenta p_{\pm}^{\parallel} parallel to the direction of the magnetic field (see figure 2.7). The kinematics of this reaction is given by (Daugherty and Harding, 1983)

$$\omega = \epsilon_+ + \epsilon_-, \quad (2.76)$$

$$\omega \cos \theta = p_+^{\parallel} + p_-^{\parallel}. \quad (2.77)$$

The energy of the incident gamma ray is conserved, as well as its longitudinal momentum. However, there is no conservation of the perpendicular momentum, that can be considered “absorbed” by the magnetic field. The threshold of the reaction is given by

$$\omega \sin \theta \geq 2m, \quad (2.78)$$

The “center-of-mass” frame is the frame in which $\hat{\theta} = \pi/2$ and is obtained by a boost along the magnetic field (thus not changing it in the absence of transverse electric field). In this frame, the energy of the photon is $\hat{\omega} = \omega \sin \theta$ and the threshold condition above reduces to the fact that the photon energy be higher than the rest-mass energy of the two leptons in this frame.

Let us specialize to the center-of-mass frame, $\hat{\theta} = \pi/2$ for a moment. The two leptons are created on Landau levels characterized by discrete energy steps related to the

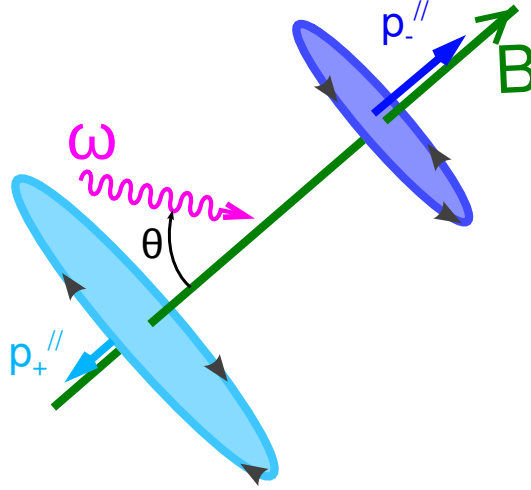


Fig. 2.7.: Sketch showing the kinematics of the photon-magnetic-field reaction. The outgoing Landau states are represented by the corresponding classical Larmor orbits. The larger the radius of the orbit the larger orbital part of the energy, quantified by n_{\pm} (see the text).

angular momentum of the particles (see appendix B). In this frame denoted by a hat, $\hat{p}_-^{\parallel} = -\hat{p}_+^{\parallel}$, and the reaction rate can be proven to have resonances whenever $\hat{p}_-^{\parallel} = \hat{p}_+^{\parallel} = 0$ (Daugherty and Harding, 1983). As a consequence, the energy of the photon is mostly converted into orbital energy of the pairs rather than in longitudinal energy. In the frame of the observer, this translates with a good approximation into

$$p_+^{\parallel} \sim p_-^{\parallel} \sim \frac{1}{2}\omega \cos \theta. \quad (2.79)$$

Going back in the center-of-mass frame, resonance occurs for every pair of integers n_{\pm} quantifying the energy of electron (n_-) and the positron (n_+) such that $\hat{\omega} = \epsilon_+(n_+) + \epsilon_-(n_-)$, with (see section ??)

$$\epsilon_{\pm}(n_{\pm}) = \sqrt{m^2 + 2\epsilon_B n_{\pm}}. \quad (2.80)$$

As a consequence of the square root dependence, the reaction rate spectrum is a set of peaks spaced by a typical energy $\epsilon_B = m\frac{B}{B_c}$ when the energy of the photon is low above threshold, and asymptotically tends to a continuum with large $\hat{\omega}$. The spacing between peaks becomes small compared to the center-of-mass energy of the gamma photon when

$$\xi = \frac{\hat{\omega}}{\epsilon_B} = \frac{\omega \sin \theta}{\epsilon_B} \gg 1, \quad (2.81)$$

assuming the threshold 2.78 is already reached. Notice that the second equality above is invariant by Lorentz transformation parallel to the field.

Assuming that both conditions (2.78) and (2.81) are fulfilled, Tsai and Erber (1975) give an expression for the reaction rate per unit length in the continuum approximation, averaged over polarizations of the incident photon,

$$R_{\gamma B} \simeq \sin \theta \frac{B \alpha_{\text{fs}}}{B_c \lambda_C} \frac{\sqrt{3}}{18\pi\chi} \int_0^1 dv \frac{9-v^2}{1-v^2} K_{\frac{2}{3}} \left(\frac{4}{3\chi(1-v^2)} \right) \text{ cm}^{-1} \quad (2.82)$$

$$\chi = \frac{B \hbar \omega \sin \theta}{B_c 2mc^2} \quad (2.83)$$

where $\lambda_C = \frac{\hbar}{mc}$ is the Compton wavelength, α_{fs} is the fine structure constant and $B_c = \frac{m^2 c^3}{e\hbar} \simeq 4.4 \cdot 10^9$ Teslas is the critical field of quantum electrodynamics. The angle between the photon momentum and the magnetic-field vector is given by θ .

The reaction rate (2.82) can be developed in two asymptotic forms (Daugherty and Harding, 1983)

$$R_{\gamma B} \underset{\chi \ll 1}{\sim} \frac{3\sqrt{3}}{16\sqrt{2}} \frac{\alpha_{\text{fs}}}{\lambda_C} \frac{B}{B_c} \sin \theta \exp \frac{-4}{3\chi} \simeq 0.23 \frac{\alpha_{\text{fs}}}{\lambda_C} \frac{B}{B_c} \sin \theta \exp \frac{-4}{3\chi}, \quad (2.84)$$

$$R_{\gamma B} \underset{\chi \gg 1}{\sim} \frac{30\pi}{7\sqrt[3]{3}\Gamma(1/6)^2} \frac{\alpha_{\text{fs}}}{\lambda_C} \frac{B}{B_c} \sin \theta \chi^{-1/3} \simeq 0.30 \frac{\alpha_{\text{fs}}}{\lambda_C} \frac{B}{B_c} \sin \theta \chi^{-1/3}. \quad (2.85)$$

In pulsars, with $B \ll B_c$, the form (2.84) is more often useful (see section 2.3). It is to be noted that if $B \geq B_c$, then the threshold condition (2.78) implies that $\chi \geq 1$ and the form (2.84) is never valid.

Besides, Daugherty and Harding (1983) give an approximation for $\chi \ll 1$ which extends (2.84) to low values of ξ by giving the approximate average behavior of the complete reaction rate for low and moderate values of ξ (when the sawtooth behavior of the cross section is important),

$$R_{\gamma B} \underset{\chi \ll 1}{\sim} \frac{3\sqrt{3}}{16\sqrt{2}} \frac{\alpha_{\text{fs}}}{\lambda_C} \frac{B}{B_c} \sin \theta \exp \frac{-4f(\omega \sin \theta, B)}{3\chi}, \quad (2.86)$$

$$f(\omega \sin \theta, B) = 1 + 0.42 \left(\frac{B}{B_c} \right)^{-0.0038} \left(\frac{\omega \sin \theta}{2m} \right)^{-2.7}. \quad (2.87)$$

The distribution of energy between the two created leptons is important in the perspective of pair cascades, as a particle created on a high Landau level will subsequently radiate more synchrotron radiation that may feed the cascade (see section 2.3). From equation (2.82), Daugherty and Harding (1983) showed, up to a mistake corrected in Baring (1988), that the energy spectrum of creation of a pair

with one of the leptons of energy $\hat{\epsilon}_{\pm}$ is given in the center-of-mass frame by (Baring, 1988)

$$\frac{d\hat{R}_{\gamma B}}{d\hat{\epsilon}_{\pm}} \simeq \frac{1}{2} \frac{\alpha_{\text{fs}}}{\lambda_C} \frac{1}{\pi\sqrt{3}} \frac{mc^2}{\hbar\omega} \left[\frac{1}{\hat{\epsilon}_{\pm}(1-\hat{\epsilon}_{\pm})} K_{\frac{2}{3}} \left(\frac{1}{3\chi\hat{\epsilon}_{\pm}(1-\hat{\epsilon}_{\pm})} \right) - \int_{\frac{1}{3\chi\hat{\epsilon}_{\pm}(1-\hat{\epsilon}_{\pm})}}^{\infty} K_{5/3}(x) dx \right], \quad (2.88)$$

$$\frac{d\hat{R}_{\gamma B}}{d\hat{\epsilon}_{\pm}} \simeq \frac{1}{2} \frac{B\alpha_{\text{fs}}}{B_c\lambda_C} \frac{\sqrt{3}}{9\pi\chi} \frac{2 + \hat{\epsilon}_{\pm}(1-\hat{\epsilon}_{\pm})}{\hat{\epsilon}_{\pm}(1-\hat{\epsilon}_{\pm})} K_{\frac{2}{3}} \left(\frac{4}{3\chi\hat{\epsilon}_{\pm}(1-\hat{\epsilon}_{\pm})} \right), \quad (2.89)$$

where $\hat{\epsilon}_{\pm} = \hat{\epsilon}_{\pm}/\hat{\omega}$ is the energy of the outgoing lepton normalized to the energy of the incident photon in the center-of-mass frame. When one lepton is created with energy $\hat{\epsilon}_{\pm}$, the energy of the other is symmetrically given by $\hat{\epsilon}_{\mp} = 1 - \hat{\epsilon}_{\pm}$. For $\chi \ll 1$, the energy is equally distributed between the two leptons, while for $\chi \gg 1$ the energy is almost entirely concentrated into one particle while the other is created with its rest mass energy (i.e. in its fundamental Landau level).

Notice that all the present results are valid if no electric field is present. If a transverse electric field E such that $B^2 - E^2 > 0$ and $\vec{E} \cdot \vec{B} = 0$, as is the case in pulsar magnetospheres, the results must be Lorentz transformed with the drift velocity $c\vec{E} \times \vec{B}/B^2$ (Daugherty and Harding, 1983). The result was worked out by Daugherty and Lerche (1976) in the case where a parallel electric field is present. However, the parallel electric fields are usually very small compared to cB in the regions of interest of the magnetosphere (section 2.3).

Photon-photon pairs

In this section, we will use units with $\hbar = c = 1$ except otherwise specified.

The present section considers the creation of a free electron-positron pair from the collision of free photons. It is very similar to the Compton scattering of free particles of section 2.2.2, for the reason that it is a different channel of the same generalized reaction (Berestetskii et al., 1982). We therefore use the same notations. Besides, this topic is the object of chapter 4. The creation of pairs in a strong magnetic field, where the two leptons are created on Landau levels (see appendix B) and not on free-space states, is not considered here. It is similar to the photon-magnetic-field process (previous section 2.2.3) and to resonant Compton scattering (section 2.2.2) in that the transition occurs between Landau states. However, resonant photon-photon pair creation is particularly active in very strong magnetic fields (say $> 10^8$ Teslas) where the photon-magnetic-field process is expected to be dominant (Harding and Lai, 2006) anyway. The corresponding transition rates were derived by Kozlenkov and Mitrofanov (1986).

The invariant probability per unit time per unit volume that an incident photon (usually a gamma ray) of momentum $K_i = (K_i^0, \vec{k}_i)$ reacts with photons labeled by four momenta $K = (K^0, \vec{k})$ from a distribution $f(\vec{k})$ converts into an electron-positron pair of four momenta $P_{\pm} = (P_{\pm}^0, \vec{p}_{\pm})$ is given by equation (2.61) with a current j and an invariant cross-section $d^2\sigma$ (Berestetskii et al., 1982)

$$j = c \frac{K \cdot K_i}{V K_i^0 k}, \quad (2.90)$$

$$d^2\sigma_{\gamma\gamma} = -ds 8\pi r_e^2 \frac{m^2}{t^2} \times \left[\left(\frac{m^2}{s-m^2} + \frac{m^2}{u-m^2} \right)^2 + \left(\frac{m^2}{s-m^2} + \frac{m^2}{u-m^2} \right) - \frac{1}{4} \left(\frac{s-m^2}{u-m^2} + \frac{u-m^2}{s-m^2} \right) \right], \quad (2.91)$$

and kinematic invariants

$$s = (P_- - K_i)^2 = (P_+ - K)^2, \quad (2.92)$$

$$t = (K_i + K)^2 = (P_+ + P_-)^2, \quad (2.93)$$

$$u = ((P_- - K_w)^2 = (P_+ - K_i)^2. \quad (2.94)$$

$$(2.95)$$

As in section 2.2.2 $s + t + u = 2m^2$, and $ds = -2k_i p_- d \cos \theta$ with $\theta = (\vec{k}_i, \vec{p})$, and the cross section is averaged over 2π around the axis defined by \vec{k}_i . Note that all expressions are completely symmetric under the exchange of P_+ by P_- and vice versa.

The conservation laws are

$$K + K_i = P_- + P_+, \quad (2.96)$$

$$P_{\pm}^2 = m^2. \quad (2.97)$$

The Lorentz-invariant threshold of the reaction is given by

$$t \geq 4m^2, \quad (2.98)$$

where the kinematic invariant t is the energy in the center of mass of the two photons.

The cross section integrated over outgoing angles is (Berestetskii et al., 1982)

$$\sigma_{\gamma\gamma} = \frac{\pi r_e^2}{\tau^3} \left(\left(\tau^2 + \tau - \frac{1}{2} \right) \ln \left(\frac{\sqrt{\tau} + \sqrt{\tau-1}}{\sqrt{\tau} - \sqrt{\tau-1}} \right) - (\tau+1) \sqrt{\tau} \sqrt{\tau-1} \right), \quad (2.99)$$

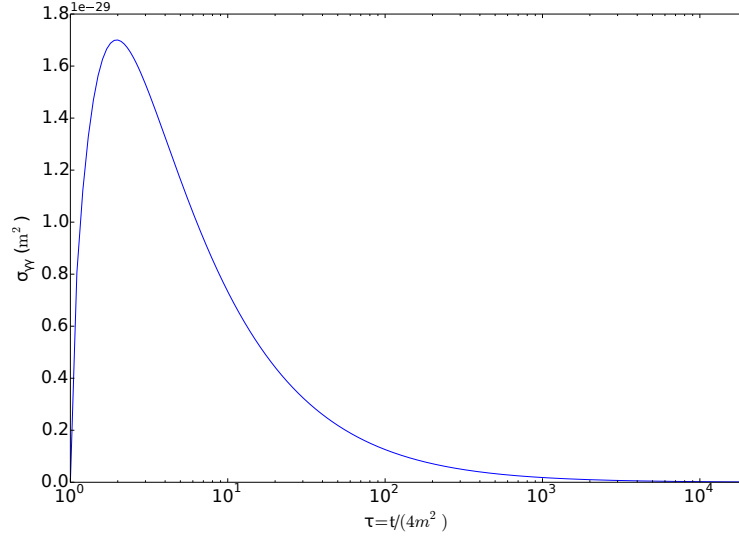


Fig. 2.8.: Photon-photon pair creation cross section integrated over outgoing angles, equation (2.99).

where $\tau = t/(4m^2)$, such that $\tau = 1$ at threshold (2.98). Figure 2.8 shows a plot of the integrated cross-section. It admits asymptotic expressions

$$\sigma_{\gamma\gamma} \xrightarrow{\tau \rightarrow 1} \frac{\sqrt{\tau - 1} \pi r_e^2}{2\tau} \quad (2.100)$$

$$\underset{\tau \gg 1}{\sim} \frac{\pi r_e^2}{2\tau} (\ln 4\tau - 1). \quad (2.101)$$

In the center-of-mass frame, the momenta of the two leptons are exactly opposite, and the same for the photons. All particles share the same energy $\hat{\epsilon}$, and there is an angle $\hat{\theta}$ between the axis of the leptons and the axis of the photons. Taking the photon axis as a reference, the cross-section is azimuthally symmetric around this axis and

$$\frac{d\sigma}{d\hat{\theta}} = 2\pi \frac{r_e^2 m^2 \hat{p}}{4\hat{\epsilon}^3} \left[\frac{\hat{\epsilon}^2 + \hat{p}^2 (1 + \sin^2 \hat{\theta})}{\hat{\epsilon}^2 - \hat{p}^2 \cos^2 \hat{\theta}} - \frac{2\hat{p}^4 \sin^4 \hat{\theta}}{(\hat{\epsilon}^2 - \hat{p}^2 \cos^2 \hat{\theta})^2} \right] \quad (2.102)$$

where \hat{p} is the norm of the momentum of the electron or the positron in the center-of-mass frame. For $\tau \rightarrow 1$ the leptons are created with their rest-mass energy and $\hat{p} \rightarrow 0$ and the cross section is isotropic in the center-of-mass frame. In the high-energy limit,

$$\frac{d\sigma}{d\hat{\theta}} = 2\pi \frac{r_e^2 m^2}{2\hat{\epsilon}^2 (\hat{\theta}^2 + m^2/\hat{\epsilon}^2)} + \mathcal{O}\left(\frac{m^2}{\hat{\epsilon}^2}\right). \quad (2.103)$$

The cross-section strongly peaks at $\hat{\theta} = 0$ (and symmetrically at $\hat{\theta} = \pi$) such that leptons and photons are aligned.

2.3 Active regions

We have seen in the previous section a set of microphysical processes susceptible to providing sources of plasma and radiations to the magnetosphere. A common assumption is to consider that these mechanisms are efficient enough for the magnetosphere to be overall filled with plasma. A convenient leading-order approximation for the distribution of plasma consists in a stationary corotating magnetosphere, that we briefly expose in section 2.3.1. A large part of the work on pulsar magnetospheres then considers that the active parts of the magnetosphere (i.e. where plasma and radiation is produced) lies in local variations. These variations are often called gaps, in reference to sharp local drops in plasma density and electric potential. In some sense, the study of the magnetosphere is thus transformed in a perturbation problem, much more tractable than the global problem. However, the local problems remain highly complex and multiscale. Therefore, it is convenient to adopt a heuristic approach in which one proposes a set of mechanisms and regions that are assumed to be isolated enough from the rest of the magnetosphere, solve the local problem within such restricted assumptions and check of consistency a posteriori. We describe some general properties (section 2.3.2) and some of the main properties of the polar cap (section 2.3.3), the slot gap (section 2.3.4), and the outer gap (section 2.3.5).

These different sets of assumptions may turn out to be irrelevant (see section 2.4.3), starting with the principal hypothesis which consists in assuming it to be possible to treat separately small regions. Already, some sets of assumptions can exclude each other (the slot gap and the outer gap for example, see below). However, we consider that these models develop in different ways the key elements of the physics of pulsar magnetospheres, and that as such they form the fertile ground on which to build the solution of the general magnetosphere problem. It is to be noted that the list of elements touched below is by no mean complete. For example, the magnetosphere is understood as the region within the light cylinder and therefore the wind is not treated although it may very well be very active (see Kirk et al. (2009) for a review), and the magnetic field is assumed to be well below the critical magnetic field $B_c = 4.4 \cdot 10^9$ T such that high-field specific phenomena can be ignored (see Harding and Lai (2006) for a review).

2.3.1 The corotating magnetosphere

Corotating magnetospheres were introduced in particular in Goldreich and Julian, 1969. In this model the plasma in the magnetosphere is assumed to be corotating with the star, trailed by the intense magnetic field, any force other than electromagnetic is neglected. Thus, the magnetosphere is essentially an extension of the inside of the star, the charge density and electric field being determined exactly in the

same way as in section 2.1.1, and there is no discontinuity at the surface of the star. Consequently, the electric field outside the star satisfies condition (2.2),

$$\vec{E} + (\vec{\Omega}_* \times \vec{r}) \times \vec{B} = 0, \quad (2.104)$$

which implies the frame-invariant condition $\vec{E} \cdot \vec{B} = 0$, and the electric field does not work (see 2.1.2).

In turn, equation (2.104) gives the corotation charge density (2.10), often called the Goldreich-Julian density in reference to Goldreich and Julian (1969)

$$\rho_c = \epsilon_0 \vec{\nabla} \cdot \vec{E} = -2\epsilon_0 \frac{\vec{\Omega}_* \cdot \vec{B}}{1 - (\vec{\Omega}_* \times \vec{r})^2/c^2}. \quad (2.105)$$

We recall that $\rho_c = -2\epsilon_0 \vec{\Omega}_* \cdot \vec{B} + \mathcal{O}(\Omega_* r/c)$ which is usually an accurate approximation close to the star. Indeed the theoretical lower limit for a neutron star spin period is $P \sim 1\text{ms}$, which for a fiducial radius of 10km amounts to a few percent of the speed of light. To leading order then, the corotation charge $\rho_c \propto -\cos\theta/r^3$ where θ is the angle between the rotation and magnetic axis and r the distance from the center of the star. This simple dependence has two important consequences:

- The charge density is much higher close to the star,
- There are positively charged and negatively charged regions in the magnetosphere,
- These regions are separated by null surfaces, where the charge density is zero.

In the simple case of the aligned rotator, solving for $\rho_c = 0$ at leading relativistic order shows that in this case the null surface is a cone of axis the spin axis, apex the center of the star, and opening angle $\theta_n = \pm \arccos 1/\sqrt{3} \simeq 55^\circ$ see figure 2.9).

In the case of a perpendicular rotator, the first order null surface corresponds to the union of the rotational equator and the magnetic equator (see section 2.3).

The corotating approximation is well adapted if:

- a) plasma motion perpendicular to field lines is negligible,
- b) the plasma is located on closed field lines, and therefore is trapped since perpendicular motion is forbidden by a),

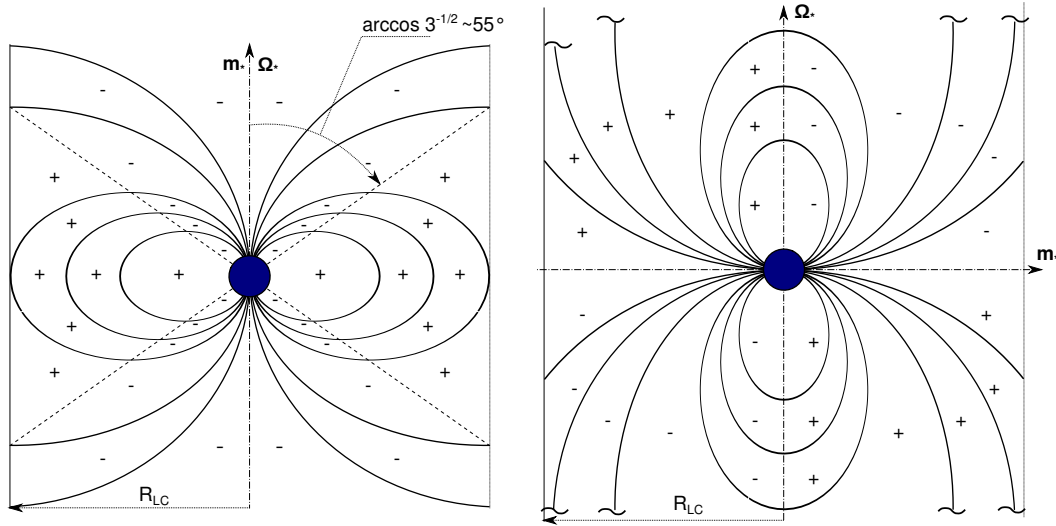


Fig. 2.9.: Corotating magnetosphere in a purely dipolar magnetic field. Left: dipole moment aligned with the spin axis $\vec{\Omega}_* \cdot \vec{m}_* = |\vec{\Omega}_*| |\vec{m}_*|$. The corotation charge is negative within a cone of opening angle $\arccos 1/\sqrt{3} \sim 55^\circ$ centered on the common axis, and positive elsewhere. Right: orthogonal rotator with $\vec{\Omega}_* \cdot \vec{m}_* = 0$. The null surfaces are the magnetic and rotation equators, superimposed on this sketch with the rotation and magnetic axis respectively. The magnetic field lines ending with a \sim are closed field lines that have been truncated for compactness.

- c) the corotation velocity is small compared to the speed of light, otherwise plasma inertia is no longer negligible.

In other words, the corotating magnetosphere is particularly relevant in the closed-magnetic-field region (b), which is located sufficiently close to the star such that the amount of momentum transferred to the plasma be small enough (c and right-hand-side of (2.104)) and the magnetic field be intense enough (a) to relax perpendicular momentum through synchrotron emission very efficiently.

It is to be noted that the assumption that the magnetic field is able to rigidly trail the plasma necessarily fails close to the light cylinder (also c) above). Indeed, the plasma approaches the speed of light and its kinetic energy becomes infinitely large within the corotation assumption. Instead, one infers (e.g. Goldreich and Julian (1969)) that the magnetic field develops a strong toroidal component.

2.3.2 Some general properties of gaps

We assume a perfectly corotating magnetosphere (section 2.3.1) with $\vec{E} \cdot \vec{B} = 0$ and density (2.105) $\rho_c = -2\epsilon_0 \vec{\Omega}_* \cdot \vec{B} + \mathcal{O}(\Omega_* r/c)$. As mentioned in the previous section, these two conditions may be relevant within the closed-magnetic-field-line region, but become questionable on the open-magnetic-field-line bundle defined by the field

lines crossing the surface of the star within the polar cap (see section 2.1.4). The reason is that these field lines are open, and therefore do not prevent the plasma pulled by centrifugal forces to flow through the light cylinder (see also section 2.4.1). If this escaping plasma is not replaced by a source within the light cylinder, it will progressively create vacuum gaps where parallel electric fields $\vec{E} \cdot \vec{B} \neq 0$ develop until an equilibrium can be reached. In the case of an aligned rotator like in the seminal paper by Goldreich and Julian (1969), such an equilibrium solution is given for example by the electrosphere discussed in section 2.4.2 (see also Smith et al. (2001)).

If the plasma is replaced then the gaps may be completely quenched rendering the corotating magnetosphere stable. More generally, gaps develop to a certain extent until they become limited by pair creation, as explained in the next sections. In this case, a common approximation consists in assuming that the gap is surrounded by an undistorted corotating magnetosphere which is further assumed to have an infinite conductivity. The latter assumption is justified from the relatively high density of plasma compared to the gap. Since $\vec{E} \cdot \vec{B} = 0$ in the corotating magnetosphere, the magnetic-field lines surrounding a gap are electric equipotentials, which simplifies the description of the boundary conditions of the gap as can be seen on figure 2.10.

Maxwell equations in the corotating frame

Gaps are more easily described in the frame corotating with the star, where Maxwell equations read (Schiff, 1939)

$$\vec{\nabla} \cdot \vec{E} = \frac{\rho - \rho_c}{\epsilon_0}, \quad (2.106)$$

$$\vec{\nabla} \times \vec{B} = \mu_0(\vec{J} - \vec{J}_c) + \frac{1}{c^2} \frac{\partial \vec{E}}{\partial t}, \quad (2.107)$$

$$\vec{\nabla} \cdot \vec{B} = 0, \quad (2.108)$$

$$\vec{\nabla} \times \vec{E} = -\frac{\partial \vec{B}}{\partial t}, \quad (2.109)$$

$$(2.110)$$

where J_c is a complicated function of \vec{E} and \vec{B} (see e.g. Fawley et al. (1977)), and ρ and J are charge and current density as measured in the corotating frame. Remarkably, the Maxwell equations keep exactly the same form in this frame, the only difference being the appearance of ρ_c and J_c as inertial charge and current densities (analogous to inertial forces in mechanics).

Furthermore, if on the one hand we assume that the magnetic field of the star dominates over the magnetic induction by currents in the magnetosphere, and on the other hand that the plasma is in a steady state in the corotating frame, then the time derivatives give zero and equations (2.107), (2.108), (2.109) become essentially irrelevant so that we end up with a problem of electrostatics. One then only has to solve for the electric potential in the corotating frame defined by $\vec{E} = -\vec{\nabla}\Phi$, and

$$\Delta\Phi = -\frac{\rho - \rho_c}{\epsilon_0}. \quad (2.111)$$

It follows that the total steady state electric field in the frame of the observer is given by

$$\vec{E}_{\text{obs}} = -(\vec{\Omega}_* \times \vec{r}) \times \vec{B} - \vec{\nabla}\Phi. \quad (2.112)$$

The boundary conditions to the electrostatic problem are part of the main assumptions made in gap electrodynamics. We will see some of the main examples in the next sections.

One also notices that, in this frame, if the field inside the star is assumed to be dipolar as was our assumption in section 2.1.1, the surface of the star is equipotential (usually set to 0). The force-free condition $\vec{E} \cdot \vec{B} = 0$ translates in this frame in $\vec{E} = 0$. Outside of the gaps, the corotating plasma has a charge density $\rho = \rho_c$, and therefore a gap is a region within the magnetosphere where $|\rho| < |\rho_c|$ in the corotating frame. In the ideal case where perfect vacuum is achieved in the observer's frame, the effective charge density is $-\rho_c$ in the corotating frame.

Current density

Another common approximation consists in considering that the current in the corotating frame \vec{J} flows along the magnetic field lines. This is a result of the assumption of null momentum perpendicular to the field owing to synchrotron relaxation. Therefore one can always write that

$$\vec{J} = \alpha\vec{B}. \quad (2.113)$$

If steady state is assumed, the continuity equation yields $\vec{\nabla} \cdot \vec{J} = 0$. Using the appropriate vector identity one obtains

$$\vec{\nabla} \cdot \vec{J} = \vec{B} \cdot (\vec{\nabla}\alpha) + \alpha\vec{\nabla} \cdot \vec{B} = \vec{B} \cdot (\vec{\nabla}\alpha) = 0 \quad (2.114)$$

where the transformation from the second to the third equality results from the nullity of the divergence of the magnetic field (2.108). It follows that α is constant along a magnetic field line and that α can be parametrized by the coordinates of the feet of the magnetic-field lines on the surface of the star.

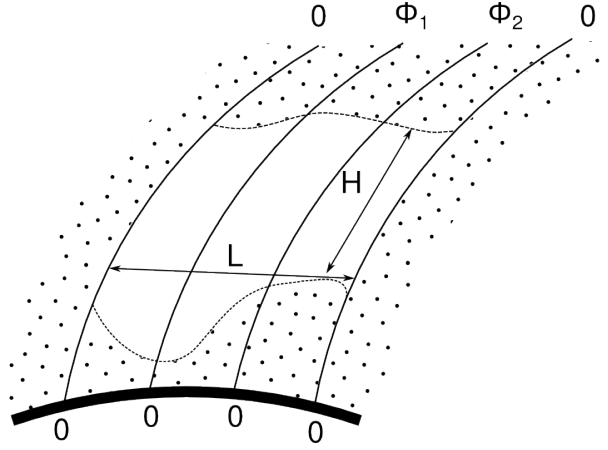


Fig. 2.10.: An example of gap in a corotating magnetosphere. The surface of the star is represented by the thick line and is grounded in the corotating frame. Magnetic-field lines, the solid thin lines, are equipotentials on their portions within the corotating plasma, represented by dots. The dashed lines represent the boundaries of the gap along the field lines. The potential changes from 0 to Φ_1 and Φ_2 for the two field lines that cross the gap.

Estimate of the potential drop

The potential difference between each side of the gap is roughly the potential created by the amount of charge removed from the gap. Indeed, integrating the divergence of the electric field over the volume of the gap and using Green-Ostrogradski's theorem one finds that, in the observer's reference frame,

$$\bar{E} = -\frac{Q_c}{\epsilon_0 S} \quad (2.115)$$

where $Q_c = \int dV \rho_c$ is the total missing charge inside the volume of the gap, $\bar{E} = S^{-1} \oint \vec{E} \cdot d\vec{S}$ is the averaged intensity of the electric field over the surface S of the boundary of the gap. In a variety of geometries like a cylindrically symmetric gap or a thin gap in the direction of the magnetic field ($H \ll L$ on figure 2.10), and more generally when the electric field within the gap can be expected to be mostly parallel to the magnetic field, the edge of the gap parallel to the field does not participate in the average. Then, H is approximately the length of the gap and \bar{E} the electric field along the gap. This gives an estimate of the potential drop across the gap

$$\Delta\Phi = \frac{Q_c H}{\epsilon_0 L}. \quad (2.116)$$

Further, one side of the gap usually bears a null electric field in the corotating frame as we will see in the next sections. Taking the volume of the gap to be equal to $V = L^2 H$ where H is the "height" of the gap (see figure 2.10), namely its characteristic length along the magnetic field, and integrating as before over a

volume L^2x where $x \in [0, H]$ is the in the direction of the field within the gap, one obtains an estimate of the electric field

$$\vec{E} \sim -\frac{\bar{\rho}_c x}{\epsilon_0}, \quad (2.117)$$

and of the potential drop

$$\Delta\Phi \sim \frac{\bar{\rho}_c x^2}{2\epsilon_0} \sim \Delta\Phi_{\text{cap}} \cos\bar{\theta} \left(\frac{R_*}{R}\right)^3 \left(\frac{x}{R_*\theta_c}\right)^2, \quad (2.118)$$

where $\bar{\rho}_c = Q_c/(L^2H) \sim -2\epsilon_0\bar{\Omega}_* \cdot \vec{B}(\bar{R}, \bar{\theta})$ is the average corotating charge within the gap, and $\Delta\Phi_{\text{cap}} \simeq 6 \cdot 10^{12} R_{*4}^3 B_{*8} P_{*1}^{-2}$ V is the potential drop across the polar cap, equation (2.147). The length x scaled to the size of the polar cap $R_*\theta_c$ (assuming $\theta_c \ll 1$, see equation (2.25)) which is relevant for the inner part of the open magnetosphere. For the outer magnetosphere, a scaling to the light cylinder radius R_{LC} could be more relevant. We will use expressions (2.117) and (2.118) as far as we are concerned with orders of magnitude. However, it should be noted that here we made the very sharp approximation of a discontinuity in parallel electric field on both sides of the gap which implies charge layers at the top and bottom of the gap. A smoother assumption would be to consider that the charge density in the gap comes back progressively to ρ_c , such that both edges of the gap can be considered to have a null parallel electric field.

Radiative losses

Let us consider what happens to a particle accelerated by an electric field such as calculated previously. In order so simplify, we assume that this electric field is parallel to the local magnetic field.

The special relativistic equation of motion followed by this particle is given by

$$\frac{d\vec{p}}{dt} = q\vec{E} - \sum_{\text{radiations}} \vec{R}_i \quad (2.119)$$

where $q = \pm e$ is the charge of the particle assumed to be a lepton, and its momentum is $\vec{p} = \gamma m\vec{v}$, with γ the Lorentz factor and \vec{v} the velocity. The reaction forces are derived from the radiation mechanisms, typically : curvature radiation, synchrocurvature and synchrotron radiations, Compton scattering. See section 2.2.2 for these processes. The equation of motion above is valid as long as a great number of photons are interacting with the particle which allows a continuous treatment. If a small number of particles are interacting, then the most relevant procedure is to use a Monte-Carlo simulation (see e.g. Timokhin (2010) for such a treatment in the context of pulsar magnetospheres). Besides the radiation is assumed to be intense

enough to make the motion perpendicular to the magnetic field negligible, which results in the absence of the magnetic term of the Lorentz force in the right-hand side of equation (2.119).

If the radiation is assumed to be continuous, then we can estimate the radiation forces \vec{R}_i . For the family of radiations that can be classically described from retarded potentials, an appropriate formalism is the so-called Abraham-Lorentz-Dirac force (see e.g. Jackson (1998) or Landau et al. (1966)). However, the force is described by first and second derivatives of the momentum of the particle, which makes it not very handy. In pulsar magnetospheres, however, the radiation is expected to undergo an extreme relativistic beaming due to the very large Lorentz factors $\gamma \gg 1$ resulting in a radiation emitted within a cone with a very narrow opening angle $\sim 1/\gamma \ll 1$ opposite to the instantaneous velocity of the particle. One then uses this property to approximate the force to

$$R_i = \frac{P_i}{\|\vec{v}\|} \vec{u}_v \quad (2.120)$$

where $\vec{u}_v = \vec{v}/\|\vec{v}\|$ is the unit vector associated with the velocity, and P_i is the radiated power. A last simplification that arises directly from the ultra-relativistic motion of the particle is the fact that $\|\vec{v}\| \simeq c$.

A common and rather easily computable case is given by synchrocurvature radiation. Following Viganò et al. (2015b), we assume that the electric field is parallel to the local magnetic field, and that perpendicular losses can be averaged over the cyclotron period such that the problem is only two-dimensional with a component parallel to the magnetic field $p_{\parallel} = \gamma mc \cos \alpha$ and one perpendicular $p_{\perp} = \gamma mc \sin \alpha$, with α the pitch angle of the trajectory. These two components obey the following equations of motion

$$\frac{dp_{\parallel}}{dt} = -P_{sc} \sin \alpha / c, \quad (2.121)$$

$$\frac{dp_{\perp}}{dt} = q\vec{E} - P_{sc} \cos \alpha / c. \quad (2.122)$$

$$(2.123)$$

where P_{sc} is the power radiated through synchrocurvature (2.52). In a constant electric field everywhere aligned with a magnetic field of constant curvature ρ , the solution of these equations is asymptotically given by

$$\gamma_{\max}^{(\text{CR})} = \left(\frac{4\pi\epsilon_0 \|\vec{E}\| \rho^2}{e} \right)^{1/4} \simeq 5 \cdot 10^7 E_{12}^{1/4} \rho_5^{1/2}, \quad (2.124)$$

$$\sin \alpha = \sin \alpha_0 \exp \frac{-q\|\vec{E}\|t}{\gamma_{\max}^{(\text{CR})} mc}. \quad (2.125)$$

The first line results from the balance between the the radiation reaction force and the electric field and is identical to the case of pure curvature radiation (because we took the asymptotic value, hence the (CR) superscript). The second line shows that the pitch angle is exponentially decaying due to radiation, and started with the initial value α_0 . We will come back to the decay of the pitch angle and its consequences in chapter 3.

For our present discussion, the important point is to notice that if the particle accelerates fast enough, then its energy depends only on the electric field and not directly on any other property of the gap. Let us notice that the acceleration length scale for an isolated particle (thus neglecting here any collective screening that could interfere) is

$$\lambda_a = \frac{mc}{q \|\vec{E}\|} c \simeq 5 \cdot 10^{-7} E_{12}^{-1} \text{m}. \quad (2.126)$$

Pair production

To limit the expansion of the gap, the important question to solve is: how many gamma-ray photons can transform into a pair ? A necessary condition is that the energy of the gamma-ray be larger than the mass energy of the pair, whether it be formed by photon-photon or by photon-magnetic field interaction since the background photons in the former will generally have an energy $\epsilon_w \ll mc^2$. The typical photon energies of the main mechanisms are summarized here,

$$\epsilon_{\text{Th}} = \gamma^2 \epsilon_w, \quad (2.127)$$

$$\epsilon_{\text{KN}} = \gamma mc^2, \quad (2.128)$$

$$\epsilon_R = 2\gamma B/B_c mc^2, \quad (2.129)$$

$$\epsilon_C = \max\left(\frac{3}{2} \hbar \Omega \gamma^3, \gamma mc^2\right), \quad (2.130)$$

$$\epsilon_S = \max\left(\frac{3}{2} \hbar \omega_B \gamma^3, \gamma mc^2\right), \quad (2.131)$$

where ϵ_w is the energy of the weak photon scattered in the Thomson regime to an energy ϵ_{Th} in the frame of the observer, ϵ_{KN} is the energy of the photon scattered in the Klein-Nishina regime, ϵ_R in the resonant regime, ϵ_C in the curvature radiation peak with $\Omega = c/\rho$ and the synchrotron radiation peak with $\omega_B = eB/(m\gamma)$ (see section 2.2.2 for more details). The maximum function for the two last mechanisms arises because for very high Lorentz factors the radiation has to be dealt with in the quantum regime and the emission saturates close the energy of the radiating particle. This is particularly important for synchrotron radiation in very strong fields, since although the Lorentz factor dependence is only a power of two, $\gamma \omega_B \gg \Omega$ by

an extremely large amount. Therefore, a necessary criterion for gamma photons to make pairs is

$$\hat{\epsilon}_\gamma > 2mc^2, \quad (2.132)$$

where $\gamma = [\text{Th}, \text{KN}, R, C]$ and the hat specifies that this condition applies in the center-of-mass frame of the reaction.

The second important criterion is the mean free path of the photon. It should be smaller than the size of the gap. Ideally, this should be treated as a random process but a common (and fairly good) proxy is to consider that a pair is created as soon as the optical depth τ reaches 1

$$\tau(d) = \int_0^d \frac{dx}{l(x)}, \quad (2.133)$$

where d is the distance and $1/l$ is the reaction rate per unit length of the process. A quick estimate of d is given by the inverse of the reaction rates for the two main reactions expected

$$l_{\gamma\gamma} \sim \left(\sigma(\epsilon_\gamma, \epsilon_w, \mu) \int n(\epsilon_w) d\epsilon_w \right)^{-1} \quad (2.134)$$

$$l_{\gamma B} \sim \left(0.23 \frac{\alpha_{\text{fs}}}{\lambda_C} \frac{B}{B_c} \sin \theta(d) \exp \frac{-4}{3\chi(\theta)} \right)^{-1} \quad (2.135)$$

where $\chi(\theta) = \frac{B}{B_c} \frac{\hbar\omega \sin \theta}{2mc^2}$, equation (2.83) (see section 2.2.2 for more details on the notations), and n is the weak photon density.

If the cross section integrated over outgoing angles for photon-photon pair creation is roughly approximated to its peak value (equation (2.99) and figure 2.8), then $\sigma \sim 10^{-29} \text{m}^2$ and the total number of photons per unit volume should be $\int n(\epsilon_w) d\epsilon_w \sim 10^{28} \text{photon}/\text{m}^3$ to have a mean free path of the order of ten meters. For a black-body, this is achieved for a temperature of $T \sim 10^6 \text{K}$, which is a possible temperature for the neutron-star crust and corresponds to X rays.

For pairs created on the magnetic field, a common approximation consists in using the exponential dependence to end up with a criterion on χ only. Let us assume that the size of the gap along the magnetic field is much shorter than the radius of curvature of the magnetic field ($H \ll \rho$ on figure 2.10). Since pair production limits the expansion of the gap, this implies that the mean free path satisfies $l_{\gamma B} \ll \rho$ as well, and it is safe to say that the magnetic intensity B is constant along the path of the photon. Then for a given photon energy $\hbar\omega$ we have a direct relation between χ and the incidence angle θ , equation (2.136). Locally, it is also safe to assume a convex geometry of the magnetic field, which implies that a photon emitted tangentially will always have a growing incidence angle with the magnetic field. In the simple geometry of figure 2.12, magnetic field lines are concentric, and the

angle grows linearly with the distance traveled with the photon at first order in the variation of radius of curvature, namely

$$\sin \theta = \frac{d}{\rho} + o(\delta\rho/\rho) = \chi \frac{2mc^2}{\hbar\omega} \frac{B_c}{B}. \quad (2.136)$$

Therefore $\chi \propto d$ grows linearly with the travel distance and the mean free path diminishes quasiexponentially with d . On average, once a photon has flown a distance d_{\max} such that

$$d_{\max} = l_{\gamma B}(d_{\max}), \quad (2.137)$$

the distance δd such that the optical depth following d_{\max} be equal to 1 is given by

$$\int_{d_{\max}}^{d_{\max}+\delta d} \frac{dx}{l_{\gamma B}(x)} = 1 \quad (2.138)$$

is necessarily much smaller owing to the exponential dependence. Then, within an error $\delta d \ll d_{\max}$ the average travel distance flown by a photon is given by (2.137).

Inserting equation (2.135) and (2.136) in (2.137) one obtains

$$\chi(d_{\max}) = \sqrt{\frac{\lambda_C}{\rho} \frac{\hbar\omega}{2mc^2} \frac{\exp \frac{2}{3\chi(d_{\max})}}{\sqrt{0.23\alpha_{\text{fs}}}}} \quad (2.139)$$

Solving this equation for χ is not straightforward. However the exponential makes the value of $\chi(d_{\max})$ not very sensitive on the prefactor, allowing to use the same value as a reasonable approximation for a range of ω and ρ . In particular it is often considered that d_{\max} is reached whenever $\chi \gtrsim 1/15$ for second pulsars (Ruderman and Sutherland, 1975). This value is accurate whenever the prefactor $\sqrt{(\lambda_C/\rho)(\hbar\omega/2mc^2)} \simeq 1.2 \cdot 10^{-7}$, which is the case for typical values like $\hbar\omega \sim 0.4\text{GeV}$ and $\rho = 10^5\text{m}$. With our simple geometry this latter estimate corresponds to

$$l_{\gamma B} \sim d_{\max} \simeq 7.4 \cdot 10^2 \frac{\chi}{1/15} B_8^{-1} \rho_5 \frac{0.4\text{GeV}}{\hbar\omega} \text{m}, \quad (2.140)$$

which is consistent with the assumption that $d_{\max} \ll \rho$. The very sharp dependence on distance of magnetic pair creation is at the origin of the so-called pair formation fronts, which defines a surface perpendicular to the magnetic field beyond which significant pair creation occurs. We will come back to this in the section 2.3.3. For very different values of the prefactor, one can solve numerically equation (2.133) which gives figure 2.11 (Timokhin and Harding, 2015).

Pair multiplicity

The multiplicity of a pair cascade is the ratio between the number of primary leptons injected in the gap and the number of particles produced in the gap after the full

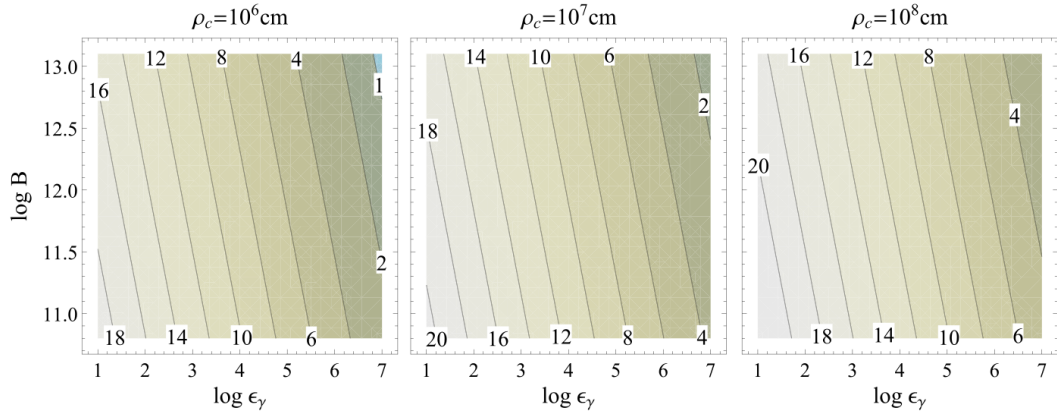


Fig. 2.11.: From Timokhin and Harding (2015). Contour plot of $1/\chi$ as a function of the logarithms of the magnetic field strength B in Gauss, and photon energy ϵ_γ normalized to the electron rest energy, for three values of the radius of curvature of magnetic field lines. Values of $1/\chi$ are solution of (2.133) with $l = l_{\gamma B}$, equation (2.135), and integrating as a function d after changing variable using equation (2.136).

cascade developed. This number depends on the dynamics of gap, for example if a lot of particles of opposite sign compared to the primary can be reversed and accelerated backward by the electric field instead of exiting the gap, or if the secondaries (we call such all the later members of the cascade) can get a lot of energy from the electric field before escaping. If these dynamical effects are ignored and one follows a radiation-only cascade then some limits can be set by assuming that every photon pair produce as long as it is above threshold. Then, the gross maximum limit of the pair multiplicity is given by the ratio between the primary energy $\gamma_0 mc^2$ and the lowest possible particle energy that can radiate a photon above the threshold $2mc^2$, multiplied by two to account for the two particles created,

$$M_{\max} = \gamma_0. \quad (2.141)$$

This limit is modulated by the effectiveness of the various processes to channel the energy of the primary into smaller and smaller pieces before the cascade leaves the active region (no more accelerating electric field and/or no more efficient pair creation process). A more accurate estimate of the multiplicity is then given by the ratio between the energy of the primary and the lowest energy (times two) at which a secondary can be produced, $\gamma_{\text{last}} mc^2$, and which is in general larger than the threshold energy (see e.g. Hirschman and Arons (2001) or Timokhin and Harding (2015)), then $M < \gamma_0 / (2\gamma_{\text{last}})$.

More generally, each generation of lepton of four momentum $(\gamma_n mc, \vec{p}_n)$ at a location \vec{x}_n radiates photons of characteristic energy $\omega_n = \omega(\gamma_n, \vec{p}_n, \vec{x}_n)$ according to the

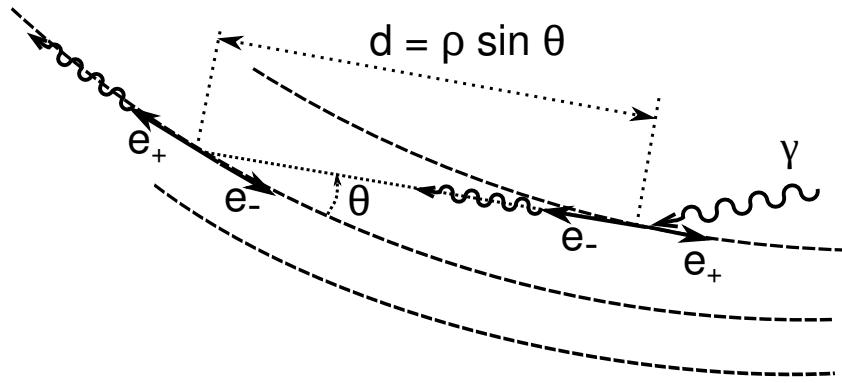


Fig. 2.12.: Sketch of a pair cascade using the photon-magnetic field mechanism in a convex-field-line geometry, where the radius of curvature ρ increases in the outward direction. Magnetic field lines are assumed to be locally concentric circles represented by dashed lines, photons by undulated arrows, and leptons by straight arrows. A gamma photon γ reacts with the magnetic field to produce an electron e_- and a positron e_+ . Almost instantaneously the most energetic lepton radiates gamma photons almost parallel to the field that continue the cascade (both leptons can radiate in principle, but for clarity we consider the case where only one radiate photons that can pair produce). In this geometry, gamma photons move toward the least curved field line, and since the pair production mechanism is sensitive to the component of the magnetic field perpendicular to the photon direction (and proportional to $\sin \theta$), the cascade may extinguish itself.

leading mechanism for these parameters. One then has a sequence where the energy of the generation $n + 1$ of leptons depends of the generation n

$$\gamma_{n+1} \sim \frac{\omega(\gamma_n, \vec{p}_n, \vec{x}_n)}{2mc^2}. \quad (2.142)$$

This is approximate since the repartition of energy between the two members of the pair will vary according to its center-of-mass energy: close to threshold each particle takes half of the energy, high above the repartition becomes very asymmetric. The momentum, and position (and therefore the interaction with the local magnetic field or with background photons) evolves according to the processes and geometry at stake in an essentially markovian sequence. It is also important to notice that the main processes at stake can be changing during the cascade. A well studied example is that of a cascade starting with a primary radiating curvature radiation followed by secondaries mostly radiating synchrotron radiation in very strong magnetic fields (Daugherty and Harding, 1982; Timokhin and Harding, 2015). This owes to the fact that in strong fields $\epsilon_S \gg \epsilon_C$, see (2.130).

An important geometrical limit noticed from the start by Sturrock (1971) is that if convex field line geometries such as on figures 2.10 and 2.12 and magnetic field pair production are involved, then the cascades necessarily moves towards the least

curved field line. In the case of a polar cap, the central field line has a null curvature. It follows that the cascade may stop only because of this geometrical characteristic.

We also assume a primary of energy ϵ_0 which radiates through one of the reaction mechanisms mentioned above (to simplify we consider that one mechanism dominates all the others) gamma photons with a characteristic energy $\omega_0 = \omega(\epsilon_0)$ (\hbar is omitted to simplify the notations). Note that in general ω is not only a function of energy.

Total energy and particle loss

The energy loss of a gap is basically the quantity of energy that leaves the gap to infinity, mostly under the form of accelerated particles and high energy radiation. It is to be compared to the total spindown power $L_{\text{sd}} = I_* \Omega_* \dot{\Omega}_*$ (see table 1.1) to see how much the gap contribute to the energy budget. Besides, if a particular type of radiation is expected, it is to be compared to the observed luminosity. This is particularly true since the advent of gamma ray observatories, in particular EGRET and its successor Fermi.

A gross estimate of the energy loss can be made by considering that, if the gap pair production limits the expansion of the gap then the number of leptons $(\rho_T/e)L^2c$ sent away per unit time to infinity by the gap is at least equal to that given by the corotation density, and $(\rho_T/e)L^2c > (\rho_c/e)L^2c$ (ρ_T is the total charge density, see section 2.1.2, and it is here implicitly assumed that the plasma is charge separated). The energy transferred by the magnetosphere to these particles is at most $e\Delta\Phi$, and although some of them can leave the gap with a lower energy the difference can exit under the form of radiated photons. The gap luminosity is estimated to be

$$L_{\text{gap}} \sim \rho_T \Delta\Phi L^2 c \sim 4 \cdot 10^{23} \frac{\rho_T}{\rho_c} \frac{\Delta\Phi}{\Delta\Phi_{\text{cap}}} \left(\frac{R_*}{r}\right)^3 \left(\frac{L}{R_* \theta_c}\right)^2 R_*^6 B_*^2 P_{*1}^{-4} \text{W} \quad (2.143)$$

where r is the distance from the star, $\theta_c \simeq (R_*/R_{\text{LC}})^{1/2}$ is the polar cap angle (2.25), and the polar cap potential drop (2.147) is $\Delta\Phi_{\text{cap}} \simeq 6 \cdot 10^{12} R_*^3 B_*^3 P_{*1}^{-2}$.

Similarly the number of particle released by the gap is expected to be of the order of

$$\dot{N}_{\text{gap}} \sim \frac{|\rho_T|}{e} L^2 c \simeq 4 \cdot 10^{29} \frac{\rho}{\rho_c} \left(\frac{R_*}{R^3}\right)^3 \left(\frac{L}{R_* \theta_c}\right)^2 P_{*1}^{-2} B_*^3 R_*^3 \text{s}^{-1} \quad (2.144)$$

Depending on pair multiplicity, the actual values of L_{gap} and \dot{N}_{gap} can be much larger, as ρ_T/ρ_c ranges from 100 to 10^6 for typical pulsar parameters (see section 2.3.3 below). In cases where ρ_c is about the density of primaries as in the case of a

space-charge-limited flow near the polar cap (see below), ρ_T/ρ_c gives the multiplicity of the pair cascade.

Death line

The death line of a pulsar is often related to the ability of the magnetosphere to limit the extent of the gap by pair creation. This limit depends on the pair creation as well as the radiation mechanisms considered. A necessary, but not sufficient, condition is that the radiation mechanism produces photons above the pair mass energy $2mc^2 \sim 1\text{MeV}$. This occurs when the energy of the radiating electron (resp. positron) is sufficiently high. The maximum energy of the radiating lepton is given by the potential drop of the gap $e\Delta\Phi$ if radiation reaction is negligible, or by the balance between radiation reaction and the electric field within the gap otherwise. Eventually, this narrows down to a minimum potential drop or electric field along the field lines crossing the gap, depending on the regime of radiation reaction.

Historically, curvature radiation was considered to be a necessary mechanism. In this case a necessary condition to pair produce is that $\epsilon_C > 2mc^2$ which implies that

$$\gamma^{(\text{CR})} > \left(\frac{4 mc^2}{3 \hbar \Omega} \right)^{1/3} \simeq 7 \cdot 10^6 \rho_5^{1/2}. \quad (2.145)$$

If one neglects radiation reaction then $\gamma mc^2 = e\Delta\Phi$ and the curvature radiation dominated death line is set by

$$\Delta\Phi > 0.4 \cdot 10^{12} \rho_5^{1/2} \text{V}. \quad (2.146)$$

Coupled with equation (2.116) or (2.118) this also gives a criteria for the size of the gap.

Besides, an estimate of the maximum potential drop that a gap can develop is given by the potential drop of an aligned vacuum magnetosphere from the surface of the star to infinity at the pole (see equation (2.13)). It is equal to the potential drop from the pole to the edge of the polar cap given by equation (2.6) (and identical in the case of a corotating magnetosphere), with $\sin \theta = \sin \theta_c = \sqrt{R_*/R_{\text{LC}}}$ (equation (2.25)),

$$\Delta\Phi_{\text{cap}} \simeq \frac{B_* R_*^3 \Omega_*^2}{2c} \simeq 6 \cdot 10^{12} R_{*4}^3 B_{*8} P_{*1}^{-2}. \quad (2.147)$$

As can be seen from the numbers, second pulsars are not so far from the curvature deathline, equation (2.146). Actually, observations show that some pulsars are below this deathline, but their survival can be explained by other radiation mechanisms (see e.g. Hibsichman and Arons (2001) and the next sections).

2.3.3 Polar cap

The polar cap is defined as the locus of all the open magnetic field lines (see section 2.1.4 for a dipole). As such it connects the neutron star to all the potentially active regions, by contrast with the assumed closed and inactive magnetosphere. Therefore it is expected to be the major provider of the plasma flowing along the open bundle. Fortunately, it is also very well equipped to perform this task: the magnetic-field strength is at its maximum, with potentially additional multipoles, and can efficiently create electron-positron pairs from gamma rays as proposed by Sturrock (1971). Moreover if the star or at least the polar cap is hot enough then the region is bathed into thermal x rays that can undergo resonant and non-resonant Compton scattering on leptons as well as photon-photon pair creation with gamma rays. For these reasons it received much attention since the early days of pulsar magnetosphere modeling.

In this section, we review some of the main properties and results of the main models encountered in the literature. They vary in terms of limit conditions, vacuum gap for Ruderman and Sutherland (1975) or space-charge-limited flow, the accelerating mechanisms and in particular the frame dragging, and the detailed study of the pair discharge with notably the notion of pair formation front (PFF) and first-principle studies.

The polar vacuum gap model

We summarize here one of the seminal works by Ruderman and Sutherland (1975). The main assumptions on which this work was based are:

- a) The magnetic field is anti-aligned with the spin axis, more generally pulsars are stars with $\Omega_* \cdot m_* < 0$ and anti-pulsars stars with $\Omega_* \cdot m_* > 0$ (Note that it is often, if not usually, defined as the contrary).
- b) Ion binding on the surface is strong enough to keep ions in the crust, with the probable exception of very young pulsars such as the Crab.
- c) Electrons have a small binding energy and can flow freely from the outer part of the cap, where the electric field is relevantly oriented.
- d) The pair cascades, called sparks, are large enough to quench the gap when they are triggered.

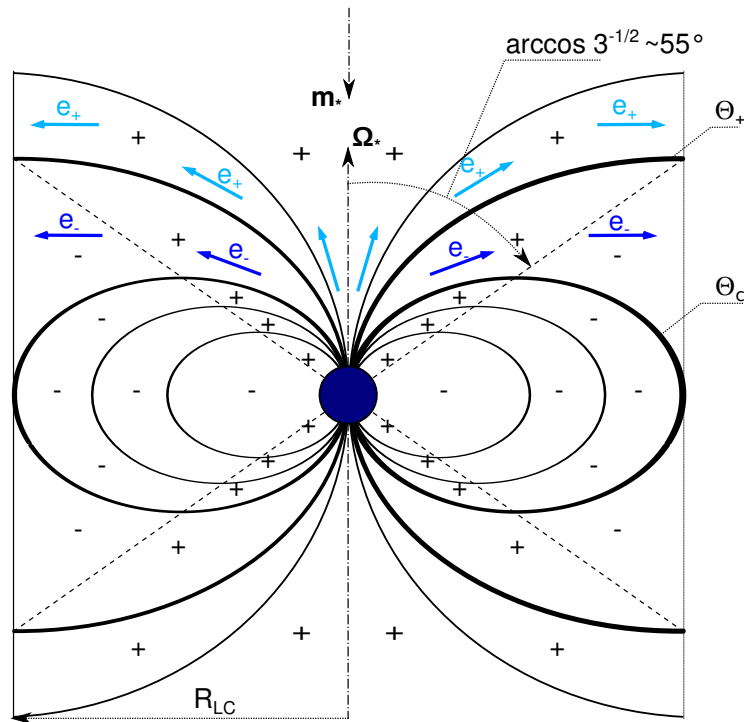


Fig. 2.13.: Sketch of the magnetosphere in the Ruderman and Sutherland (1975) model. The blue sphere is the star, thin vertical lines represent the light cylinder, dot-dashed lines are the magnetic and rotation axis which are anti-aligned, dashed lines represent the limit between the positively and the negatively charged regions, the null surfaces, and black “+” and “-” show the sign the charge density. The other lines represent magnetic field lines. The thick lines are labeled by the angle of their feet on the star with respect to the spin axis, θ_c is the polar cap and θ_+ the inner edge of the negative-current annulus (see text). Field lines between with feet between θ_+ and θ_c cross a negatively charged region before the light cylinder such that a current of electrons flows out along these lines from the star. This current is represented by blue arrows. In the rest of the open-field line-bundle the charge density is everywhere positive such that positrons flow out along these lines. Positron currents are represented by light-blue arrows.

Assumption a) implies that the corotating charge be positive above the polar cap. However, the sign of the charge escaping the magnetosphere is defined by the sign of the corotating charge density at the light cylinder. One sees on figure 2.13 that the field lines closest to the magnetic axis have the same charge density from the surface of the star to the light cylinder. For field lines with foot having an opening angle (angle from the spin axis with apex at the center of the star) larger than θ_+ the charge density next to the light cylinder is negative. The locus of the feet of these field lines form an annulus between θ_+ and the polar cap angle $\theta_c \simeq (R_*/R_{LC})^{1/2}$ (2.25). The angle θ_+ is defined by the foot of the field line crossing the null surface exactly at the light cylinder and is obtained by solving the field line equation (2.23),

$$\theta_+ = (2/3)^{1/2}\theta_c. \quad (2.148)$$

The region within θ_+ is the positron current zone, and the annulus between θ_+ and θ_c is the electron current zone.

Assumption b) implies that, as the plasma is pulled out through the light cylinder, no ions can come from the positron current zone of the cap to replace the escaping charges while assumption c) implies that the star will readily supply the necessary electrons to the electron current zone.

Thus, with this geometry a vacuum gap develops above the positron current zone, but also above the surface covered by the field lines with foot at θ_+ (see figure 2.14). It is to be noted, however, that in their later outer gap model (see section 2.3.5) the authors reconsidered in the case of an inclined rotator the hypothesis that an electron flow from the star could quench the region beyond the null surface and instead assumed no flow at all. The reason is not a change in hypothesis c), but rather that the surface is electrically screened from the region beyond the null surface by the region within. Nevertheless, the following discussion is weakly affected by the retained hypothesis.

The gap potential drop above the pole can be estimated by equation (2.118) in the limit of small gap height $h \ll R_*\theta_+$

$$\Delta\Phi \sim \rho_c h^2 / \epsilon_0 \quad (2.149)$$

where h is the height of the gap above the cap.

The assumed boundary conditions are $\vec{E} \cdot \vec{B} = 0$ along the last positive field line and on the upper side of the gap. The potential is assumed to be constant, typically $\Phi = 0$ on the surface of the star and along the last positive lines.

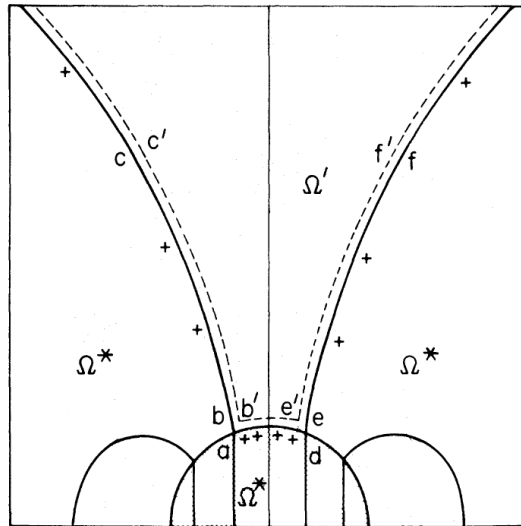


Fig. 2.14.: From Ruderman and Sutherland (1975). “Magnetosphere of a rotating neutron star with antiparallel dipole field above the surface ad . There is zero charge in the magnetosphere between the solid and dashed lines; additional charge is designated within the star. The magnetosphere between the equator and the cone of abc and def corotates with the star. The magnetosphere within the cone of $c'b'e'f'$ rotates with angular velocity $\Omega' < \Omega_*$: Ω' is constant only along magnetic field lines. Significant departures of $E \cdot B$ from zero occur only within the polar gap $ab'e'd$. ”

The only assumed radiation mechanism in the original model of Ruderman and Sutherland (1975) was curvature radiation, and pair production was assumed to occur on the magnetic field. As mentioned in the previous section, the maximum height of the gap is given by $h_{\max} \simeq d_{\max}$ (2.137) by assuming that a discharge occurs as soon as $\chi \simeq 1/15$ (equation (2.133)). This leads to

$$h_{\max} \simeq 96 \rho_5^{2/7} P_*^{3/7} B_{*8}^{-4/7} \text{m}. \quad (2.150)$$

A particular property outlined by Ruderman and Sutherland (1975) is the fact that the magnetosphere above the gap no longer exactly corotates. Indeed, the electric field above the gap is modified by the potential drop, and since the corotation velocity is enforced by the drift velocity $\vec{E} \times \vec{B}/B^2$ a small differential rotation. This differential rotation is interpreted by the authors as the origin of the radio drifting subpulses.

The space-charge-limited-flow (SCLF) models

Other authors considered zones where the plasma, including ions, is free to flow out of the surface of the star. Over time, and due to the limitation on the ion binding

energy, more attention seem to have been given to electron zones, like the outer annulus of Ruderman and Sutherland (1975) exposed in the previous section.

It was quickly realized (see in particular Michel (1974) and Fawley et al. (1977) and references therein) that under the circumstance of a very low binding energy (compared to the temperature of the star and potential) the flow of electron out of the surface is essentially space-charge-limited, that is to say the current flowing from the crust is only determined by the dynamics of the flow and electrostatics above the surface. More specifically, one makes the approximation that

- the work function is null, implying a null electric field at the surface,
- the surface of the star is metallic and can provide an unlimited number of electrons,
- the extracted plasma flow is cold,
- there is only one sign of charge present,
- charges are extracted with a null velocity.

If these approximations are applied to the cathode of a planar diode and a stationary flow is assumed, one obtains the well-known Child-Langmuir flow (see e.g. Davidson (2001)). This case is geometrically simpler, but still retains some of the essential features of neutron-star space-charge-limited flows, which makes it worth a short review here.

The model is 1D with coordinate x , there is no magnetic field, the cathode is located at $x = 0$ and the anode at $x = d$. The boundary conditions on the potential and the electric field are given by

$$\Phi(x = 0) = \partial\Phi/\partial x(x = 0) = 0 \text{ and } \Phi(x = d) = V. \quad (2.151)$$

Moreover, electrons are assumed to be emitted from the anode at zero velocity

$$v(x) = 0. \quad (2.152)$$

Figure 2.15 summarizes the setup. There is only one sign of charge in the diode gap and the stationary continuity equation implies that the current be constant: $J(x) = \rho(x)v(x) = \text{constant}$, where $\rho(x)$ is the charge density and $v(x)$ the velocity

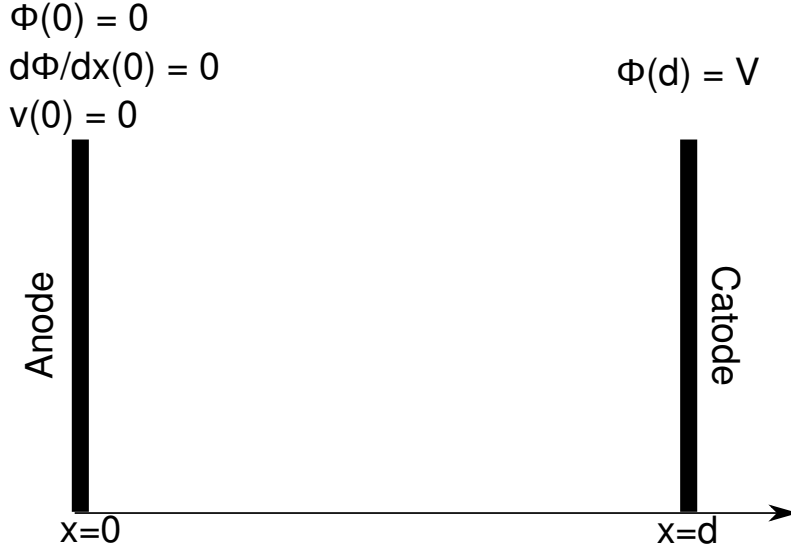


Fig. 2.15.: Setup of a planar diode fitting conditions (2.151) through which goes a Child-Langmuir flow.

of the flow. This condition is essential, and is the analog in this configuration of equation (2.113). Conservation of energy together with Poisson's equation gives

$$\left. \begin{aligned} (\gamma(x) - 1)mc^2 - e\Phi(x) &= 0 \\ \frac{\partial^2 \Phi}{\partial x^2} &= -\frac{\rho}{\epsilon_0} = -\frac{J}{v(x)\epsilon_0} \end{aligned} \right\} \Rightarrow \frac{\partial^2 \gamma}{\partial x^2} = -\frac{eJ}{\epsilon_0 mc^3} \frac{\gamma}{(\gamma^2 - 1)^{1/2}}, \quad (2.153)$$

where γ is the Lorentz factor of an element of fluid, and we used the fact that $\rho = J/v$ and $v = c(1 - \gamma^{-2})^{1/2}$. The boundary conditions on Φ transpose trivially into conditions on γ using the energy conservation equation. Let us remark that we have only a second order differential equation to solve but three independent boundary conditions (equations (2.151), condition (2.152) is already used in setting the total energy of the system to zero), which is explained by the fact that the constant current J is also undetermined. After multiplying equation 2.153 by $d\gamma/dx$ one integrates with respect to x and obtains

$$\frac{1}{2} \left(\frac{d\gamma}{dx} \right)^2 = \frac{-eJ}{\epsilon_0 mc^3} (\gamma^2 - 1)^{1/2}. \quad (2.154)$$

Separating variables, and integrating from the anode to the cathode, one gets the expression of the current

$$J = -\frac{\epsilon_0 mc^3}{2ed^2} \left(\int_1^{1+\frac{eV}{mc^2}} \frac{d\gamma}{(\gamma^2 - 1)^{1/4}} \right)^2 = \begin{cases} -\frac{8}{9\sqrt{2}} \frac{\epsilon_0 mc^3}{ed^2} \left(\frac{eV}{mc^2} \right)^{3/2} & \text{if } \frac{eV}{mc^2} \ll 1, \\ -2 \frac{\epsilon_0 mc^3}{ed^2} \left(\frac{eV}{mc^2} \right) & \text{if } \frac{eV}{mc^2} \gg 1. \end{cases} \quad (2.155)$$

The acceleration length to relativistic speeds is given by plasma skin depth $\lambda_p = c/\omega_p = c\sqrt{m/(e\rho_c\epsilon_0)} \simeq 0.02P_{*1}^{1/2}B_8^{-1/2}\text{m}$ for a typical plasma density close to the corotation density ρ_c (Fawley et al., 1977), ω_p being the plasma pulsation.

In the case of a neutron-star polar cap, the same kind of derivation applies with some differences:

- The electric potential $\Phi = 0$ on the surface of the star (top of the layer) and on the closed magnetosphere around (edge of the polar cap in particular),
- The current is given by (2.113), $\vec{J} = \alpha\vec{B}$ where α is constant along field lines,
- The position of the cathode and its potential are unknown, therefore it is convenient to replace this boundary condition by $\vec{E} \cdot \vec{B} = 0$ far from the star, justified by the fact that one expects to return in a corotating plasma (Fawley et al., 1977; Scharlemann et al., 1978).

Note that the essential property of the anode, that of evacuating charges, is conserved. This can only happen in open-field-line regions, while in closed-field-line regions charges accumulate and make such a derivation irrelevant. Besides, the flow can be considered ultra-relativistic everywhere except within a very thin layer above the surface given by the skin depth (see above and (Fawley et al., 1977)). This layer is sometimes called the inertial skin in the sense that it is where the effect of the finite mass of the electron plays a role since $v < c$. As emphasized by Michel (1974), a small potential drop necessarily results from this acceleration phase, as the corotation current would be satisfied if the electrons were emitted from the surface directly at the speed of light, which would be the case if they were considered massless, as in the rest of the corotating or force-free magnetosphere. Nevertheless, this inertial charge difference and the resulting potential turn out to be negligible compared to other effects that we will discuss below. It is also possible to consider that the plasma is extracted not directly from the crust but from an atmosphere that would surround the star (Harding and Muslimov, 1998). In this case extraction of ions would also occur within appropriate regions.

We will now consider only the region where the plasma is flowing at the speed of light. Then, the density of charges is $\rho = \|\vec{J}\|/c$ since the flow is completely charge separated. The electric potential has to satisfy the Poisson equation (2.111) $\Delta\Phi = -\frac{\rho-\rho_c}{\epsilon_0}$ with the boundary conditions given above in the reference frame of the rotating star. The electric field is generated by the difference between the charge

density and the effective corotation density. However these two densities have in general different dependences on location, and

$$\rho - \rho_c = \alpha \left\| \vec{B} \right\| / c + 2\vec{\Omega}_* \cdot \vec{B} \quad (2.156)$$

at leading relativistic order for ρ_c . Reminding that α is constant along a field line, one then sees that the charge density difference increases if a field line is bending towards the rotation axis, and decreases otherwise as was shown by Scharlemann et al. (1978). It follows that the intensity of the potential drop created by the space-charge-limited flow depends heavily on the geometry of the magnetic field. In this particular case, the same authors showed that the aligned dipolar rotator cannot efficiently accelerate particles since every field lines are bending away while in the perpendicular case half of the polar cap only would develop a significant potential drop. In the orthogonal-dipolar-magnetic-field case the potential drop reached (Scharlemann et al., 1978)

$$\gamma_{\max} \simeq 10^5 B_{*8} R_{*4}^{5/2} P^{-5/2} \quad (2.157)$$

is only sufficient to reach the magnetic pair creation threshold of curvature photons (equation (2.145)) in fast spinning, high-magnetic-field pulsars. Of course, other mechanisms can play a role for slower pulsar, such as inverse Compton and synchrotron radiation.

Some effects of general relativity

Space-charge-limited polar caps were renewed by the introduction of inertial frame dragging effects by Muslimov and Tsygan (1992). More generally, the authors solved Maxwell's equations within the assumptions given above, but assumed an asymptotically flat, steady-state, axisymmetric spacetime near the rotating neutron star, instead of a flat spacetime. Taking into account general relativity then results in a number of important consequences:

- The opening angle of the polar cap field lines can be narrower by up to 30% than in flat space time.
- The corotation condition $\vec{E} + (\vec{\Omega}_* \times \vec{r}) \times \vec{B} = 0$ becomes $\alpha \vec{E} + (1 - \kappa(R_*/r)^3) \times (\vec{\Omega}_* \times \vec{r}) \times \vec{B} = 0$ where $\alpha = (1 - 2GM_*/rc^2)^{1/2}$ is the metric lapse function, $\kappa = \Theta(I_*/(M_*R_*^2)) \sim 0.15I_{*39}R_{*4}^{-6}$ with the compactness parameter $\Theta = 2GM_*/R_*c^2 \sim 0.5$ and $I_* \sim M_*R_*^2 \sim 10^39M_{*31}R_{*4}^2\text{kgm}^2$ the moment of inertia of the star.

- The electric field grows quasi exponentially until a height comparable to the size of the polar cap and then decays like $1/r^4$. Consequently, most of the potential drop is achieved within a height $\theta_c R_*$.
- The space-charge-limited electric field due to general relativity is $\Theta(c/\Omega R_*)^{1/2} \sim 100P_*^{1/2}$ larger than in flat spacetime.

The fields \vec{E} and \vec{B} are those seen by an observer with zero angular momentum (ZAMO). The general relativistic corotation conditions translates in a general relativistic corotation density that has modified position dependence, leading to the extra potential drop along magnetic field lines. In the case of a quasialigned dipole field close to the surface, the corrected corotation density is

$$\rho_c^{GR} \simeq \rho_c \left(1 - \frac{\kappa}{(r/R_*)^3} \right). \quad (2.158)$$

It is to be noted that this effect is independent of the magnetic geometry and completely supersedes the effect of the field line curvature. One more consequence is that the aligned dipole develop large enough potential drops for pair creation thanks to this mechanism.

Besides, Gonthier and Harding (1994) studied the effects of a Schwarzschild spacetime on gamma-ray propagation close to the polar cap. In particular:

- The observed gamma-ray profile is similar to flat spacetime.
- The magnetic field intensity is larger near the surface by a factor ~ 1.5 compared to flat spacetime, thus enhancing pair production on the magnetic field. A 1 GeV photon can have a mean free path twice as short as in a dipolar field.
- Light bending may broaden pulses.
- Photons from near the surface are delayed by ~ 80 microseconds.

Pair formation fronts (PFF)

The pair formation front above the polar cap is defined by Hibsman and Arons (2001) as « the point above the polar cap where enough pairs have been formed to halt any further acceleration of the beam ». A direct consequence is that the PFF sets the end of the gap, as the potential drop above is screened and therefore, $\vec{E} \cdot \vec{B} = E_{\parallel} = 0$ at the PFF. Some authors also add the constrain that $\nabla_{\parallel} E_{\parallel} = 0$ if the pair cascade is efficient enough, thus avoiding the creation of a charge layer (Arons, 1981; Hibsman and Arons, 2001).

In an environment where photon-magnetic-field pair creation dominates, as is expected in the strongly magnetized environment close to the surface of the neutron star, pair formation is expected to occur on a distance δh very small compared to the extent of the accelerating region (gap) h : $\delta h \ll h$. The basic argument for that is that it is due to the very sharp, exponential dependence of the pair creation optical depth, as was discussed in section 2.3.2. A detailed demonstration is given in Arons (1981) and Arons (1983), in the context of a SCLF. Eventually, the position of the PFF defines the position of the anode of the gap in the diode language of the previous section on SCLF.

Determining the exact height of the PFF depends on the radiation mechanism and approximations at stake. One way is to start with a minimum photon energy ϵ_{\min} , determine for each possible radiation mechanism at what Lorentz factor $\gamma_{\min}(\epsilon_{\min})$ an electron can emit at least one photon at ϵ_{\min} . Assuming monotonous acceleration in a steady flow, there is a correspondence on each field line between the height above the cap and the energy reached by the the particle: said differently, to each minimum Lorentz factor corresponds an acceleration height $h_a(\gamma_{\min})$. Similarly, to each photon at ϵ_{\min} assumed to be emitted at or below h_a there is a distance $d_{\max}(h_a, \epsilon_{\min})$ usually determined by a unit optical depth (see also (2.137))

$$\int_0^{d_{\max}} (l_{\gamma B})^{-1}(s) ds = 1 \quad (2.159)$$

where s is the abscissa along the path of the photon. The height of the PFF can then be determined by (Harding and Muslimov, 1998)

$$H = \min(h_a(\gamma_{\min}) + d_{\max}(h_a, \epsilon_{\min})). \quad (2.160)$$

Note that here a 1D geometry is implicitly assumed (d_{\max} is along the same direction as h_a).

Analytical estimates of the height of the PFF for different radiation mechanisms were carried out analytically by Hibschan and Arons (2001). Numerical computations were carried out by Harding and Muslimov (1998). In both cases, curvature radiation, inverse compton scattering (ICS) both in the Klein-Nishina (KN) and Thomson (Th) regimes and resonant inverse compton scattering (RICS) were considered. Compton scattering is assumed to occur through interaction with blackbody X-rays from the polar cap with temperatures around 10^6 K. The electrostatic conditions are those of SCLF. The dominant mechanism is then the one which gives the lowest PFF i.e. screens first the electric field, which typically happens at a few tenth of stellar radius, compatible with the earlier work of Arons and Scharlemann (1979). Note that the pair cascade itself is not simulated here. Instead, the altitude H is a proxy giving

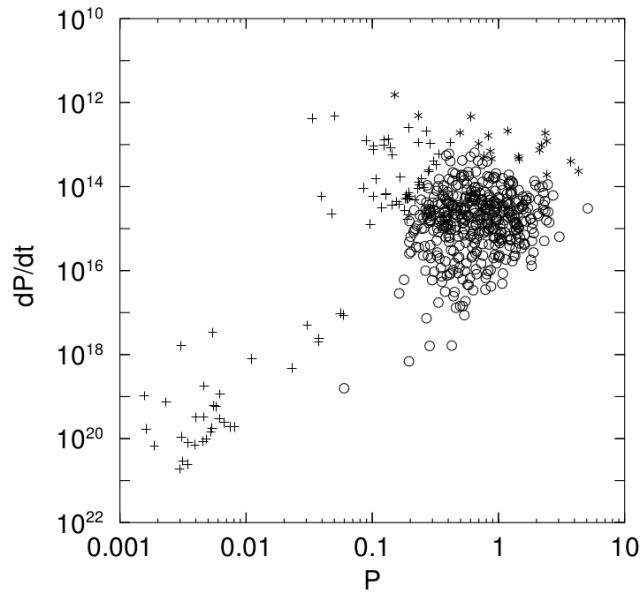


Fig. 2.16.: From Hibschan and Arons (2001). $P - \dot{P}$ diagram showing which pulsars have their PFF height set by curvature (crosses), non resonant ICS (circles), and RICS (asteriks). The bulk of pulsars is dominated by Compton scattering, except for millisecond pulsars (bottom left) and young pulsars such as the Crab (upper center).

the altitude beyond which the cascade should develop somewhat exponentially and screen the gap.

The family of Compton scattering processes usually dominate except for millisecond pulsars or if a thick atmosphere (Harding and Muslimov, 1998) makes the gap start quite far from the surface (and therefore with a lower thermal flux, thus diminishing the probability of Compton scattering). In the other cases curvature is expected to dominate. In both cases the reason is that Compton scattering is very sensitive to the X-ray flux, which is expected to be smaller for old millisecond pulsars as well. Electrons close to the polar cap are mostly sensitive to RICS while returning positron which are seeing x rays face-on interact in the KN regime. The maximum Lorentz factor of particle depends quite strongly on the dominant mechanism: $\gamma_{\max} \sim 10^5 - 10^6$ Compton scattering dominates, but $\gamma_{\max} \sim 10^7 - 10^8$ when curvature radiation dominates (Harding and Muslimov, 1998). This owes to the larger efficiency of Compton scattering as a radiation reaction mechanism at lower energies, provided a sufficient soft-photon background is present.

In principle, if enough positrons are turned around in the PFF and return to the crust, this raises the possibility of creating a second positron PFF near but above the surface. Created at the surface, a second PFF would not change anything from an electrostatic point of view since the parallel electric field is already assumed to be null on the surface (SCLF). It is in this sense a symmetric PFF. However, if created above

the surface, the second PFF would screen the electric field driving the creation of the first PFF and the solution becomes inconsistent with a steady flow. This possibility is studied by Harding and Muslimov (1998), and it is shown that Compton driven polar caps are susceptible to develop a second asymmetric PFF (i.e. above the start of the acceleration zone) due to the fact that the radiation mechanism is different for electron and positron (respectively in the resonant and Klein-Nishina regimes).

Polar pair cascades from first principles

The pair cascade problem is probably the hardest problem to deal with in pulsar gaps. It is highly nonlinear and multiphysical and can only be isolated from the other steps raised in this section and the previous at the price of important assumptions, whether it be in the Ruderman and Sutherland gap type or in the SCLF regime. The principal assumption usually met are the steady state (in the corotating frame) and the selection of some particular radiation and pair creation phenomena, supposed to be dominant in a given situation. Early models based on Arons and Scharlemann (1979) and Ruderman and Sutherland (1975) usually consider that curvature radiation is the only radiation mechanism and pair - magnetic field interaction is the only pair creation mechanisms. While the latter is probably well justified in high magnetic field close to the polar cap, the former can only produce small multiplicities per particle. Indeed, if one uses equation (2.142) with the fact that the steep curvature spectrum needs a Lorentz factor of at least $\gamma_{\max}^{(\text{CR})} = 7 \cdot 10^6 \rho_5^{1/2}$ (equation (2.145)) to produce a photon above pair threshold, one sees that even in the radiation reaction dominated regime, equation (2.124), only a few generations of photons will be produced before the cascade dies out. We neglected the acceleration provided by the parallel electric field in the gap, however curvature radiation can only radiate ~ 1 photon/meter at radiation-reaction-limited energies which limits significantly the total number of primary photons that can be radiated.

The other important mechanisms that can occur are synchrotron radiation from secondaries, and also Compton scattering of soft photons, mostly thermal from the surface of the star. Synchrotron radiation cascades were studied in particular by Daugherty and Harding (1982). The idea is that primary particles can only radiate curvature, if Compton scattering is ignored, because there is no momentum perpendicular to the magnetic field. However, if a first generation of secondary pair is created, these particles are created with a given perpendicular momentum. Although it may be small compared to the longitudinal momentum, the smaller dependence on the Lorentz factor of the synchrotron characteristic pulsation $\omega_c = 3/2 \omega_B \gamma^3 \propto \gamma^2$ (equation (2.35)), than the curvature pulsation $\propto \gamma^3$ together with the much higher cyclotron pulsation than the curvature pulsation $\gamma \omega_B = eB/m \gg \Omega_C = c/\rho$ makes synchrotron radiation much more susceptible to radiate above-threshold photons

from leptons at lower energy than with curvature radiation. The equivalent of the curvature minimum Lorentz factor $\gamma^{(\text{CR})}$, equation (2.145), is for synchrotron radiation

$$\gamma_{\perp}^{(\text{SR})} = \left(\frac{4m^2c^2}{3eB\hbar} \right)^{1/2} \simeq 7.7B_8^{-1/2} \ll \gamma^{(\text{CR})}, \quad (2.161)$$

where the perpendicular Lorentz factor is to be understood as the Lorentz factor of a lepton of four momentum $P = (P^0, P^{\parallel}, P^{\perp})$ in the frame where the component of its momentum perpendicular to the magnetic field is null: $\gamma_{\perp} = (P^{02} - P^{\parallel 2})^{1/2} / (mc)^2 \simeq 1 + \gamma \sin \theta + \mathcal{O}(1/\gamma^2 + \beta_{\perp}^2)$, with $\sin \theta = P^{\perp} / P^{\parallel}$ and $P^{\perp} \ll P^{\parallel}$. Using estimate (2.140), the angle between the field line and the pair at creation is $\theta \simeq d/\rho \simeq 7.4 \cdot 10^{-3} B_8^{-1} (\chi/(1/15)) (0.4 \text{ GeV} / \hbar\omega)$. In this case, $\gamma_{\perp} \simeq 1 + 3(\chi/(1/15)) B_8^{-1}$. According to (2.161), we need at least $\chi \simeq 7$ which corresponds to a photon energy of $\hbar\omega \gtrsim 100 \text{ GeV}$ according to the exact solution of equation (2.133) given on figure 2.11 for our present parameters. At such energies, synchrotron is radiated in or close to the quantum regime, and the characteristic photon energy saturates near the energy of the radiating lepton, making the cascade very efficient. Besides, all the perpendicular energy of each lepton will be radiated within a very short time and all synchrotron radiation can be assumed to be radiated on the spot (Tademaru, 1973). Assuming a constant accelerating electric field of 10^{13} V , Daugherty and Harding (1982) found a pair multiplicities from $\sim 10^2$ to $\sim 10^4$ for crablike pulsars.

The second important assumption is steady state. Cascades were assumed to be time dependent by Sturrock (1971) but little theoretical effort was made until recently on this track. In the recent years some analytical or semi-analytical work has been done to challenge the steady-state approximation (Melrose et al., 2005; Beloborodov, 2008), and one-dimensional first-principle simulations have been developed in particular by Timokhin (2010). In this work and the following one (Timokhin and Arons, 2013), radiation is treated using a Monte Carlo algorithm while particles are treated using a particle-in-cell (PIC) code. Only electrons and positrons are part of the simulations, and only curvature radiation and magnetic pair production are taken into account.

Moreover, the cornerstone of this simulation is that instead of imposing boundary conditions on the electric potential, one considers that the much higher impedance of the rest of the magnetosphere imposes the average current. The electric field in the gap is then found from Maxwell-Ampère's equation

$$\frac{dE}{dt} = -\mu_0(j(x, t) - j_m(x, t)) \quad (2.162)$$

where $j_m = \nabla \times B_{\text{magnetosphere}}$ is the current imposed by the twist of the magnetic due to the rest of the magnetosphere. This twist can come from the sweepback

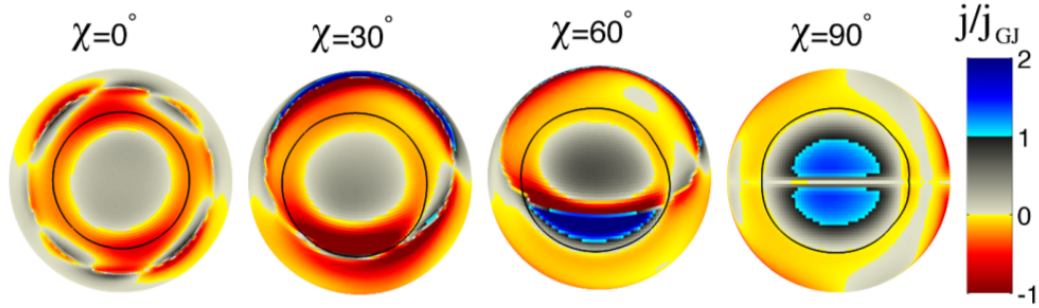


Fig. 2.17.: From Timokhin and Arons (2013). Field-aligned current density at the polar cap of the force-free rotator, with j_{\parallel} measured in units of the corotation current density $j_c = -2\epsilon_0\vec{\Omega}_* \cdot \vec{B}_c$ ($j_c \equiv j_{GJ}$ on the figure). The black circle is the rim of the polar cap - the footprints of the field lines that pass outside the light cylinder fall within that circle. the distributed current is shown. The current sheet component coincides with the polar cap boundary. This plot was made using results of force-free magnetosphere simulations presented in Bai and Spitkovsky (2010)

of the magnetic field near the light cylinder, the plasma currents in a force free-magnetosphere (see figure 2.17), or asymmetric currents within the neutron star (Harding and Muslimov, 2011). It follows that the electric field is determined on the boundaries, and at the surface of the star in particular, by the self consistent microphysics involved in the simulation. In particular, in Timokhin and Arons (2013) the authors treat the SCLF problem without imposing $\vec{E} \cdot \vec{B} = 0$ on the surface of the star. Instead, a system of numerical « ghost » cells is implemented to provide as many charges from the star as needed by the gap.

Magnetic field twists observed in the polar cap region in force-free simulation generates magnetospheric currents in the range $j_m/j_c \in [-1, 2]$ where $j_c = c\rho_c$, figure 2.17. Starting from that, three qualitatively different regimes are found along different magnetic field lines in the force-free magnetosphere: $0 < j_m/j_c < 1$ called sub-Goldreich-Julian (sub-GJ), $1 < j_m/j_c$ called super-Goldreich-Julian (super-GJ) and $j_m/j_c < 0$ called anti-Goldreich-Julian (anti-GJ). In all cases the flow is oscillatory but only in the super-GJ and anti-GJ cases acceleration is efficient enough to start pair creation. In these two cases a number of properties of the flow show a limit cycle behaviour for all physical parameters allowing pair creation. A typical quasi-oscillation goes as follow:

- 1) Formation of a vacuum gap
- 2) The particles in the gap are accelerated and produce pairs in an explosive manner, they form a blob . The blob propagates at ultra relativistic speed.

- 3) The electric field is screened, pair creation stops, the blob progressively leaves to the magnetosphere. It leaves a tail of mildly relativistic particles and/or new particles arrive from the crust and restart phase 1.

Besides, the resulting flow has the following characteristics:

- On average, the current produced is very close to the imposed j_m .
- The average density is close to ρ_c .
- The time scale between two cycles is much larger than the flyby time across the gap (h/c where h is the height of the gap), and therefore regulates the average flow out of the gap.
- A steady state is never found, questioning the results of previous works with this assumption.

Note that the two first points are achievable together only if time dependence and currents of positrons counter-streaming the electrons are allowed. Although Compton scattering is not considered here, this is a possible solution to the asymmetric double PFF inconsistency raised in Harding and Muslimov (1998) (see also section 2.3.3 above).

In the anti-GJ case, the negative current means that no electrons can flow out of the crust (and ions are assumed to be bound). This is equivalent to Ruderman & Sutherland type of gap that has been treated as well in Timokhin (2010). The super-GJ case dominates in the force-free perpendicular rotator (figure 2.17). It turns out to be even more important when synchrotron radiation and cascades beyond the screening altitude, where $\vec{E} \cdot \vec{B}$ returns to zero, are taken into account. Indeed, the multiplicity is then amplified to very high pair multiplicity.

Thus, with the full treatment of the synchrotron cascade at high altitudes (Timokhin and Harding, 2015), super-GJ flows turn out to be capable of providing a flow with multiplicities larger than $10^5 \rho_c$ while previous works realized at best 10^4 (e.g. Daugherty and Harding (1982) and Hibsichman and Arons (2001)). However anti-GJ flows reach 10^3 and a polar cap is a mix of the different kinds of flow that depends heavily on the inclination of the magnetic axis (figure 2.17). However, even assuming the best case where most of the polar cap is super GJ (90° inclination) and multiplying by to account for the second polar cap, one falls short of the necessary multiplicity to explain the Crab nebula luminosity by an order of magnitude: $4 \cdot 10^{39}$ particles per second compared to a minimum flow deduced from the inverse Compton emission from the Crab nebula of $4 \cdot 10^{40} \text{s}^{-1}$ (Jager et al., 1996). This remains a major problem

since the polar cap is expected to provide much more particles than the other gaps, as it extends over a much wider magnetic-field-line bundle. Another prediction by this model is the observation of a synchrotron component up to 10 – 100MeV. Unfortunately, this is the lower end of the current Fermi-LAT telescope and therefore it may not be detectable.

2.3.4 Slot gap

The slot gap was introduced by Arons and Scharlemann (1979) and Arons (1983) as a natural consequence of the polar cap pair formation front models with a space-charge-limited flow (SCLF) (see previous section). Indeed, given a polar cap bounded by the surface of last open field lines, the electrostatic problem (in the corotating frame) is solved by considering the last open surface as equipotential. It then naturally follows that the electric field parallel to the magnetic field must continuously tend to zero near the boundary of the domain. It follows that the acceleration of electrons extracted from the surface is less efficient near the edge of the polar cap, preventing efficient pair production from curvature radiation until increasingly high altitudes as one gets close to the edge of the gap. The screening altitude of the parallel electric field asymptotically goes to infinity on last open field lines. In early slot gap models, the gap was also developing at the center of the polar cap although for a different reason: only curvature radiation being included in the model, pair creation along the magnetic axis becomes impossible because the corresponding magnetic field line has zero curvature. However, later studies of Harding and Muslimov (1998) showed that the pair formation front (defined by the locus where pair creation shields the electric field) can be created on the central field line by the inclusion of Compton scattering of thermal x rays from the star as a source of gamma rays. Consequently, if the central part of the slot gap probably does not exist, the gap along the last open field lines necessarily exists as long as SCLF is involved and $\vec{E} \cdot \vec{B} = 0$ is assumed along the last open field lines.

However emission from slot gaps turned out to be too weak in their original version (Arons, 1983; Arons, 1996) to account for the gamma luminosity of pulsars. Nonetheless, the work by Dyks and Rudak (2003) suggested that gamma emission from low altitude regions of the last-open-field-line bundle could very well be specifically responsible for some features of the observed gamma pulse profiles. The so-called two pole caustic model (Dyks and Rudak, 2003) is a heuristic model that assumes a homogeneous gamma emissivity everywhere along the last closed field lines. This includes the outer gap at high altitudes (see next section), and terminates on the polar cap along the slot gap (see figure 2.21). However, it does not treat the electrodynamics of the region considered, but it reproduces many characteristics of gamma ray profiles (such as the characteristic two peaks with bridge emission,

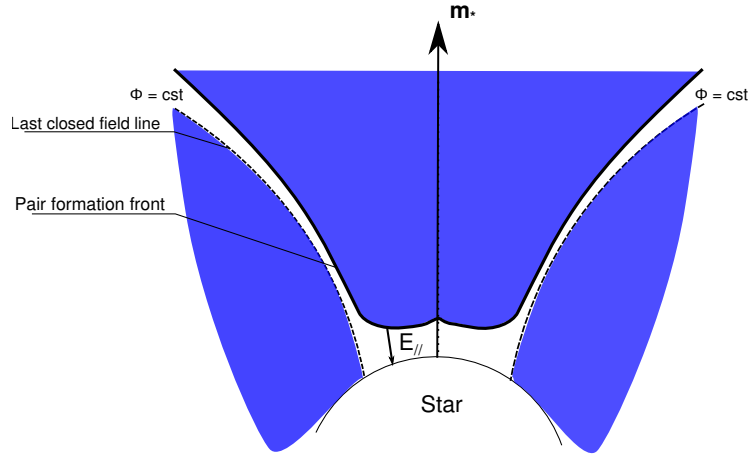


Fig. 2.18.: Slot gap and polar cap. The spin axis is not shown, areas with a corotating plasma density are in blue, plasma starved areas in white. The pair formation front is represented by the thick line. The pair formation front from curvature radiation photons would also form a gap along the magnetic axis where curvature radiation is inefficient but it is likely that other mechanisms prevent it, like Compton scattering (see text). Thus we choose to represent a PFF that goes higher but is not broken as a reminder of this effect. Last closed field lines are equipotential, $\Phi = cst$, which make $E_{||}$ tend to zero close to this boundary, producing the slot gap.

see figure 2.19) by accounting for propagation delays and relativistic aberration, resulting in the formation of caustics, similarly to the outer gap models (see next section). The fact that the radiating region extends all the way to the star gives the possibility of observing caustics originating from both hemispheres, contrary to outer gap models (Romani and Yadigaroglu, 1995). It is to be noticed here that in the early studies of (Arons and Scharlemann, 1979; Arons, 1983), the polar cap and slot gap electrodynamics was worked out in a low altitude approximation, and therefore the result has no reason to match the outer gap. Besides, in these models SCLF was not enhanced by frame dragging effects (see previous section and Muslimov and Tsygan (1992)), that can boost the parallel electric field by a factor of $\sim 100P_*^{1/2}$.

Slot gaps were reconsidered by Muslimov and Harding (2003) with account for frame dragging effects. These authors also have taken into account the additional screening of the inner boundary of the gap, that was not considered in the earlier work, but important owing to the narrowness of the gap. As before, a necessary condition for the formation of slot gaps is the ability of curvature radiation to create a PFF. Even with the opposite effect of the narrowness of the gap, frame-dragging-enhanced SCLF improves very significantly the energetics of the slot gap. The slot gap is estimated to have an angular thickness $\Delta\theta$ at the feet of the magnetic field lines relative to the polar cap angle θ_c

$$\frac{\Delta\theta}{\theta_c} \simeq 0.2P_{*-1} (\lambda B_{*8})^{-4/7} I_{*39}^{-3/7} \quad (2.163)$$

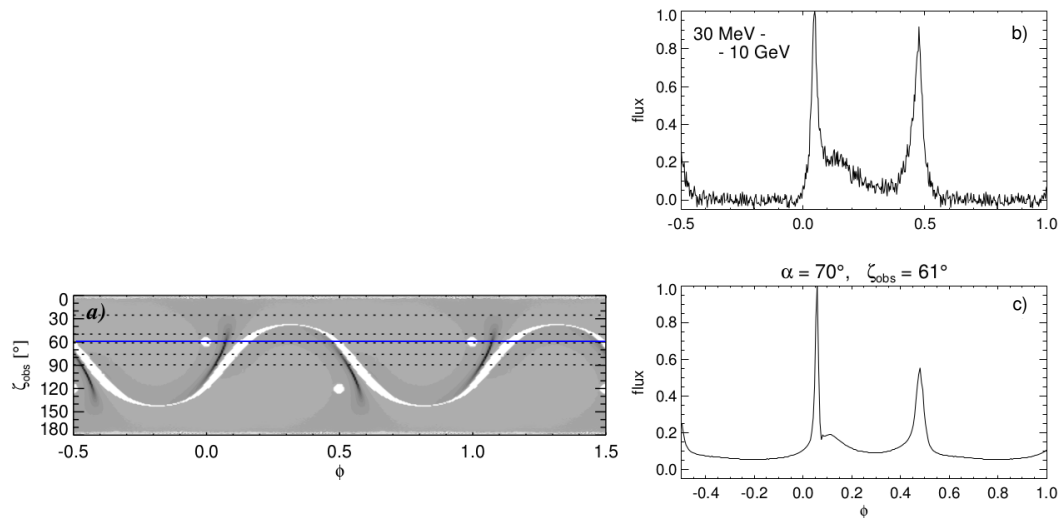


Fig. 2.19.: From Dyks and Rudak (2003). a) Two-pole-caustic-model photon mapping in the $(\zeta_{\text{obs}}, \phi)$ plane for the magnetic inclination $\alpha = 60^\circ$. ζ_{obs} is the angle of the line of sight with respect to the spin axis, ϕ the spin phase angle of the pulsar. Notice the location of the polar caps (white spots; in this particular case, their size corresponds to the rotation period $P = 0.033\text{s}$) as well as two dominant caustics (in black) formed in the trailing parts of the magnetosphere (with respect to two magnetic poles). The pulse profile seen by an observer at $\zeta_{\text{obs}} = 61^\circ$ is the cross section by the blue line. b) Gamma-ray light curve of the Vela pulsar obtained with EGRET (Kanbach, 1999). c) Vela light curve computed with the two-pole caustic model for a magnetic angle $\alpha = 70^\circ$ and $\zeta_{\text{obs}} = 61^\circ$. The caustics produce the peaks. It would correspond to the blue line on a photon mapping like that of panel a) but with different parameters. The flux on the vertical axis is in arbitrary units.

where λ is a free parameter in the range $\lambda \sim 0.1 - 0.5$. Therefore, it is consistent to assume that radiations come from a narrow layer as in the model of Dyks and Rudak (2003).

In Muslimov and Harding (2004), the authors have extended the previous solution to high altitudes with the idea of providing a physical motivation to Dyks and Rudak (2003). Indeed, some important problems arise at high altitudes in the solution of Muslimov and Harding (2003). Most important is the fact that the charge density difference between the charge inside the gap and the corotating charge outside increases with altitude until $|\rho - \rho_c| > |\rho_c|$. This, in turn, leads to the impossibility for the gap boundaries to sustain the jump of the perpendicular electric field. resulting in particular from the corotation condition $\vec{E} + (\vec{\Omega}_* \times \vec{r}) \times \vec{B} = 0$. Indeed, it is then dubious that enough charges can accumulate on the boundary surfaces without important currents, thus breaking the underlying steady state assumption (given that the charge density of the surrounding magnetosphere is assumed to be ρ_c). The solution in view of these authors, is that the charge density difference saturates at high altitudes, beyond r_s , to the corotation density

$$|(\rho - \rho_c)(r > r_s)| = |\rho_c(r_s)|. \quad (2.164)$$

Beyond this saturation altitude, a current across the gap compensates for the unbalance. This current across the magnetic field lines is justified by the occurrence of a growing centrifugal slingshot effect as the cylindrical distance rises. Schematically, at large cylindrical distances, corotation implies an important effective centrifugal force \vec{F}_c that results in a drifting velocity of the charges $\propto \vec{F}_c \times \vec{B}$, very much like the cross field drift velocity $\propto \vec{E} \times \vec{B}$ responsible for corotation itself (except that $\vec{F}_c \times \vec{B}$ depends on the sign of the charge, and thus $\vec{F}_c \times \vec{B}$ creates a current, contrary to $\vec{E} \times \vec{B}$). This result in a steady state crossfield velocity of the charges. The altitude of saturation must then be determined by matching the high altitude solution to the low altitude solution of Muslimov and Harding (2003), and is typically a few R_* .

As a result, the acceleration of charges continues up to the light cylinder, and leptons can be considered to be curvature radiation reaction limited at high altitudes. The saturation Lorentz factor is similar to that which can be derived near the polar cap. For example, for the Crab one finds $\gamma \sim 4 \cdot 10^7$. Importantly, this solution implies a disruption of a potential outer gap (see next section). Indeed, outer gaps are located on the outer zone of the extended slot gap described here, but models assume no current from the star. A space-charge-limited flow from the star, therefore carrying a quantity of charges similar to the corotation charge at the surface of the star, would certainly disrupt outer gaps. However, in some particular situations of high magnetic inclination and/or fast rotation, the field-line-curvature-independent enhancement of SCLF becomes too weak, and one recovers the notion of favorably or unfavorably

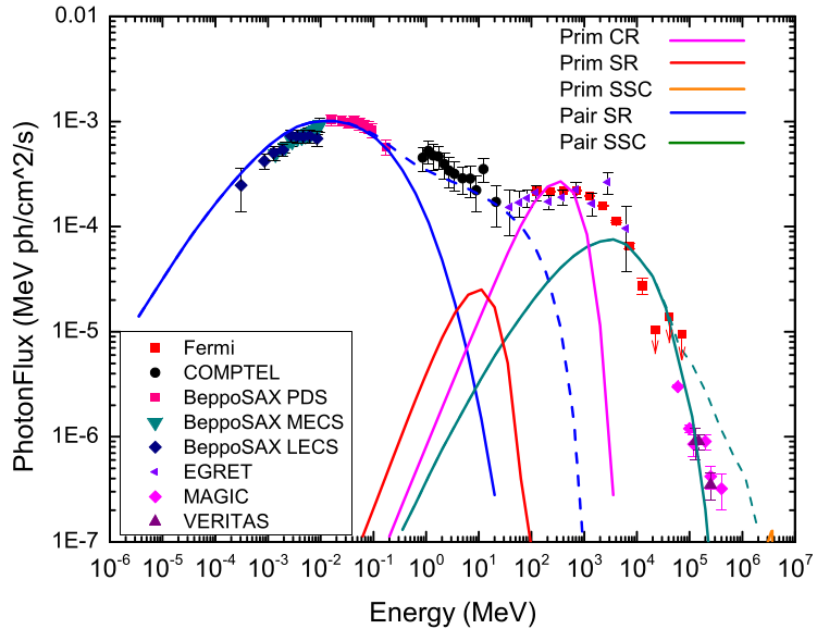


Fig. 2.20.: From Harding and Kalapotharakos (2015). Model spectra of phase-averaged pulsed emission components from primary electrons and pairs (as labeled, curvature radiation CR, synchrotron radiation SR, synchrotron self-Compton SSC) from the Crab pulsar, for magnetic inclination $\alpha = 45^\circ$ and observer angle $\zeta = 60^\circ$ and pair multiplicity $M_+ = 3 \cdot 10^5$. The dashed lines are SR and SSC spectra resulting from a power-law extension (without physical motivation) to the cascade pair spectrum. Data points are from Kuiper et al. (2001), The Fermi-LAT collaboration (2013) and, Aleksić et al. (2011), and VERITAS Collaboration et al. (2011).

curved field lines (see Scharlemann et al. (1978) and the polar cap section above) with respect to the possibility of developing an accelerating electric field for the current. In this case, a traditional outer gap along unfavorably curved field lines (bent away from the spin axis) could coexist with extended slot gap along favorably curved field lines (bent towards the spin axis).

One of the most complete numerical model of slot gaps is probably that of Harding and Kalapotharakos (2015), which mainly targets young pulsars such as the Crab. The authors use the geometry given to the last open field lines by a force free magnetosphere simulation. Besides, the initial pair spectrum generated at low altitude ($< R_* \theta_c$) is given by the averaged result of time dependent simulations in an offset dipole magnetic field (see previous section and Timokhin and Harding (2015)) which allows to inject into the gap a very high pair multiplicity up to 10^6 (instead of a maximum of 10^4 in steady state). This is a major difference compared to Muslimov and Harding (2003) and Muslimov and Harding (2004) that assumed a steady-state cascade. The pair cascade is then developed using a great variety of emission mechanisms: curvature radiation, synchrotron radiation of pairs everywhere in the magnetosphere then used for self-Compton emission, resonant Compton scattering

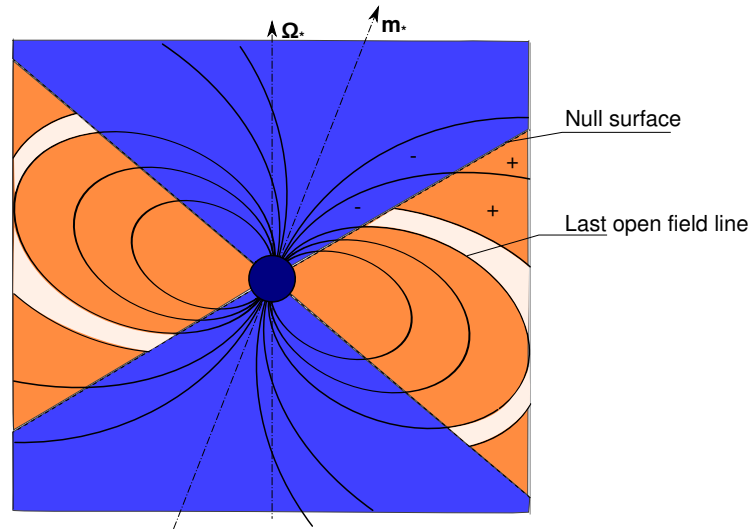


Fig. 2.21.: Corotating magnetosphere with outer gaps in white. The magnetic field is dipolar of momentum m_* inclined with respect to the spin axis $\vec{\Omega}_*$, the view is in the plane $(\vec{\Omega}_*, m_*)$. Plain lines represent magnetic field lines. The areas where the corotation charge is negative are in blue, and orange is used where it is positive. The transition occurs on the null surface, where the charge is zero, represented by dashed lines on a white background.

of radio photon (Lyubarskii and Petrova, 1998), Compton scattering. It is found that: losses are dominated by curvature radiation for primaries as in the more basic models, synchrotron self-Compton can explain very high energy emission of young pulsars (see figure 2.20 and e.g. Aleksić et al. (2011) for the Crab with MAGIC, and section 1.4), synchrotron and curvature dominate the spectrum of middle-age pulsars (like Vela), and x-ray and optical emissions are well accounted for by synchrotron emission.

2.3.5 Outer gap

The outer gap was introduced by Holloway (1973) and Cheng et al. (1976), but the theory developed in in this section was presented in two seminal papers, Cheng et al. (1986b) and Cheng et al. (1986a). It is based on the observation that there exists null surfaces within the corotating magnetosphere, where the corotating charge cancels. Along open magnetic field lines that cross the null surface within the light cylinder, a gap forms on the outer side of the null surface.

Null surfaces are defined as the locus where the corotating charge density is zero, i.e. $\rho_c = 0$. At leading relativistic order, this turns into the implicit relation $\vec{\Omega}_* \cdot \vec{B} = 0$. Therefore, null surfaces are heavily dependent on the shape of the magnetic field, and its overall inclination with respect to the spin axis.

Outer gaps are assumed to form on the outer side of the null surfaces (by opposition to the inner side which leads to the star), see figure 2.21 and preferentially along the last open field line. The mechanism of formation of the gap can be summarized with the following gedanken experiment. Starting from a fully corotating magnetosphere:

- a) The plasma escapes along the open field lines at the light cylinder.
- b) In the corotating frame, this creates an effective charge density of $-\rho_c$ and therefore an electric field pulling inner charges outward.
- c) This continues until a null surface is reached. Naively, charges on the inner side of the surface are pushed inward instead of being pulled, because they are of the opposite sign.
- d) If the potential drop created is large enough, particles still in the gap are accelerated, radiate, and pair produce.
- e) Pair creation quenches the gap everywhere except for a slice above the last open field line.

These steps call for a number of comments. Step a) assumes that there is no significant charges coming in through the light cylinder that would immediately quench the gap. At step c), we already see that stopping the gap exactly at the null surface is a very naive view, it may actually go further inward. However this depends on how much pair creation processes can quench the gap. If pair creation is insufficient then the whole outer magnetosphere goes outside the light cylinder and the pulsar presumably ends up in an electrosphere configuration.

Step e) is based on the assumption that magnetic field lines are convex toward the closed zone. Given that electrons and positrons flow along the field lines, and that the pair producing photons they radiate are necessarily very collimated along the trajectory by relativistic effects, the pairs are necessarily produced on a field line that is on the nonconvex side (we shall say upper side) of the field line: lower parts of the gap can quench upper parts of the gap but not the other way. The only region of the gap without lower part to quench it is the part of the gap following the last open field lines (see figure 2.22). Therefore, if the pair cascade is strong enough one expects it to be limited to a fairly thin layer above the last open field lines.

The number of gaps created in the outer magnetosphere is also questionable. From figure 2.21, it is possible to consider up to four gap regions. However the smaller ones, are usually thought to be too small to be visible as they are too short to

develop large enough potential gaps. It is also possible to consider only two gaps, azimuthally very extended, potentially covering every last closed field line (Romani and Yadigaroglu, 1995) which turns out to be able to reproduce gamma-ray pulse profiles well. Besides, from an observational point of view it is important to notice that the viewing angle is potentially very wide, up to 90° (Romani and Yadigaroglu, 1995), as is more generally expected on geometrical grounds from a source in the outer magnetosphere. This has important consequences on the population of visible gamma-ray pulsars (Pierbattista et al., 2012).

The cascade mechanisms appeal mostly to photon-photon pair creation. Indeed, at this distance from the star the magnetic field is expected to be too weak to efficiently producing pairs. Therefore the question amounts to identify abundant sources of soft photons. In the Cheng et al. (1986b), the authors assume that this source is provided by the synchrotron and synchrocurvature radiation of the secondary particles. In particular, the lower end of the cascade is expected to be an abundant source of optical photons, as well as x rays, and radiated with a wide range of angles (smaller relativistic collimation) that allows it to come back into the lower part of the gap, figure 2.22. Other works (Romani, 1996; Cheng et al., 2000) consider mostly a source of thermal x rays from the star surface, in particular near the null surface that is closer to the star than the rest of the gap in every reasonable geometry. This latter source then acts directly to control the starting point of the gap on its inner side. Compton scattering is expected to be important as well, including in the resonant regime near the inner side (Cheng et al., 2000).

In both cases, soft photon from secondaries or from the neutron star, a self-maintaining mechanism is at work. If a lot of pairs are produced, a lot of secondary radiation is produced and more pairs can be made. If the source of x rays is the star, then if more pairs are produced, more leptons are accelerated back to the gap (positrons in our picture) which heats the surface of the star which in turns produces more x rays (see Zhang et al. (2004) for a model of self-limitation of the gap in this case).

However, outer-gap models allow fairly robust predictions concerning the shape of the gamma-ray pulses, and have proven to be able to explain some of their main characteristics: in particular a double peak with strong bridge emission. This is due to the fact that, whatever the detail of the radiation mechanisms, a big part of the mechanisms forming the profiles is geometrical, as with the two-pole caustic models (previous section and Dyks and Rudak (2003)). The choice of field line geometry is particularly important. In particular, Romani and Yadigaroglu (1995) and Cheng et al. (2000) could reproduce typical shape of the pulse profile of the Crab pulsar, figure 2.23, as well as the optical polarization sweep by considering a rotating dipole geometry (figure 2.1 and Deutsch (1955), Pétri (2015), and Bonazzola et al. (2015)) instead of a static dipole. Besides, the aberration of the radiation due to the

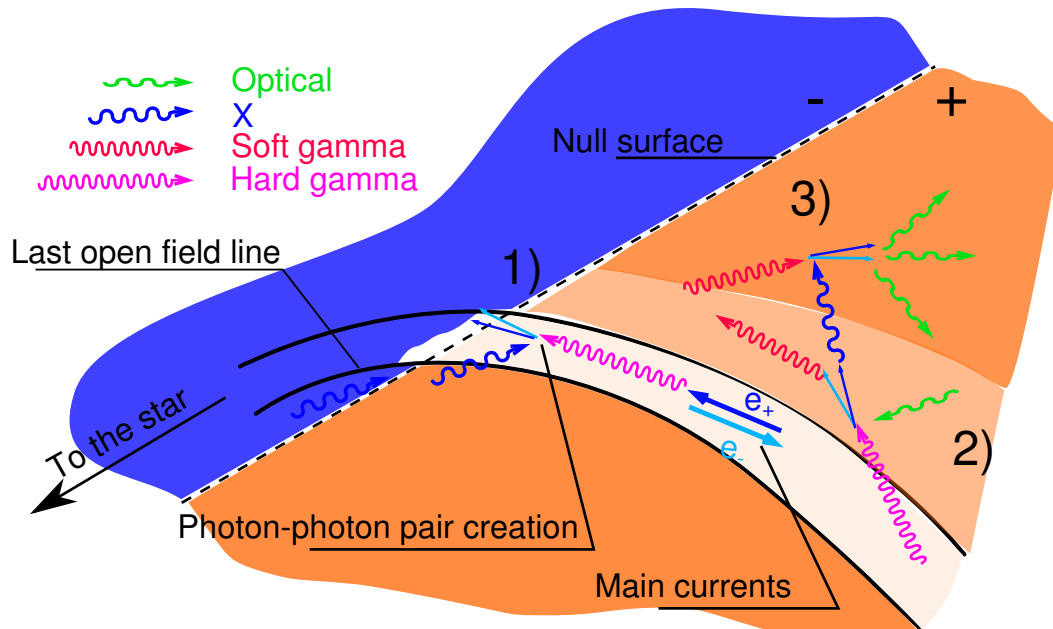


Fig. 2.22.: Outer gap at the null surface in a magnetosphere with $\vec{\Omega}_* \cdot \vec{m}_* > 0$. Negative corotating charge density is shown in blue (left-hand side), positive in orange (right-hand side). The two solid lines represent the magnetic field lines bounding the gap, the lower one being the last open field line. On the outer side (right-hand side of the null surface) the plasma density goes from almost zero in the gap to full corotation density below the last open field line and in area 3), and is coded by an increasing intensity of orange. 1) Inner boundary of the outer gap. X-ray photons from the star interact here with gamma photons from particles accelerated in the gap to form pairs, and are Compton-scattered by the electrons and positrons. This x-ray source is expected to play a major role here, in particular in determining the position of the gap boundary. The current returning from the gap (here positrons) heats the surface of the star and participates in sustaining the x-ray flux (see e.g. Romani (1996), Cheng et al. (2000), and Zhang et al. (2004) and the text). 2) Gamma rays produced along the gap magnetic-field lines tend to produce pairs above the gap because of the convexity of the field lines. To pair produce, they can interact with x-rays and lower energy photons from the star (see 1)), or from synchrocurvature and synchrotron of secondaries in area 2) and 3). The plasma density is still lower than the corotation density. 3) Last area in which pairs are still produced from gamma rays from the gap and from area 2). The lower energy of the pairs make them radiate optical and infrared photons (Cheng et al., 1986b).

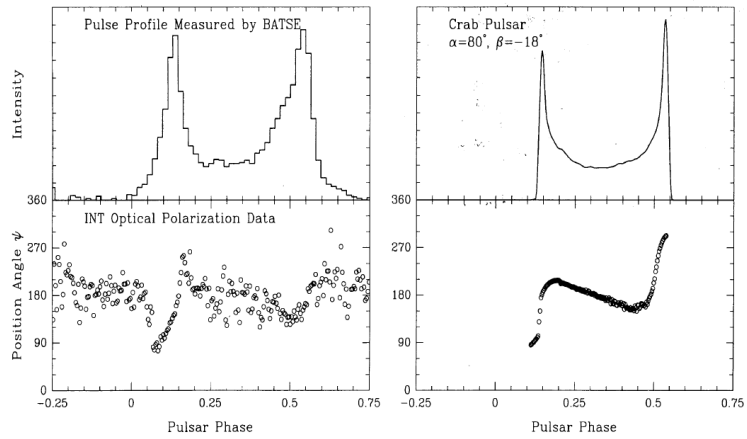


Fig. 2.23.: From Romani and Yadigaroglu (1995), Crab pulsar profiles and polarization sweep. Left-hand side: high energy light curve data from BATSE (Fishman, 1992), INT optical polarization data (Smith et al., 1988). Right-hand side: Model results for Crab outer gap. One recognizes the characteristic two peaks bridged with a strong emission.

rotation of the magnetosphere must be taken into account, as well as the flight path difference between the different regions of the gap but also between the two gaps that can be visible at the same time (one in front and one behind). These effects result in the possibility of forming caustics along the observer’s line of sight. Another important consequence of these effects is that the angular position observed is not necessarily a monotonically increasing function of the rotating phase of the pulsar (consequences that are common to all outer magnetosphere models, in particular extended slot gaps).

An important difference with the two-pole caustic model (previous section and Dyks and Rudak (2003)) is that only one magnetic hemisphere is usually responsible for the observed light curve, implying different viewing geometries to model the same two peaks. For instance, Romani and Yadigaroglu (1995) model the Vela pulsar with a magnetic inclination angle of $\alpha = 65^\circ$ and a viewing angle (angle between the line of sight and the spin axis) of $\zeta_{\text{obs}} \simeq 80^\circ$ while with the two-pole caustic model Dyks and Rudak (2003) use $\alpha = 65^\circ; \zeta_{\text{obs}} = 61^\circ$.

It is to be noticed that the outer gap can accommodate a large number of observations just by varying the angle between the dipole and the spin axis. For example, in the case of a perpendicular rotator the outer gap turns out to be very close to the surface of the star, while for an aligned rotator it rings the pole and starts at a large distance. It is also independent from the alignment or anti-alignment of the projection of magnetic moment onto the spin axis. The thickness and azimuthal extent of the gap, as well as the energetics along it depend on the radiative and pair creation model considered. However, the radiative properties are shown to have direct links with

the geometry, in particular the gamma-ray luminosity L_γ of the gap is related to the spindown luminosity L_{sd} by $L_\gamma \sim f^3 L_{\text{sd}}$ where $f < 1$ is the volume occupation factor of the gap (Cheng et al., 1986b; Zhang et al., 2004).

2.4 Global solutions with matter

2.4.1 The force-free magnetosphere

Generalities

The natural continuation of corotating magnetospheres (section 2.3.1) is force-free magnetosphere. In this case, equation (2.104) is replaced by the condition

$$\rho \vec{E} + \vec{J} \times \vec{B} = 0, \quad (2.165)$$

where ρ is the density of charges and \vec{J} the current. This approximation can be written in a covariant form as the conservation of energy and momentum

$$J_\nu F^{\mu\nu} = 0 = \partial_\nu T_{\text{em}}^{\mu\nu}, \quad (2.166)$$

where T_{em} is the symmetric electromagnetic-field energy-momentum tensor and F the electromagnetic field tensor. Under this form, it is clear that this approximation amounts to neglect any momentum transfer between matter and fields, hence the force-free label.

As a consequence, the system can be entirely described by the electromagnetic fields. Indeed, the current density can be expressed as a function of the fields by taking the crossproduct of equation (2.104) with \vec{B} ,

$$\vec{J} = \rho \frac{\vec{E} \times \vec{B}}{B^2} + \left(\text{component } \parallel \text{ to } \vec{B} \right), \quad (2.167)$$

which implies that $E < cB$ everywhere in a force-free magnetosphere. Notice that this relation is frame invariant since $E^2 - B^2 c^2$ is Lorentz-invariant. Coupled with the fact that $\vec{E} \cdot \vec{B} = 0$ from eq. (2.104), this has an important consequence: there is always a frame in which the electric field is locally zero, and since only the electric field works on the particles, it follows that a force-free magnetosphere does not accelerate particles. Another way of seeing this is to simply check from (2.167) that $\vec{E} \cdot \vec{J} = 0$. Similarly, one deduces that the current flows along field lines plus a perpendicular drift velocity driven by the first term of (2.167). It follows that the synchrotron motion has to be efficiently suppressed by radiation reaction.

The density of charges ρ is found from the divergence of the electric field and is the so-called Goldreich-Julian charge density. The component of the current perpendicular to the magnetic field is immediately found from (2.169) and the parallel component is found by replacing the terms of $\partial \vec{E} \cdot \vec{B} / \partial t$ with their expressions from Maxwell's equations. Finally, force-free equations are given by (Gruzinov, 2006)

$$\rho = \epsilon_0 \nabla \cdot \vec{E}, \quad (2.168)$$

$$\vec{J} = \frac{(\mu_0^{-1} \vec{B} \cdot \nabla \times \vec{B} - \epsilon_0 \vec{E} \cdot \nabla \times \vec{E}) \vec{B} + \epsilon_0 (\nabla \cdot \vec{E}) \vec{E} \times \vec{B}}{B^2}, \quad (2.169)$$

and one solves for \vec{E} and \vec{B} by inserting the two above expressions into Maxwell's equations.

The pulsar equation

Using the force-free condition (2.165) in an axially symmetric case, it is possible to derive an equation for the current and magnetic field everywhere in the magnetosphere known as the pulsar equation (Michel, 1973b; Scharlemann and Wagoner, 1973). Let the magnetic field be defined through the functions $\Psi(r_1, z)$ and I

$$\vec{B} = \nabla \Psi \times \vec{e}_\phi / r_1 + \mu_0 I \vec{e}_\phi \quad (2.170)$$

where r_1 is the radial coordinate in the cylindrical coordinate system (r_1, z, ϕ) and \vec{e}_ϕ is the azimuthal unit vector. The first term represents the poloidal component of the magnetic field and the second represents the toroidal components that results from a (poloidal) current I . Indeed, if $I = 0$ one finds a purely poloidal field as would be a vacuum dipole.

Further, it can be shown that Ψ and I are constants along field lines such that $I = I(\Psi)$. Moreover, the magnetic flux $\Phi(r_1, z)$ through a circle centered on the z axis at height z and of radius r_1 is directly related to Ψ , as the total current J through the same circle is related to I ,

$$\Phi(r_1, z) = 2\pi \Psi(r_1, z) \quad (2.171)$$

$$J(r_1, z) = 2\pi I(r_1, z). \quad (2.172)$$

After manipulation similar to that to obtain (2.169) one gets the so-called pulsar equation

$$\nabla^2 \Psi - \frac{1}{r_1} \frac{R_{LC}^2 + r_1^2}{R_{LC}^2 - r_1^2} \partial_{r_1} \Psi - \mu_0^2 \frac{I \partial_\Psi I}{R_{LC}^2 - r_1^2} = 0 \quad (2.173)$$

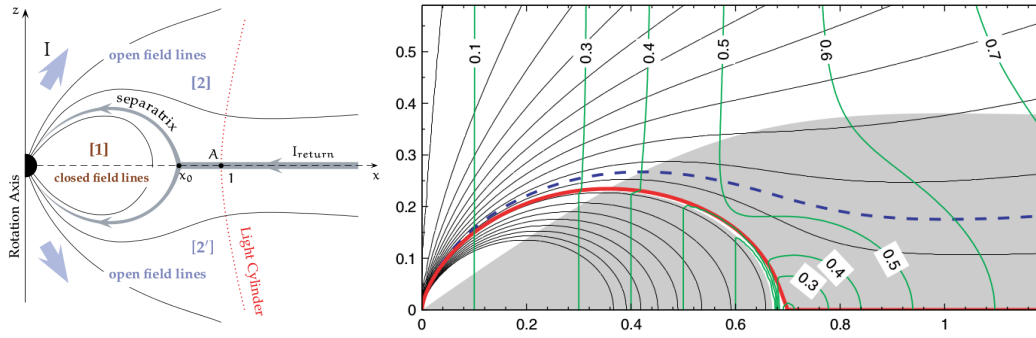


Fig. 2.24.: From Timokhin (2006). *Left-hand-side panel:* Configuration of the magnetic field in the magnetosphere of an aligned rotator with a Y null point. After the null point x_0 the separatrix goes along the equatorial plane. The volume current I flows in the open field line zones [2] and [2']. The current circuit closes somewhere beyond the light cylinder. There could be a volume return current along some open field lines, but the largest part of it flows along the separatrix (see right panel). *Right-hand-side panel:* Global structure of the magnetosphere with the Y point located at $0.7R_{LC}$. The magnetic flux surfaces are shown by thin solid lines, the labelled vertical lines are contours of the drift velocity and the grey area is the domain where the GJ charge density is positive. The dashed line separates regions with direct (above the line) and return (below the line) volume currents. The separatrix is shown by the solid thick line. Distances along the two axes are measured in units of the light cylinder radius R_{LC} .

This equation was solved with a split monopole boundary conditions on the surface of the star by Michel (1973b), but it is only numerically that Contopoulos et al. (1999) could solve the equation for a dipolar magnetic field. Schematically, one needs to “try” current functions I . One needs to assume a given topology for the magnetic field, the « standard » one being the Y-point configuration (Timokhin, 2006), described on figure 2.24. In this topology, there is a singular point at a radial distance $x_0 = r_{i0}/R_{LC}$ beyond which the magnetic field is purely toroidal in the equatorial plane. This is the only free parameter of this topology. Such boundary conditions imply an infinitely thin current sheet along the separatrix (surface of last open field lines) that carries most of the return current, although in some cases it is found a volume current as well (e.g. Timokhin (2006) and figure 2.24).

Inclined rotator and summary

The extension of the solution for the aligned rotator is of course the oblique rotator. Such solution was achieved in particular by Spitkovsky (2006) using a fully 3D force-free-magnetohydrodynamics code. However it is to be noted that the parameter used are not that of a realistic pulsar (for example the ratio $R_{LC}/R_* < 3$) owing to computational limitations. It is found an Y oblique configuration with an oscillating current sheet leaving the magnetic equator of the last open field line. The last open surface forms inside the light cylinder, although contrary to the case of the previous

section it is not a free parameter. Instead, in this solution the size of the closed zone results from magnetic reconnection inside the light cylinder.

An important result in Spitkovsky (2006) is that the spin-down luminosity is summarized as a function of the magnetic colatitude χ by

$$L \simeq \frac{\mu_0 m_*^2 \Omega_*^4}{c^3} (1 + \sin^2 \chi) = L_{\text{vac}} \frac{1 + \sin^2 \chi}{\sin^2 \chi} \quad (2.174)$$

where the vacuum dipole value is $L_{\text{vac}} = \mu_0 m_*^2 \Omega_*^4 / c^3 \sin^2 \chi$. One notices that, contrary to the vacuum model, the spindown power is never zero. This is due to the fact that the toroidal component of the magnetic is no longer null owing to the effective inertia given to the magnetic field through (2.169) (see Michel, 1973a).

So far, we can say that the force-free approximation has the following properties:

- Inertia of particles is neglected. Formally, particles are only used to derive the effective interaction law of the fields with themselves equation (2.169),
- Force-free magnetospheres do not accelerate particles,
- Force-free magnetospheres do not account for the cyclotron orbits,
- The corotating magnetosphere is a particular not self-consistent case where the drift velocity (first term of (2.169)) is equal to the corotation velocity $\vec{\Omega} \times \vec{r}$.

Detailed solutions were obtained in various cases. Analytically, a solution can be found in the case of an aligned split monopole (Michel, 1973b). To go further, numerical solutions proved so far necessary in the aligned-dipole case (Contopoulos et al., 1999; Timokhin, 2006) and inclined dipole (Spitkovsky, 2006). They all show the same characteristics

- A current sheet forms on the separatrix surface (surface between the last closed field line and the first open field line).
- A Y point forms near and inside the light cylinder beyond the current sheet continues in the equatorial plane.

Force-free solutions are useful to obtain a global picture of the magnetosphere at a somewhat low computational cost. However, it is doubtful that such solutions represent accurately the zone near the light cylinder or where magnetic-field lines are open. Besides, they do not give any information about particle acceleration,

synchrotron radiation (at least without ad hoc models) or the nature and the source of the particles filling the magnetosphere.

2.4.2 Electrosphere

Electrosphere solutions to the electromagnetic field assume that the work function at the surface is negligible, that the magnetic moment is aligned with the rotation axis (aligned rotator), and that an electrostatic equilibrium between the star and the surrounding plasma is reached. It follows that the surface charge can be lifted into the magnetosphere by the intense electric field of potential (2.17) until an equilibrium is found. Such solutions were originally pointed out in Jackson (1976).

For an aligned rotator with zero net charge it is clear from equation (2.14) that positive charges (ions) are extracted from a belt around the equator of the star while negative charges (electrons) are extracted from a cap above the star, as can be seen on figure 2.25. They form two clouds of charges respectively named torus and dome. Were the magnetic field anti-aligned with the rotation axis, the dome and the torus would have opposite charges to the aligned case.

One looks for a solution in electrostatic equilibrium. Since the plasma is charge-separated,

$$\vec{E} + \vec{v} \times \vec{B} = 0, \quad (2.175)$$

or equivalently, when $\vec{v} \cdot \vec{B} = 0$ is assumed, \vec{v} follows the drift velocity,

$$\vec{v} = \frac{\vec{E} \times \vec{B}}{B^2}. \quad (2.176)$$

The boundary conditions are those exposed in section 2.1.1, minus the lifted surface charge. Forces other than electromagnetic are neglected (see section 2.1.1).

Several numerical solutions were worked out over time (in particular Krause-Polstorff and Michel (1985), Pétri et al. (2002b)). The result is that the plasma is and remains charged separated. In particular, Pétri et al. (2002b) showed that for second pulsars the vacuum between the two charged areas is stable to breakdown under electron-positron discharges, resulting either from photon-magnetic-field or photon-photon mechanisms. However, the authors conclude that old millisecond pulsars could be unstable to photon-magnetic-field vacuum breakdown, and therefore the magnetosphere could end up completely filled with plasma. Other properties are deduced:

- The radial extent of the electrosphere is finite as long as the total charge of the system is much smaller than $3Q_i$ (see equation (2.7)).

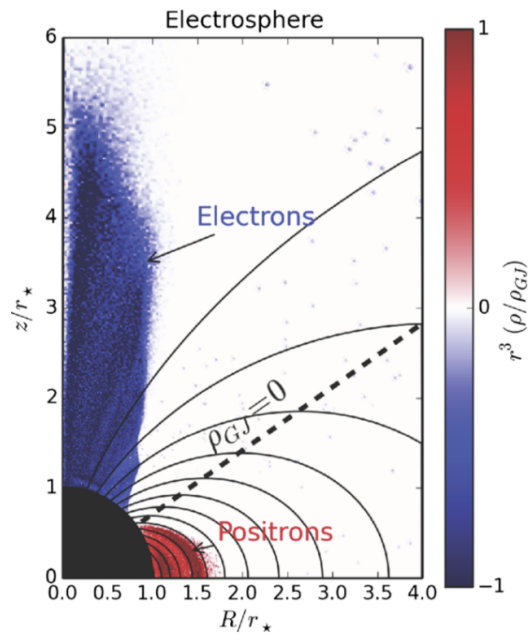


Fig. 2.25.: From Cerutti and Beloborodov (2016). Fully charge-separated (electrosphere) of the aligned rotator obtained with a 2D axisymmetric PIC simulation after one rotation period. Electrons (blue) form a dome above the magnetic pole while positive charges (here positrons, in red) form the equatorial torus. Both species are confined well within the light-cylinder radius, here set at $R_{LC} = 6R_*$. Charge densities are normalized by the surface Goldreich-Julian (corotational) density at the pole. Solid curves show the magnetic-field lines and the oblique dashed line shows the null line (where $\rho_c = 0$ at an angle from the spin axis of $\theta \simeq 55^\circ$).

- The dome and the inner part of the torus are corotating with the star, and super-rotating at larger distances from the star's rotation axis.
- The charge density in the torus is larger than the corotation density in the super-rotating part.

This perfectly static configuration cannot generate any loss of energy from the system: neither particle outflow nor electromagnetic radiations. It results that the pulsar does not spin-down and does not shine: it is dead. However, the differential rotation of the torus makes this configuration sensitive to the diocotron instability (Pétri et al., 2002a), an analogue of the Kelvin-Helmoltz instability of fluid mechanics. However it was shown (Pétri, 2007) that relativistic effects near the light cylinder tend to suppress this instability near the light cylinder. It results that the aligned electrosphere is stable, but Spitkovsky and Arons (2002) showed that the inclined electrosphere may again be susceptible to develop diocotron instabilities. Moreover, Smith et al. (2001) showed that the corotating magnetosphere introduced by Goldreich and Julian (1969) is unstable (as far as numerical experiences could be performed) and always relaxes to an electrosphere-like configuration.

In the case of the in

2.4.3 Kinetic solutions

In the recent years, computer simulations solving self-consistently the kinetic and electromagnetic equations of pulsar magnetosphere have appeared starting with Philippov and Spitkovsky (2014) and Chen and Beloborodov (2014). The numerical method used is the so-called particle-in-cell method (PIC). In such codes, at each time step the electromagnetic field is interpolated from grid to the particle positions, the particles are propagated, currents and charge densities are calculated from the new particle states, and electromagnetic fields are computed again from these new sources. Each particle is actually an effective particle, representing many real particles, in order to make the whole scheme computationally affordable. However, kinetic codes remain particularly expensive in terms of computational costs and sharp approximations still have to be made to reach a solution within reasonable computing time. Indeed, pulsar-magnetosphere physics stretches over a very large hierarchy of scales from the Larmor radius $r_L = mc\gamma_{\perp}/eB$, to the light cylinder radius through the plasma skin depth $\lambda_p = c\sqrt{m/(e\rho_c\epsilon_0)}$ (giving the length scale of acceleration in a SCLF flow, see section 2.3.3) and typically gives for a young 10ms pulsar (where the scale separation is smallest),

$$\frac{r_L}{R_*} \ll \frac{\lambda_p}{R_*} \ll \frac{R_{LC}}{R_*} \Leftrightarrow 2 \cdot 10^{-15} \gamma_{\perp 1} B_8^{-1} \ll 2 \cdot 10^{-7} P_{*1}^{1/2} B_8^{-1/2} \ll 50 P_{*2}^{-1}, \quad (2.177)$$

for $R_* = 10^4 \text{m}$. For example, in Chen and Beloborodov (2014) care is taken of keeping the same hierarchy of scales but reduced to be numerically tractable

$$\frac{\lambda_p}{R_*} \sim \cdot 10^{-2} \ll \frac{R_{LC}}{R_*} \sim 10. \quad (2.178)$$

The Larmor radius can be considered to be zero close to the star, and near the light cylinder to be $r_L(R_{LC})/R_{LC} = \gamma/425$ whereas in a real pulsar one has $r_L(R_{LC})/R_{LC} \sim 4 \cdot 10^{-12} \gamma_{\perp 1} B_8^{-1} P_{*2}^4$.

The great benefit of this kind of simulation lies in their ability to consistently, namely within the approximated physics of the simulation, solve the plasma dynamics including plasma acceleration and radiation which, by construction, force-free models are unable to do. Therefore, in a PIC simulation the plasma is created from pair creation and flow from the star. Here again, the laws for pair creation are defined ad hoc to be able to cope with computational efficiency. However, it allows to obtain from « first pinciples » different results so far imposed by different sets of approximations (Cerutti et al., 2015):

- If pair creation is low one obtains an electrosphere-like plasma configuration.
- With a high pair-creation rate one obtains a Y-point, separatrix and current sheet configuration, similar to the force-free approximation.

In the latter case, the usual gaps (slot gap, outer gap) are not observed, however a strong activity is observed along the separatrix, with the development of a time dependent gap of very high plasma density (several ρ_c , contrary to the usual analytic outer gaps that assume $\sim \rho_c$) (Cerutti and Beloborodov, 2016).

These simulations also show a significant rate of magnetic dissipation, up to 20%, being responsible for the location of the Y point inside the light cylinder. This is similar to what is observed in MHD solution (Spitkovsky, 2006). Overall the electromagnetic spindown power law is very similar to the MHD one (equation (2.174)) as can be seen on figure 2.26.

Kinetic simulations are the only ones able to develop consistently acceleration and radiation zones, and it is therefore instructive to compute the corresponding high-energy radiation maps. Force free and dissipative MHD simulations this can also allow to study acceleration and radiation, but at the price of adding ad hoc accelerating gaps in the first case (e.g. Bai and Spitkovsky (2010) or Harding and Kalapotharakos (2015)) or assuming ad hoc conductivity distributions in the second case (Kalapotharakos et al., 2012). Using a kinetic simulation, a proof of principle was made by Cerutti et al. (2016) for high pair multiplicity pulsars (so presumably

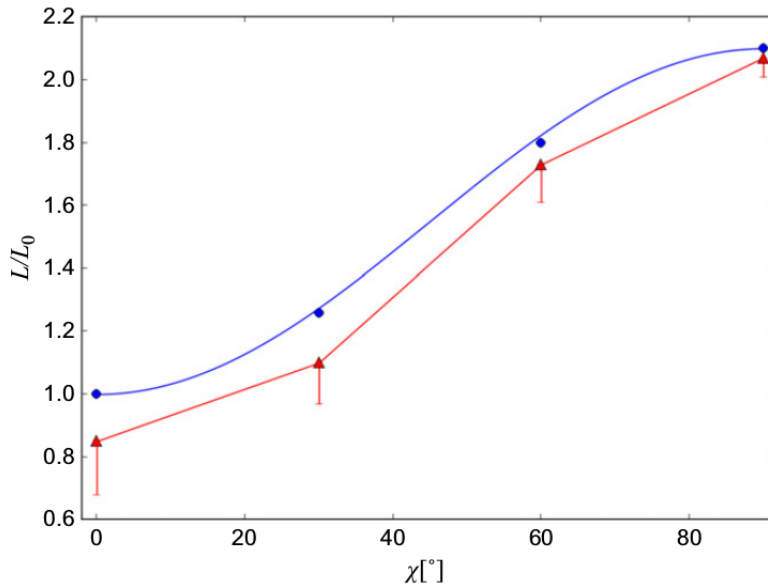


Fig. 2.26.: From Philippov et al. (2015). Poynting flux luminosity of solutions with realistic pair production in units of $L_0 = m_*^2 \Omega_*^4 / c^3$ as a function of the inclination angle (red triangles), measured at the stellar surface. The error bars correspond to the dissipated fraction of the Poynting flux within $2R_{LC}$. Blue points show the results of PIC simulations with abundant pair formation of Philippov et al. (2015), and the blue curve shows the prediction of the MHD model (Spitkovsky, 2006).

more applicable to young pulsars). Synchrotron, curvature and syncho-curvature were included in the simulation. We show some of these results on figure (2.27), and note in particular that:

- The Y point and the equatorial current sheet (see also figure 2.24, left panel) are mainly responsible for the high-energy emission.
- The typical two-peak light curve observed in most gamma-ray pulsars are observed in most simulations. This is mostly geometrical.
- At high dipolar inclination, $\chi \gtrsim 45^\circ$, wind components also appear although this might be due to the smaller separation of scales in the simulation compared to real pulsars.
- Electrons and positrons have different radiating patterns. Electron radiation is less widespread and more concentrated near the Y-point while positrons fill the whole current layer until $2R_{LC}$.
- A large part of the radiation comes from beyond the light cylinder, in particular at the highest energies.

- High energy emissions represent from a few percent of spindown luminosity for very inclined pulsars, $\chi > 60^\circ$, and up to 10% for almost aligned pulsars.

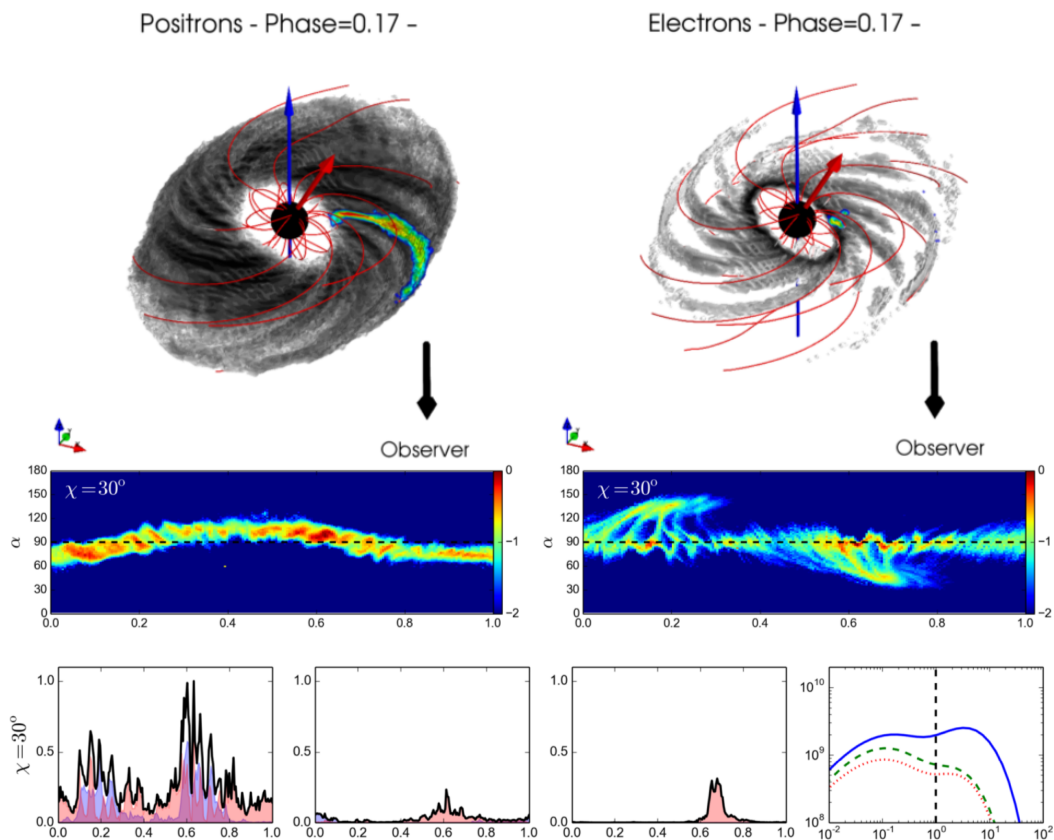


Fig. 2.27.: From Cerutti et al. (2016). All figures represent radiations from a simulated magnetosphere with a dipole inclined at $\chi = 30^\circ$ seen by a distant observer in the rotational equator i.e. at an angle $\alpha = 90^\circ$. *Upper panel:* 3D rendering of the high-energy radiation flux from positrons (left) and electrons (right). In black and white is shown the emission integrated over all directions. In color is the emission in the direction of the observer at rotational phase $\Phi_P = 0.17$. The extended beam of positronic emission shows evidence of a caustic in the emission pattern from the current sheet. The blue arrow represents the spin axis and the red arrow the magnetic momentum, and red lines the magnetic-field lines. The radius varies from R_* to $3R_{LC}$. *Middle panel:* The whole sky map of high energy emission of the two species (see above). The dashed line shows the cross section seen by an observer in the equatorial plane. The log of the intensity is shown and normalized to the maximum value. *Lower panel:* Light curves (cross sections of the sky maps) for the viewing angles $\alpha = 90^\circ$, $\alpha = 60^\circ$ (right) and $\alpha = 45^\circ$ from left to right. The filled blue lines show the radiation flux emitted by positrons, the red filled line by electrons, and the black solid line is the sum for both species. The fourth, rightmost, panel shows the phase averaged spectrum for the three viewing angles, respectively in blue-solid, green-dashed, and red-dotted.

Quantum theory of curvature and synchrocurvature radiation

3.1 On the necessity of treating curvature radiation within quantum electrodynamics (QED)

Electron and positron states with very low momentum perpendicular to the magnetic field have been of interest in the field of rotating neutron-star magnetospheres almost since their discovery (Hewish et al., 1968)¹. Indeed, the community soon realized that the extremely intense rotating magnetic fields of those magnetospheres, ranging from $\sim 10^4$ Teslas at the surface of old millisecond pulsars to $\sim 10^{11}$ Teslas at the surface of some magnetars with a typical $\sim 10^8$ Teslas Viganò et al., 2015a, could generate extremely large electric-potential gaps along the open magnetic-field lines (see chapter 2) which in turn accelerate charged particles to energies only limited by radiation reaction. It is believed that these magnetospheres are mostly filled with electrons and positrons resulting from a cascade of pair creations : pairs are created by quantum-electrodynamics processes involving gamma rays, and in turn radiate their kinetic energy in gamma-rays that make other pairs. The process of radiation is that of an accelerated charge that inspirals around a curved magnetic field. Because the magnetic field \vec{B} is so intense, radiation reaction quickly forces the particle to follow very closely the field line. It follows that electrons and positrons are believed to radiate mostly because of their motion along the curved field line rather than perpendicular to it. Such motion and radiation are described either by the synchrocurvature regime or the curvature regime Ruderman and Sutherland, 1975, depending on whether the residual perpendicular motion is taken into account or neglected. We recall in section 3.1.1 the treatment of curvature radiation within the framework of classical electrodynamics and we demonstrate in section 3.1.2 that in neutron-star magnetospheres it quickly leads to apply the classical theory when momentum is already significantly quantized.

¹This section is a slightly modified version of a previously published proceeding (Voisin et al., 2016).

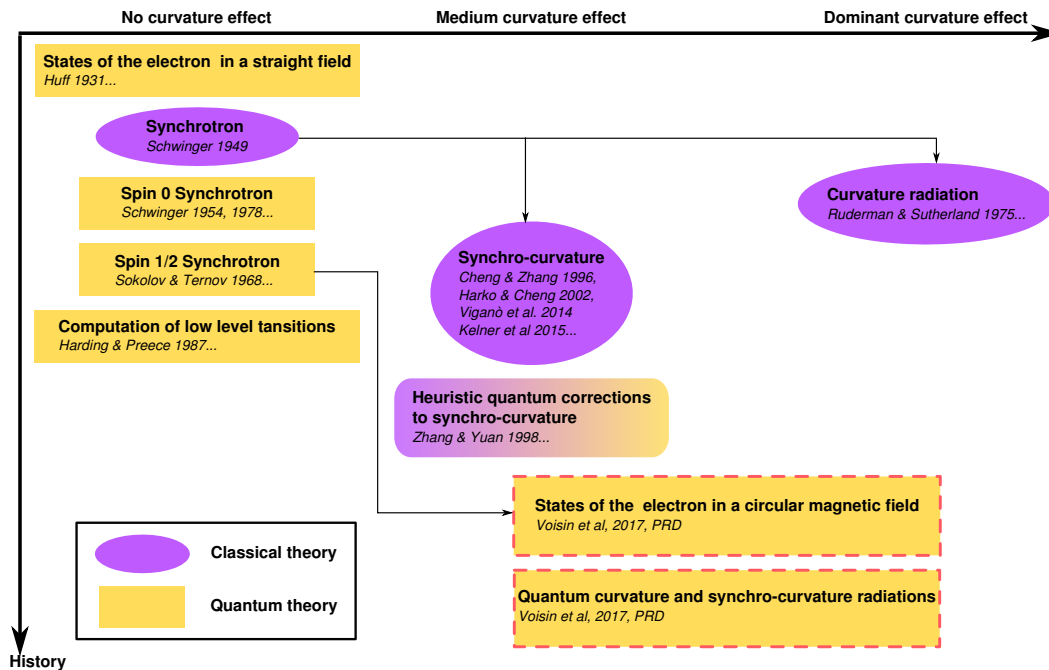


Fig. 3.1.: Overview of the efforts carried out to understand radiation electrons and positrons in magnetic fields. The horizontal axis shows how important is the effect of curvature in the radiation : "no curvature effect" means that the field is considered perfectly homogeneous and therefore the radiation results from the usual synchrotron orbit, while "dominant curvature effect" means that almost all the radiation is due to the curvature of the magnetic field. Yellow square boxes stand for quantum theories and purple elliptic boxes for classical theories. The single round-corner square box with both colors stands for a semi-classical theory. The two papers produced during this thesis are rounded with red dashed contours.

3.1.1 Consistency of the classical theory of curvature radiation

In the ultra-relativistic regime, the classical treatment of curvature radiation is fundamentally the same as that of the synchrotron radiation (Jackson, 1998). In the extreme environments surrounding pulsars and magnetars we are interested in, the ultra-relativistic approximation will very often be appropriate. There are mostly two reasons to this similarity. First in the ultra-relativistic regime the beam of emitted light is very collimated with a typical angle $\sim 1/\gamma$ where $\gamma \gg 1$ is the relativistic Lorentz factor. It follows that the light finally caught by an observer was necessarily emitted on a very small portion of the trajectory, which in turn needs only be locally circular. The second reason is the neglecting of radiation back-reaction on the motion of the particle, that allows to treat motion and radiation in a completely separated way. Therefore, the fact that the path be curved because of a magnetic field or any other source does not matter. Finally, classical synchrotron radiation appears as a particular case of curvature radiation.

In the context of pulsar magnetospheres, the path followed by electrons and positrons is assumed to be a magnetic-field line, to which one can add the well known $\vec{E} \times \vec{B}$ drift, where \vec{E} is the electric field, \vec{B} the magnetic field. This motion is not physical, since it does not follow the usual helicoidal solution of the motion of a charged particle in a magnetic field. In the case of a particle following a magnetic-field line, the Lorentz force $\vec{v} \times \vec{B}$ is the only force acting on the particle and is exactly zero. Therefore, a charged particle cannot follow a magnetic-field line without turning, even slightly, around the field.

However, one assumes such a path as a result of the extreme radiation reaction undergone by a charged particle. Let's take a few numbers that we will consider typical of a pulsar polar cap gap. We need an accelerating electric field of intensity E , assumed collinear to the magnetic field of intensity B . Close to the neutron star surface, a dipolar magnetic field locally has a radius of curvature ρ of the order of magnitude of the neutron star radius. Assuming the electric field is given by a force-free condition around a star rotating at Ω_* (see e.g. (Arons, 2009)) one has

$$\rho \sim 10^5 \text{m}, \Omega_* \sim 1 \text{s}, B \sim 10^8 \text{Teslas}, E = \Omega_* R_* B \sim 10^{12} \text{V/m}. \quad (3.1)$$

In these conditions, an electron or a positron accelerates almost instantaneously, that it on a length scale much shorter than the size of the gap, until radiation reaction balances the electric field. If one assumes that losses are only due to curvature radiation then the radiated power is $\propto \Omega_C^2 \gamma^4$, with $\Omega_C = c/\rho$ the pulsation of an imaginary circular trajectory of radius ρ traveled at the speed of light c , the equilibrium Lorentz factor is (Viganò et al., 2015b)

$$\gamma_{\max} = \left(\frac{3}{2} \frac{4\pi\epsilon_0 E \rho}{e} \right) \sim 4 \cdot 10^7 E_{12}^{1/4} \rho_5^{1/4}, \quad (3.2)$$

with $-e$ the charge of the electron and ϵ_0 the vacuum electric permittivity (in international system units), and we use the notation $X_n = 10^{-n} X$. If the particle bears an initial momentum perpendicular to the magnetic field, it can only be small compared to the longitudinal momentum, because in the opposite case the dominant losses are from synchrotron which follows the same scaling law but with a pulsation ω_B much larger than the curvature pulsation Ω_C

$$\omega_B = \frac{eB}{\gamma m} \sim 10^{12} B_8 \gamma_7^{-1} \gg \Omega_C \sim 3 \cdot 10^3 \rho_5^{-1}, \quad (3.3)$$

resulting in a dissipation $10^{17} B_8^2 \gamma_7^{-2} \rho_5^{-2}$ times more efficient for the same Lorentz factor². That is why an electron or positron cannot have a perpendicular momentum

²Note that this estimate is largely inaccurate since the synchrotron radiation is in the quantum-limited regime for such a Lorentz factor (see section 2.2.2). However, it is enough to emphasize the discrepancy between the efficiencies of the two mechanisms

even comparable to its longitudinal momentum. This is the justification of curvature radiation, that assumes that all perpendicular momentum is dissipated.

However, a small perpendicular component must remain. It suggests to compute the radiation of a particle following an helix in the approximation of a small pitch-angle α , approximation usually called synchro-curvature radiation (see e.g. Cheng and Zhang, 1996, Harko and Cheng, 2002, Viganò et al., 2015b or Kelner et al., 2015). One understands that curvature radiation, however based on an unphysical path, is the natural mathematical limit when $\alpha \rightarrow 0$ of synchro-curvature radiation. If one assumes that thanks to relativistic beaming the radiation-reaction force is directed in the exact opposite direction to the velocity of the particle and that radiation-reaction balances the electric field, one can quickly obtain the evolution of the pitch-angle of the particle (See e.g. Viganò et al., 2015b)

$$\sin \alpha = \sin \alpha_0 \exp \left(-\frac{t}{\tau_\alpha} \right), \quad (3.4)$$

where α_0 is the initial pitch angle and

$$\tau_\alpha = \frac{\gamma_{\max} mc}{eE} \sim 2 \cdot 10^{-8} \gamma_{\max} E_{12}^{-1} \text{s}, \quad (3.5)$$

is the characteristic decay time.

As a consequence, the classical theory predicts an arbitrary decay of the pitch angle on very short distances.

3.1.2 Limit of the classical theory

The quantum theory of a relativistic electron in a uniform magnetic field was derived by several authors (Huff (1931), Johnson and Lippmann (1949), Melrose and Parle (1983), Sokolov and Ternov (1968)). It is applicable to all spin 1/2 particles, however we use here the example of an electron to simplify the presentation without loss of generality. The electron is described by the quantified angular momentum around the magnetic field, quantified momentum parallel to the field and two possible spin orientations. The energy of the particle is then given, as in the classical theory, by the sum of the squared perpendicular and longitudinal momenta plus the squared rest mass energy

$$E = \sqrt{m^2 c^4 + \underbrace{\hbar \omega_{\text{cyc}} mc^2 n}_{\text{Perpendicular momentum}} + \underbrace{(cp_{\parallel})^2}_{\text{Parallel momentum}}} \quad (3.6)$$

where n is an integer quantifying the perpendicular momentum, $\omega_{\text{cyc}} = eB/m$ is the cyclotron pulsation and p_{\parallel} the parallel momentum. The two spin orientations

are degenerate with respect to the energy. The levels quantified by the number n are sometimes referred to as Landau levels (see also appendix B), we will call them perpendicular levels. Transitions between perpendicular levels are at the origin of synchrotron radiation.

The classical limit of a quantum theory means, in particular, that the quantized step of a given quantity is negligible compared to the value of this quantity such that transitions between states involve a quasicontinuous change in energy. In the case of ultra-relativistic synchrotron radiation, the perpendicular component of the energy (3.6) dominates and

$$E = \sqrt{n\hbar\omega_{\text{cyc}}mc} \left[1 + \mathcal{O} \left(\frac{mc^2 + (cp_{\parallel})^2}{E} \right) \right], \quad (3.7)$$

such that the energy step between two successive perpendicular states is

$$\Delta E \simeq \sqrt{\hbar\omega_{\text{cyc}}mc}. \quad (3.8)$$

Therefore, the classical limit requires $\Delta E/E = n^{-1/2} \ll 1$ which is achieved for $n \gg 1$.

The decay of pitch-angle calculated in the previous section corresponds in the quantum theory to the decay of n . If one extrapolates a little the theory from a uniform field to a curved magnetic field, one understands that the limit of curvature radiation then corresponds to $n = 0$. This means a regime in which perpendicular momentum cannot be treated classically. But is this regime ever reached ? For an ultra-relativistic particle most of the energy is in the longitudinal term $cp_{\parallel} \sim \gamma mc^2$, and one can estimate the pitch angle of the first perpendicular state as

$$\alpha_1 \simeq \frac{1}{\gamma} \sqrt{\frac{\hbar\omega_{\text{cyc}}}{mc^2}} \sim 10^{-8} B_8^{1/2} \gamma_7^{-1}. \quad (3.9)$$

Clearly, equation 3.5 implies that this pitch angle would be reached in barely 10 meters if the classical theory is correct. However, from this result it is not obvious that it is.

3.2 Quantum toy model of radiation from a rotating charged particle

In the classical theory of the radiation of an accelerated charged particle, one can completely separate the trajectory from the radiation theory : one can easily prescribe a trajectory and compute the resulting radiation. Within the framework of quantum

mechanics, the emission of a photon results from the transition of the radiating particle between two allowed states. The allowed states are given as proper functions of the Hamiltonian of the particle which determines the “trajectories”. Therefore, one cannot consistently separate the radiation from the solution of some equation of motion, or within the vocabulary of quantum mechanics the transitions from the proper states of some Hamiltonian. However, it is possible to postulate an ad hoc Hamiltonian fulfilling some prescription for the states of the particle. In the case of the synchrotron or curvature radiation, the classical trajectory prescription is exactly the same : one assumes a circular trajectory and then specifies its characteristics (radius, velocity) a posteriori depending of the physical mechanism at the origin of the trajectory. In this section, we prescribe a simple Hamiltonian whose main property is to have proper states circularly symmetric, thus providing the equivalent of classical circular trajectories. We then show that in the classical limit one obtains the well-known curvature or synchrotron radiation expressions.

This toy model presents the advantage of going through all the steps necessary for the derivation of quantum synchrocurvature radiation but with much simpler expressions. The theory of quantum synchrocurvature radiation is the topic of two articles published during this thesis (Voisin et al., 2017b; Voisin et al., 2017c). The first article treats of the proper states of an electron in a curved magnetic field and is presented in section 3.3 and the second article in section 3.4 treats of the radiation itself.

3.2.1 States of a toy electron

Let us assume spin 1/2 particles living on a circle C of radius ρ parametrized by the angle θ . C is a submanifold embedded in a 3D-space. On this submanifold rotation invariance plays the role of translational invariance in flat spaces. To enforce rotational invariance, proper states of the Hamiltonian must be common with those of the generalized angular momentum \hat{J}_x around the axis \vec{x} of the circle C . Indeed, the angular momentum operator \hat{J}_x is also the generator of elementary rotations around \vec{x} . Spin 1/2 particles are bound to C while photons may travel in any direction of the 3D space.

The circle C is parametrized by the angle θ ,

$$\theta \rightarrow (0, \rho \cos \theta, \rho \sin \theta). \quad (3.10)$$

In this one-dimensional coordinate system (ρ is fixed) the Dirac Hamiltonian takes the form

$$\hat{H}_C = -i\hbar c\alpha^\theta + \beta mc^2, \quad (3.11)$$

where α^θ is obtained from the Dirac matrices $(\alpha^i)_{i=\{x,y,z\}}$ through a change of coordinates

$$\alpha^\theta = \frac{1}{\rho} (-\sin\theta\alpha^y + \cos\theta\alpha^z), \quad (3.12)$$

and the Dirac matrices taken in their standard representation (Berestetskii et al., 1982)

$$\alpha^i = \begin{pmatrix} 0 & \sigma_i \\ \sigma_i & 0 \end{pmatrix}, \quad (3.13)$$

where the σ_i are the so-called Pauli matrices

$$\sigma_x = \begin{pmatrix} 0 & 1 \\ 1 & 0 \end{pmatrix}, \sigma_y = \begin{pmatrix} 0 & i \\ -i & 0 \end{pmatrix}, \sigma_z = \begin{pmatrix} 1 & 0 \\ 0 & -1 \end{pmatrix}. \quad (3.14)$$

The angular momentum operator \hat{J}_x is defined by

$$\hat{J}_x = (-i\hbar)(y\frac{\partial}{\partial z} - z\frac{\partial}{\partial y}) + \frac{\hbar}{2}\Sigma_x = -i\hbar\frac{\partial}{\partial\theta} + \frac{\hbar}{2}\Sigma_x, \quad (3.15)$$

where

$$\Sigma_i = \begin{pmatrix} \sigma_i & 0 \\ 0 & \sigma_i \end{pmatrix} \quad (3.16)$$

is the generator of spin 1/2 rotations around x .

Using expressions 3.15 and (3.12) and the commutation relations

$$[\Sigma_x, \alpha^y] = 2i\alpha^z, \quad (3.17)$$

$$[\Sigma_x, \alpha^z] = -2i\alpha^y, \quad (3.18)$$

one can check that the Hamiltonian (3.11) commutes with the angular momentum operator (3.15), which is the condition for them to share common proper states.

Let χ_λ be a proper state of integer proper value l_\parallel of \hat{J}_x , then it can be shown that

$$\chi_{l_\parallel}(\theta) = e^{i l_\parallel \theta} \begin{pmatrix} c_1 e^{-i \frac{\theta}{2}} - c_2 e^{i \frac{\theta}{2}} \\ c_1 e^{-i \frac{\theta}{2}} + c_2 e^{i \frac{\theta}{2}} \\ c_3 e^{-i \frac{\theta}{2}} - c_4 e^{i \frac{\theta}{2}} \\ c_3 e^{-i \frac{\theta}{2}} + c_4 e^{i \frac{\theta}{2}} \end{pmatrix}. \quad (3.19)$$

Inserting 3.19 in the Hamiltonian 3.11 one obtains the following system with proper energies E_{l_\parallel}

$$\hat{H}_C \chi_{l_\parallel}(\theta) = E_{l_\parallel} \chi_{l_\parallel}(\theta) \Leftrightarrow \begin{cases} \left(\frac{1}{2} + l_\parallel\right) c_{4,2} = \epsilon c_{1,3} \\ \left(-\frac{1}{2} + l_\parallel\right) c_{3,1} = \epsilon c_{2,4} \end{cases}, \quad (3.20)$$

with $\epsilon = \frac{\rho E_{l_\parallel}}{\hbar c}$.

This system has a non trivial solution if and only if its determinant is zero which imposes

$$E_{l_\parallel} = \pm \left(\hbar \Omega \sqrt{-\frac{1}{4} + l_\parallel^2} \right), \quad (3.21)$$

with $\sigma = \pm 1$. Keeping only the positive solution (the other being the anti-particle) and assuming the ultra-relativistic limit such that $l_\parallel \gg 1$ we obtain

$$E_{l_\parallel} = \hbar \Omega l_\parallel + \mathcal{O}(l_\parallel^{-1}), \quad (3.22)$$

and the system 3.20 simplifies into

$$\begin{cases} c_{4,2} = c_{1,3} \\ c_{3,1} = c_{2,4} \end{cases}. \quad (3.23)$$

We impose the normalization condition of the wave functions

$$\int d\theta \chi_{l_\parallel}^\dagger \chi = 1 \Leftrightarrow \sum_{i=1}^4 c_i^* c_i = \frac{1}{2\pi}, \quad (3.24)$$

and eventually all the coefficients in equation (3.19) are equal to $\frac{1}{\sqrt{8\pi}}$.

At this stage we have determined the proper states of the toy Hamiltonian, and we have reached the end of the motion part of the problem corresponding to the first article of section 3.3 in the case of synchrocurvature radiation. We now continue to the second part which consists in computing the transition rates of an electron following the Hamiltonian (3.11), and that is described by the article in section 3.4 for the synchrocurvature theory.

3.2.2 Radiation of the toy electron

We compute the interaction of the electron with the photon vacuum to the first order of perturbation theory. The Hamiltonian of interaction is

$$\hat{H}_{\text{int}} = \int ec \bar{\Psi}_f \gamma^\mu \Psi_i \hat{A}_\mu d^3 \vec{x}, \quad (3.25)$$

where Ψ_i is the initial state of the electron, $\bar{\Psi}_f = \Psi_f^* \gamma^0$ the Dirac conjugate of the final state, and $\Psi_{i,f} = e^{-itE_{i,f}/\hbar} \chi_{i,f}$. The vacuum amplitude operator³ \hat{A} in the Heisenberg representation is given by

$$\hat{A}_\mu = \sqrt{\frac{\hbar}{2\epsilon_0 V}} \sum_{\vec{k}, \vec{e}} \frac{1}{\sqrt{\omega_k}} \left(a_{\vec{k}, \vec{e}} e_\mu(\vec{k}) e^{i(\vec{k} \cdot \vec{x} - \omega_k t)} + a_{\vec{k}, \vec{e}}^\dagger e_\mu^*(\vec{k}) e^{-i(\vec{k} \cdot \vec{x} - \omega_k t)} \right) \quad (3.26)$$

where we consider photons of four-vector $(\hbar\omega_k/c, \hbar\vec{k})$ with polarizations $e_\mu(\vec{k})$ in the transverse (Coulomb) gauge characterized by $\vec{k} \cdot \vec{e} = 0$, $\epsilon_0 \simeq 8.854 \cdot 10^{-12}$ F/m is the electric permittivity of vacuum, and $V \equiv L^3$ the volume of quantification. The operators $a_{\vec{k}, \vec{e}}^\dagger$ and $a_{\vec{k}, \vec{e}}$ are respectively the operators of creation and destruction of photons in the modes (\vec{k}, \vec{e}) . Since the number of electrons does not vary we do not need to quantify the electron field Ψ , namely there is no need to attribute creation and destruction operators to the electron.

The rate of transition from vacuum to a state with one photon characterized by (\vec{k}, \vec{e}) while the electron switches from an initial state "i" to a final state "f" is given by

$$w_{fi} = \frac{\partial}{\partial t} \left\| \int_0^t d\tau e^{i\frac{E_f + \hbar\omega - E_i}{\hbar} \tau} \langle 1_{\vec{k}, \vec{e}}, f | \frac{\hat{H}_{\text{int}}}{\hbar} | 0, i \rangle \right\|^2. \quad (3.27)$$

After standard manipulation (e.g. Berestetskii et al. (1982), Sokolov and Ternov (1968)),

$$w_{fi} = \|M_{fi}\|^2 2\pi \hbar \delta(E_f + \hbar\omega - E_i), \quad (3.28)$$

³SI version of the amplitude operator taken from Bellac (2003), equation 11.98.

where $M_{fi} = \langle 1_{\vec{k}, \epsilon}, f | \frac{\hat{H}_{\text{int}}}{\hbar} | 0, i \rangle$ is the matrix element of the transition. Here it can be explicitly written for each mode,

$$M_{fi} = e \frac{j^\mu e_\mu}{\sqrt{2\epsilon_0 \hbar \omega_k V}}, \quad (3.29)$$

where the j^μ are the components of the transition current,

$$j^\mu = c \int \bar{\Psi}_f \gamma^\mu \Psi_i e^{-i\vec{k} \cdot \vec{x}} d^3x. \quad (3.30)$$

In the continuum limit, we obtain the differential probability of radiating a photon of wave vector \vec{k} in the solid angle $d\Omega$ and at a pulsation in $d\omega$ by multiplying by the number of such photons in the wave-vector volume element ⁴ $\frac{\omega^2 d\Omega d\omega}{c^3 (2\pi)^3 / V}$,

$$dw_{fi} = \|M_{fi}\|^2 2\pi \hbar \delta(E_f + \hbar\omega - E_i) \frac{\omega^2 d\Omega d\omega}{c^3 (2\pi)^3 / V} \quad (3.31)$$

To obtain the radiated intensity we need only multiply by the photon energy $\hbar\omega$ the differential probability 3.124, and sum over every possible final energy states applying $\int \frac{dE_f}{\hbar\Omega}$ in the continuum limit, where $dE_f/(\hbar\Omega)$ is the number of states of energy (3.6) in the interval dE_f . The intensity per pulsation per solid angle reads

$$\frac{d^2 I_{\sigma_f, i}^{\vec{e}}}{d\Omega d\omega} = \frac{\hbar\omega^3 V}{(2\pi)^2 c^3} \|M_{fi}\|^2 (E_f = E_i - \hbar\omega). \quad (3.32)$$

The most general matrix element for proper state of the type (3.19) is

$$M_{fi} = \frac{ec}{\sqrt{2\epsilon_0 \hbar \omega_k V}} \int_{-\pi}^{\pi} d\theta (4(c_1 c_4 - c_2 c_3) e_1 - (c_2 c_3 + c_1 c_4)(\cos \theta e_3 - \sin \theta e_2)) e^{i(\Delta l_{\parallel} - \vec{k} \cdot \vec{x})}, \quad (3.33)$$

where $\Delta l_{\parallel} = l_{\parallel f} - l_{\parallel i}$ is the difference between the parallel quantum number of the initial state of the electron and of the final state.

In the continuum limit, the variation of energy between to neighboring states compared to the energy $\hbar\Omega/E \ll 1$ which implies $l_{\parallel} \gg 1$. This is compatible with the ultrarelativistic approximation made so far and it allows to consider l_{\parallel} as a continuous parameter instead of an integer so that the energy $\hbar\omega$ of the radiated photon can be written

$$\hbar\omega = \Delta l_{\parallel} \frac{\partial E}{\partial l_{\parallel}} \quad (3.34)$$

⁴Each photon is analogous to a classical proper mode of a cavity of volume $V = L^3$ (see e.g. Bellac (2003)). The transverse electric field of such modes vanishes on the edges of the cavity which requires that $\vec{k} = 2\pi/L(n_x, n_y, n_z)$ where $n_{i \in \{x, y, z\}}$ are integers. The number of modes allowed in a box of wave-vector space of volume $(\delta k)^3$ is then $(\delta k / (2\pi/L))^3$. At the infinitesimal limit and in spherical coordinates this gives $\omega^2 d\Omega d\omega / (c^3 (2\pi)^3 / V)$.

where

$$\frac{\partial E}{\partial l_{\parallel}} = \hbar\Omega. \quad (3.35)$$

The variation of the quantum number l_{\parallel} during the transition can thus be expressed as a function of the pulsation of the photon

$$\Delta l_{\parallel} = \frac{\omega}{\Omega}. \quad (3.36)$$

Inserting the previous expression (3.36) and $c_i = 1/\sqrt{8\pi}$ obtained with equation (3.24) into the matrix element (3.33)

$$M_{fi} = -\frac{ec}{\sqrt{16\pi\epsilon_0\hbar\omega_k V}} \int_{-\pi}^{\pi} d\theta (e_3 \cos \theta - e_2 \sin \theta) e^{i(\theta\frac{\omega}{\Omega} - \vec{k}\vec{x})}. \quad (3.37)$$

There is only the polarization (coefficients e_2 and e_3) left to define. We use the basis defined in section 2.2.2, equation (3.135), that we recall here,

$$\vec{e}_{\parallel} = (0, 1, 0), \quad (3.38)$$

$$\vec{e}_{\perp} = \vec{k} \wedge \vec{e}_{\parallel} = (-\cos \kappa, 0, \sin \kappa), \quad (3.39)$$

where κ is the angle between the direction of motion and photon wave vector (see also figure 2.3).

Eventually putting everything into the intensity 3.32, performing the change of variable $\theta \rightarrow \Omega t$, and extending the boundaries of integration to infinity, one finds the intensities of the classical theory of a charge traveling a circle at pulsation Ω (see e.g. Jackson (1998)),

$$\frac{d^2 I^{\parallel}}{d\omega d\Omega} = \left\| \sqrt{\frac{e^2\omega^2}{16\pi^3\epsilon_0 c}} \int_{-\infty}^{+\infty} dt \sin(\Omega t) \cos(\kappa) e^{i\omega(t - \frac{1}{\Omega} \cos(\kappa) \sin(\Omega t))} \right\|^2, \quad (3.40)$$

$$\frac{d^2 I^{\perp}}{d\omega d\Omega} = \left\| \sqrt{\frac{e^2\omega^2}{16\pi^3\epsilon_0 c}} \int_{-\infty}^{+\infty} dt \cos(\Omega t) \cos(\kappa) e^{i\omega(t - \frac{1}{\Omega} \cos(\kappa) \sin(\Omega t))} \right\|^2. \quad (3.41)$$

Extending the boundaries to infinity is a mathematical simplification that occurs in the classical theory as well. In the latter, it is easily justified in physical terms from the very strong beaming in the forward direction of the radiation of a relativistic particle. The particle radiates within an angle $\sim 1/\gamma$, such that only the portion of the trajectory $\Omega t \lesssim 1/\gamma \ll 1$ effectively participates in the radiation in the direction of the wave vector \vec{k} . Although such an argument physically holds only for a point particle and does not make sense for a wave function (that defined everywhere on the circle at the same time), the underlying mathematics are the same.

3.3 Article: *Dirac states of an electron in a circular intense magnetic field*

The present section contains the article Voisin et al. (2017b) written in collaboration with Silvano Bonazzola⁵ and Fabrice Mottez⁶. A preprint version close to the journal style can be downloaded on the HAL and Arxiv preprint servers and the final version on the Physical Review D site⁷.

Abstract

Neutron-star magnetospheres are structured by very intense magnetic fields extending from 100 to 10^5 km traveled by very energetic electrons and positrons with Lorentz factors up to $\sim 10^7$. In this context, particles are forced to travel almost along the magnetic field with very small gyro-motion, potentially reaching the quantified regime.

We describe the state of Dirac particles in a locally uniform, constant and curved magnetic field in the approximation that the Larmor radius is very small compared to the radius of curvature of the magnetic field lines.

We obtain a result that admits the usual relativistic Landau states as a limit of null curvature. We will describe the radiation of these states, that we call quantum curvature or synchro-curvature radiation, in an upcoming paper.

3.3.1 Introduction

Electron and positron states with very low momentum perpendicular to the magnetic field have been of interest in the field of rotating neutron stars magnetospheres almost since their discovery in 1968 Hewish et al., 1968. Indeed, the community soon realized that the extremely intense rotating magnetic fields of those magnetospheres, ranging from $\sim 10^4$ Teslas at the surface of old millisecond pulsars to $\sim 10^{11}$ Teslas at the surface of some magnetars with a typical $\sim 10^8$ Teslas Viganò et al., 2015a, could generate extremely large electric-potential gaps along the open magnetic-field lines (see e.g. Arons, 2009 for a review) which in turn accelerate charged particles to energies only limited by radiation reaction. It is believed that these magnetospheres are mostly filled with electron and positrons resulting from a cascade of pair creations

⁵LUTh, Observatoire de Paris, PSL Research University, 5 places Jules Janssen 92190 Meudon, France

⁶LUTh, Observatoire de Paris, PSL Research University - CNRS, 5 places Jules Janssen 92190 Meudon, France

⁷HAL : <https://hal.archives-ouvertes.fr/hal-01490584>. Arxiv : <https://arxiv.org/abs/1703.05193>. Physical Review D : <https://journals.aps.org/prd/abstract/10.1103/PhysRevD.95.085002>

: pairs are created by quantum-electrodynamics processes involving gamma rays, and in turn radiate their kinetic energy in gamma-rays that make other pairs. The process of radiation is that of an accelerated charge that inspirals around a curved magnetic field. Because the magnetic field \vec{B} is so intense, the gyro-frequency $\omega = \frac{eB}{m\gamma}$ of an electron of charge $-e$, mass m and Lorentz factor γ , is so large that the momentum perpendicular to the local field is dissipated to very low values almost instantaneously because of synchrotron radiation reaction. It follows that electrons and positrons are believed to remain mostly very close to the local field line, radiating mostly because of their motion along the curved field line rather than perpendicular to it. Such motion and radiation are described either by the synchro-curvature regime (see e.g. Cheng and Zhang, 1996; Zhang and Yuan, 1998; Harko and Cheng, 2002; Viganò et al., 2015b; Kelner et al., 2015) or the curvature regime Ruderman and Sutherland, 1975, depending on whether the residual perpendicular motion is taken into account or neglected. With basic energetic arguments one then realizes that this can lead the particle to fall down in the quantified regime, both because radiation is efficient and because the energy levels are large in intense magnetic fields. This led the community to study transitions between low-lying Landau levels, see in particular the work of Harding and Preece, 1987. However, Landau levels are defined as the states of an electron in a constant uniform magnetic field and therefore are unable to produce transitions of momentum along the magnetic field, no more that they can explain a curved trajectory of the particle. Additionally, one will notice that the case of curvature radiation corresponds to an unphysical motion : a particle of charge e with a velocity \vec{v} aligned with the local magnetic field \vec{B} cannot undergo the Lorentz force $e\vec{v} \wedge \vec{B}$, and therefore cannot follow the magnetic field line.

Therefore, in this paper our purpose is to generalize the quantum motion of electrons and positrons to the motion in a locally uniform, circular and constant magnetic field, within the assumption that the radius of curvature is large compared to the Larmor radius. To this end we found a very precious help in the previous works about the motion of an electron in a constant uniform magnetic field by Huff, 1931, Johnson and Lippmann, 1949 and particularly Sokolov and Ternov, 1968. Basing ourselves on the present paper, we will then be able to derive in an upcoming article the radiation of an electron on its lowest perpendicular levels, which could be called quantum synchro-curvature radiation.

We shall start by setting up the symmetries of the problem in section 3.3.2, before deriving the solutions for a Klein-Gordon particle and more generally for the second order Dirac's equation in section 3.3.3. Based on those results we derive the full set of Dirac's Hamiltonian proper states in section 3.3.4. Finally in section 3.3.5 we propose an interpretation of the obtained states.

3.3.2 Symmetries

We consider a particle along a circular magnetic field line of radius ρ and of axis \vec{x} , that we call in the following the main circle.

Further we assume that the characteristic extension Δr of the wave function perpendicular to the magnetic field is very small compared to the radius of curvature. This, of course, must be checked a posteriori. In this case one may consider that the magnetic field is locally homogeneous upon an error of $\sim \frac{\Delta r}{\rho} B$.

Within these assumptions we have locally three symmetries of the system : one rotation around \vec{x} , one rotation around the magnetic-field line and one radial translation from the magnetic-field line. This generates a solid torus around the field line. According to Noether's theorem there will be three corresponding conserved quantities, and so three quantum numbers characterizing the proper states of a particle in such a field, to which one has to add one for the spin symmetry :

- s that quantizes the orthogonal translation,
- l_{\perp} that quantizes the rotation around the field line,
- l_{\parallel} that quantizes the rotation around \vec{x} ,
- ζ that accounts for the spin orientation.

The only difference with the assumptions prevailing in the computation of regular Landau states is that the invariance by translation along the magnetic field is replaced by a rotation around the \vec{x} axis.

3.3.3 Second order and Klein-Gordon solutions

In this paper, except otherwise stated, we always assume summation over repeated indices, latin indices for space components and greek for space-time with a metric of signature $(+ - - -)$.

We start from Dirac's Hamiltonian for an electron of charge $-e$ with minimal coupling to a classical magnetic field given by a potential \vec{A}

$$\hat{H} = \alpha^i \hat{P}_i + \beta mc^2, \quad (3.42)$$

where $i = \{x, y, z\}$ and the generalized impulsion is given by

$$\hat{P}_i = -i\hbar \left(\partial_i + i \frac{e}{\hbar} A_i \right). \quad (3.43)$$

Dirac's matrices α^i are given in standard representation (e.g. Berestetskii et al., 1982§21 eq. 20)

$$\beta = \begin{pmatrix} 1 & 0 \\ 0 & -1 \end{pmatrix}, \alpha^i = \begin{pmatrix} 0 & \sigma^i \\ \sigma^i & 0 \end{pmatrix}, \quad (3.44)$$

where the σ^i are the Pauli matrices :

$$\sigma^x = \begin{pmatrix} 0 & 1 \\ 1 & 0 \end{pmatrix}, \sigma^y = \begin{pmatrix} 0 & -i \\ i & 0 \end{pmatrix}, \sigma^z = \begin{pmatrix} 1 & 0 \\ 0 & -1 \end{pmatrix}. \quad (3.45)$$

We need a coordinate system that makes explicit both the assumed rotation invariance around axis \vec{x} and the part orthogonal to the magnetic field. Such a system is given by the "toroidal" coordinates, represented in figure 3.4. Toroidal coordinates are related to the cartesian system (x, y, z) by the homeomorphism

$$T : (r, \theta, \phi) \rightarrow \begin{pmatrix} x = r \cos \phi \\ y = \cos \theta (\rho + r \sin \phi) \\ z = \sin \theta (\rho + r \sin \phi) \end{pmatrix}, \quad (3.46)$$

where θ represents the direct angle with respect to the \vec{y} axis in the (\vec{y}, \vec{z}) plane. ϕ represents the direct angle with respect to \vec{x} in the plane (\vec{x}, \vec{y}') of the local frame $(\vec{x}, \vec{y}', \vec{u}_\theta)$ image of $(\vec{x}, \vec{y}, \vec{z})$ by a rotation of θ around \vec{x} and r represents the distance to the main circle. In particular we will need

$$\vec{u}_\theta = (0, -\sin \theta, \cos \theta)_{(\vec{x}, \vec{y}, \vec{z})}. \quad (3.47)$$

In order to write Dirac's equation in this system of coordinates we need to use the Jacobian of T , J_T , given in by formula (3.209) in 3.A.

Then the covariant quantities, and in particular the impulsion operators transform as follow,

$$\hat{p}_j = (J_T^{-1})_{ij} \hat{p}_i \quad (3.48)$$

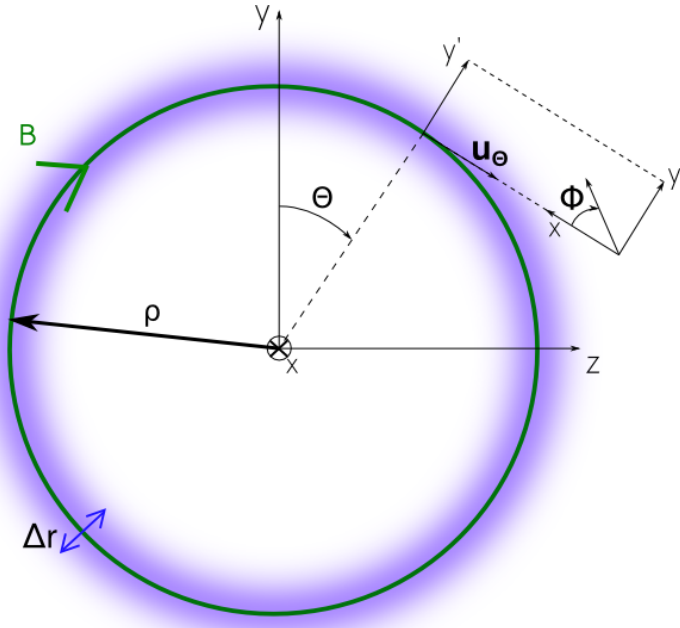


Fig. 3.2.: Representation of a circular magnetic field line (green) of radius ρ , that we call in this paper the main circle. The blue shadow around the line represents the wave function of a ground orthogonal level with a characteristic extent λ . The relation between the toroidal coordinates (r, θ, ϕ) and the cartesian coordinates (x, y, z) is also shown.

where $i' = \{r, \theta, \phi\}$.

It is can be shown that Dirac's Hamiltonian keeps the same shape as in (3.42) if we express it with Dirac's matrices transformed in a "contravariant" way (see appendix 3.A), namely

$$\alpha^{i'} = \alpha^j (J_T^{-1})_{i'j}. \quad (3.49)$$

It follows that Dirac's Hamiltonian reads

$$\hat{H} = \alpha^{i'} \hat{P}_{i'} + \beta mc^2. \quad (3.50)$$

We define a suited expression for the magnetic potential \vec{A} in toroidal coordinates. Since the magnetic field is along $\vec{\partial}_\theta$, A_r or A_ϕ are its only non zero components. Since we impose rotation invariance \vec{A} does not depend on θ and the local quasi-uniformity hypothesis implies the dependency in r and ϕ should be negligible as long as $r \ll \rho$, and more precisely on the scale of the wave function Δr . From the expression of the rotational in toroidal coordinates given by (3.226) in 3.A, a simple potential yielding a constant magnetic field to lowest order in r/ρ along ∂_θ is

$$A^r = 0, A^\theta = 0, A^\phi = -\frac{1}{2}B. \quad (3.51)$$

Using the metric g_T (3.217) we obtain the covariant component

$$A_\phi = \frac{1}{2}r^2B. \quad (3.52)$$

This corresponds to a magnetic field

$$\vec{B} = B\vec{u}_\theta + \mathcal{O}(r/\rho). \quad (3.53)$$

Let's remark that this is compatible with the uniform homogeneous field when $\rho \rightarrow \infty$, as required, since the toroidal coordinates then tend to the cylindrical system.

Following the procedure described in Berestetskii et al., 1982, we seek a second order equation of which solutions include Dirac's equation solutions by the taking covariant form of Dirac's equation

$$\hat{D}\Psi = 0 \Leftrightarrow (c\gamma^\mu \hat{P}_\mu - mc^2)\Psi = 0, \quad (3.54)$$

and applying to it the operator $\hat{C} = (c\gamma^\mu \hat{P}_\mu + mc^2)$. One obtains what we call here the second-order Dirac equation

$$\hat{C}\hat{D}\Psi = 0 \Leftrightarrow \hbar^2 \partial_{t_2}^2 \Psi = \hat{H}_2 \Psi. \quad (3.55)$$

Where \hat{H}_2 is the second-order "Hamiltonian" which for the magnetic potential given in (3.51) is explicitly given by

$$\begin{aligned} \hat{H}_2 = & (\hbar c)^2 \left[\partial_r^2 + \frac{1}{r} \partial_r + \frac{\cos \phi}{\rho+r \cos \phi} \partial_r + \frac{1}{r^2} \partial_\phi^2 - \frac{\sin \phi}{r(\rho+r \cos \phi)} \partial_\phi \right. \\ & - 2i \frac{e}{\hbar} A^\phi \partial_\phi + \frac{e^2}{\hbar^2} A^\phi A_\phi - i e \frac{r \sin \phi}{\rho+r \cos \phi} A^\phi \\ & \left. + \frac{1}{(\rho+r \cos \phi)^2} \partial_\theta^2 - \frac{e}{\hbar} \vec{B} \cdot \vec{\Sigma} - \frac{m^2 c^2}{\hbar^2} \right] \end{aligned} \quad (3.56)$$

where $\vec{\Sigma} = \begin{pmatrix} \vec{\sigma} & 0 \\ 0 & \vec{\sigma} \end{pmatrix}$ are the spin $\frac{1}{2}$ rotation generators in standard representation.

The full derivation of (3.56) is given in 3.B.

Now we notice that the interaction between the magnetic field and the state of the electron involves the characteristic magnetic length scale

$$\lambda = \left(\frac{2\hbar}{eB} \right)^{1/2}. \quad (3.57)$$

Anticipating on the result, we shall consider that λ defines the characteristic perpendicular extent of the wave-function for low-perpendicular-momentum states. This is backed by the fact that the same magnetic length scale plays a similar role in the uniform-magnetic-field case (see e.g. Sokolov and Ternov, 1968, where λ^{-2} is denoted γ).

We can define a dimensionless coordinate $x \equiv \frac{r}{\lambda}$ and the parameter $\epsilon \equiv \frac{\lambda}{\rho}$. Following our primary assumptions we shall consider that $\epsilon \ll 1$. One can check that this is particularly well verified in the case of a typical pulsar magnetic field of intensity $B \sim 10^8$ Teslas and curvature radius $\rho \sim 10^4$ meters

$$\epsilon \sim 10^{-16} B_8^{-1/2} \rho_4^{-1}, \quad (3.58)$$

where $\rho_4 = \rho/10^4$ and $B_8 = B/10^8$. Notice it could also be true in large particle accelerators, because of the soft (square-root) dependance on the magnetic-field intensity.

We can now give a quantitative meaning to the assumption of low perpendicular momentum, that is

$$\partial_x \sim \partial_\phi \ll \epsilon^{-1}. \quad (3.59)$$

The longitudinal momentum can be larger. However we assume that

$$\partial_\theta \ll \epsilon^{-3/2}, \quad (3.60)$$

and justify this approximation at the end of this section, where (3.87) translates in terms of maximum Lorentz factor the above approximation.

We now rewrite \hat{H}_2 (3.56) in terms of x , ϵ and λ keeping only the lowest order terms in ϵ

$$\begin{aligned} \hat{H}_2 = & \\ & \left(\frac{\hbar c}{\lambda} \right)^2 \left[\partial_x^2 + \frac{1}{x} \partial_x + \frac{1}{x^2} \partial_\phi^2 + 2i \partial_\phi - x^2 \right. \\ & \left. + \epsilon^2 \partial_\theta^2 - 2\vec{u}_\theta \cdot \vec{\Sigma} - \frac{m^2 c^2 \lambda^2}{\hbar^2} \right] + \mathcal{O}(\epsilon). \end{aligned} \quad (3.61)$$

Compared to (3.56) the rightmost term of the two first lines have vanished and we used the fact that $\frac{1}{\rho+r\sin\phi} = \frac{\epsilon}{\lambda} + \mathcal{O}(\epsilon^2)$ to simplify the others. The eigen problem of operator (3.61) is separable, which would not have been the case if we had considered $\partial_\theta \geq \epsilon^{-3/2}$ since we would have to take into account an additional $2\epsilon^3 x \cos\phi \partial_\theta^2$. It is also worth noticing that, as expected, this equation is very similar to the one found when solving the uniform field problem in cylindrical coordinates (see Sokolov and Ternov, 1968).

Our symmetry requirements impose that the sought states be proper states not only of the Dirac Hamiltonian but also of two rotation generators

$$\hat{J}_\theta = -i\hbar\partial_\phi + \frac{\hbar}{2}\vec{u}_\theta \cdot \vec{\Sigma}, \quad (3.62)$$

$$\hat{J}_x = -i\hbar\partial_\theta + \frac{\hbar}{2}\Sigma_x, \quad (3.63)$$

where \hat{J}_θ is the angular-momentum operator around the magnetic field centered on the main circle and J_x is the angular-momentum around the axis of the main circle. These operators commute exactly, while commutation with the Dirac Hamiltonian is ensured to order ϵ ,

$$[\hat{J}_\theta, \hat{J}_x] = 0, \quad (3.64)$$

$$[\hat{H}, \hat{J}_x] = \mathcal{O}(\epsilon). \quad (3.65)$$

This leads to consider proper states of both operators which are of the form

$$\chi_{l_\parallel, j_\perp}(\theta, \phi) = \frac{1}{2}e^{ij_\perp\phi + i\theta l_\parallel} \begin{pmatrix} e^{-\frac{i\theta}{2}}(b_1 e^{\frac{i\phi}{2}} + b_2 e^{-\frac{i\phi}{2}}) - e^{\frac{i\theta}{2}}(b_1 e^{\frac{i\phi}{2}} - b_2 e^{-\frac{i\phi}{2}}) \\ e^{-\frac{i\theta}{2}}(b_1 e^{\frac{i\phi}{2}} + b_2 e^{-\frac{i\phi}{2}}) + e^{\frac{i\theta}{2}}(b_1 e^{\frac{i\phi}{2}} - b_2 e^{-\frac{i\phi}{2}}) \\ e^{-\frac{i\theta}{2}}(b_3 e^{\frac{i\phi}{2}} + b_4 e^{-\frac{i\phi}{2}}) - e^{\frac{i\theta}{2}}(b_3 e^{\frac{i\phi}{2}} - b_4 e^{-\frac{i\phi}{2}}) \\ e^{-\frac{i\theta}{2}}(b_3 e^{\frac{i\phi}{2}} + b_4 e^{-\frac{i\phi}{2}}) + e^{\frac{i\theta}{2}}(b_3 e^{\frac{i\phi}{2}} - b_4 e^{-\frac{i\phi}{2}}) \end{pmatrix}, \quad (3.66)$$

where b_1, b_2, b_3, b_4 are constants of ϕ and θ , and $\hbar j_\perp$ and $\hbar l_\parallel$ are the proper values of \hat{J}_θ and \hat{J}_x respectively. l_\parallel and j_\perp are half-integers $\dots -\frac{3}{2}, -\frac{1}{2}, \frac{1}{2}, \frac{3}{2}, \dots$

We seek a solution to the eigen problem

$$\hat{H}_2 \Psi = E^2 \Psi, \quad (3.67)$$

where one can show that $\pm E$ are also a proper energies of the Dirac Hamiltonian \hat{H} . We seek a solution of the problem (3.67) with the help of the ansatz

$$\Psi(x, \theta, \phi) = \chi(\theta, \phi) \Phi(x). \quad (3.68)$$

Inserting this ansatz into (3.67) one gets for χ an eigen problem of the form

$$\left(\epsilon^2 \partial_{\theta^2}^2 - \vec{u}_\theta \cdot \vec{\Sigma} \right) \chi(\theta, \phi) = -C_\theta \chi(\theta), \quad (3.69)$$

where C_θ is a constant. As expected, the operator on the left hand side of equation (3.69) commutes with \hat{J}_x and \hat{J}_θ . Therefore χ is necessarily a combination of $\chi_{l_\parallel, j_\perp}$. Moreover, it can be shown that the operator in (3.69) is degenerate with respect to j_\perp but not to l_\parallel . Therefore we have that

$$\chi(\theta, \phi) = \sum_{j_\perp} \chi_{l_\parallel, j_\perp}(\theta, \phi), \quad (3.70)$$

where each $\chi_{l_\parallel, j_\perp}$ has a different set of unknowns $(b_i) = (b_i^{j_\perp})$, i ranging from 1 to 4.

However, we notice that a solution of (3.69) can be found with a combination of only two states, $\chi(\theta, \phi) = \chi_{l_\parallel, j_\perp-1} + \chi_{l_\parallel, j_\perp}$, if for a given j_\perp one takes $b_1^{j_\perp} = b_3^{j_\perp} = b_2^{j_\perp-1} = b_4^{j_\perp-1} = 0$, giving

$$\chi(\theta, \phi) = e^{il_\parallel \theta} e^{il_\perp \phi} \begin{pmatrix} e^{-i\frac{\theta}{2}} (b_1^{j_\perp-1} + b_2^{j_\perp}) - e^{i\frac{\theta}{2}} (b_1^{j_\perp-1} - b_2^{j_\perp}) \\ e^{-i\frac{\theta}{2}} (b_1^{j_\perp-1} + b_2^{j_\perp}) + e^{i\frac{\theta}{2}} (b_1^{j_\perp-1} - b_2^{j_\perp}) \\ e^{-i\frac{\theta}{2}} (b_3^{j_\perp-1} + b_4^{j_\perp}) - e^{i\frac{\theta}{2}} (b_3^{j_\perp-1} - b_4^{j_\perp}) \\ e^{-i\frac{\theta}{2}} (b_3^{j_\perp-1} + b_4^{j_\perp}) + e^{i\frac{\theta}{2}} (b_3^{j_\perp-1} - b_4^{j_\perp}) \end{pmatrix}, \quad (3.71)$$

where we define $l_\perp \equiv j_\perp - \frac{1}{2}$. With this choice, l_\perp is no longer the exact angular momentum, it will however simplify upcoming calculations and allow a direct comparison with the uniform case as presented in Sokolov and Ternov, 1968. We will give its exact meaning in section (3.3.5).

Then, χ is a solution provided that the remaining free coefficients satisfy the following systems, obtained after inserting (3.71) back into (3.69) ,

$$M_\theta \begin{pmatrix} b_{2,4}^{j_\perp} \\ b_{1,3}^{j_\perp-1} \end{pmatrix} = 0, \quad (3.72)$$

where M_θ is defined by the matrix coefficients

$$\begin{aligned} M_{\theta 11} &= -\epsilon^2(2l_\parallel + 1)^2 - 4(2 - C_\theta), \\ M_{\theta 12} &= (2l_\parallel + 1)^2\epsilon^2 - 4(2 + C_\theta), \\ M_{\theta 21} &= -(1 - 2l_\parallel)^2\epsilon^2 - 4(2 - C_\theta), \\ M_{\theta 22} &= -(1 - 2l_\parallel)^2\epsilon^2 + 4(C_\theta + 2). \end{aligned} \quad (3.73)$$

This system has a none trivial solution only if

$$C_\theta^\sigma = \frac{1}{4} \left(4l_\parallel^2\epsilon^2 + \epsilon^2 + \sigma 4\sqrt{l_\parallel^2\epsilon^4 + 4} \right), \quad (3.74)$$

which leads to the solution coefficients

$$b_{2,4\sigma}^{j_\perp} = c_{1,2}^\sigma \left(2 - l_\parallel\epsilon^2 + \sigma\sqrt{l_\parallel^2\epsilon^4 + 4} \right), \quad (3.75)$$

$$b_{1,3\sigma}^{j_\perp-1} = c_{1,2}^\sigma \left(-2 - l_\parallel\epsilon^2 + \sigma\sqrt{l_\parallel^2\epsilon^4 + 4} \right), \quad (3.76)$$

where c_1 and c_2 are for now arbitrary constants describing the two proper spaces found for $(b_2^{j_\perp}, b_1^{j_\perp-1})$ (two first lines of χ) and $(b_4^{j_\perp}, b_3^{j_\perp-1})$ (two last lines of χ) respectively. The number $\sigma = \pm 1$ distinguishes two classes of solutions that we shall denote $\uparrow = +1$ and $\downarrow = -1$ for reasons that will become obvious when we see its physical meaning in section 3.3.5.

Let's now solve the equation for $\Phi(x)$. After inserting our ansatz (3.68) including the previously found expression for χ , we get the equation

$$\left(\partial_{x^2}^2 + \frac{1}{x}\partial_x - \frac{l_\perp^2}{x^2} - x^2 - 2l_\perp \right) \Phi(x) = -C_x\Phi(x), \quad (3.77)$$

where C_x is a constant to be determined. We give the detailed resolution of this equation in 3.C, where we find that

$$\Phi(x) = x^{l_\perp} e^{-\frac{x^2}{2}} L_s^{l_\perp}(x^2) \quad (3.78)$$

$$C_x = 4 \left(n + \frac{1}{2} \right), \quad (3.79)$$

where L_s^l is a generalized Laguerre polynomial of degree s as defined in Olver and National Institute of Standards and Technology (U.S.), 2010 (§18.5) by

$$L_s^l(x) = \sum_{i=0}^s \frac{(l+i+1)_{s-i}}{(s-i)!i!} (-x)^i, \quad (3.80)$$

where $(a)_n = \Gamma(a+n)/\Gamma(a)$ is a Pochhammer's symbol.

Besides, $n = s + l_\perp$ is the primary perpendicular quantum number, s is a positive integer and the perpendicular angular momentum must be positive or null $l_\perp \geq 0$ to ensure that the wave function vanishes at infinity and is square-integrable. We will come back later to the interpretation of these quantum numbers. Notice that we use the same notations as in Sokolov and Ternov, 1968 for the uniform-magnetic-field case, where the radial dependency has exactly the same form but is expressed with a different coordinate system. Notice as well that (3.78) is proportional to a normalization constant that we dropped here for simplicity. Normalization will be determined farther on.

Putting the whole Ψ back into the main equation (3.67), we get the proper energies

$$E^2 = m^2 c^4 + \frac{\hbar^2 c^2}{\lambda^2} (C_x + C_\theta^\sigma), \quad (3.81)$$

which develops as

$$E = \pm m c^2 \left[1 + 2 \frac{\hbar \omega_c}{m c^2} \left(n + \frac{1}{2} \right) + \sigma \frac{\hbar \omega_c}{m c^2} \sqrt{1 + (\epsilon^2 l_\parallel)^2} + \left(\frac{\hbar \Omega}{m c^2} \right)^2 \left(\frac{1}{4} + l_\parallel^2 \right) \right]^{\frac{1}{2}}, \quad (3.82)$$

where $\omega_c = \frac{eB}{m}$ is the cyclotron pulsation and $\Omega = \frac{c}{\rho}$ is the pulsation of the circular trajectory.

Proper functions Ψ and proper values E^2 are the exact solutions of eigen problem of the approximated operator \hat{H}_2 (3.61). However, our approximations do not allow us to take meaningfully into account terms of order ϵ and higher. At this order, the complete solutions of the second order eigen problem (3.67) is explicitly given by

$$\Psi_2(x, \theta, \phi) = 4x^{l_\perp} e^{-\frac{x^2}{2}} L_s^{l_\perp}(x^2) e^{il_\parallel\theta} e^{il_\perp\phi} \begin{pmatrix} c_1^\sigma \left(\sigma e^{-i\frac{\theta}{2}} + e^{i\frac{\theta}{2}} \right) \\ c_1^\sigma \left(\sigma e^{-i\frac{\theta}{2}} - e^{i\frac{\theta}{2}} \right) \\ c_2^\sigma \left(\sigma e^{-i\frac{\theta}{2}} + e^{i\frac{\theta}{2}} \right) \\ c_2^\sigma \left(\sigma e^{-i\frac{\theta}{2}} - e^{i\frac{\theta}{2}} \right) \end{pmatrix} + \mathcal{O}(\epsilon), \quad (3.83)$$

$$E = \pm mc^2 \sqrt{1 + 2 \frac{\hbar\omega_c}{mc^2} \left(n + \frac{1+\sigma}{2} \right) + \left(\frac{\hbar\Omega}{mc^2} \right)^2 l_\parallel^2}, \quad (3.84)$$

where in such a development, one has to remind that l_\parallel can be of order ϵ^{-1} . In this limit we obtain degenerate states : indeed states with $n, \sigma = +1$ have the same energy as states with numbers $n + 1, \sigma = -1$. The only exception is for what we will from now on call the perpendicular fundamental state : $n = 0, \sigma = -1$, which is non-degenerate.

Before going farther, let's notice that we already obtained the solution of the Klein-Gordon equation for an electron in a circular magnetic field. Indeed, \hat{H}_2 corresponds to the Klein-Gordon "Hamiltonian" plus a spin term $\vec{u}_\theta \cdot \Sigma$. Neglecting this term it comes that $\chi(\theta, \phi) = e^{il_\parallel\theta} e^{il_\perp\phi}$ and the proper states of energy (3.84) are given by

$$\Psi_{\text{KG}}(x, \theta, \phi) = e^{il_\parallel\theta} e^{il_\perp\phi} x^{l_\perp} e^{-\frac{x^2}{2}} L_s^{l_\perp}(x^2). \quad (3.85)$$

We now justify a posteriori approximation (3.60). Assuming as in typical pulsar magnetospheres that the motion is dominated by the momentum along the field and that particles are ultra-relativistic with a classical Lorentz factor $\gamma \gg 1$ we obtain, using equation (3.84),

$$E = \gamma mc^2 = \hbar\Omega l_\parallel + \mathcal{O}\left(\frac{1}{l_\parallel}\right). \quad (3.86)$$

This allows to translate approximation (3.60) in terms of a limit on the Lorentz factor

$$\gamma \ll 6 \cdot 10^6 \rho_4^{1/2} B_8^{3/4}, \quad (3.87)$$

compatible with a variety of pulsar magnetospheres situations. We briefly come back to the interpretation in terms of possible drifts at the end of section 3.3.5.

3.3.4 Dirac's equation solutions

General solution

It can be shown from the derivation of the second order equation (3.55) that from any second-order solution a first-order solution can be obtained by applying the \hat{C} operator to it like

$$\Psi(x, \theta, \phi) = \hat{C} e^{-i\frac{E}{\hbar}t} \Psi_2(x, \theta, \phi). \quad (3.88)$$

This is the approach suggested in Berestetskii et al., 1982. However, following naively this procedure leads to obtain as many first order solutions as second order solutions while there should be half as many. One can check that we now have 4 independent second-order solutions for each triplet $(n, l_{\perp}, l_{\parallel})$, two for each value of σ , as shown in equations (3.75) and (3.76). Moreover, one can check that the obtained second-order solutions are neither directly solutions of \hat{C} or of \hat{D} which implies that proper states for a given energy must be linear combinations of the second order solutions.

We are going to show that such solutions can be obtained using the combination

$$\Psi = e^{-i\frac{E}{\hbar}t} (\Psi_{2l_{\perp}-1, \sigma=+1} + \Psi_{2l_{\perp}, \sigma=-1}), \quad (3.89)$$

$$E = \pm mc^2 \sqrt{1 + 2\frac{\hbar\omega_c}{mc^2}n + \left(\frac{\hbar\Omega}{mc^2}\right)^2 l_{\parallel}^2}. \quad (3.90)$$

The state Ψ above is thus defined by the superposition of two states having the same quantum number s . The proper energy (3.90) can be equivalently defined as $E^2_{l_{\perp}-1, \sigma=+1}$ or $E^2_{l_{\perp}, \sigma=-1}$. We chose the second option in (3.90). Remark that as such Ψ is undefined for $l_{\perp} = 0$. Prescribing that $\Psi_{2l_{\perp}=-1} = 0$, we find the perpendicular fundamental state as the particular case $\Psi_{s=0, l_{\perp}=0}$,

One can show that solving the equation $\hat{D}\Psi = 0$ amounts to solve the linear problem

$$M_D \begin{pmatrix} c_1^- \\ c_2^- \\ c_1^+ \\ c_2^+ \end{pmatrix} = 0, \quad (3.91)$$

Calculations to obtain the matrix M_D are lengthy but appeal to relatively simple operations for which a formal calculation engine can be helpful. We consider the details of it would be of little interest for the reader, for this reason we give here only the main steps. It goes as follow :

- Divide by the following common factor to isolate the "spinor part" of the equation

$$S \equiv \hat{D}\Psi / (e^{il_{\parallel}\theta} e^{i(l_{\perp}-1)\phi} x^{l_{\perp}} e^{-\frac{x^2}{2}}) = 0. \quad (3.92)$$

- The remaining function can be expanded on the basis of the four orthogonal functions : $(e^{ai\frac{\theta}{2}} e^{bi\phi})$, where $a = \pm 1$ and $b = \{0, 1\}$. Taking into account the four spinor components, labeled by j hereafter, this gives us 16 coefficients depending on the four unknowns $(c_1^{\downarrow}, c_2^{\downarrow}, c_1^{\uparrow}, c_2^{\uparrow})$ that we call $s_{j,a,b}$. It follows that the equation $\hat{D}\Psi = 0$ reduces to a linear system of 16 equations

$$\forall j, \forall a, \forall b, s_{j,a,b} = 0. \quad (3.93)$$

Notice that, at this stage, the coefficients still depend on functions of x .

- A lot of these equations are actually equivalent. The coefficients with $a = +1$ are proportional to coefficients with $a = -1$ for any given doublet (j, b) . Also notice that the components of the spinor are related two by two : $s_{1,a,b} \propto s_{2,a,b}$ and $s_{3,a,b} \propto s_{4,a,b}$ for all a and b . Finally, there are only four a priori independent equations. To fix ideas, we will go on with the system

$$\begin{cases} s_{1,1,1} = 0 \\ s_{3,1,1} = 0 \\ s_{1,1,0} = 0 \\ s_{3,1,0} = 0 \end{cases}. \quad (3.94)$$

- Using the two relations

$$L_s^{l_{\perp}+1}(x^2) = L_{s-1}^{l_{\perp}+1}(x^2) + L_s^{l_{\perp}}(x^2), \quad (3.95)$$

$$L_s^{l_{\perp}}(x^2) = \frac{(1 + l_{\perp})L_s^{l_{\perp}+1}(x^2) - x^2 L_{s-1}^{l_{\perp}+2}(x^2)}{(s + l_{\perp} + 1)} \quad (3.96)$$

which can be derived from the Laguerre-polynomial recurrence relations given in Olver and National Institute of Standards and Technology (U.S.), 2010 §18.9, one shows that $s_{1,1,1}$ and $s_{3,1,1}$ are proportional to $xL_s^{l_{\perp}+1}$ while $s_{1,1,0}$ and $s_{3,1,0}$ are proportional to $L_s^{l_{\perp}}$.

- It follows from the previous point that after dividing each equation by its respective x polynomial as well as $2\hbar c/\lambda$ (to make it dimensionless), the system (3.94) gives (3.91) with

$$M_D = \begin{pmatrix} \frac{E-mc^2}{\hbar c/\lambda} & \epsilon l_{\parallel} & 0 & 2i \\ -\epsilon l_{\parallel} & -\frac{E+mc^2}{\hbar c/\lambda} & -2i & 0 \\ 0 & -2i(1+n) & \frac{E-mc^2}{\hbar c/\lambda} & -\epsilon l_{\parallel} \\ 2i(1+n) & 0 & \epsilon l_{\parallel} & -\frac{E+mc^2}{\hbar c/\lambda} \end{pmatrix}. \quad (3.97)$$

The determinant of M_D is null which means, as expected, that the kernel of M_D is not empty. One finds two independent solutions given by

$$\begin{pmatrix} c_1^{\downarrow} \\ c_2^{\downarrow} \end{pmatrix} = \begin{pmatrix} \frac{E+mc^2}{\hbar c/\lambda} \\ -\epsilon l_{\parallel} \end{pmatrix} \quad \text{and} \quad \begin{pmatrix} c_1^{\uparrow} \\ c_2^{\uparrow} \end{pmatrix} = 2n \begin{pmatrix} 0 \\ i \end{pmatrix}, \quad (3.98)$$

$$\begin{pmatrix} c_1^{\downarrow} \\ c_2^{\downarrow} \end{pmatrix} = \begin{pmatrix} -\epsilon l_{\parallel} \\ \frac{E-mc^2}{\hbar c/\lambda} \end{pmatrix} \quad \text{and} \quad \begin{pmatrix} c_1^{\uparrow} \\ c_2^{\uparrow} \end{pmatrix} = 2n \begin{pmatrix} i \\ 0 \end{pmatrix}. \quad (3.99)$$

Notice that the perpendicular fundamental state comes out naturally from the two solutions (3.98) and (3.99). Indeed, for $n = 0$ the $\sigma = \uparrow$ coefficients vanish, and the energy becomes $E = mc^2 \sqrt{1 + \left(\frac{\hbar\Omega}{mc^2}\right)^2 l_{\parallel}^2}$. Then the two solutions are proportional, as expected from the non degeneracy of the perpendicular fundamental, since one finds (3.99) by simply multiplying (3.98) by $-\frac{E-mc^2}{\hbar c/\lambda}$. The two solutions (3.98) and (3.99) correspond to two spin states that we shall respectively label by $\zeta = -1$ and $\zeta = +1$. Some more details will be given in section 3.3.5.

Normalization

We now have obtained the three parts of the wave function. We still need to impose normalization with

$$\int d^3\vec{x} \sum_{i=1}^4 \Psi_i^* \Psi_i = 1. \quad (3.100)$$

We need the Jacobian determinant of the toroidal coordinates

$$d^3\vec{x} = |r(\rho + r \sin \phi)| dr d\theta d\phi. \quad (3.101)$$

Expressing it as a function of the dimensionless variable x ,

$$d^3\vec{x} = \lambda^2 \rho |x(1 + \epsilon x \sin \phi)| dx d\theta d\phi, \quad (3.102)$$

it becomes obvious that the $\sin \phi$ term can be removed at lowest order in ϵ .

For the integration over x the following integral Olver and National Institute of Standards and Technology (U.S.), 2010

$$\int_{x=0}^{+\infty} x^{2l} e^{-x^2} [L_s^l(x^2)]^2 x dx = \frac{(s+l)!}{2s!} \quad (3.103)$$

is useful.

We get the normalization

$$N = 4\pi \sqrt{\rho \lambda^2 \frac{(n-1)! \left(\left(\frac{E + \zeta m c^2}{\hbar c / \lambda} \right)^2 + (\epsilon l_{\parallel})^2 n + 2n^2 \right)}{2s!}}. \quad (3.104)$$

Complete proper states

Eventually the proper states of a particle of energy E (3.90) in a toroidal magnetic field can be explicitly given by

$$\Psi = \frac{1}{N} e^{-\frac{x^2}{2}} e^{i l_{\parallel} \theta} e^{i(l_{\perp} - \frac{1}{2})\phi} \left(e^{-i\frac{\phi}{2}} x^{l_{\perp}-1} L_s^{l_{\perp}-1}(x^2) \chi_{\zeta}^{\uparrow}(\theta) + e^{i\frac{\phi}{2}} x^{l_{\perp}} L_s^{l_{\perp}}(x^2) \chi_{\zeta}^{\downarrow}(\theta) \right). \quad (3.105)$$

The two χ_{ζ}^{σ} spinors are explicitly given by

$$\chi_{\zeta}^{\downarrow} = \begin{pmatrix} \left(\frac{1+\zeta}{2} \frac{E+mc^2}{\hbar c/\lambda} - \frac{1-\zeta}{2} \epsilon l_{\parallel} \right) \left(-e^{-i\frac{\theta}{2}} + e^{i\frac{\theta}{2}} \right) \\ \left(\frac{1+\zeta}{2} \frac{E+mc^2}{\hbar c/\lambda} - \frac{1-\zeta}{2} \epsilon l_{\parallel} \right) \left(-e^{-i\frac{\theta}{2}} - e^{i\frac{\theta}{2}} \right) \\ \left(-\frac{1+\zeta}{2} \epsilon l_{\parallel} + \frac{1-\zeta}{2} \frac{E-mc^2}{\hbar c/\lambda} \right) \left(-e^{-i\frac{\theta}{2}} + e^{i\frac{\theta}{2}} \right) \\ \left(-\frac{1+\zeta}{2} \epsilon l_{\parallel} + \frac{1-\zeta}{2} \frac{E-mc^2}{\hbar c/\lambda} \right) \left(-e^{-i\frac{\theta}{2}} - e^{i\frac{\theta}{2}} \right) \end{pmatrix}, \quad (3.106)$$

$$\chi_{\zeta}^{\uparrow} = 2ni \begin{pmatrix} \frac{1-\zeta}{2} \left(e^{-i\frac{\theta}{2}} + e^{i\frac{\theta}{2}} \right) \\ \frac{1-\zeta}{2} \left(e^{-i\frac{\theta}{2}} - e^{i\frac{\theta}{2}} \right) \\ \frac{1+\zeta}{2} \left(e^{-i\frac{\theta}{2}} + e^{i\frac{\theta}{2}} \right) \\ \frac{1+\zeta}{2} \left(e^{-i\frac{\theta}{2}} - e^{i\frac{\theta}{2}} \right) \end{pmatrix}. \quad (3.107)$$

One can see that the constant uniform-magnetic-field case can be recovered by taking the limit $\rho \rightarrow \infty$ in (3.105) after having performed the replacements : $\theta \rightarrow z/\rho$, $l_{\parallel} \rightarrow \rho k^z$ where \vec{z} is the axis along the magnetic field and k^z is the associated wave number.

3.3.5 Interpretation of the quantum numbers

In this section we consider an electron state (positive energy) to simplify the discussion without any loss of generality.

The parallel quantum number l_{\parallel} quantifies, by construction, the angular momentum around the \vec{x} axis. From the expression of the proper energy we can also interpret $\hbar\Omega l_{\parallel}$ as the "component" of the energy corresponding to the motion along the magnetic field.

We move on to interpreting the perpendicular motion. Our treatment is similar to that of Sokolov and Ternov, 1968. The energy of the motion perpendicular to the magnetic field is quantified by the quantum number $n = s + l_{\perp}$. It can be interpreted as the quantification of the square of the radius of the trajectory of the electron since the classical gyroradius can be expressed as $r_g = p_{\perp}/(m\omega_c)$ with p_{\perp} the perpendicular momentum and, in case of a purely perpendicular motion, $E^2 = p_{\perp}^2 + m^2c^4$. We see below that this assertion can be very quickly proven in the classical limit in the particular case $n = l_{\perp}$.

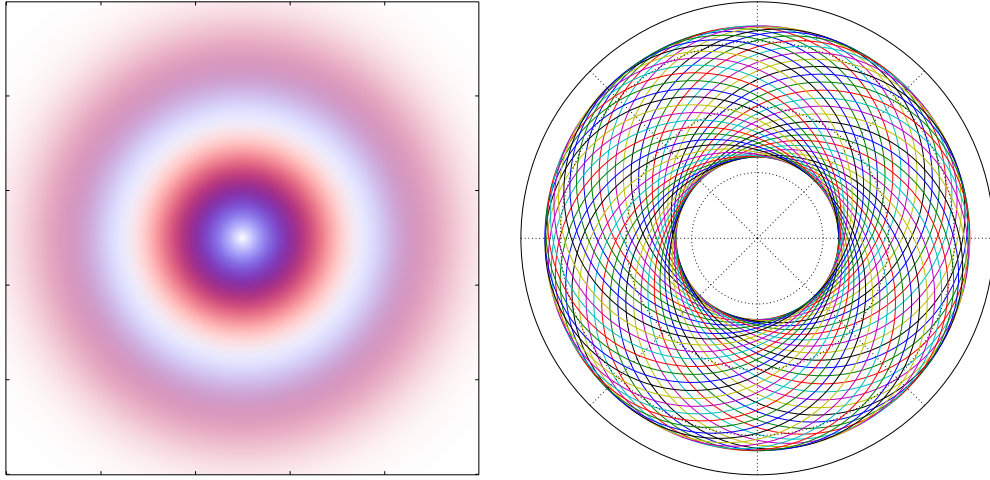


Fig. 3.3.: Left panel : probability density of detecting an electron in a state $s = 1, l_{\perp} = 1$ in a plane orthogonal to the magnetic-field line of radius ρ . The color goes from blue (inner part of each ring), spin aligned with the magnetic field, to red (outer part of each ring), spin anti-aligned. Here the parallel motion is small, $l_{\parallel} \lesssim \epsilon^{-1}$ such that both spin components are almost equally important. In the case of a relativistic parallel motion, $l_{\parallel} > \epsilon^{-1}$, only the anti-aligned (red) component plays a significant role as one can see from equation (3.105), (3.106) and (3.107). Right panel : representation of a family of off-centered classical trajectories defined by $a = 1.5$ where a is defined in (3.278).

As we saw in the previous section the wave function is not defined for a strictly negative l_{\perp} . From a classical point of view this is easily understandable since l_{\perp} quantifies the angular momentum around the local axis of the magnetic field. Therefore, $l_{\perp} > 0$ corresponds to a rotation in the direct sense, which is the orientation that an electron takes under the action of the classical Lorentz force $\vec{v} \wedge \vec{B}$, where \vec{v} is the speed of the electron.

Going a little bit deeper, one can show that the solution (3.105) is a proper state of the angular momentum around the magnetic field \hat{J}_{θ} of proper value $\hbar(l_{\perp} - 1/2)$. This means that the perpendicular fundamental has a negative angular momentum of $-\hbar/2$. However, it does not mean that the electron classically turns backwards around the magnetic field, but rather that the spin is oriented backward, while the orbital angular momentum is zero. Indeed, one can show that the spinors χ_{ζ}^{σ} are proper states of the operator of projection of the spin onto the main circle of the magnetic field, $\frac{\hbar}{2}\vec{u}_{\theta} \cdot \vec{\Sigma}$ (the spin part of \hat{J}_{θ}), with proper values $\hbar\sigma/2$. We here justify the notation \uparrow or \downarrow for $\sigma = \pm 1$ as meaning that the spin is aligned or anti-aligned with the magnetic field. The perpendicular fundamental state is thus the only purely anti-aligned state, as we will see. Since it has no orbital momentum, one cannot interpret the trajectory of the particle following the magnetic field as the result of the classical Lorentz force but rather as a strictly quantum phenomenon of the

interaction between spin and magnetic field. States with $n > 0$ (i.e. $l_{\perp} > 0$ or $s > 0$) are in a superposed spin state, both aligned and anti-aligned with the magnetic field which results into a degeneracy into two states parametrized by ζ . It is in theory possible to find measurable quantities, hermitian operators that commute with the Hamiltonian, such that this degeneracy would be lifted and the spin orientation fixed (see e.g. Sokolov and Ternov, 1968 or Melrose and Parle, 1983 for possibilities in the case of a uniform homogeneous magnetic field). However, it is usually impossible to determine the state of the spin, in particular in astrophysics. We therefore prefer to consider the most general case in which a state of energy E is the superposition of the two ζ states of (3.105) combined through a mixing angle η ,

$$\Psi = \cos(\eta)\Psi_{\zeta=-1} + \sin(\eta)\Psi_{\zeta=+1}. \quad (3.108)$$

Parametrization by such an angle takes into account the constrain of having a norm of the final state that is still one. Notice that it is impossible to form a purely aligned or anti-aligned state for any value of the mixing angle, as we previously stated.

We now explain the role of the quantum numbers s and l_{\perp} and why their role in the energy is degenerated. First consider an electron with $s = 0$, then the radial part of the wave function (3.105) is merely $\propto e^{-x^2} x^{2p}$ where $p = l_{\perp} - 1$ for the anti-aligned term and $p = l_{\perp}$ for the aligned term. Now, this function is peaked at $x_p = \sqrt{p}$ with an amplitude at the peak of p^p . This means that, apart for the perpendicular fundamental, the electron always has a double orbit : one of aligned spin and, a bit further, one of anti-aligned spin, as shown in figure 3.3.

Considering a high value of the perpendicular angular momentum one can quickly recover classical results analogous to the uniform magnetic field case. For simplicity we will consider that momentum along the field is zero, $l_{\parallel} = 0$. From the previous discussion the particle orbits at a distance $r_p \simeq \lambda\sqrt{l_{\perp}}$. Expressing l_{\perp} as a function of the energy one gets

$$l_{\perp} = \frac{E^2 - m^2c^4}{2mc^2\hbar\omega_c}. \quad (3.109)$$

In the classical limit the numerator simply identifies with the square of the perpendicular momentum of the particle p_{\perp}^2 . Inserting (3.109) into r_p , we obtain the classical (relativistic) Larmor radius :

$$r_p = r_g = \frac{p_{\perp}}{eB} \quad (3.110)$$

This is in agreement with the more general result given above. Moreover, it confirms that the typical extent of the wave-function can be taken to be the gyro-radius, at least for high enough quantum numbers, and approximation (3.59) can be written in a more intuitive way

$$r_g \ll \rho \quad (3.111)$$

Similarly, one finds that the group velocity of a wave-packet, $v_g = \frac{\partial \omega}{\partial k}$, can be found after identifying $\omega = E/\hbar$ and $k = l_\perp/r_p : v_g = r_p \omega_c/\gamma$ with $\gamma = E/(mc^2)$. We here recognize the classical relativistic gyro-frequency ω_c/γ of an electron in a uniform magnetic field.

Now, for a same energy we may as well have states of lower l_\perp and higher s . This degeneracy also appears, to some extent, in the classical treatment of this problem. Since the radial part of the motion is mostly identical to the uniform-magnetic-field case, we can use the later to better understand the former. We developed in 3.D the Newtonian solution of the uniform problem based on the Hamilton-Jacobi formalism which, because of its parenting with quantum mechanics, allows a formulation in similar terms. In particular, it is found that there are two terms in the perpendicular energy : one related with the angular momentum (noted p_θ in the classical case) and the other to a shift of distance r_0 of the center of the trajectory with respect to the origin of the coordinate. This is summarized in formula (3.289) recalled here,

$$E = p_\theta \omega_c + \frac{1}{2} m r_0^2 \omega_c^2. \quad (3.112)$$

We will follow that guide. If l_\perp obviously corresponds to the angular-momentum, p_θ term, we can show that s corresponds to the second term. The position of the center of the trajectory given by equation (3.287) can be generalized as the operator

$$\hat{x}_0 = \hat{x} + \frac{\hat{J} \wedge \hat{p}}{m \omega_c |\hat{J}|} \quad (3.113)$$

Where \hat{x} is the position operator, \hat{p} the impulsion and \hat{J} the angular momentum with respect to the coordinate origin. For our set of solutions $\hat{J} = \hat{J}_\theta$ and the previous operator simplifies to the two components

$$\hat{x}_0 = \hat{x} - \frac{\hat{p}_{y'}}{m \omega_c}, \quad (3.114)$$

$$\hat{y}'_0 = \hat{y}' + \frac{\hat{p}_x}{m \omega_c}, \quad (3.115)$$

where (x, y') are the coordinates locally perpendicular to the magnetic field as defined in figure 3.4. From that, an operator $\hat{r}_0^2 = \hat{x}_0^2 + \hat{y}'_0^2$ is readily obtained. Using the dimensionless coordinate $x = r/\lambda$

$$\hat{r}_0^2 = \lambda^2 \left(x^2 - \partial_{x^2}^2 - \frac{1}{x} \partial_x - \frac{1}{x^2} \partial_{\phi^2}^2 + 2i \partial_\phi \right), \quad (3.116)$$

where one recognizes the radial part of the second order equation previously solved (see (3.77) or (3.247)) except for the ∂_ϕ term which sign is reversed. From that observation it is straightforward to see that the proper values of \hat{r}_0^2 are

$$r_0^2 = 4\lambda^2(s + \frac{1}{2}). \quad (3.117)$$

The $\frac{1}{2}$ term comes from the spin interaction that broadens the orbits as we saw previously. Now interpreting the trajectory as an off-centered circle obviously breaks the assumed rotation invariance around the coordinate center. This apparent paradoxe is solved by considering that a proper wave-function is analogous not to a single classical trajectory but to the set of all the trajectories corresponding to the invariants of motion defining the proper state : n or the perpendicular energy and l_\perp or the perpendicular angular momentum. We see from the expression of the trajectory (3.276) that this set is classically parametrized by the constant of integration θ_0 . This constant is defined by the initial conditions of the motion, and sets the position of the center of trajectory on the circle of radius r_0 centered on the main circle. Then it is obvious that this set is invariant by rotation, as shown in figure 3.3. Thus, we recover the interpretation of s as characterizing the radial symmetry assumed in section 3.3.2.

One notices that in the present solution, the particle remains localized around the magnetic-field line, and therefore there is no drift perpendicular to the line as in the classical theory where the drift is due to the centrifugal force (see e.g. Kelner et al., 2015). This is justified by the fact that we considered only the lowest perpendicular states and a "moderate" longitudinal momentum (3.60) that allows us to neglect coupling terms between longitudinal motion (∂_θ terms) and perpendicular motion (x , ∂_x and ∂_ϕ terms). We notice that several works on the classical theory of synchro-curvature radiation (for example Cheng and Zhang, 1996; Zhang and Yuan, 1998; Harko and Cheng, 2002; Viganò et al., 2015b) did not take this drift into account either, and this approximation is widely used for lepton trajectories in pulsar magnetospheres even with Lorentz factors largely above the limit given in (3.87). Besides, in Kelner et al., 2015 the authors show that the effect on radiation of the drift classically results in an effective radius of curvature.

3.3.6 Conclusion

In this paper we were able to generalize the relativistic Landau states to the case of circular magnetic field (3.105), in the approximation that the curvature radius is large compared to the Larmor radius of the particle while the momentum along the field is not excessively large ((3.59) or (3.111) and (3.60)). Our main interest is for applications to the very intense magnetic fields around rotating neutron stars, pulsars

and magnetars, in which radiation from very low perpendicular momentum electrons and positrons is believed to be ubiquitous. In an upcoming paper, we will address the problem of radiations from transitions between the states derived in the present paper. We could call them quantum curvature radiation for transitions involving only the ground perpendicular state and more generally quantum synchro-curvature radiation (see e.g. Cheng and Zhang, 1996).

3.4 Article: *Quantum theory of curvature and synchro-curvature radiation in a strong and curved magnetic field, and applications to neutron star magnetospheres*

The present section contains the article Voisin et al. (2017c) written in collaboration with Silvano Bonazzola⁸ and Fabrice Mottez⁹. A preprint version close to the journal style can be downloaded on the HAL and Arxiv preprint servers and the final version on the Physical Review D site¹⁰.

Abstract

In a previous paper, we derived the quantum states of a Dirac particle in a circular, intense magnetic field in the limit of low momentum perpendicular to the field with the purpose of giving a quantum description of the trajectory of an electron, or a positron, in a typical pulsar or magnetar magnetosphere.

Here we continue this work by computing the radiation resulting from transitions between these states. This lead us to derive from first principles a quantum theory of the so-called curvature and synchro-curvature radiations relevant for rotating neutron star magnetospheres.

We find that, within the approximation of an infinitely confined wave-function around the magnetic field and in the continuous energy-level limit, classical curvature radiation can be recovered in a fully consistent way. Further we introduce discrete transitions to account for the change of momentum perpendicular to the field and derive expressions for what we call quantum synchro-curvature radiation. Additionally, we express deconfinement and quantum recoil corrections.

⁸LUTH, Observatoire de Paris, PSL Research University, 5 places Jules Janssen 92190 Meudon, France

⁹LUTH, Observatoire de Paris, PSL Research University - CNRS, 5 places Jules Janssen 92190 Meudon, France

¹⁰HAL : <https://hal.archives-ouvertes.fr/hal-01519896>. Arxiv : <https://arxiv.org/abs/1705.03790>. Physical Review D : <https://journals.aps.org/prd/abstract/10.1103/PhysRevD.95.105008>

3.4.1 Introduction

In a previous paper (Voisin et al., 2017b) (hereafter paper 1), we derived the states of an electron in a curved strong magnetic field within the approximation of a very low momentum perpendicular to the magnetic field. To ease calculations, it is convenient to consider a “circular” magnetic field, that is the field lines are of constant curvature and so form circles. In this paper, we compute the transition rates between these states in the limit of high momentum parallel to the magnetic field, in such a way that parallel transition can be considered approximately continuous. Our goal is to derive a quantum-electrodynamics theory of curvature radiation and low synchro-curvature radiation in the context of rotating neutron star magnetospheres. These magnetospheres are characterized by intense magnetic field from 10^5 Teslas for recycled millisecond pulsars to 10^{11} Teslas for magnetars. The radius of curvature of magnetic field lines is typically larger than 10 km, which is the typical radius of the star, within the assumption of a dipolar magnetic field. Extremely large electric-potential gaps along the open magnetic-field lines (see e.g. Arons (2009) for a review) accelerate charged particles to energies only limited by radiation reaction at Lorentz factors as high as $10^5 - 10^8$.

In this regime, an electron loses all of its momentum perpendicular to the magnetic field after traveling a few meters in the synchro-curvature regime (see hereafter and Voisin et al. (2016)). When only parallel momentum remains, radiation reaction is attributed to the so-called curvature radiation along the magnetic field (Ruderman and Sutherland, 1975), which is the radiation of a charged particle following exactly a locally circular trajectory. Synchrotron radiation can be seen as a particular case where the trajectory is the cyclotron trajectory. However, curvature radiation usually refers to the case of a magnetic-field-line trajectory, and therefore is not strictly physical, in the sense that a particle not rotating around the field does not undergo any force capable of keeping it along. Therefore, curvature radiation is better seen as the mathematical zero-perpendicular-momentum limit of the so-called synchro-curvature radiation (Cheng and Zhang, 1996) that describes the classical theory of radiation by a charged particle with low perpendicular momentum in a locally circular magnetic field. Quantum corrections were added by Zhang and Yuan (1998) and later by Harko and Cheng (2002) in the form of an effective correction to classical expressions in analogy with equivalent photon theories developed for synchrotron radiation which essentially amounts to the replacement $\omega \rightarrow \omega(1 + \hbar\omega/E)$ in the transition probability $\omega^{-1}I(\omega)$ accounting for quantum recoil, where I is the intensity per pulsation ω and E is the energy of the particle. A formalism based on effective electric fields was developed (Harko and Cheng, 2002) to deal with further inhomogeneities of the magnetic field such as a perpendicular gradient of intensity. A more compact but equivalent formalism for synchro-curvature radiation

was also developed (Viganò et al., 2015b). Recently, a description (Kelner et al., 2015) with a self-consistent trajectory that takes carefully into account the drift along the cylinder generated by the circular field showed that the drift effectively changes the curvature radius for relatively large Lorentz factors or low magnetic field intensities. As we pointed out in paper 1, classical synchro-curvature (CSC) radiation results in numerous cases in a very fast decay of the perpendicular momentum of the particle which can reach the first Landau levels, if one assumes the well-known quantum theory of an electron in a homogeneous-intensity uniform-orientation magnetic field (see e.g. Sokolov and Ternov (1968)). One then has to take into account discrete transitions from one Landau level to another (Latal, 1986), (Harding and Preece, 1987). This is particularly interesting when the plasma is at rest in the frame of the star such that the uniform-magnetic-field theory is locally relevant. This is the case for example in x-ray binaries where x-ray cyclotron lines have been observed and where two levels are typically separated by $11.6B_8$ keV with $B_8 = B/(10^8 \text{Teslas})$ (Caballero and Wilms, 2012).

Therefore, classical synchro-curvature cannot hold for very low perpendicular momenta since the synchrotron part becomes discrete. This effect cannot be taken into account with the usual quantum recoil corrections which apply in the continuous limit. Besides it does not take into account the fact that two quantum numbers are changing, one for parallel and another for perpendicular momenta. Simultaneously, cyclotron transitions are irrelevant for particles with high parallel momenta since they do not take into account longitudinal transitions, that is the curvature part of the radiation. In this paper, we start from first principles using the quantum states derived in paper 1. The resulting radiation results from transitions in the continuous approximation for parallel momentum variations and discrete for perpendicular momentum variations. Parallel transitions are treated in a similar way as Sokolov and Ternov (1968) did for the quantum theory of synchrotron radiation (see also Schwinger (1954) and Schwinger and Tsai (1978)). With this formalism synchro-curvaturelike and curvaturelike components appear in a very distinct fashion. As mentioned in paper 1, we neglect every drift of the particle, which is very appropriate except at extremes of the magnetic-field and Lorentz-factor ranges mentioned above. We also find additional corrections in $(\hbar\omega/E)^p(B_c/B)^q$ where p, q are positive integers, $B_c = 4.4 \cdot 10^9$ Teslas being the critical field of Landau states and B being the magnetic-field intensity. We interpret these as deconfinement corrections, in the sense that they give the difference between a pointlike particle and an extended wave function around the magnetic-field line. At leading order, we find the classical curvature (CC) radiation.

This paper is organized as follows: in section 3.4.2 we introduce the general formalism to compute quantum transitions; in section 3.4.3 we develop this formalism in the particular case of curvature radiation which allows us to introduce notations and

concepts that we generalize in section 3.4.4 to the general case of synchro-curvature radiation; in section 3.4.5 we integrate the previously found expressions over solid angles to obtain power spectra; and in section 3.4.6 we discuss these results around the example of a millisecond pulsar.

3.4.2 Radiation of confined particles in quantum electrodynamics

We compute the interaction of the electron with the photon vacuum to the first order of perturbation theory. The Hamiltonian of interaction is

$$\hat{H}_{\text{int}} = \int e c \bar{\Psi}_f \gamma^\mu \Psi_i \hat{A}_\mu d^3 \vec{x}, \quad (3.118)$$

where Ψ_i is the initial state of the electron, $\bar{\Psi}_f = \Psi_f^* \gamma^0$ being the Dirac conjugate of the final state. \hat{A} is the vacuum amplitude operator (see e.g. Bellac (2003) equation 11.98), in the Heisenberg representation

$$\hat{A}_\mu = \sqrt{\frac{\hbar}{2\epsilon_0 V}} \sum_{\vec{k}, e} \frac{1}{\sqrt{\omega_k}} \left(a_{\vec{k}, z} e_\mu(\vec{k}) e^{i(\vec{k} \cdot \vec{x} - \omega_k t)} + a_{\vec{k}, \epsilon}^\dagger e_\mu^*(\vec{k}) e^{-i(\vec{k} \cdot \vec{x} - \omega_k t)} \right), \quad (3.119)$$

where we consider photons of four-vector $(\hbar\omega_k/c, \hbar\vec{k})$ with polarizations $e_\mu(\vec{k}) = (e_0(\vec{k}), \vec{e}(\vec{k}))$ in the transverse (Coulomb) gauge such that: $\vec{k} \cdot \vec{e} = 0$. $\epsilon_0 \simeq 8.854 \cdot 10^{-12}$ F/m is the electric permittivity of vacuum and $V \equiv L^3$ the volume of quantification.

Since the number of electrons does not vary we need not quantify the electron field Ψ .

The rate of transition from vacuum to a state with one photon characterized by (\vec{k}, e) while the electron switches from an initial state i to a final state f is given by

$$w_{fi} = \frac{\partial}{\partial t} \left\| \int_0^t d\tau e^{i \frac{E_f + \hbar\omega - E_i}{\hbar} \tau} \langle 1_{\vec{k}, e}, f | \frac{\hat{H}_{\text{int}}}{\hbar} | 0, i \rangle \right\|^2, \quad (3.120)$$

which after standard manipulation (e.g. Berestetskii et al. (1982), Sokolov and Ternov (1968)) gives

$$w_{fi} = \|M_{fi}\|^2 2\pi \hbar \delta(E_f + \hbar\omega - E_i), \quad (3.121)$$

where $M_{fi} = \langle 1_{\vec{k}, \epsilon}, f | \frac{\hat{H}_{\text{int}}}{\hbar} | 0, i \rangle$ is the matrix element of the transition, which in this case can be explicitly written for each mode as

$$M_{fi} = e \frac{j^\mu e_\mu}{\sqrt{2\epsilon_0 \hbar \omega_k V}}, \quad (3.122)$$

where j^μ are the components of the transition current

$$j^\mu = c \int \bar{\Psi}_f \gamma^\mu \Psi_i e^{-i\vec{k} \cdot \vec{x}} d^3x. \quad (3.123)$$

In the continuum limit, we obtain the differential probability of radiating a photon in the solid angle $d\Omega$ at a pulsation in $d\omega$ by multiplying by the density of such states $\frac{\omega^2 d\Omega d\omega}{c^3 (2\pi)^3 V}$,

$$dw_{fi} = \|M_{fi}\|^2 2\pi \hbar \delta(E_f + \hbar\omega - E_i) \frac{\omega^2 d\Omega d\omega}{c^3 (2\pi)^3 V}. \quad (3.124)$$

To obtain the radiated intensity we need only multiply by the photon energy $\hbar\omega$ the differential probability (3.124), and sum over every possible final energy state applying $\int \frac{dE_f}{\hbar\Omega}$ in the continuum limit and ultrarelativistic limit defined below along with Ω . The intensity per pulsation per solid angle corresponding to a transition between an initial state i and a final state f reads

$$\frac{d^2 I_{f,i}^{\vec{e}}}{d\Omega d\omega} = \frac{\hbar\omega^3 V}{\Omega (2\pi)^2 c^3} \|M_{fi}\|^2 (E_f = E_i - \hbar\omega). \quad (3.125)$$

3.4.3 Classical curvature radiation from quantum electrodynamics

In this paper we consider ultrarelativistic particles traveling along a circular magnetic field, the states of which were derived in paper 1 (Voisin et al., 2017b). The proper energies can be written as

$$E = \sqrt{m^2 c^4 + 2m^2 c^4 \frac{B}{B_c} n + \hbar^2 \Omega^2 l_{\parallel}^2} \quad (3.126)$$

where B is the magnetic field, $B_c = \frac{m^2 c^2}{e\hbar} = 4.4 \cdot 10^9$ Teslas is the critical magnetic field for which the difference between two Landau levels is equal to the rest mass energy of the electron, and $\Omega = c/\rho$ is the pulsation of the particle along the main circle (see figure 3.4). The numbers n and l_{\parallel} are integers respectively quantifying the angular momentum around the magnetic field and around the axis of the circular magnetic field (see figure 3.4).

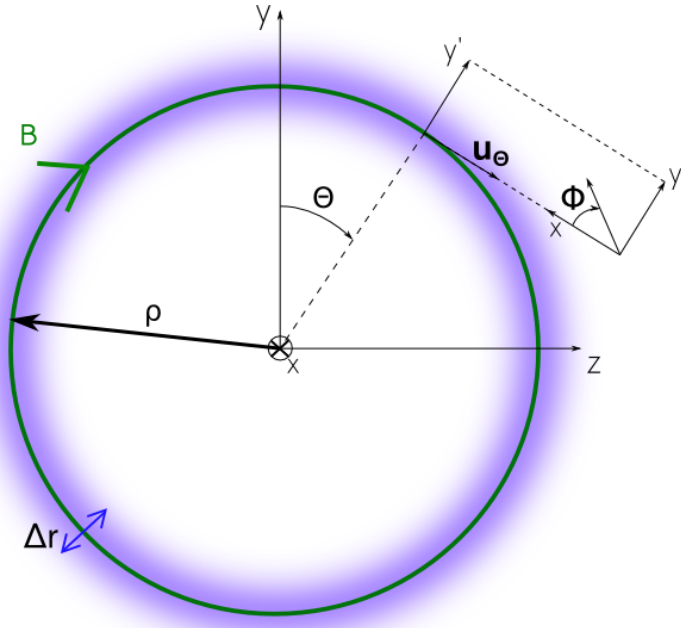


Fig. 3.4.: Representation of a circular magnetic field line (green) of radius ρ , called the “main circle” in the text. The blue shadow around the line represents the wave function of a ground orthogonal level with a characteristic extent λ . The relation between the toroidal coordinates (r, θ, ϕ) and the Cartesian coordinates (x, y, z) is also shown.

In the theory of classical curvature radiation the rotation of the particle around the trajectory is neglected. Here we therefore take the lowest perpendicular state that is $n = 0$. Moreover, recalling that in the ultrarelativistic approximation most of the energy is in the longitudinal term, we expand the energy (3.126) as

$$E = \hbar\Omega_{\parallel} \left(1 + \frac{1}{2\gamma^2} + \mathcal{O}\left(\frac{1}{\gamma^4}\right) \right) \quad (3.127)$$

where $\gamma = E/(mc^2)$ is the classical Lorentz factor. The wave function corresponding to this perpendicular fundamental state (see paper 1) is given to $\mathcal{O}(\gamma^{-2})$ by

$$\Psi_0 = \frac{e^{i l_{\parallel} \theta} e^{-x^2/2}}{2\pi\sqrt{\rho\lambda^2}} \begin{pmatrix} i \sin \frac{\theta}{2} \\ -\cos \frac{\theta}{2} \\ -i \sin \frac{\theta}{2} \\ \cos \frac{\theta}{2} \end{pmatrix}, \quad (3.128)$$

where ρ is the radius of the classical trajectory that we call here the main circle and

$$\lambda = \left(\frac{2\hbar}{eB} \right)^{1/2} \quad (3.129)$$

is the magnetic length scale which characterizes the extent of the wave function perpendicular to the main circle. We use the toroidal coordinates related to the Cartesian system (x, y, z) by the homeomorphism

$$T : (r, \theta, \phi) \rightarrow \begin{pmatrix} x = r \cos \phi \\ y = \cos \theta (\rho + r \sin \phi) \\ z = \sin \theta (\rho + r \sin \phi) \end{pmatrix}, \quad (3.130)$$

where θ represents the direct angle with respect to the \vec{y} axis in the (\vec{y}, \vec{z}) plane, ϕ represents the direct angle with respect to \vec{x} in the plane (\vec{x}, \vec{y}') of the local frame $(\vec{x}, \vec{y}', \vec{u}_\theta)$ image of $(\vec{x}, \vec{y}, \vec{z})$ by a rotation of θ around \vec{x} and r represents the distance to the main circle. For further references on the coordinate system, see paper 1 and figure 3.4. Here we use the reduced variable $x = r/\lambda$. Moreover, the approximation used in paper 1 imposes that all our expressions are given to leading order in

$$\epsilon = \lambda/\rho \ll 1. \quad (3.131)$$

We now have all the ingredients to compute the current (3.123) for a transition between two perpendicular fundamentals of initial longitudinal number $l_{\parallel i}$ and final $l_{\parallel f}$. It reads

$$j_{00} = \frac{1}{2\pi^2} \left(0, \int \sin \theta e^{-x^2} e^{i(l_i - l_f)\theta - i\lambda \vec{k} \cdot \vec{x}} d^3 \vec{x}, \quad (3.132)$$

$$\int \cos \theta e^{-x^2} e^{i(l_i - l_f)\theta - i\lambda \vec{k} \cdot \vec{x}} d^3 \vec{x} \right), \quad (3.133)$$

with a dimensionless $d^3 \vec{x} = x dx d\theta d\phi + \mathcal{O}(\epsilon)$.

In the following we restrict ourselves to wave numbers lying in the (\vec{z}, \vec{x}) plane defined as

$$\vec{k} = k(\sin \kappa, 0, \cos \kappa) \quad (3.134)$$

where κ is the direct angle from the z axis. Since \vec{x} is a symmetry axis, this is done without loss of generality. This allows us to choose the polarization basis (we use the same basis as used in the textbook Jackson (1998))

$$\begin{aligned} \vec{e}_{\parallel} &= (0, 1, 0), \\ \vec{e}_{\perp} &= \frac{\vec{k}}{k} \wedge \vec{e}_{\parallel} = (-\cos \kappa, 0, \sin \kappa). \end{aligned} \quad (3.135)$$

From a classical point of view, the parallel polarization \vec{e}_{\parallel} points towards the center of the trajectory of the electron, and the perpendicular polarization \vec{e}_{\perp} completes the direct triad $(\vec{k}/k, \vec{e}_{\parallel}, \vec{e}_{\perp})$.

From equation (3.127), one derives the relation between the variation of the parallel quantum number $\Delta l_{\parallel} = l_{\parallel i} - l_{\parallel f}$ and the variation of energy of the electron $E_i - E_f = \hbar\omega$, where ω is the pulsation of the emitted photon. Considering l_{\parallel} as a continuous parameter, the energy variation can be Taylor expanded

$$\hbar\omega = \Delta l_{\parallel} \left. \frac{\partial E_{l_{\parallel}, \sigma}}{\partial l_{\parallel}} \right|_i - \frac{\Delta l_{\parallel}^2}{2} \left. \frac{\partial^2 E_{l_{\parallel}, \sigma}}{\partial l_{\parallel}^2} \right|_i \quad (3.136)$$

which is inverted into

$$\Delta l_{\parallel} = \frac{\omega}{\Omega} \left(1 + \frac{1}{2\gamma^2} \right) + \mathcal{O} \left(\frac{\hbar\omega}{E} \right). \quad (3.137)$$

We give additional $\hbar\omega/E$ terms, which are quantum recoil corrections, in the next sections.

The imaginary exponential in the current (3.132) can be rewritten, using (3.137) and expanding the scalar product thanks to (3.130) and (3.134), as

$$e^{i \frac{\omega}{\Omega} \left(1 + \frac{1}{2\gamma^2} \right) \theta - i \rho k \cos \kappa \sin \theta} e^{-i x \lambda k (\cos \phi \sin \kappa + \sin \phi \cos \kappa \sin \theta)}. \quad (3.138)$$

The second factor above exists only in the quantum mechanical theory. One can easily be convinced of that by noticing the presence of the magnetic length λ (3.129) which contains the Planck constant $\lambda \propto \hbar^{1/2}$. To obtain the classical theory one therefore puts $\lambda = \hbar = 0$. We neglect this factor (put it to 1) in the first part of the following discussion and then reintroduce it.

As in the usual treatment of classical synchrotron or curvature radiation (see e.g. Jackson (1998)) we consider the approximation of high frequency photons in which

$$\omega \gg \Omega. \quad (3.139)$$

It follows that one can develop the phase in the first factor above to third order in θ since the exponential will oscillates heavily even for $\theta \ll 1$ as found in the literature on the classical radiation. One also expects a very high relativistic beaming implying that $\kappa \sim 1/\gamma$, and we can therefore expand $\cos \kappa = 1 - \frac{1}{2}\kappa^2 + \mathcal{O}(\kappa^4)$. We also notice that $\rho k = \omega/\Omega$. It follows that (3.138) now reads

$$e^{i \frac{\omega}{2\Omega} \left(\left(\kappa^2 + \frac{1}{\gamma^2} \right) \theta + \frac{\theta^3}{3} \right)}. \quad (3.140)$$

We check the consistency of our approximations by looking at the qualitative behavior of (3.140) above when integrated over θ as in (3.132):

- When in the integral $\theta > \bar{\theta} = \left(\kappa^2 + \frac{1}{\gamma^2}\right)^{1/2}$ the θ^3 term in the phase becomes dominant.
- If $\frac{\omega}{\Omega} \bar{\theta}^3 > 1$ then the exponential oscillates heavily for $\theta \gg \bar{\theta}$ and kills the remaining part of the integral. This sets a critical pulsation $\omega \sim \bar{\theta}^{-3} \Omega$ above which the integral starts to decay.
- The smallest critical pulsation corresponds to $\kappa = 0$. More generally, if $\kappa \gg 1/\gamma$ the transitions remain possible on a much smaller part of the spectrum, and we recover the relativistic beaming condition that transitions are most likely for $\kappa \sim 1/\gamma$. Further we use the definition given by, e.g. Schwinger (1949) or Jackson (1998) to define the critical pulsation of the dominant contribution as

$$\omega_{\text{crit}} = \frac{3}{2} \Omega \gamma^3. \quad (3.141)$$

- As a result, the dominant contribution to the integral comes from the part where $\theta \sim 1/\gamma$. This justifies the earlier expansion of trigonometric functions in θ .

Let us reintroduce the second factor in (3.138). If one assumes the previous result that $\theta \sim \kappa \sim 1/\gamma$ and $x \sim 1$ then the amplitude of the phase is about

$$\frac{\lambda k}{\gamma} = \frac{\hbar \omega}{E} \left(\frac{2B_c}{B} \right)^{1/2}. \quad (3.142)$$

Therefore there is a range of magnetic fields and electron energies (remember that $\omega \sim \omega_{\text{crit}}$) for which this amplitude is small. For example, for a typical pulsar with $B = 10^8$ Teslas, $\gamma = 10^7$ and a dipolar magnetic field with curvature next to the pole of $\rho = 10^4$ m (see e.g. (Arons, 2009)) one has

$$\frac{\lambda \omega_{\text{crit}}/c}{\gamma} \simeq 0.05 \gamma_7^2 \rho_4^{-1} B_8^{-1/2}. \quad (3.143)$$

For now, we can legitimately consider these corrections to be negligible. This amounts to considering that the particle is infinitely confined, $\lambda = 0$, as in the classical theory. We bring back the deconfinement corrections in the next sections.

We proceed to integrate the expressions in the current (3.132). Integration over ϕ simply yields a factor 2π since within our approximation of infinite confinement there is no explicit dependence in ϕ . Integration over x of $x e^{-x^2}$ yields a factor $1/2$.

To integrate over θ , we use the fact that $\sin \theta$ and $\cos \theta$ are slowly varying compared to the exponential for $\theta \gg 1/\gamma$ to develop them to first order in θ . Moreover, we extend the boundaries to infinity since the contributing part is centered on $\theta \ll 1$. We get the two following integrals

$$I_{\cos} = \int_{-\infty}^{+\infty} e^{i\frac{\omega}{2\Omega}\left(\theta\left(\kappa^2 + \frac{1}{\gamma}\right) + \frac{\theta^3}{3}\right)} d\theta, \quad (3.144)$$

$$I_{\sin} = \int_{-\infty}^{+\infty} \theta e^{i\frac{\omega}{2\Omega}\left(\theta\left(\kappa^2 + \frac{1}{\gamma}\right) + \frac{\theta^3}{3}\right)} d\theta, \quad (3.145)$$

and

$$j_{00} = \frac{1}{2\pi} (0, I_{\cos}, I_{\sin}). \quad (3.146)$$

We recognize in (3.144) an Airy integral and its derivative in (3.145). We use in this paper the definitions of special functions of Olver and National Institute of Standards and Technology (U.S.) (2010) where the Airy function is given by

$$\text{Ai}(x) = \frac{1}{2\pi} \int_{-\infty}^{\infty} dt e^{i\left(xt + \frac{t^3}{3}\right)}. \quad (3.147)$$

After performing the change of variable

$$\tilde{\theta} \rightarrow \theta = \left(\frac{\omega}{2\Omega}\right)^{-1/3} \tilde{\theta} \quad (3.148)$$

one identifies $x = (\omega/2\Omega)^{2/3} \left(\kappa^2 + \frac{1}{\gamma^2}\right)$ and obtains

$$I_{\cos} = 2\pi(\omega/2\Omega)^{-1/3} \text{Ai}(x), \quad (3.149)$$

$$I_{\sin} = -2\pi(\omega/2\Omega)^{-2/3} \text{Ai}'(x). \quad (3.150)$$

For practical calculations, the Airy integrals can be changed into modified Bessel functions K_ν

$$K_{1/3}(\xi) = \pi \sqrt{\frac{3}{|x|}} \text{Ai}(x), \quad (3.151)$$

$$K_{2/3}(\xi) = -\pi \frac{\sqrt{3}}{x} \text{Ai}'(x), \quad (3.152)$$

with $\xi = \frac{2}{3} |x|^{3/2}$ and assuming $x > 0$.

We now calculate the intensities. We need to compute the matrix elements (3.122) for both parallel and perpendicular polarizations. We seek a result to the lowest ultrarelativistic order. For this, it is useful to see that owing to the θ factor in (3.145)

$I_{\sin} \sim \frac{1}{\gamma} I_{\cos}$. Further, the polarization vectors (3.135) are expanded to first order in $\kappa \sim 1/\gamma$ such that the squared matrix elements for respectively parallel and perpendicular polarizations are

$$M_{00}^{\parallel 2} = \frac{e^2}{2\epsilon_0 \hbar \omega_k V} I_{\sin}^2, \quad (3.153)$$

$$M_{00}^{\perp 2} = \frac{e^2}{2\epsilon_0 \hbar \omega_k V} \kappa^2 I_{\cos}^2. \quad (3.154)$$

Inserting the above matrix elements in the expression of the intensity (3.125) and expressing I_{\cos} and I_{\sin} with modified Bessel functions one obtains

$$\frac{d^2 I_{00}^{\parallel}}{d\omega d\Omega} = \frac{1}{2\pi\Omega} \frac{e^2 \omega^2}{12\pi^3 \epsilon_0 c} \left(\kappa^2 + \frac{1}{\gamma^2} \right)^2 K_{2/3}^2(\xi), \quad (3.155)$$

$$\frac{d^2 I_{00}^{\perp}}{d\omega d\Omega} = \frac{1}{2\pi\Omega} \frac{e^2 \omega^2}{12\pi^3 \epsilon_0 c} \kappa^2 \left(\kappa^2 + \frac{1}{\gamma^2} \right) K_{1/3}^2(\xi), \quad (3.156)$$

where $\xi = \frac{\omega}{3\Omega} \left| \kappa^2 + \frac{1}{\gamma^2} \right|^{3/2}$. These expressions are identical to expressions found in the classical theory (see e.g. Jackson (1998)).

3.4.4 General calculation of synchro-curvature including quantum corrections

We now generalize the calculation of the previous section to transitions between states of any initial perpendicular quantum number n to a final number n' including quantum corrections up to second order in $\frac{\hbar\omega}{E}$. The need to go to second order is dictated by the occurrence of deconfinement corrections in B_c/B potentially increasing the role of this order for relatively low magnetic fields, as we see in (3.166).

The energy of an ultrarelativistic particle of perpendicular quantum number n is generalized from (3.126) and (3.127) as

$$E = \hbar\Omega l_{\parallel} \left(1 + \frac{1}{2\gamma^2} + \frac{1}{\gamma^2} \frac{B}{B_c} n + \mathcal{O}\left(\frac{1}{\gamma^4}\right) \right). \quad (3.157)$$

For $n > 0$, the perpendicular quantum number is degenerate between the perpendicular angular momentum l_{\perp} and the center-of-trajectory quantum number s since $n = l_{\perp} + s$ (see paper 1). Without loss of generality, we can consider only centered

trajectories with $s = 0$. To energies (3.157) then correspond the proper states found in paper 1 with $n = l_{\perp}$ that we develop here to first ultrarelativistic order in $1/\gamma$,

$$\Psi_n(x, \theta, \phi) = \frac{e^{-\frac{x^2}{2}} x^{n-1} e^{i(n-1)\phi}}{2\pi\sqrt{\Gamma(1+n)}\rho\lambda^2} \quad (3.158)$$

$$\begin{pmatrix} \zeta i x e^{i\phi} \sin \frac{\theta}{2} + \frac{i}{\gamma} \left(\frac{1}{2} \zeta x e^{i\phi} \sin \frac{\theta}{2} - \frac{\zeta-1}{2} n \sqrt{2} \left(\frac{B}{B_c} \right)^{1/2} \cos \frac{\theta}{2} \right) \\ -\zeta x e^{i\phi} \cos \frac{\theta}{2} - \frac{1}{\gamma} \left(\frac{1}{2} \zeta x e^{i\phi} \cos \frac{\theta}{2} + \frac{\zeta-1}{2} n \sqrt{2} \left(\frac{B}{B_c} \right)^{1/2} \sin \frac{\theta}{2} \right) \\ -i \zeta x e^{i\phi} \sin \frac{\theta}{2} + \frac{i}{\gamma} \left(\frac{1}{2} \zeta x e^{i\phi} \sin \frac{\theta}{2} + \frac{1+\zeta}{2} n \sqrt{2} \left(\frac{B}{B_c} \right)^{1/2} \cos \frac{\theta}{2} \right) \\ \zeta x e^{i\phi} \cos \frac{\theta}{2} - \frac{1}{\gamma} \left(\frac{1}{2} \zeta x e^{i\phi} \cos \frac{\theta}{2} - \frac{1+\zeta}{2} n \sqrt{2} \left(\frac{B}{B_c} \right)^{1/2} \sin \frac{\theta}{2} \right) \end{pmatrix}.$$

The parameter $\zeta = \pm 1$ describes the spin orientation and is degenerate with respect to the energy.

We now outline the computation from the transition currents $j_{nn'}$ to the intensities. We assume $n > n'$ without loss of generality. Putting (3.158) in the current (3.123) and projecting onto polarizations (3.135) one obtains the following structure

$$j_{nn'}^{\mu} e_{\mu}^{\sigma} = \zeta \zeta' \int d^3x \sum_{p=n-1-n'}^{n+1-n'} a_p e^{ip\phi} e^{i(l_i-l_f)\theta - i\lambda \vec{k} \cdot \vec{x}} \quad (3.159)$$

where σ denotes parallel or perpendicular polarization and each a_p coefficient is of the form

$$C(\kappa) x^{m_1} e^{-x^2} \cos^{m_2} \theta \sin^{m_3} \theta, \quad (3.160)$$

where C is a coefficient depending only on κ and m_1, m_2, m_3 are positive integers.

In this section we take into account corrections to second order in $\frac{\hbar\omega}{E}$ which leads to express the variation of the quantum number l_{\parallel} as

$$\Delta l_{\parallel} = \frac{\omega}{\Omega} \left\{ 1 + \frac{1}{2\gamma^2} \left[\left(1 + 2n \frac{B}{B_c} \right) \left(1 + \frac{\hbar\omega}{E} \right) - 2 \frac{E}{\hbar\omega} \frac{B}{B_c} \Delta n \right] \right\} + \mathcal{O} \left(\left(\frac{\hbar\omega}{E} \right)^3 \right) \quad (3.161)$$

where $\Delta n = n - n'$. We see that the rightmost exponential factor in (3.159) takes exactly the same form as in (3.138) if we make the replacement $\frac{1}{\gamma^2} \rightarrow \frac{1}{\gamma^2}$ where we define

$$\frac{1}{\gamma^2} = \frac{1}{\gamma^2} \left[\left(1 + 2n \frac{B}{B_c} \right) \left(1 + \frac{\hbar\omega}{E} \right) - 2 \frac{E}{\hbar\omega} \frac{B}{B_c} \Delta n \right] \quad (3.162)$$

Let us detail this effective Lorentz factor a little. The left part corresponds to transitions where the particle remains on the same perpendicular level n , with

$(1 + \hbar\omega/E)$ giving the high-energy quantum recoil correction. If $n = 0$ and we neglect the high-energy correction we therefore recover $1/\gamma^2$ as in the previous section. The second term results from the shift to a different perpendicular level. This term is particularly important for low-energy photons and high magnetic fields. Notice that it can even lead to a negative γ_2 meaning that energy is transferred from the perpendicular excitation of the electron to its longitudinal motion. We can follow the same reasoning as in the previous section [see (3.140) and thereafter] and obtain similar scalings provided one makes the replacement $\gamma \rightarrow \tilde{\gamma}$ with

$$\tilde{\gamma} = \sqrt{|\gamma_2|}, \quad (3.163)$$

then

$$\kappa \sim \theta \sim 1/\tilde{\gamma}, \quad (3.164)$$

and the critical pulsation

$$\tilde{\omega}_{\text{crit}} = \frac{3}{2}\Omega\tilde{\gamma}^3. \quad (3.165)$$

We proceed to integrate over ϕ . To obtain the relevant high-energy accuracy to second order one separates the imaginary exponential in (3.159) as in (3.138) and notices that, similarly to (3.142), its argument is of order

$$x \frac{\lambda k}{\tilde{\gamma}} \sim \sqrt{n} \frac{\gamma}{\tilde{\gamma}} \frac{\hbar\omega}{E} \left(\frac{2B_c}{B} \right)^{1/2}, \quad (3.166)$$

where we used the fact that the averaged normalized radial distance of an electron is $\sim \sqrt{n}$ as explained in paper 1. Assuming (3.166) is small compared to 1, we expand the second factor of (3.138) to second order in the argument $-ix\lambda k (\cos \phi \sin \kappa + \sin \phi \cos \kappa \sin \theta)$. We are left to integrate terms of the form

$$A_{pq} = \int_{-\pi}^{\pi} d\phi e^{ip\phi} (a \cos \phi + b \sin \phi)^q \quad (3.167)$$

where p and q are integers and $q \geq 0$, a and b can have any value independent of ϕ . One can show that

$$A_{pq} = 0 \quad \text{if} \quad \begin{cases} q < |p| \\ \text{or} \\ q - |p| \text{ odd} \end{cases}. \quad (3.168)$$

For this reason, the only transitions yielding terms of order lower or equal to $\left(\frac{\hbar\omega}{E}\right)^2$ once current (3.123) is inserted in the squared matrix element (3.122) are for $n = n'$, $n' = n - 1$ and $n' = n - 2$. Moreover, one can see that the next non-null term

of the expansion of (3.140) is of order $\left(\frac{\hbar\omega}{E}\right)^4$, pushing further the validity of our approximation. In practice, we need

$$A_{pq} = \begin{cases} \pi(a + ib) & p = -1 & q = 1 \\ \pi(a^2 + b^2) & p = 0 & q = 2 \\ \pi(a - ib) & p = 1 & q = 1 \\ \frac{\pi}{2}(a + ib)^2 & p = 2 & q = 2 \end{cases}. \quad (3.169)$$

We then integrate over x with only integrals of the type

$$\int_0^\infty dx e^{-x^2} x^{2p+1} = \frac{p!}{2}, \quad (3.170)$$

where p is a positive integer.

We are now left with integrals over θ of the type

$$B_{pq} = \int_{-\pi}^{\pi} d\theta e^{i\frac{\omega}{2\Omega}\left(\left(\kappa^2 + \frac{1}{\gamma_2}\right)\theta + \frac{\theta^3}{3}\right)} \cos^p \theta \sin^q \theta \quad (3.171)$$

where p, q are positive integers. As in the previous section, the smallness of contributing values of $\theta \sim 1/\tilde{\gamma}$ allows to extend boundaries to infinity. Moreover, to leading ultrarelativistic order one has

$$\forall(p, q), B_{pq} = \int_{-\infty}^{\infty} d\theta e^{i\frac{\omega}{2\Omega}\left(\left(\kappa^2 + \frac{1}{\gamma_2}\right)\theta + \frac{\theta^3}{3}\right)} \theta^q. \quad (3.172)$$

Using definition (3.147) one sees that B_{pq} is proportional to the q th derivative of the Airy function. Recalling that the Airy function verifies the relation (Olver and National Institute of Standards and Technology (U.S.), 2010)

$$\text{Ai}''(x) = x\text{Ai}(x) \quad (3.173)$$

one is able to express every B_{pq} in terms of Ai and Ai' , and from that in terms of I_{\cos} and I_{\sin} [(3.144), and (3.145)]. In particular, we need the following expressions

$$B_{p2} = -\left(\kappa^2 + \frac{1}{\gamma_2}\right) I_{\cos}, \quad (3.174)$$

$$B_{p3} = \frac{1}{\tilde{\gamma}^3} \frac{4\tilde{\omega}_{\text{crit}}}{3\omega} I_{\cos} - \left(\kappa^2 + \frac{1}{\gamma_2}\right) I_{\sin}, \quad (3.175)$$

where the replacement $1/\tilde{\gamma}^2 \rightarrow 1/\gamma_2$ is assumed in I_{\cos} and I_{\sin} .

Squaring (3.159), inserting it into the matrix element (3.122) and using formula (3.125) we obtain all the relevant intensities to order $\left(\frac{\hbar\omega}{E}\right)^2$. These intensities are proportional to $(\zeta\zeta')^2$ and therefore the spin average $\frac{1}{2}\sum_{\zeta,\zeta'=\pm 1}$ is immediate, giving

$$\frac{d^2 I_{nn}^{\parallel}}{d\omega d\omega} = \frac{1}{2\pi\Omega} \frac{e^2\omega^2}{16\pi^3\epsilon_0 c} \left[I_{\sin}^2 + \frac{B_c}{B} \left(\frac{\hbar\omega}{E}\right)^2 \frac{\gamma^2}{\gamma_2} (n+1) \left(I_{\sin}^2 - \frac{4}{3} \frac{\tilde{\omega}_{\text{crit}}}{\omega} \frac{I_{\cos}}{\tilde{\gamma}} I_{\sin} \right) + \left(\frac{\hbar\omega}{E}\right)^2 n^2 \kappa^2 I_{\cos}^2 \right], \quad (3.176)$$

$$\frac{d^2 I_{nn}^{\perp}}{d\omega d\omega} = \frac{1}{2\pi\Omega} \frac{e^2\omega^2}{16\pi^3\epsilon_0 c} \left[\kappa^2 I_{\cos}^2 + \frac{B_c}{B} \left(\frac{\hbar\omega}{E}\right)^2 \frac{\gamma^2}{\gamma_2} (n+1) \kappa^2 I_{\cos}^2 + \left(\frac{\hbar\omega}{E}\right)^2 n^2 I_{\sin}^2 \right], \quad (3.177)$$

$$\begin{aligned} \frac{d^2 I_{nn-1}^{\parallel}}{d\omega d\omega} &= \frac{1}{2\pi\Omega} \frac{e^2\omega^2}{16\pi^3\epsilon_0 c} \left[\frac{B}{B_c} \frac{n}{2} \frac{I_{\cos}^2}{\gamma^2} + \frac{\hbar\omega}{E} n \left(\frac{1}{\gamma_2} + \kappa^2 \right) I_{\cos}^2 + \right. \\ &\quad \left. \frac{B_c}{B} \left(\frac{\hbar\omega}{E}\right)^2 \frac{n}{2} \left(\gamma^2 \kappa^2 I_{\sin}^2 + \gamma^2 \left(\frac{1}{\gamma_2} + \kappa^2 \right)^2 I_{\cos}^2 \right) + \right. \\ &\quad \left. \left(\frac{\hbar\omega}{E}\right)^2 \frac{n^2}{4} \left(\frac{2}{\gamma_2} - \kappa^2 \frac{n-1}{n} \right) I_{\cos}^2 \right], \end{aligned} \quad (3.178)$$

$$\begin{aligned} \frac{d^2 I_{nn-1}^{\perp}}{d\omega d\omega} &= \frac{1}{2\pi\Omega} \frac{e^2\omega^2}{16\pi^3\epsilon_0 c} \left[\frac{B}{B_c} \frac{n}{2} \frac{I_{\cos}^2}{\gamma^2} - \frac{\hbar\omega}{E} n \kappa^2 I_{\cos}^2 + \right. \\ &\quad \left. \frac{B_c}{B} \left(\frac{\hbar\omega}{E}\right)^2 \frac{n}{2} \gamma^2 \kappa^2 \left(I_{\sin}^2 + \kappa^2 I_{\cos}^2 \right) + \right. \\ &\quad \left. \left(\frac{\hbar\omega}{E}\right)^2 \frac{n^2}{4} \left(\frac{2}{\gamma_2} + \frac{n-1}{n} \kappa^2 \right) I_{\cos}^2 \right], \end{aligned} \quad (3.179)$$

$$\frac{d^2 I_{nn-2}^{\parallel}}{d\omega d\omega} = \frac{1}{2\pi\Omega} \frac{e^2\omega^2}{16\pi^3\epsilon_0 c} \left[\left(\frac{\hbar\omega}{E}\right)^2 \frac{n(n-1)}{4} \left(I_{\sin}^2 + \kappa^2 I_{\cos}^2 \right) \right], \quad (3.180)$$

$$\frac{d^2 I_{nn-2}^{\perp}}{d\omega d\omega} = \frac{1}{2\pi\Omega} \frac{e^2\omega^2}{16\pi^3\epsilon_0 c} \left[\left(\frac{\hbar\omega}{E}\right)^2 \frac{n(n-1)}{4} I_{\sin}^2 \right]. \quad (3.181)$$

Our result is based on the following hierarchy of scales

$$\frac{1}{\gamma} \ll \sqrt{n} \frac{\gamma}{\tilde{\gamma}} \frac{\hbar\omega}{E} \left(\frac{2B_c}{B} \right)^{1/2} < 1 \text{ and } \frac{1}{\gamma} \ll \frac{B}{B_c}. \quad (3.182)$$

This allows to consider that all the gamma parameters have roughly the same order of magnitude compared to other terms $1/\tilde{\gamma}^2 \sim 1/\gamma_2 \sim 1/\gamma^2$. All terms are of second ultrarelativistic order since $I_{\sin} \sim I_{\cos}/\tilde{\gamma}$ and $\kappa^2 \sim 1/\tilde{\gamma}^2$. One notices that this is not a strict expansion in powers of $\frac{\hbar\omega}{E}$ and $\frac{B}{B_c}$, since $\tilde{\gamma}$ also contains such terms. It would even be impossible to perform a total, rapidly converging expansion of I_{\sin}, I_{\cos} with

respect to $\frac{B}{B_c}$ since it is not necessarily small. However, the present expansion is relatively compact and directly reflects the confinement corrections as explained in (3.142) and (3.166).

One recognizes the classical curvature intensities derived in the previous section, (3.155) and (3.156), as the first terms of (3.176) and (3.177) respectively.

3.4.5 Power spectrum

We proceed to integrate expressions (3.176)-(3.181) over the solid angle $d\omega$ which can be written explicitly as

$$d\omega = \cos \kappa d\kappa d\chi \quad (3.183)$$

where χ is an angle around the main circle. Integration of χ is trivial and yields a factor of 2π . Integration over κ requires more care. Applying the change of variable (3.148) we express all the relevant integrals over κ of (3.176)-(3.181) in terms of the integrals calculated in appendix 3.E $I_a(\xi)$, $I_b(\xi)$, $I_c(\xi)$, $I_d(\xi)$, $I_e(\xi)$ and $I_f(\xi)$

$$\int_{-\infty}^{\infty} I_{\sin}^2 d\kappa = \frac{\pi}{\sqrt{3}\tilde{\gamma}^2} \frac{2\Omega}{\omega} I_a(\xi), \quad (3.184)$$

$$\int_{-\infty}^{\infty} I_{\cos}^2 d\kappa = \frac{2\pi}{\sqrt{3}} \frac{2\Omega}{\omega} I_b(\xi), \quad (3.185)$$

$$\int_{-\infty}^{\infty} \kappa^2 I_{\cos}^2 d\kappa = \frac{\pi}{\sqrt{3}\tilde{\gamma}^2} \frac{2\Omega}{\omega} I_c(\xi), \quad (3.186)$$

$$\int_{-\infty}^{\infty} I_{\cos} I_{\sin} d\kappa = \frac{\pi}{\sqrt{3}\tilde{\gamma}} \frac{2\Omega}{\omega} I_d(\xi), \quad (3.187)$$

$$\int_{-\infty}^{\infty} \kappa^2 I_{\sin}^2 d\kappa = \frac{\pi}{4\sqrt{3}\tilde{\gamma}^4} \frac{2\Omega}{\omega} I_e(\xi), \quad (3.188)$$

$$\int_{-\infty}^{\infty} \kappa^4 I_{\cos}^2 d\kappa = \frac{\pi\sqrt{3}}{4\tilde{\gamma}^4} \frac{2\Omega}{\omega} I_f(\xi). \quad (3.189)$$

where we define

$$\xi = \frac{\omega}{\tilde{\omega}_{\text{crit}}}. \quad (3.190)$$

The values of the previous integrals are summarized here by

$$I_a(\xi) = \begin{cases} \int_{\xi}^{\infty} K_{5/3}(x) dx + K_{2/3}(\xi) & \gamma_2 > 0 \\ \pi\sqrt{3} - \int_{\xi}^{\infty} dx F_{1/3}(x, \gamma_2) - 3F_{2/3}(\xi, \gamma_2) & \gamma_2 < 0 \end{cases}, \quad (3.191)$$

$$I_b(\xi) = \begin{cases} \int_{\xi}^{\infty} K_{1/3}(x)dx & \gamma_2 > 0 \\ \pi\sqrt{3} - \int_{\xi}^{\infty} dx F_{1/3}(x, \gamma_2) & \gamma_2 < 0 \end{cases}, \quad (3.192)$$

$$I_c(\xi) = \begin{cases} \int_{\xi}^{\infty} K_{5/3}(x)dx - K_{2/3}(\xi) & \gamma_2 > 0 \\ \pi\sqrt{3} - \int_{\xi}^{\infty} dx F_{1/3}(x, \gamma_2) - & \gamma_2 < 0 \\ F_{2/3}(\xi, \gamma_2) & \end{cases}, \quad (3.193)$$

$$I_d(\xi) = -4\pi\sqrt{3}^3 \sqrt{\frac{4}{3\xi}} \int_{-\infty}^{\infty} dx \text{Ai}(x^2 + c) \text{Ai}'(x^2 + c), \quad (3.194)$$

$$I_e(\xi) = \frac{10}{3\xi} F_{1/3}(\xi, \gamma_2) + \begin{cases} \int_{\xi}^{+\infty} dx F_{1/3}(x, \gamma_2) - F_{2/3}(\xi, \gamma_2) & \gamma_2 > 0 \\ \pi\sqrt{3} - \int_{\xi}^{+\infty} dx F_{1/3}(x, \gamma_2) - F_{2/3}(\xi, \gamma_2) & \gamma_2 < 0 \end{cases}, \quad (3.195)$$

$$I_f(\xi) = \frac{2}{3\xi} F_{1/3}(\xi, \gamma_2) + \begin{cases} \int_{\xi}^{+\infty} dx F_{1/3}(x, \gamma_2) - F_{2/3}(\xi, \gamma_2) & \gamma_2 > 0 \\ \pi\sqrt{3} - \int_{\xi}^{+\infty} dx F_{1/3}(x, \gamma_2) - F_{2/3}(\xi, \gamma_2) & \gamma_2 < 0 \end{cases}. \quad (3.196)$$

Among these, only I_d could not be turned into a more convenient analytical form. Therefore we give here only its raw expression. The F functions are defined as follows

$$F_{1/3}(\xi, s) = \begin{cases} K_{1/3}(\xi) & , s > 0 \\ \frac{\pi}{\sqrt{3}} (J_{1/3}(\xi) + J_{-1/3}(\xi)) & , s < 0 \end{cases}, \quad (3.197)$$

$$F_{2/3}(\xi, s) = \begin{cases} K_{2/3}(\xi) & , s > 0 \\ \frac{\pi}{\sqrt{3}} (J_{2/3}(\xi) - J_{-2/3}(\xi)) & , s < 0 \end{cases}.$$

Performing replacements (3.184)-(3.189) we obtain the spectra per unit pulsation

$$\begin{aligned} \frac{dI_{nn}^{\parallel}}{d\omega} &= \frac{1}{2\pi\Omega} \frac{e^2\Omega\omega}{\tilde{\gamma}^2\sqrt{3}4\pi\epsilon_0c} [I_a(\xi) + \\ &\frac{B_c}{B} \left(\frac{\hbar\omega}{E}\right)^2 \frac{\gamma^2}{\gamma_2} (n+1) \left(I_a(\xi) - \frac{4\tilde{\omega}_{\text{crit}}}{3\omega} I_d(\xi)\right) + \\ &\left(\frac{\hbar\omega}{E}\right)^2 n^2 I_c(\xi)], \end{aligned} \quad (3.198)$$

$$\begin{aligned} \frac{dI_{nn}^{\perp}}{d\omega} &= \frac{1}{2\pi\Omega} \frac{e^2\Omega\omega}{\tilde{\gamma}^2\sqrt{3}4\pi\epsilon_0c} \left[I_c(\xi) + \frac{B_c}{B} \left(\frac{\hbar\omega}{E}\right)^2 \frac{\gamma^2}{\gamma_2} (n+1) I_c(\xi) + \right. \\ &\left. \left(\frac{\hbar\omega}{E}\right)^2 n^2 I_a(\xi) \right], \end{aligned} \quad (3.199)$$

$$\begin{aligned} \frac{dI_{nn-1}^{\parallel}}{d\omega} &= \frac{1}{2\pi\Omega} \frac{e^2\Omega\omega}{\tilde{\gamma}^2\sqrt{3}4\pi\epsilon_0c} \left[\frac{B}{B_c} n \frac{\tilde{\gamma}^2}{\gamma^2} I_b(\xi) + \frac{\hbar\omega}{E} n \left(2 \frac{\tilde{\gamma}^2}{\gamma_2} I_b(\xi) + I_c(\xi) \right) + \right. \\ &\frac{B_c}{B} \left(\frac{\hbar\omega}{E}\right)^2 \frac{n}{2} \left(\frac{\gamma^2}{4\tilde{\gamma}^2} I_e(\xi) + 2 \frac{\gamma^2}{\tilde{\gamma}^2} I_b(\xi) + 2 \frac{\gamma^2}{\gamma_2} I_c(\xi) + \frac{3}{4} \frac{\gamma^2}{\tilde{\gamma}^2} I_f(\xi) \right) + \\ &\left. \left(\frac{\hbar\omega}{E}\right)^2 \frac{n^2}{4} \left(4 \frac{\tilde{\gamma}^2}{\gamma_2} I_b(\xi) - \frac{n-1}{n} I_c(\xi) \right) \right], \end{aligned} \quad (3.200)$$

$$\begin{aligned} \frac{dI_{nn-1}^{\perp}}{d\omega} &= \frac{1}{2\pi\Omega} \frac{e^2\Omega\omega}{\tilde{\gamma}^2\sqrt{3}4\pi\epsilon_0c} \left[\frac{B}{B_c} n \frac{\tilde{\gamma}^2}{\gamma^2} I_b(\xi) - \frac{\hbar\omega}{E} n I_c(\xi) + \right. \\ &\frac{B_c}{B} \left(\frac{\hbar\omega}{E}\right)^2 \frac{n}{8} \frac{\gamma^2}{\tilde{\gamma}^2} (I_e(\xi) + 3I_f(\xi)) + \\ &\left. \left(\frac{\hbar\omega}{E}\right)^2 \frac{n^2}{4} \left(4 \frac{\tilde{\gamma}^2}{\gamma_2} I_b(\xi) + \frac{n-1}{n} I_c(\xi) \right) \right], \end{aligned} \quad (3.201)$$

$$\frac{dI_{nn-2}^{\parallel}}{d\omega} = \frac{1}{2\pi\Omega} \frac{e^2\Omega\omega}{\tilde{\gamma}^2\sqrt{3}4\pi\epsilon_0c} \left[\left(\frac{\hbar\omega}{E}\right)^2 \frac{n(n-1)}{4} (I_a(\xi) + I_c(\xi)) \right], \quad (3.202)$$

$$\frac{dI_{nn-2}^{\perp}}{d\omega} = \frac{1}{2\pi\Omega} \frac{e^2\Omega\omega}{\tilde{\gamma}^2\sqrt{3}4\pi\epsilon_0c} \left[\left(\frac{\hbar\omega}{E}\right)^2 \frac{n(n-1)}{4} I_a(\xi) \right]. \quad (3.203)$$

To have an estimate of the position of the peak of these spectra, following the arguments of the two previous sections one can take the critical pulsation without quantum correction for the $n \rightarrow n$ transitions, that is

$$\omega_c = \Omega \frac{\gamma^2}{1 + 2nB/B_c}. \quad (3.204)$$

However, the other transitions cannot be treated exactly with the same arguments as in section 3.4.3, (3.141) owing to the fact that the factor γ_2 becomes infinite at a pulsation

$$\omega_0 = \frac{E}{\hbar} \frac{2\Delta n B/B_c}{1 + 2nB/B_c} + \mathcal{O}\left(\frac{\hbar\omega}{E}\right). \quad (3.205)$$

If we restrict our reasoning to positive γ_2 , or equivalently $\omega > \omega_0$, one can then show that the position of the peak of the spectra given above can be estimated to be

$$\omega_p \sim \max(\omega_c, \omega_0). \quad (3.206)$$

3.4.6 Discussion and conclusion

In section 3.4.3 we showed that classical curvature radiation can be derived from first principles of quantum electrodynamics in a self-consistent manner within the ultrarelativistic approximation. Indeed, the usual derivation of curvature radiation assumes the limit of an unphysical trajectory, as mentioned in the introduction of the present paper and in Voisin et al. (2016). Curvature radiation then results from transitions between states of different longitudinal quantum numbers l_{\parallel} but both in the ground perpendicular level. The assumed ultrarelativistic regime allows us to consider l_{\parallel} as a continuous variable and obtain a continuous spectrum. Perpendicular levels are the quantum analogues of classical rotation around the magnetic field. In the perpendicular ground level, or perpendicular fundamental, we showed in paper 1 that although orbital angular momentum around the field line is null, the particle is maintained on the field line through spin-magnetic-field interaction. Therefore, curvature radiation understood as the radiation of a particle following a magnetic-field line without "turning" around it should be seen as a purely quantum phenomenon. However, this is not enough to obtain the classical result: one has to consider that the particle wave-function is infinitely confined on the magnetic-field line, which is equivalently achieved by assuming $\hbar \rightarrow 0$, obviously the classical limit, or that the magnetic field intensity $B \rightarrow \infty$ in (3.142), and to neglect the quantum recoil effect in (3.137) by assuming that the emitted photon energy $\hbar\omega \ll E$, where E is the energy of the radiating particle .

In section 3.4.4, we consider the general case of synchro-curvature radiation in the regime of very low pitch angle, so low that the perpendicular energy of the particle must be quantified. This is, to our knowledge, the first time such a derivation has been made. Therefore, the radiation becomes the sum of continuous transitions of l_{\parallel} and discrete transitions between perpendicular levels labeled by the integer n . Moreover, we take into account deconfinement and quantum recoil effects up to second order. We show that in the ultrarelativistic regime, transitions involving a change of perpendicular quantum number are significant only for $n \rightarrow n - 1$ and $n \rightarrow n - 2$ with a decreasing importance as the jump is larger. Transitions $n \rightarrow n$ are the generalization of curvature radiation on an arbitrary level n from which they differ by an effective Lorentz factor (3.163) and an amplified proportional weight of deconfinement terms (because they are proportional to n or n^2). The two

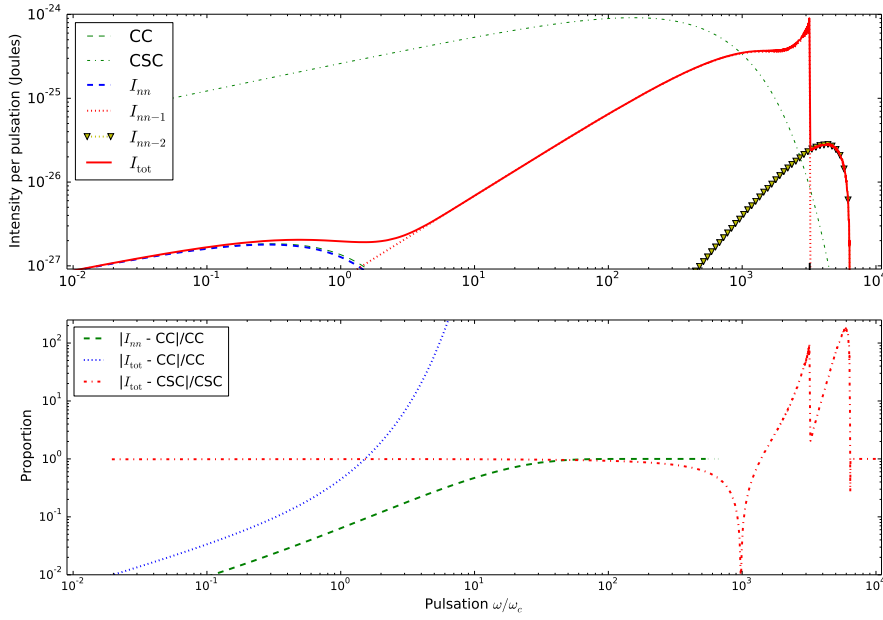


Fig. 3.5.: Upper panel: Intensities radiated by an electron following a magnetic field of radius of curvature $4 \cdot 10^4$ m, intensity 10^6 Teslas, at a Lorentz factor $\gamma = 10^5$, on a perpendicular level $n = 100$. For comparison, classical curvature (CC) and classical synchro-curvature (CSC, formula of Viganò et al. (2015b)) radiation are plotted in dashed green and dot-dashed green respectively. The thicker lines are showing plots of formulas (3.198)-(3.203) summed over photon polarizations, respectively the curvature component I_{nn} in the dashed blue, the first downward component I_{nn-1} in dotted red and the second downward component in dotted yellow with trident markers in yellow. The sum of these three components I_{tot} is plotted in plain red. Abscissa are scaled by the pulsation ω_c (3.204) and the thick ticks on lower axes show the position of the peak pulsation ω_p (3.205) of the downward components. The lower panel shows the relative differences between the curvature component I_{nn} and CC in dashed green (not represented on the full range because these components are getting numerically too small at high pulsations), the sum of all components I_{tot} and CC in dotted blue, I_{tot} and CSC in dot-dashed red. One sees that, in this case, the three peaks due to the curvature, first downward component and second downward component are distinct in the total spectrum, which corresponds well to CC at low pulsations and bridges the gap to CSC at high pulsations. However, it should be noted that the difference between the total spectrum and CSC is roughly around 100% of CSC everywhere.

other transitions can be considered as the synchrotron part of synchro-curvature radiation.

At leading order, $n \rightarrow n$ transitions have the same polarization as the classical curvature radiation, $n \rightarrow n - 1$ transitions are not polarized at all, and $n \rightarrow n - 2$ has a ratio between parallel and perpendicular polarization of $1 + I_c(\xi)/I_a(\xi)$.

It is out of the scope of this paper to proceed to a general exploration of the spectra generated by our final formulae (3.198)-(3.203) depending on magnetic field B/B_c , curvature radius ρ , Lorentz factor γ and perpendicular level n . However we show in figure 3.5 a case with parameters compatible with a polar cap of recycled millisecond pulsar (Arons, 2009), $B = 10^6$ Teslas, $\rho = 4 \cdot 10^4$ meters, a moderate Lorentz factor of 10^5 , and a perpendicular level $n = 100$. These parameters fall within our approximations given in (3.182) and paper 1 equation 19. On the upper panel of figure 3.5 we plot the curvature component I_{nn} (to make notations lighter we remove here the $\frac{d}{d\omega}$) in dashed blue, I_{nn-1} in dotted red and I_{nn-2} in dotted down-triangle yellow. In order to compare we also plotted classical curvature radiation (CC) in dashed green and classical synchro-curvature radiation (CSC) in dot-dashed green. The pitch angle α is related to n by

$$\alpha = \frac{\sqrt{2nB/B_c}}{\gamma}, \quad (3.207)$$

and here $\alpha \simeq 2 \cdot 10^{-6}$. This value is quite easily reached in simulations of motion of an electron with classical-synchro-curvature-radiation losses in pulsarlike magnetic fields in Viganò et al. (2015b) or Kelner et al. (2015).

If one neglects radiation losses, or more physically that the particle remains for a while at levels around $n \sim 100$, then one can compare the sum of the intensities of the three above mentioned transitions $I_{\text{tot}} = I_{nn} + I_{nn-1} + I_{nn-2}$ (figure 3.5, upper panel) with the intensity of the classical curvature radiation (figure 3.5, lower panel) and with the intensity of the classical synchro-curvature radiation (figure 3.5, lower panel) .

Until the peak of CC radiation, I_{nn} and CC are very close with a difference of a few percents and up to 10 percent, after which the difference mostly due to deconfinement terms (that grows with photon energy) reaches more than 100% at high energies. One obtains a similar deviation in the fundamental curvature regime, $n = 0$, but with a slightly higher Lorentz factor.

Transitions to lower perpendicular levels become important at high energies, taking over the vanishing I_{nn} component in I_{tot} they get quite close to the high-energy part of the CSC spectrum. Slight wiggles on the ascending parts of spectra I_{nn-1}

and I_{nn-2} make the line a little bit thicker on this graph around ω_0 (thick black tick) and are due to the fact that $\gamma_2 < 0$ (see (3.162)) at low photon pulsations and therefore these spectra are expressed by oscillatory Bessel functions in virtue of (3.191)-(3.196) below their peak pulsations (see the discussion around (3.206)). In particular, it is responsible in the present case for the very sharp peak and cutoff of I_{nn-1} . Spectrum I_{nn-2} takes over just above ω_0 and is responsible for the last maximum.

As a result, the total intensity I_{tot} is very close to CC radiation at low photon energies and becomes comparatively closer to CSC radiation at the highest energies. Although we see on the lower panel that the CSC spectrum is quasislways $\sim 100\%$ or more more intense than I_{tot} , this agrees with the general tendency in the classical theory of synchro-curvature radiation to show broader spectra at high energies compared to curvature radiation while tending to the curvature spectrum at lower energies, see e.g. Kelner et al. (2015). We also notice that this transition of behavior between quasicurvature and synchro-curvature is much sharper in the quantum theory in the case of figure 3.5. The sharpness of this transition depends on the difference between ω_c and ω_0 : if $\omega_0 \gg \omega_c$ as is the case on figure 3.5 the downward components have more "time" to grow before they cut off, on the contrary if $\omega_0 < \omega_c$ or $\omega_0 \sim \omega_c$ the transition is much smoother or even insignificant and the spectrum resembles closely the classical curvature spectrum CC.

More generally, it comes out of equations (3.198)-(3.203) that the $n - 1$ and $n - 2$ components are increasing with the intensity of the magnetic field and with the perpendicular level n . The Lorentz factor has a significant impact on the relative importance of the deconfinement terms since their relative importance to the main term grows like $(\hbar\omega_{\text{crit}}/E)^p \sim \gamma^{2p}$ where $p = 1, 2$. In the case of terms going like $\propto B_c/B$, this can even lead them to become dominant at low magnetic field and high Lorentz factors. However, in this case one falls under the limitation of (3.182) and our approximation starts to fail, needing computation of higher order terms.

It is to be noticed that perpendicular upward transitions, from $n - 1$ and $n - 2$ to n are also possible. As mentioned, the only difference between upward and downward transitions is in the effective Lorentz factor (3.166). The probability of upward transition is generally lower than the downward transitions because the effective Lorentz factor is lower. However, for very high Lorentz factors this difference becomes smaller. Because of the necessity of high Lorentz factors, the range of parameters where significant upwards rates can be computed safely is quite narrow (see (3.166) and approximation 19 in paper 1). In the case of figure 3.5, the upward spectra are not represented because they are numerically 0. However, we can speculate on other configurations. First we can speculate beyond our approximations: our scheme remains convergent even outside the validity region, the results keep

the same qualitative behavior as shown above, and approximation 19 of paper 1 is regularly overcome in classical calculations (see paper 1). For example, an electron with Lorentz factor of $6.3 \cdot 10^6$ (reasonable in a pulsar magnetosphere gap) on the perpendicular level $n = 100$ with a magnetic field of 10^6 Teslas and a radius of curvature of 10^4 m yields in this formalism a ratio of 0.6 between the first upward and first downward components. This last example suggests that the decay to the perpendicular fundamental may be slow and not monotonous if the Lorentz factor of the particle is high enough, and that a computation of the total radiated spectrum may need to take into account the random perpendicular jumps along the trajectory. This would especially be important due to the smallness of neutron star magnetospheres.

The particular case where we deal with a jump between the perpendicular fundamental and the first excited level can also be seen as the lowest spin-flip transition possible, in the sense that the perpendicular fundamental is the only state having a nondegenerate spin state and the only way to flip the spin is therefore to go to the first level (see paper 1). This is what we called spin-flip curvature radiation in a preliminary work (Voisin et al., 2017a).

3.A Toroidal coordinates toolbox

The toroidal coordinates are defined by the following diffeomorphism T

$$T : \begin{pmatrix} r \\ \theta \\ \phi \end{pmatrix} \rightarrow \begin{pmatrix} x \\ y \\ z \end{pmatrix} = \begin{pmatrix} r \cos \phi \\ \cos \theta (\rho + r \sin \phi) \\ \sin \theta (\rho + r \sin \phi) \end{pmatrix}, \quad (3.208)$$

such that surfaces of constant r are torii centered on the circle of radius $\rho > 0$.

The primed quantities denote quantities in the basis $\left(\frac{\partial T}{\partial r}, \frac{\partial T}{\partial \theta}, \frac{\partial T}{\partial \phi}\right)$.

Jacobian

The Jacobian of this coordinate system is

$$J_T = \begin{pmatrix} \cos \phi & 0 & -r \sin \phi \\ \cos \theta \sin \phi & -\sin \theta (\rho + r \sin \phi) & r \cos \theta \cos \phi \\ \sin \theta \sin \phi & \cos \theta (\rho + r \sin \phi) & r \sin \theta \cos \phi \end{pmatrix}, \quad (3.209)$$

with determinant $\det J_T = -r(\rho + r \sin \phi)$, and inverse

$$J_T^{-1} = \begin{pmatrix} \cos \phi & \cos \theta \sin \phi & \sin \theta \sin \phi \\ 0 & -\frac{\sin \theta}{\rho + r \sin \phi} & \frac{\cos \theta}{\rho + r \sin \phi} \\ -\frac{\sin \phi}{r} & \frac{\cos \theta \cos \phi}{r} & \frac{\sin \theta \cos \phi}{r} \end{pmatrix}. \quad (3.210)$$

Transformation of covariant quantities

Covariant quantities transform like $A_i \rightarrow A'_i$

$$A' = {}^t J_T A \Leftrightarrow A'_i = (J_T)_{ji} A_j, \quad (3.211)$$

$$A = {}^t (J_T^{-1}) A' \Leftrightarrow A_i = (J_T^{-1})_{ji} A'_j. \quad (3.212)$$

Here is an example with the derivation operators ,

$$\partial_x = \cos \phi \partial_r - \frac{\sin \phi}{r} \partial_\phi, \quad (3.213)$$

$$\partial_y = \cos \theta \sin \phi \partial_r - \frac{\sin \theta}{\rho + r \sin \phi} \partial_\theta + \frac{\cos \theta \cos \phi}{r} \partial_\phi, \quad (3.214)$$

$$\partial_z = \sin \theta \sin \phi \partial_r + \frac{\cos \theta}{\rho + r \sin \phi} \partial_\theta + \frac{\sin \theta \cos \phi}{r} \partial_\phi. \quad (3.215)$$

The Minkowski metric $\eta = (1, -1, -1, -1)$ transforms according to

$$M_T = \begin{pmatrix} 1 & 0 \\ 0 & J_T \end{pmatrix}, \quad (3.216)$$

which gives

$$\eta_T = {}^t M_T g_E M_T = \begin{pmatrix} 1 & 0 & 0 & 0 \\ 0 & -1 & 0 & 0 \\ 0 & 0 & -(\rho + r \sin \phi)^2 & 0 \\ 0 & 0 & 0 & -r^2 \end{pmatrix}. \quad (3.217)$$

Transformation of contravariant quantities

Contravariant quantities transform like $A^i \rightarrow A'^i$

$$A' = J_T^{-1} A \Leftrightarrow A'^i = (J_T^{-1})_{ij} A^j, \quad (3.218)$$

$$A = J_T A' \Leftrightarrow A^i = (J_T)_{ij} A'^j. \quad (3.219)$$

This is the case for example of the magnetic potential or of the Dirac matrices α (which are not really contravariant but we use this type of transformation in the text).

In particular,

$$\alpha^r = \cos \phi \alpha^x + \cos \theta \sin \phi \alpha^y + \sin \theta \sin \phi \alpha^z, \quad (3.220)$$

$$\alpha^\theta = \frac{1}{\rho + r \sin \phi} (-\sin \theta \alpha^y + \cos \theta \alpha^z), \quad (3.221)$$

$$\alpha^\phi = -\frac{\sin \phi}{r} \alpha^x + \frac{\cos \theta \cos \phi}{r} \alpha^y + \frac{\sin \theta \cos \phi}{r} \alpha^z. \quad (3.222)$$

Transformation of differential operators

Laplacian

The Laplacian is needed for the kinetic part of the second order Dirac equation,

$$\begin{aligned} \nabla_T^2 = & \frac{1}{r|\rho+r\sin\phi|} (\partial_r (r|\rho+r\sin\phi| \partial_r) + \\ & \partial_\theta \left(\frac{r}{|\rho+r\sin\phi|} \partial_\theta \right) + \partial_\phi \left(\frac{|\rho+r\sin\phi|}{r} \partial_\phi \right)) \end{aligned} \quad (3.223)$$

Practically, we always have $\rho + r \sin \phi > 0$ in this paper.

Divergence

The divergence can be used to derive the second order Dirac equation and is given by

$$\begin{aligned} \nabla_T \cdot A' = & \frac{1}{|r(\rho+r\sin\phi)|} (\partial_r (|r(\rho+r\sin\phi)| A'^r) + \\ & \partial_\theta (|r(\rho+r\sin\phi)| A'^\theta) + \\ & \partial_\phi (|r(\rho+r\sin\phi)| A'^\phi)). \end{aligned} \quad (3.224)$$

Rotational of covariant components

We need the rotational of the magnetic covariant vector which gives the magnetic field

$$B^{x'} = (\nabla_T \wedge (A'_i))^{x'}, \quad (3.225)$$

which explicitly reads

$$\begin{aligned} B^r &= - \left(-\frac{|\rho+r \sin \phi|}{r} \partial_\phi + 2 \sin \phi \right) A^\theta + \\ &\quad \frac{r}{|\rho+r \sin \phi|} \partial_\theta A^\phi, \\ B^\theta &= -\frac{1}{|\rho+r \sin \phi|} \left(\frac{1}{r} \partial_\phi A^r - (2 + r \partial_r) A^\phi \right), \\ B^\phi &= -\frac{1}{r|\rho+r \sin \phi|} \left(-\partial_\theta A^r + \right. \\ &\quad \left. \left(2 \cos \phi |\rho + r \sin \phi| + |\rho + r \sin \phi|^2 \partial_r \right) A^\theta \right). \end{aligned} \quad (3.226)$$

3.B Dirac equation in toroidal coordinates

Greek indices are used for Minkowski space-time of metric signature $(+ - - -)$ while latin indices are used for the spatial part only. $\eta_{\mu\nu}$ represents the Minkowski metric, ϵ^{ijk} the fully antisymmetric (Ricci) pseudo-tensor, $\mathbf{1}$ represents the identity.

We start with the derivation of the second-order Dirac equation in Cartesian coordinates and then turn it into toroidal coordinates. We take into account the coupling of an electron of charge $-e$ to a classical electromagnetic field defined by a four-potential $(A^\mu) = (\Phi/c, \vec{A})$ through the covariant derivative defined as

$$D_\mu \Psi = \left(\partial_\mu + \frac{i}{\hbar} e A_\mu \right) \Psi. \quad (3.227)$$

For convenience we use the natural units such that $\hbar = c = 1$. Then the Dirac equation reads

$$(i\gamma^\mu D_\mu - mc) \Psi = 0, \quad (3.228)$$

on which we apply the "squaring" operator $(i\gamma^\mu D_\mu + mc)$.

The second-order Dirac equation then takes the form

$$- \left((\gamma^\mu D_\mu) (\gamma^\nu D_\nu) + m^2 \right) \Psi = 0. \quad (3.229)$$

Developing the kinetic part one finds

$$(\gamma^\mu D_\mu)(\gamma^\nu D_\nu) = (\partial^\mu \partial_\mu + (ie)^2 A^\mu A_\mu) + ie\{\gamma^\mu A_\mu, \gamma^\nu \partial_\nu\}, \quad (3.230)$$

where

$$\{\gamma^\mu A_\mu, \gamma^\nu \partial_\nu\} = \{\gamma^\mu, \gamma^\nu\} A_\mu \partial_\nu + \gamma^\nu \gamma^\mu \partial_\nu (A_\mu), \quad (3.231)$$

and where

$$\begin{aligned} \gamma^\nu \gamma^\mu \partial_\nu (A_\mu) &= \frac{1}{2} [\gamma^\mu \gamma^\nu \partial_\mu (A_\nu) + \gamma^\nu \gamma^\mu \partial_\nu (A_\mu)] \\ &= \frac{1}{2} [\gamma^\mu \gamma^\nu (\partial_\mu A_\nu - \partial_\nu A_\mu) + 2\eta^{\mu\nu} \partial_\nu A_\mu]. \end{aligned} \quad (3.232)$$

Using the identities

$$\{\gamma^\mu, \gamma^\nu\} = 2\eta^{\mu\nu} \mathbf{1}, \quad (3.233)$$

$$\gamma^i \gamma^j = -\delta_{ij} - i\epsilon_{ijk} \Sigma^k, \quad (3.234)$$

$$\gamma^0 \gamma^i = \alpha^i, \quad (3.235)$$

and recognizing the electromagnetic field tensor,

$$F_{\mu\nu} = \partial_\mu A_\nu - \partial_\nu A_\mu, \quad (3.236)$$

from which we get the contravariant components of the electric and magnetic fields (see e.g. Gourgoulhon (2013))

$$E^i = \eta^{ij} F_{0j} = -F_{0i}, \quad (3.237)$$

$$B^i = \epsilon^{ijk} F_{jk}, \quad (3.238)$$

we get

$$\gamma^\nu \gamma^\mu \partial_\nu (A_\mu) = -\vec{\alpha} \cdot \vec{E} - i\Sigma^k \underbrace{\epsilon^{ijk} \partial_i A_j}_{\text{curl}(A)^k = B^k} + 2\eta^{\mu\nu} \partial_\nu A_\mu. \quad (3.239)$$

The anti-commutator (3.231) then becomes

$$\{\gamma^\mu A_\mu, \gamma^\nu \partial_\nu\} = 2(A^\mu \partial_\mu + \frac{1}{2} \partial_\mu A^\mu) - \vec{\alpha} \cdot \vec{E} - i\vec{B} \cdot \vec{\Sigma}. \quad (3.240)$$

Inserting (3.240) back into (3.230), and reorganizing the terms a little we obtain

$$\begin{aligned}
& (\gamma^\mu D_\mu) (\gamma^\nu D_\nu) = \\
& \underbrace{\left(\partial^\mu \partial_\mu + 2i \frac{e}{\hbar} (A^\mu \partial_\mu + \frac{1}{2} \partial_\mu A^\mu) - \frac{e^2}{\hbar^2} A^\mu A_\mu \right)}_{(\partial_\mu + i \frac{e}{\hbar} A_\mu)^2} - , \quad (3.241) \\
& ie\vec{\alpha} \cdot \vec{E} + e\vec{B} \cdot \vec{\Sigma}
\end{aligned}$$

from what we get the same expression for the second-order Dirac equation as in Berestetskii et al. (1982) (One will pay attention that in Cartesian coordinates $A_x = -A^x$ and that the usual magnetic potential \vec{A} is defined as a contravariant quantity. With the metric signature used here : $A^0 = \Phi/c = A_0$.),

$$\begin{aligned}
& (\hbar c)^2 \left[\left(\frac{1}{c} \partial_t + i \frac{e}{\hbar c} \Phi \right)^2 - \sum_{x \in \{x,y,z\}} (\partial_x + i \frac{e}{\hbar} A_x)^2 - \right. \\
& \left. i \frac{e}{\hbar c} \vec{\alpha} \cdot \vec{E} + \frac{e}{\hbar} \vec{B} \cdot \vec{\Sigma} + \frac{m^2 c^2}{\hbar^2} \right] \Psi = 0 \quad (3.242)
\end{aligned}$$

We now switch to another spatial coordinate system denoted by primes, with the only assumption that this system is orthogonal. The Jacobian of the transformation is given by (J^{ij}) . In (3.243) we separate the time components from the space components,

$$\begin{aligned}
& (\gamma^\mu D_\mu) (\gamma^\nu D_\nu) = (\partial_t + ie\Phi)^2 - \\
& \left(\Delta' - 2i \frac{e}{\hbar} \left(A'^i \partial'_i + \frac{1}{2} \nabla' \cdot \vec{A}' \right) + \frac{e^2}{\hbar^2} A'^i A'_i \right) - . \quad (3.243) \\
& ie\vec{\alpha} \cdot \vec{E} + e\vec{B} \cdot \vec{\Sigma}
\end{aligned}$$

Where $A'_i = J^{ij} A_j$ and Δ', ∇' represent the Laplacian and the divergence in the primed system of coordinates. We have used the orthogonality of J_{ij} to eliminate cross terms. If only spatial coordinates change the electric field \vec{E} here transforms like a covariant vector and $\vec{\alpha}$ like a contravariant quantity (as shown in the text) such that $\vec{\alpha} \cdot \vec{E} = \vec{\alpha}' \cdot \vec{E}'$. The rules of transformation of the magnetic field are less straightforward and it might be simpler to just express it as a function of the primed variables without changing its basis. That is the choice of this paper.

In the case proposed in this paper, we use the toroidal coordinates defined in 3.A, with a Laplacian and a divergence respectively given by (3.223) and (3.224). The magnetic potential is assumed to be only along the third direction : $\vec{A}' = (0, 0, A^\phi)$. All replacements made we obtain

$$\begin{aligned}
& -(\hbar c)^2 \left[-\frac{1}{c^2} \partial_{t^2}^2 + \right. \\
& \partial_r^2 + \frac{1}{r} \partial_r + \frac{1}{(\rho+r \cos \phi)^2} \partial_{\theta^2}^2 + \frac{1}{r^2} \partial_{\phi^2}^2 - \\
& \left. 2i \frac{e}{\hbar} A^\phi \partial_\phi + \frac{e^2}{\hbar^2} A^\phi A_\phi - \frac{e}{\hbar} \vec{B} \cdot \vec{\Sigma} - \frac{m^2 c^2}{\hbar^2} + \right. \\
& \left. \frac{\cos \phi}{\rho+r \cos \phi} \partial_r - \frac{\sin \phi}{r(\rho+r \cos \phi)} \partial_\phi - i e \frac{r \sin \phi}{\rho+r \cos \phi} A^\phi \right] \Psi = 0
\end{aligned} \tag{3.244}$$

The non-negligible (see the text) Laplacian terms are on the second line. The terms involving the magnetic potential are on the third line. All the terms on the fourth line are neglected in this paper, the two leftmost terms coming from the Laplacian and the rightmost term being the divergence.

3.C Resolution of the radial differential equation

In this appendix, we develop the detailed solution of the differential equation (3.77) giving the radial dependency of the proper states of Dirac's equation. Here we recall the equation

$$\left(\partial_{x^2}^2 + \frac{1}{x} \partial_x + \frac{1}{x^2} \partial_{\phi^2}^2 + 2i \partial_\phi - x^2 + C \right) f(x, \phi) = 0, \tag{3.245}$$

Where $-C$ is the proper value of the equation, to be determined.

Assuming the following form for f :

$$f(x, \phi) = e^{i\xi\phi} g(x) \tag{3.246}$$

And inserting it into (3.247) we obtain

$$\left(\partial_{x^2}^2 + \frac{1}{x} \partial_x - \frac{\xi^2}{x^2} - 2\xi - x^2 + C \right) g(x) = 0. \tag{3.247}$$

We notice that

$$\left(\partial_{x^2}^2 + \frac{1}{x} \partial_x \right) g(x) = \frac{1}{\sqrt{x}} \partial_{x^2}^2 (\sqrt{x} g(x)) + \frac{1}{4x^2} g(x), \tag{3.248}$$

which once put into (3.247) gives the following form

$$\partial_{x^2}^2 (\sqrt{x} g(x)) + \left(\frac{\frac{1}{4} - \xi^2}{x^2} - 2\xi - x^2 + C \right) (\sqrt{x} g(x)) = 0. \tag{3.249}$$

Here we recognize the differential equation giving generalized Laguerre functions given in Olver and National Institute of Standards and Technology (U.S.) (2010), table 18.8.1,

$$\left(\partial_{x^2}^2 + \frac{\frac{1}{4} - \alpha^2}{x^2} - x^2 + 4s + 2\alpha + 2 \right) h(x) = 0, \quad (3.250)$$

where α is a real parameter strictly larger than -1 , s a positive integer and the solution h is

$$h(x) = e^{-\frac{x^2}{2}} x^{\alpha+1/2} L_s^{(\alpha)}(x^2). \quad (3.251)$$

Identifying α and C in (3.249) we find

$$\alpha = \begin{cases} \pm |\xi| & \text{if } |\xi| < 1 \\ |\xi| & \text{if } |\xi| \geq 1 \end{cases}, \quad (3.252)$$

and

$$C = \begin{cases} 4s + 2(\xi \pm |\xi|) + 2 & \text{if } |\xi| < 1 \\ 4s + 2(\xi + |\xi|) + 2 & \text{if } |\xi| \geq 1 \end{cases}. \quad (3.253)$$

Finally the solutions of equation (3.247) are

$$f(x, \phi) = e^{i\xi\phi} e^{-\frac{x^2}{2}} x^{\alpha} L_s^{(\alpha)}(x^2). \quad (3.254)$$

In the specific case of this paper we have $\xi = l_{\perp}$. Therefore we obtain

$$\alpha = \begin{cases} \pm \frac{1}{2} & \text{if } l_{\perp} = \frac{1}{2} \\ |l_{\perp}| & \text{otherwise} \end{cases}, \quad (3.255)$$

and

$$C = \begin{cases} 4s + 2 & \text{if } l_{\perp} \leq 0 \\ 4(s + l_{\perp}) + 2 & \text{if } l_{\perp} \geq 0 \end{cases}. \quad (3.256)$$

3.D Resolution of the Newtonian Hamilton-Jacobi problem of an electron in a constant uniform magnetic field

We work out the general solution, without assuming the center of motion, of the motion of an electron in a uniform constant magnetic field in polar coordinates using the Hamilton-Jacobi formalism of Newtonian mechanics. Although heavy, this way of obtaining a common result is interesting in view of the comparison with the quantum mechanical result, given the parenting between the Hamilton-Jacobi formalism and Hamiltonian quantum mechanics.

Without loss of generality we restrict ourselves to a plane motion with polar coordinates (r, θ) . The position vector \vec{r} and the velocity $\dot{\vec{r}}$ are then expressed in the polar basis $(\vec{u}_r, \vec{u}_\theta)$ by

$$\vec{r} = r\vec{u}_r, \quad (3.257)$$

$$\dot{\vec{r}} = \dot{r}\vec{u}_r + r\dot{\theta}\vec{u}_\theta. \quad (3.258)$$

The link with cartesian coordinates comes with $\vec{u}_r = (\cos \theta, \sin \theta)$ and $\vec{u}_\theta = (-\sin \theta, \cos \theta)$.

We choose to write the magnetic potential giving a field of flux intensity B orthogonal to the plane of motion in a symmetric gauge with

$$\vec{A} = \frac{1}{2}rB\vec{u}_\theta. \quad (3.259)$$

Then the Lagrangian of an electron of charge $-e$ is given by

$$L = \frac{1}{2}m(\dot{r}^2 + (r\dot{\theta})^2) - \frac{1}{2}er^2\dot{\theta}B. \quad (3.260)$$

We readily see that θ is a cyclic coordinate as only its derivative participates in the Lagrangian. Therefore, its conjugate momentum is a constant of motion

$$p_\theta = \frac{\partial L}{\partial \dot{\theta}} = mr^2(\dot{\theta} - \frac{\omega_c}{2}). \quad (3.261)$$

Notice that p_θ is actually the angular momentum of the particle.

We may now define the typical time scale T and length scale λ

$$(\omega_c/2)^{-1} = \left(\frac{eB}{2m} \right)^{-1}, \quad (3.262)$$

$$\lambda = \sqrt{\frac{2p_\theta}{m\omega_c}}, \quad (3.263)$$

which define an energy scale

$$\epsilon = m(\lambda\omega_c/2)^2. \quad (3.264)$$

We switch now to dimensionless coordinates

$$r \rightarrow x = r/\lambda, \quad (3.265)$$

$$t \rightarrow \tau = \frac{\omega_c}{2}t, \quad (3.266)$$

and to a dimensionless Lagrangian

$$\tilde{L} = L/\epsilon = \frac{1}{2} \left(x'^2 + \theta'(1+x^2) \right) - 1 - x^2, \quad (3.267)$$

where $'$ denotes the derivation with respect to τ while $\dot{}$ was with respect to t .

The momentum conjugated to x is simply

$$p_x = \frac{\partial \tilde{L}}{\partial x'} = x'. \quad (3.268)$$

The Legendre transform of \tilde{L} gives us the corresponding Hamiltonian

$$\tilde{H} = p_x x' + p_\theta \theta' - \tilde{L} = \frac{1}{2} \left(p_x^2 + \frac{1}{x^2} + 2 + x^2 \right), \quad (3.269)$$

where we made obvious that θ was an ignorable coordinate by using (3.261) to get that $\theta' = 1/x^2 + 1$.

Let's now introduce the Hamilton characteristic function W (see e.g. Goldstein (1980)), of which we consider only the x dependence. We get the following Hamilton-Jacobi equation

$$\left(\frac{\partial W}{\partial x} \right)^2 + \frac{1}{x^2} + 2 + x^2 = 2\tilde{E}, \quad (3.270)$$

where $\tilde{E} = E/\epsilon$ is the dimensionless energy of the system. It follows that one gets the following Hamilton function

$$W = \pm \int dx \sqrt{\tilde{E} - \frac{1}{x^2} - 2 - x^2}. \quad (3.271)$$

Choosing \tilde{E} as the new momentum we get that its conjugate coordinate is :

$$Q_{\tilde{E}} = \frac{\partial W}{\partial \tilde{E}} = \pm \int \frac{dx}{2\sqrt{\tilde{E} - \frac{1}{x^2} - 2 - x^2}} \quad (3.272)$$

which integrates as

$$Q_{\tilde{E}} = \pm \frac{1}{2} \arctan \left(\frac{a - x^2}{\sqrt{2ax^2 - x^4 - 1}} \right) \quad (3.273)$$

where $a = \tilde{E} - 1$.

The denominator of the arctan argument in (3.273) is necessarily positive since it is proportional to $\left(\frac{\partial W}{\partial x}\right)^2$. By construction we now have $Q'_{\tilde{E}} = \frac{\partial \tilde{H}}{\partial \tilde{E}} = 1$. Integrating and equating to (3.273) one obtains :

$$\frac{a - x^2}{\sqrt{2ax^2 - x^4 - 1}} = \pm \tan(2\tau + \theta_0) \quad (3.274)$$

Solving for x^2 in (3.274), one obtains

$$x^2 = a \pm \sqrt{a^2 - 1} |\sin(2\tau + \theta_0)|. \quad (3.275)$$

In order to keep a continuous trajectory, one will switch from the + to the - solution whenever the sin function switches as well.

Finally, we use the conservation of angular momentum (3.261) to obtain the equation for θ and switch back to the international unit system

$$\begin{aligned} r &= \lambda \sqrt{a + \sqrt{a^2 - 1} \sin(\omega_c t + \theta_0)}, \\ \theta &= \frac{\omega_c}{2} t + \arctan \left[a \tan \left(\frac{\omega_c}{2} t + \frac{\theta_0}{2} \right) + \sqrt{a^2 - 1} \right] + n\pi, \end{aligned} \quad (3.276)$$

with

$$\lambda = \sqrt{\frac{2p\theta}{m\omega_c}}, \quad (3.277)$$

$$a = \frac{E}{\frac{1}{2}p\theta\omega_c} - 1, \quad (3.278)$$

and

$$n = \frac{\pi}{2} + \text{floor} \left(\frac{\frac{\omega_c}{2} t + \frac{\theta_0}{2} - \frac{\pi}{2}}{\pi} \right). \quad (3.279)$$

Thus, we obtained a solution depending only on the invariants of motion, E and p_θ , and a constant of integration θ_0 depending on the initial conditions.

Let's interpret the different trajectories. First, if we assume that r or $\dot{\theta}$ is constant, from the expression of p_θ (3.261) we see that the other one is constant as well. From (3.276) we see that this is allowed only for $a = 1$. In this case we find readily that

$$r = \lambda, \quad (3.280)$$

$$\theta = \omega_c t. \quad (3.281)$$

Using the relation between the conjugate momentum p_θ and the orthogonal "kinetic" momentum $p_\perp = mr\dot{\theta}$

$$p_\theta = rp_\perp - mr^2 \frac{\omega_c}{2}. \quad (3.282)$$

Replacing r by λ in the above expression one obtains that the radius of the trajectory is the usual Larmor radius

$$r = \lambda = \frac{p_\perp}{m\omega_c} \quad (3.283)$$

In this configuration the radial momentum is zero, and

$$E = p_\theta \omega_c. \quad (3.284)$$

In this particular configuration we see that p_\perp is constant as well.

We see that by construction : $a \geq 1$. Now, we consider the solutions for higher energies i.e. higher values of a . We see that they are all circles after computing the curvature radius using the formula

$$\rho = \frac{(\frac{dr}{d\theta}^2 + r^2)^{3/2}}{2\frac{dr}{d\theta}^2 + r^2 - r\frac{d^2r}{d\theta^2}}. \quad (3.285)$$

We obtain, after a lengthy but straightforward calculation, the general formula for the radius of curvature

$$\rho = \lambda \sqrt{\frac{a+1}{2}} = \sqrt{\frac{2E}{m\omega_c^2}}. \quad (3.286)$$

Reminding that the magnetic field does not work, we find that the kinetic energy is constant and therefore these circles are circulated at constant speed $\omega_c \rho$. This allow us to find the center of each circle \vec{r}_0 by simple geometric considerations

$$\vec{r}_0 = \vec{r} - \frac{1}{\omega_c} \frac{d\vec{r}}{dt} \wedge \frac{\vec{p}_\theta}{p_\theta}, \quad (3.287)$$

where \vec{p}_θ is the vectorial angular momentum, which here is orthogonal to the plane of motion. The distance of the center of motion to the origin of coordinates takes a simple form

$$\|\vec{r}_0\| = \sqrt{\rho^2 - \lambda^2} = \sqrt{2 \frac{E - p_\theta \omega_c}{m \omega_c^2}}. \quad (3.288)$$

Put differently, this gives a simple expression for the energy in terms of

$$E = p_\theta \omega_c + \frac{1}{2} m r_0^2 \omega_c^2. \quad (3.289)$$

Thus we found the very intuitive result that, when the trajectory is centered on the origin of coordinates all the energy is stored in the angular momentum. However, we also see that the energy is "degenerate" with another invariant of motion, r_0^2 , as in the quantum case. In any case, according to equation (3.286) the radius of the trajectory is proportional to the square-root of the full energy.

3.E Integration of squared Airy integrals

Here we compute different expressions that differ slightly. We therefore detail the first case and then proceed faster for the others.

We use the functions $F_{1/3}$ and $F_{2/3}$ defined in (3.292). We here give an alternative definition that is useful in the developments of this appendix

$$\begin{aligned} F_{1/3}(\xi) &= \sqrt{3} \int_0^{+\infty} dx \cos\left(\frac{3}{2}\xi \left(sx + \frac{x^3}{3}\right)\right), \\ F_{2/3}(\xi) &= \sqrt{3} \int_0^{+\infty} dx x \sin\left(\frac{3}{2}\xi \left(sx + \frac{x^3}{3}\right)\right), \end{aligned} \quad (3.290)$$

with $s \in [-1, 0, 1]$. We recall their definition from (3.197)

$$F_{1/3}(\xi, s) = \begin{cases} K_{1/3}(\xi) & , s > 0 \\ \frac{1}{3^{2/3}\Gamma(\frac{2}{3})} & , s = 0 \\ \frac{\pi}{\sqrt{3}} \left(J_{1/3}(\xi) + J_{-1/3}(\xi) \right) & , s < 0 \end{cases} , \quad (3.291)$$

$$F_{2/3}(\xi, s) = \begin{cases} K_{2/3}(\xi) & , s > 0 \\ -\frac{1}{3^{1/3}\Gamma(\frac{1}{3})} & , s = 0 \\ \frac{\pi}{\sqrt{3}} \left(J_{2/3}(\xi) - J_{-2/3}(\xi) \right) & , s < 0 \end{cases} .$$

They are related to the Airy function and its derivative by

$$F_{1/3}(\xi, s) = \pi \sqrt{\frac{3}{|x|}} \text{Ai}(x), \quad (3.292)$$

$$F_{2/3}(\xi, s) = -\pi \frac{\sqrt{3}}{x} \text{Ai}'(x), \quad (3.293)$$

where $x = \text{sign}(s) \left(\frac{3}{2}\xi \right)^{2/3}$.

We also frequently use the following integrals

$$\int_{-\infty}^{\infty} d\tau \tau^n \exp [ia\tau^2] = \frac{\Gamma\left(\frac{n+1}{2}\right)}{|a|^{\frac{n+1}{2}}} e^{i\left(\frac{\pi}{4} - \frac{\arg(a)}{2}\right)(n+1)}, \quad (3.294)$$

where a is a complex with argument $0 < \arg(a) < \pi$ and n a positive integer. For practical purposes we give particular value of the Γ function (Olver and National Institute of Standards and Technology (U.S.), 2010)

$$\Gamma\left(\frac{1}{2}\right) = \sqrt{\pi}, \Gamma(1) = 1, \Gamma\left(\frac{3}{2}\right) = \frac{\sqrt{\pi}}{2}, \Gamma\left(\frac{5}{2}\right) = \frac{3\sqrt{\pi}}{4}. \quad (3.295)$$

First case

We compute the following expression, where c is a constant:

$$I_a = \frac{\sqrt{3}}{\pi |c|} \int_{-\infty}^{\infty} dx \left| \int_{-\infty}^{\infty} d\tau \tau \exp \left[i \left((c + x^2)\tau + \frac{\tau^3}{3} \right) \right] \right|^2. \quad (3.296)$$

The present derivation is directly inspired by that of Cheng and Zhang (1996), however, correcting for a mistake that we point out below.

Since

$$A_i(y) = \frac{1}{2\pi} \int_{-\infty}^{\infty} d\tau \exp \left[i \left(y\tau + \frac{\tau^3}{3} \right) \right], \quad (3.297)$$

one remarks that

$$I_a = \frac{\sqrt{3}}{\pi|c|} \int_{-\infty}^{\infty} dx \left| 2\pi A'_i(c+x^2) \right|^2, \quad (3.298)$$

where A'_i is the derivative of the Airy function as defined in Olver and National Institute of Standards and Technology (U.S.) (2010).

We seek to evaluate I through its integral formulation (3.296). Developing the squared Airy integral we get

$$I_a = \frac{\sqrt{3}}{\pi|c|} \int_{-\infty}^{\infty} dx \int_{-\infty}^{\infty} d\tau_1 \int_{-\infty}^{\infty} d\tau_2 \tau_1 \tau_2 \exp \left[i(\tau_1 - \tau_2) \left((c+x^2) + \frac{1}{3}(\tau_1^2 + \tau_1\tau_2 + \tau_2^2) \right) \right] \quad (3.299)$$

In order to separate as much as possible the integrals we introduce the following variables:

$$(\tau_1, \tau_2) \rightarrow \left(\tau_+ = \frac{1}{2}(\tau_1 + \tau_2), \tau_- = \frac{1}{2}(\tau_1 - \tau_2) \right) \quad (3.300)$$

The Jacobian of this transformation is

$$\left| \frac{\partial(\tau_1, \tau_2)}{\partial(\tau_+, \tau_-)} \right| = \begin{vmatrix} 1 & 1 \\ 1 & -1 \end{vmatrix} = 2 \quad (3.301)$$

and we notice that

$$\tau_1 \tau_2 = \tau_+^2 - \tau_-^2 \quad (3.302)$$

$$\tau_1^2 + \tau_1 \tau_2 + \tau_2^2 = 3\tau_+^2 + \tau_-^2 \quad (3.303)$$

such that we get the form

$$I_a = \frac{\sqrt{3}}{\pi|c|} \int_{-\infty}^{\infty} dx \left\{ 2 \int_{-\infty}^{\infty} d\tau_+ \int_{-\infty}^{\infty} d\tau_- \exp \left[2i\tau_- \left((c+x^2) + \frac{\tau_-^2}{3} \right) \right] (\tau_+^2 - \tau_-^2) \exp [2i\tau_- \tau_+^2] \right\}. \quad (3.304)$$

Here one splits the computation in two integrals

$$\begin{aligned}
C &= \int_{-\infty}^{\infty} dx \int_{-\infty}^{\infty} d\tau_+ \int_{-\infty}^{\infty} d\tau_- \\
&\quad \exp [2i\tau_- \tau_+^2] \exp \left[2i\tau_- \left((c + x^2) + \frac{\tau_-^2}{3} \right) \right] \tau_-^2 \\
D &= \int_{-\infty}^{\infty} dx \int_{-\infty}^{\infty} d\tau_+ \tau_+^2 \int_{-\infty}^{\infty} d\tau_- \\
&\quad \exp [2i\tau_- \tau_+^2] \exp \left[2i\tau_- \left((c + x^2) + \frac{\tau_-^2}{3} \right) \right]
\end{aligned} \tag{3.305}$$

such that

$$I_a = 2 \frac{\sqrt{3}}{\pi |c|} (D - C). \tag{3.306}$$

Here it would be nice to integrate over τ_+ first since these integrals are of Gaussian type. However, the integrals cannot be swapped in D without becoming divergent, as done in Cheng and Zhang (1996). We circumvent this problem by introducing a positive real parameter ϵ ,

$$\begin{aligned}
D &= \lim_{\epsilon \rightarrow 0^+} \\
&\quad \int_{-\infty}^{\infty} dx \int_{-\infty}^{\infty} d\tau_+ \tau_+^2 \int_{-\infty}^{\infty} d\tau_- \exp [2i(\tau_- + i\epsilon)\tau_+^2] \\
&\quad \exp \left[2i(\tau_- + i\epsilon) \left((c + x^2) + \frac{(\tau_- + i\epsilon)^2}{3} \right) \right]
\end{aligned} \tag{3.307}$$

which is allowed by the theorem of dominated convergence using for example the following hat function

$$\begin{aligned}
g(\tau_+, \tau_-) &= \\
&\quad \left\{ \begin{array}{l} \tau_+^2 \left(\max \left(0, \cos \left[\tau_- \left((c + x^2) + \tau_+^2 + \frac{\tau_-^2}{3} \right) \right] \right) \right) + \\ \quad i \max \left(0, \sin \left[\tau_- \left((c + x^2) + \tau_+^2 + \frac{\tau_-^2}{3} \right) \right] \right) \\ |\tau_-| \tau_+^2 \left(\max \left(0, \cos \left[\tau_- \left((c + x^2) + \tau_+^2 + \frac{\tau_-^2}{3} \right) \right] \right) \right) + \\ \quad i \max \left(0, \sin \left[\tau_- \left((c + x^2) + \tau_+^2 + \frac{\tau_-^2}{3} \right) \right] \right) \end{array} \right\} .
\end{aligned} \tag{3.308}$$

Then we can first integrate over τ_+ using (3.294),

$$\begin{aligned}
C &= \int_{-\infty}^{\infty} dx \int_{-\infty}^{\infty} d\tau_- \sqrt{\frac{\pi}{2|\tau_-|}} e^{i\frac{\pi}{4}s\tau_-} \\
&\quad \exp \left[2i\tau_- \left((c+x^2) + \frac{\tau_-^2}{3} \right) \right] \tau_-^2, \\
D &= \lim_{\epsilon \rightarrow 0^+} \int_{-\infty}^{\infty} dx \int_{-\infty}^{\infty} d\tau_- \sqrt{\frac{\pi}{2|\tau_- + i\epsilon|}} e^{i\frac{\pi}{4}s\tau_- + i\Delta_\epsilon} \\
&\quad \exp \left[2i(\tau_- + i\epsilon) \left((c+x^2) + \frac{(\tau_- + i\epsilon)^2}{3} \right) \right] \frac{i}{4(\tau_- + i\epsilon)}
\end{aligned} \tag{3.309}$$

where $\Delta_\epsilon = -\frac{1}{2}(\arg(x+i\epsilon) - \arg(x))$.

Summing over x ,

$$\begin{aligned}
C &= \int_{-\infty}^{\infty} d\tau_- \frac{i\pi}{2} \tau_- \exp \left[2i\tau_- \left(c + \frac{\tau_-^2}{3} \right) \right] \\
D &= \lim_{\epsilon \rightarrow 0^+} \int_{-\infty}^{\infty} d\tau_- \frac{-\pi}{8(\tau_- + i\epsilon)^2} \\
&\quad \exp \left[2i(\tau_- + i\epsilon) \left(c + \frac{(\tau_- + i\epsilon)^2}{3} \right) \right]
\end{aligned} \tag{3.310}$$

Performing the following change of variable in C

$$\tau_- \rightarrow y = \frac{2}{\sqrt[3]{4}} \tau_-, \tag{3.311}$$

we recognize that C is proportional to the derivative of the Airy integral with respect to $c' = \sqrt[3]{4}c$. Expressing it with a modified Bessel function according to 3.293

$$C = \begin{cases} -\pi \frac{c}{\sqrt[3]{3}} K_{2/3}(\xi) & c > 0 \\ \pi^2 \frac{c}{3} \left(J_{2/3}(\xi) - J_{-2/3}(\xi) \right) & c < 0 \end{cases} \tag{3.312}$$

where $\xi = \frac{4}{3}c^{3/2}$.

For D , we perform the following change of variable

$$\tau_- \rightarrow y = \frac{1}{\sqrt{|c|}} (\tau_- + i\epsilon), \tag{3.313}$$

which means integrating in the complex plane on the line defined by $y = \frac{i\epsilon}{\sqrt{|c|}}$.

Taking again $\xi = \frac{4}{3}|c|^{3/2}$ and $s_c = \text{sign}(c)$ we write

$$D = \frac{-\pi}{8c^{1/2}} \lim_{\epsilon \rightarrow 0^+} \int_{y=\frac{i\epsilon}{\sqrt{|c|}}} dy \frac{1}{y^2} \exp \left[\frac{3}{2}\xi i \left(s_c y + \frac{y^3}{3} \right) \right]. \tag{3.314}$$

After integration by parts

$$D = \frac{-i\pi c}{4} \lim_{\epsilon \rightarrow 0^+} \int_{y=\frac{i\epsilon}{\sqrt{|c|}}} dy \left(\frac{s_c}{y} + y \right) \exp \left[\frac{3}{2} \xi i \left(y + \frac{y^3}{3} \right) \right]. \quad (3.315)$$

Here we can swap again the integral and the limit except for the cosine part of the $1/y$ term. Indeed, if we go back to the $\tau_- = \sqrt{c}y - i\epsilon$ variable we see that

$$\begin{aligned} p_\epsilon(\tau_-) &= \frac{\cos \left[\frac{3}{2} \xi \left(y + \frac{y^3}{3} \right) \right]}{y} \\ &= \frac{\cos \left[2 \left(c(\tau_- + i\epsilon) + \frac{(\tau_- + i\epsilon)^3}{3} \right) \right]}{(\tau_- + i\epsilon)}. \end{aligned} \quad (3.316)$$

We see that because of the pole in $\tau_- = 0$ it is impossible to find a hat function g such that

$$\forall \epsilon > 0, \forall \tau_- \in \mathbb{R}, g(\tau_-) > |p_\epsilon(\tau_-)|, \quad (3.317)$$

and therefore the swapping is forbidden.

However, we may compute $\lim_{\epsilon \rightarrow 0} \int_{-\infty}^{+\infty} d\tau_- p_\epsilon(\tau_-)$ directly. Let us first write

$$\begin{aligned} \forall \epsilon, L > 0, \int_{-\infty}^{+\infty} d\tau_- p_\epsilon(\tau_-) &= \\ \int_{-L}^{+L} d\tau_- p_\epsilon(\tau_-) + \underbrace{\int_{\mathbb{R} \setminus [-L, L]} d\tau_- p_\epsilon(\tau_-)}_{(a)}. \end{aligned} \quad (3.318)$$

The first term on the right-hand side can be written

$$\begin{aligned} \int_{-L}^{+L} d\tau_- p_\epsilon(\tau_-) &= \int_{-L}^{+L} d\tau_- \frac{\cos(2c(\tau_- + i\epsilon))}{\tau_- + i\epsilon}, \\ &+ \circ((L + i\epsilon)^5). \end{aligned} \quad (3.319)$$

where the notation $\circ(x)$ is to be understood as $\circ(x) = xf(x)$ where f is analytical and tends to 0 as x tends to 0.

The first term on the right-hand side can be expressed as

$$\int_{-L}^{+L} d\tau_- \frac{\cos(2c(\tau_- + i\epsilon))}{\tau_- + i\epsilon} = \int_{-\infty}^{+\infty} d\tau_- \frac{\cos(2c(\tau_- + i\epsilon))}{\tau_- + i\epsilon} - \underbrace{\int_{\mathbb{R} \setminus [-L, L]} d\tau_- \frac{\cos(2c(\tau_- + i\epsilon))}{\tau_- + i\epsilon}}_{(b)}. \quad (3.320)$$

The first term on the right-hand side can be developed as

$$\int_{-\infty}^{+\infty} d\tau_- \frac{\cos(2c(\tau_- + i\epsilon))}{\tau_- + i\epsilon} = \cos(2ci\epsilon) \int_{-\infty}^{+\infty} d\tau_- \frac{\cos(2c\tau_-)}{\tau_- + i\epsilon} - \underbrace{\sin(2ci\epsilon) \int_{-\infty}^{+\infty} d\tau_- \frac{\sin(2c\tau_-)}{\tau_- + i\epsilon}}_{(c)}. \quad (3.321)$$

The integral in (b) is a well-known integral (Gradshteyn and Ryzhik, 2007) given by

$$\int_{-\infty}^{+\infty} d\tau_- \frac{\cos(2c\tau_-)}{\tau_- + i\epsilon} = -i\pi e^{-2c\epsilon}. \quad (3.322)$$

Now we can take the limit $\epsilon \rightarrow 0$. One can obviously swap the integral and limit in (a), (b) and (c). (a) and (b) cancel because the integrand is odd while (c) cancels because of the sine prefactor. It follows that

$$\lim_{\epsilon \rightarrow 0} \int_{-\infty}^{+\infty} d\tau_- p_\epsilon(\tau_-) = -i\pi + o(L^5). \quad (3.323)$$

Since the left-hand side does not depend on L it follows that $o(L^5)$ is a constant proportional to L^5 , namely 0.

For the other terms in D , we swap the limit and integral. When $c > 0$ we use the following relations demonstrated by Schwinger (1949) (Schwinger (1949) uses the definitions of Watson (1966) for the Bessel functions while we use those, slightly different, of Olver and National Institute of Standards and Technology (U.S.) (2010). However one can show that the relations 3.324 and 3.325 are not affected by the change of convention.)

$$\int_0^{+\infty} dx \frac{\sin\left(\frac{3}{2}\xi\left(x + \frac{x^3}{3}\right)\right)}{x} = \frac{\pi}{2} - \frac{1}{\sqrt{3}} \int_\xi^{+\infty} dx K_{1/3}(x), \quad (3.324)$$

and

$$\int_0^{+\infty} dx \left(\frac{1}{x} + 2x \right) \sin \left(\frac{3}{2} \xi \left(x + \frac{x^3}{3} \right) \right) = \frac{\pi}{2} + \frac{1}{\sqrt{3}} \int_{\xi}^{+\infty} dx K_{5/3}(x), \quad (3.325)$$

to obtain

$$D = \frac{\pi c}{2} \left(-\frac{1}{\sqrt{3}} \int_{\xi}^{\infty} K_{1/3}(x) dx + \frac{1}{\sqrt{3}} K_{2/3}(\xi) \right) \quad (3.326)$$

$$= \frac{\pi c}{2} \left(\frac{1}{\sqrt{3}} \int_{\xi}^{\infty} K_{5/3}(x) dx - \frac{1}{\sqrt{3}} K_{2/3}(\xi) \right). \quad (3.327)$$

Here, Cheng and Zhang (1996) find a result exactly three times larger. We successfully compared our results with direct numerical integrations.

Finally when $c > 0$

$$I_a = \int_{\xi}^{\infty} K_{5/3}(x) dx + K_{2/3}(\xi). \quad (3.328)$$

The case $c < 0$ needs to demonstrate the equivalent of (3.324) and (3.325) when $c < 0$. The demonstration is similar to that of Schwinger (1949). Let us first notice that

$$\begin{aligned} \frac{d}{d\xi} \int_{-\infty}^{+\infty} dx \frac{\sin \left(\frac{3}{2} \xi \left(-x + \frac{x^3}{3} \right) \right)}{x} &= \\ \int_{-\infty}^{+\infty} dx \frac{3}{2} \left(-x + \frac{x^3}{3} \right) \cos \left(\frac{3}{2} \xi \left(-x + \frac{x^3}{3} \right) \right). \end{aligned} \quad (3.329)$$

In the right-hand side, one recognizes an exact primitive minus a cosine term. The exact primitive cancels for reasons of parity and we are left with

$$\begin{aligned} \frac{d}{d\xi} \int_{-\infty}^{+\infty} dx \frac{\sin \left(\frac{3}{2} \xi \left(-x + \frac{x^3}{3} \right) \right)}{x} &= \\ - \int_{-\infty}^{+\infty} dx \cos \left(\frac{3}{2} \xi \left(-x + \frac{x^3}{3} \right) \right), \end{aligned} \quad (3.330)$$

where the right-hand side identifies with the function $F_{1/3}(\xi)$ in (3.290). Noticing that

$$\lim_{L \rightarrow \infty} \int_{-\infty}^{+\infty} dx \frac{\sin \left(\frac{3}{2} L \left(-x + \frac{x^3}{3} \right) \right)}{x} = -\pi, \quad (3.331)$$

we obtain,

$$\int_0^{+\infty} dx \frac{\sin\left(\frac{3}{2}\xi\left(-x+\frac{x^3}{3}\right)\right)}{x} = -\frac{\pi}{2} + \frac{\pi}{3} \int_{\xi}^{+\infty} dx \left(J_{1/3}(x) + J_{-1/3}(x)\right). \quad (3.332)$$

Using this and (3.290) we obtain D and I_a in the case $c < 0$,

$$D = \frac{\pi^2}{2} |c| \left(1 - \frac{1}{3} \int_{\xi}^{\infty} dx \left(J_{1/3}(x) + J_{-1/3}(x)\right) - \frac{1}{3} \left(J_{2/3}(\xi) - J_{-2/3}(\xi)\right)\right), \quad (3.333)$$

and, using functions F (3.292),

$$I_a = \pi\sqrt{3} - \int_{\xi}^{\infty} dx F_{1/3}(x) - 3F_{2/3}(\xi). \quad (3.334)$$

Second case

We compute

$$I_b = \frac{\sqrt{3}}{2\pi} \int_{-\infty}^{\infty} dx \left| \int_{-\infty}^{\infty} d\tau \exp \left[i \left((c+x^2)\tau + \frac{\tau^3}{3} \right) \right] \right|^2. \quad (3.335)$$

Performing the change of variables 3.300 we get:

$$I_b = \frac{\sqrt{3}}{2\pi} \int_{-\infty}^{\infty} dx \left\{ 2 \int_{-\infty}^{\infty} d\tau_+ \int_{-\infty}^{\infty} d\tau_- \exp \left[2i\tau_- \left((c+x^2) + \frac{\tau_-^2}{3} \right) \right] \exp [2i\tau_- \tau_+^2] \right\}. \quad (3.336)$$

Integrating over τ_+ we obtain

$$I_b = 2\frac{\sqrt{3}}{2\pi} \int_{-\infty}^{\infty} dx \int_{-\infty}^{\infty} d\tau_- \sqrt{\frac{\pi}{2|\tau_-|}} e^{i\frac{\pi}{4}s\tau_-} \exp \left[2i\tau_- \left((c+x^2) + \frac{\tau_-^2}{3} \right) \right]. \quad (3.337)$$

Here we need to be careful to deal with the singularity of the cosine term. Consequently, before swapping the integrals and integrating over x one must perform the change of variables (3.313), then take the limit of the cosine term using (3.323) and

×compute the sine term using (3.324) if $c > 0$ or (3.332) if $c < 0$. One eventually obtains

$$I_b = \begin{cases} \int_{\xi}^{\infty} K_{1/3}(x)dx & , c > 0 \\ \pi\sqrt{3} - \int_{\xi}^{\infty} dx F_{1/3}(x) & , c < 0 \end{cases} \quad (3.338)$$

Third case I_c

We compute

$$I_c = \frac{\sqrt{3}}{\pi|c|} \int_{-\infty}^{\infty} dx x^2 \left| \int_{-\infty}^{\infty} d\tau \exp \left[i \left((c + x^2)\tau + \frac{\tau^3}{3} \right) \right] \right|^2. \quad (3.339)$$

Here it is enough to see that the x^2 factor yields exactly the same result as the τ_+ factor in D . Therefore

$$I_c = 2D = \begin{cases} \int_{\xi}^{\infty} K_{5/3}(x)dx - K_{2/3}(\xi) & c > 0 \\ \pi\sqrt{3} - \int_{\xi}^{\infty} dx F_{1/3}(x) - F_{2/3}(\xi) & c < 0. \end{cases} \quad (3.340)$$

Remark that we put here only the expression using $K_{5/3}$, but one could also express it as a function of $K_{1/3}$ as in equation 3.326.

Fourth case I_d

We compute

$$I_d = \frac{\sqrt{3}}{\pi\sqrt{|c|}} \int_{-\infty}^{\infty} dx \left(\int_{-\infty}^{\infty} d\tau \exp \left[i \left((c + x^2)\tau + \frac{\tau^3}{3} \right) \right] \int_{-\infty}^{\infty} d\tau \tau \exp \left[i \left((c + x^2)\tau + \frac{\tau^3}{3} \right) \right] \right). \quad (3.341)$$

However we could not find a way to obtain a complete analytical expression for this integral. One has to compute it numerically using the following equivalent formula

$$I_d = -4\pi\sqrt{\frac{3}{|c|}} \int_{-\infty}^{\infty} dx \text{Ai}(x^2 + c) \text{Ai}'(x^2 + c). \quad (3.342)$$

Fifth case I_e

We compute

$$I_e = \frac{4\sqrt{3}}{\pi c^2} \int_{-\infty}^{\infty} dx x^2 \left| \int_{-\infty}^{\infty} d\tau \tau \exp \left[i \left((c+x^2)\tau + \frac{\tau^3}{3} \right) \right] \right|^2. \quad (3.343)$$

Performing the change of variable (3.300) we get that

$$I_e = 2 \frac{4\sqrt{3}}{\pi c^2} (D - C) \quad (3.344)$$

with

$$C = \int_{-\infty}^{\infty} dx x^2 \int_{-\infty}^{\infty} d\tau_+ \int_{-\infty}^{\infty} d\tau_- \tau_-^2 \exp \left[2i\tau_- \tau_+^2 \right] \exp \left[2i\tau_- \left((c+x^2) + \frac{\tau_-^2}{3} \right) \right], \quad (3.345)$$

$$D = \int_{-\infty}^{\infty} dx x^2 \int_{-\infty}^{\infty} d\tau_+ \tau_+^2 \int_{-\infty}^{\infty} d\tau_- \exp \left[2i\tau_- \tau_+^2 \right] \exp \left[2i\tau_- \left((c+x^2) + \frac{\tau_-^2}{3} \right) \right]. \quad (3.346)$$

Integrating C is quite straightforward by using two times (3.294), once for τ_+ , once for x . One is left with an Airy integral and

$$C = \frac{-\pi^2}{4\sqrt[3]{2}} \text{Ai} \left(2^{2/3} c \right). \quad (3.347)$$

For D , as for I_a in section 3.E integrals cannot be exchanged without obtaining a divergent integrand. To avoid this we apply the same recipe, that is we introduce a positive real parameter ϵ such that

$$D = \lim_{\epsilon \rightarrow 0} \int_{-\infty}^{\infty} dx x^2 \int_{-\infty}^{\infty} d\tau_+ \tau_+^2 \int_{-\infty}^{\infty} d\tau_- e^{2i(\tau_- + i\epsilon)\tau_+^2} e^{2i(\tau_- + i\epsilon) \left((c+x^2) + \frac{(\tau_- + i\epsilon)^2}{3} \right)}. \quad (3.348)$$

It is possible to invert the integrals and we perform integration over τ_+ and x using (3.294). Performing the change of variable (3.313), we get

$$D = \lim_{\epsilon \rightarrow 0} \frac{-i\pi}{32|c|} \int_{y=\frac{i\epsilon}{\sqrt{|c|}}}^{\infty} dy \frac{e^{i\frac{3}{2}\xi \left(y^3 c + \frac{y^3}{3} \right)}}{y^3} \quad (3.349)$$

where as before $s_c = \text{sign}(c)$ and $\xi = \frac{4}{3} |c|^{3/2}$. Performing an integration by part we have

$$D = \lim_{\epsilon \rightarrow 0} \frac{\pi \sqrt{|c|}}{32} \int_{y=\frac{i\epsilon}{\sqrt{|c|}}} dy \left(\frac{s_c}{y^2} + 1 \right) e^{i \frac{3}{2} \xi \left(y s_c + \frac{y^3}{3} \right)}. \quad (3.350)$$

The second term corresponds to $F_{1/3}(\xi, s_c)$ by definition (3.292). The first term is, up to a factor, the same integral as in (3.314).

With D and C we use formula (3.344) and expressing C with a $F_{1/3}$ function using (3.292), we obtain

$$D = \frac{\pi |c|^{1/2}}{16\sqrt{3}} \left[F_{1/3}(\xi) + 2 |c|^{3/2} \begin{cases} \int_{\xi}^{+\infty} dx F_{1/3}(x) - F_{2/3}(\xi) & c > 0 \\ \pi\sqrt{3} - \int_{\xi}^{+\infty} dx F_{1/3}(x) - F_{2/3}(\xi) & c < 0 \end{cases} \right] \quad (3.351)$$

$$I_e = \frac{5}{2 |c|^{3/2}} F_{1/3}(\xi) + \begin{cases} \int_{\xi}^{+\infty} dx F_{1/3}(x) - F_{2/3}(\xi) & c > 0 \\ \pi\sqrt{3} - \int_{\xi}^{+\infty} dx F_{1/3}(x) - F_{2/3}(\xi) & c < 0 \end{cases}. \quad (3.352)$$

Sixth case I_f

We compute

$$I_f = \frac{4}{\pi \sqrt{3} c^2} \int_{-\infty}^{\infty} dx x^4 \quad (3.353)$$

$$\left| \int_{-\infty}^{\infty} d\tau \exp \left[i \left((c + x^2) \tau + \frac{\tau^3}{3} \right) \right] \right|^2.$$

Performing the change of variable (3.300) we get that

$$I_f = 2 \frac{4}{\pi \sqrt{3} c^2} \int_{-\infty}^{\infty} dx x^4 \int_{-\infty}^{\infty} d\tau_+ \int_{-\infty}^{\infty} d\tau_- \quad (3.354)$$

$$\exp [2i\tau_- \tau_+] \exp \left[2i\tau_- \left((c + x^2) + \frac{\tau_-^2}{3} \right) \right].$$

It is not possible to exchange integration over x with integration over τ_- . We work around this by inserting a positive real parameter ϵ

$$I_f = \frac{8}{\pi \sqrt{3} c^2} \lim_{\epsilon \rightarrow 0} \int_{-\infty}^{\infty} dx x^4 \int_{-\infty}^{\infty} d\tau_+ \int_{-\infty}^{\infty} d\tau_- \quad (3.355)$$

$$e^{[2i(\tau_- + i\epsilon)\tau_+^2]} e^{[2i(\tau_- + i\epsilon) \left((c + x^2) + \frac{(\tau_- + i\epsilon)^2}{3} \right)]},$$

and perform integrations over τ_+ and x using (3.294). We then perform the change of variable (3.313) to obtain

$$I_f = \frac{24}{\pi\sqrt{3}c^2} \lim_{\epsilon \rightarrow 0} \frac{-i\pi}{32|c|} \int_{-\infty}^{\infty} dy \frac{e^{\left[\frac{3}{2}\xi i \left(y s_c + \frac{y^3}{3}\right)\right]}}{y^3},$$

where $s_c = \text{sign}(c)$.

Here we recognize integral (3.349), the value of which is given in (3.351). Therefore the final result is

$$I_f = \frac{1}{2|c|^{3/2}} F_{1/3}(\xi) + \begin{cases} \int_{\xi}^{+\infty} dx F_{1/3}(x) - F_{2/3}(\xi) & c > 0 \\ \pi\sqrt{3} - \int_{\xi}^{+\infty} dx F_{1/3}(x) - F_{2/3}(\xi) & c < 0 \end{cases}. \quad (3.356)$$

Distribution of electron-positron free pairs from gamma-ray collisions

4.1 The need of accounting for photon anisotropy and pair spectrum in pulsar magnetospheres

In pulsar magnetospheres the population of photons is made of gamma rays from synchrocurvature radiation, synchrotron or Compton scattering on the one hand, and of weak (or soft) photons in the x-ray range or lower. The latter may be of thermal origin from the crust of the star, but there is also evidence of strong non-thermal components in some pulsars (see section 1.3) presumably originating from the magnetosphere. Moreover x-ray emissions are pulsed, at least partly (section 1.3), which is an evidence in favor of strong anisotropy in the distribution of the weak radiation field.

From a theoretical point of view, the photon-photon mechanism of pair production is invoked essentially in the outer magnetosphere (see chapter 2 and in particular section 2.3.5), but could also play a role near the polar cap of millisecond pulsars, where the magnetic field can be of the same order of magnitude as in the outer magnetosphere of some normal or young pulsars. In the outer magnetosphere, the magnetic field is too weak to efficiently create pairs by interaction with gamma photons (see section 2.2.3). However, a pair cascade could be somehow self-sustained by taking photons from the large number of soft photons produced by the low-energy end of the cascade, and reprocessing them into pairs through collisions with gamma photons from primary particles. Gamma rays from primary particles are emitted along the magnetic field lines (along the velocity of the primary particle), which also gives them a very anisotropic distribution. Besides, their number is very small compared to the number of soft photons. Soft photons are expected to have a broader angular distribution than gamma rays since they are produced by less relativistic electrons and positrons.

When a pair is created, the pitch angle of each member of the pair with respect to the local magnetic field determines strongly the radiation from synchrotron and

synchrocurvature. The peak energy and power of synchrotron both evolve like $\sim (\gamma \sin \alpha)^2$, while the peak of the curvature radiation limit of synchrocurvature evolves like γ^3 and the power like γ^4 , where γ is the Lorentz factor of the particle and α its pitch angle (see section 2.2.2). Therefore, the energy and angular spectrum of the created particles may play an important role in the cascade dynamics : owing to the strong nonlinearity of the radiation processes, assuming that each member of the pair takes away the same energy may turn out to yield very different results from assuming that one takes almost all the energy and the other only its rest mass energy.

4.2 Introduction to the computation of pair spectra

The basic theory of the production of free electron-positron pairs by collisions of photons is described in section 2.2.3. However, the power and angular spectra of the created pairs was not discussed, for it involves technical issues which are the object of the next section. Assuming the reaction occurs between an isolated gamma ray and a continuous background of weak photons, then the probably creating a pair from the gamma ray results from the integration over all the possible pairs of photons (the gamma ray and a photon from the background). The four momenta of each pair of photons are related to the four momenta of each pair of leptons by the conservation law

$$K + K_w = P + P', \quad (4.1)$$

where K is the four-momentum of the gamma ray, K_w of a weak photon, P and P' are the four momenta of the members of the lepton pair (as far as only momenta are involved, electron and positron can be exchanged). If one is only interested in the creation rate and not in the spectrum, then the cross section $d\sigma_{\gamma\gamma}/d\omega$ (equation (2.91)) can be integrated over the solid angle $d\omega$ of one of the outgoing leptons (say P), and the other lepton momentum is determined $P' = K + K_w - P$ as a result of (4.1). The only restriction is that the leptons be on their mass shell $P^2 = P'^2 = m^2 c^4$, but it is easily taken into account in integral boundaries (Berestetskii et al., 1982) and one obtains the angle-integrated cross section $\sigma_{\gamma\gamma}(K, K_w)$ (2.99) that depends only on the photon momenta. One can then integrate over the distribution of soft photons $f_w(\vec{k}_w)$ to the obtain rate of pair creation (probability per unit time per unit volume),

$$W_{\gamma\gamma} = c \int_{K_w^0 \geq \frac{2m^2 c^4}{K^0(1-\cos \xi)}} d^3 \vec{k}_w f_w(\vec{k}_w) (1 - \cos \xi) \sigma_{\gamma\gamma}(K, K_w), \quad (4.2)$$

where the factor $1 - \cos \xi = K_w \cdot K / (K_w^0 K^0)$ arises from the elementary current in equation (2.90), with ξ the angle between the two photons. The domain of integration is only limited by the lower energy threshold which is directly obtained

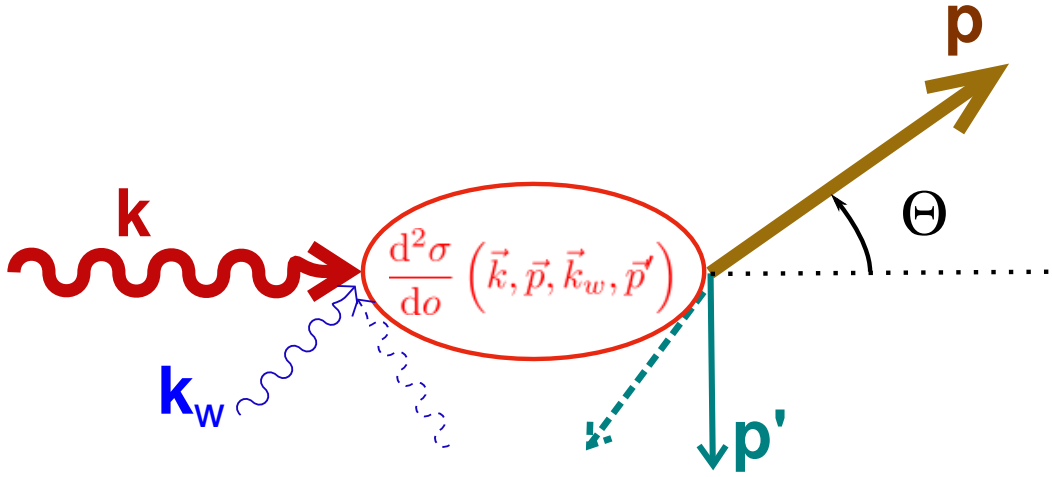


Fig. 4.1.: Sketch of a gamma photon of momentum \vec{k} producing after collision with a weak photon of momentum \vec{k}_w a lepton of momentum \vec{p} and another of momentum \vec{p}' with cross section $d\sigma_{\gamma\gamma}/do$. For \vec{k} and \vec{p} fixed, \vec{k}_w and \vec{p}' are related by the conservation equation (4.1). There is an infinity of possible combination respecting this constrain, two of them being shown in solid and dashed lines respectively, and for each the cross section has a different value. To obtain the spectrum of leptons produced as a function of \vec{p} , one has to sum over all these possibilities.

by squaring equation (4.1) and considering that because the leptons have a minimum rest-mass energy $(K + K_w)^2 = (P + P')^2 \geq 4m^2c^4$ (see equation (2.98)).

If one wants the spectrum, then P is fixed (see figure 4.1) since one wants $dW_{\gamma\gamma}/d^3\vec{p}$, and one has to resort to the differential cross section $d\sigma_{\gamma\gamma}/do$. From the conservation equation (4.1) it follows that there is a direct relationship between K_w and P' for each couple (K, P) (see figure 4.1) which determines the domain of integration allowed. This computation is carried out in the next section.

4.3 Article: *Electron-positron pair production by gamma rays in an anisotropic flux of soft photons, and application to pulsar polar caps*

The present section contains an article submitted to MNRAS written in collaboration with Fabrice Mottez¹ and Silvano Bonazzola^{2, 3}

¹LUTH, Observatoire de Paris, PSL Research University - CNRS, 5 places Jules Janssen 92190 Meudon, France

²LUTH, Observatoire de Paris, PSL Research University, 5 places Jules Janssen 92190 Meudon, France

³This article has been accepted for publication in MNRAS while the thesis was being reviewed. Some substantial revisions have been made to the article, in particular its section 6, and I would recommend any interested reader to get the final version either from MNRAS at <https://doi.org/10.1093/mnras/stx2658> or from the open archive <https://hal.archives-ouvertes.fr/hal-01614371>.

Abstract

Electron-positron pair production by collision of photons is investigated in view of application to pulsar physics. We compute the absorption rate of individual gamma-ray photons by an arbitrary anisotropic distribution of softer photons, and the energy and angular spectrum of the outgoing leptons.

We work analytically within the approximation that $1 \gg mc^2/E > \epsilon/E$, with E and ϵ the gamma-ray and soft-photon maximum energy and mc^2 the electron mass energy. We give results at leading order in these small parameters. For practical purposes, we provide expressions in the form of Laurent series which give correct reaction rates in the isotropic case within an average error of $\sim 7\%$.

We apply this formalism to gamma rays flying downward or upward from a hot neutron star thermally radiating at a uniform temperature of 10^6K . Other temperatures can be easily deduced using the relevant scaling laws. We find differences in absorption between these two extreme directions of almost two orders of magnitude, much larger than our error estimate. The magnetosphere appears completely opaque to downward gamma rays while there are up to $\sim 10\%$ chances of absorbing an upward gamma ray. We provide energy and angular spectra for both upward and downward gamma rays. Energy spectra show a typical double peak, with larger separation at larger gamma-ray energies. Angular spectra are very narrow, with an opening angle ranging from 10^{-3} to 10^{-7} radians with increasing gamma-ray energies.

4.3.1 Introduction

Electron-positron pair creation by collision of two photons, also called Breit-Wheeler process, is important in a series of astrophysical questions (Ruffini et al., 2010). Among them is the filling of recycled pulsar magnetospheres with plasmas.

The cross-section of two-photon-pair creation has been derived in Berestetskii et al. (1982). This is a function of the four-momentum of both electrons. In pulsar magnetospheres, there is generally a huge reservoir of low-energy photons and a small number of high-energy photons. In order to decrease computational cost compared to pairwise calculations, the cross-section is integrated over the distribution of the low-energy photons. The exact formula for the reaction rate on an isotropic soft-photon background was first derived in Nikishov (1962) to estimate the absorption of gamma rays by the extragalactic background light. Numerical integration was needed to obtain practical results. In contexts such as active galactic nuclei or X-ray binaries, various formulations and approximations were developed. Approximated

analytical expressions were given in Bonometto and Rees (1971) and Agaronyan et al. (1983) in the case of an isotropic soft-photon background distribution and averaging over outgoing angles of the produced leptons. The expression of Agaronyan et al. (1983) also applies for a bi-isotropic photon distribution (both strong and weak photon distributions are isotropic) without angle averaging over leptons. In these papers, the authors provide the energy spectrum of the outgoing leptons. An exact expressions in the case of bi-isotropic photon distribution is derived in Boettcher and Schlickeiser (1997), as well as a comparison to the previous approximations that favors the approach in Agaronyan et al. (1983) for its better accuracy.

The standard picture of a pulsar magnetosphere assumes that its inner part is filled with plasma and corotates with the neutron star with angular velocity Ω_* . The primary plasma is made of matter lifted from the neutron-star surface by electric fields (Goldreich and Julian, 1969). These particles have highly relativistic energies; their motion in the neutron-star magnetic field generates synchrotron and curvature gamma-ray photons. In addition to primary particles, Sturrock (1971) has shown that electron-positron pairs are created in or near the acceleration regions of the magnetosphere. This provides plasma capable of screening the electric field component parallel to the magnetic field. There are two processes of pair creation : two-photon process, and one-photon in the presence of a strong magnetic field. The one-photon process is the most efficient with young and standard pulsars, of which magnetic field is in the range $B \sim 10^6 - 10^8$ T (Burns and Harding, 1984). The photon-photon pair-creation process can become more important with high-temperature polar caps, and when the magnetic field is below 10^6 T as in recycled pulsar magnetospheres. Anisotropy of the soft-photon sources is prone to be important as they are expected to come either from the star (hot spots) or from synchrotron radiation in magnetospheric gaps. That is the main reason of our present investigation.

Many detailed studies of pair-creation cascades in pulsar magnetospheres are based only on the one photon process. This is for instance the case in the recent studies in Timokhin and Harding (2015). Others take the two reactions into account (Chen and Beloborodov, 2014; Harding et al., 2002).

In numerical simulations of pulsars, the pair-creation rate is generally estimated with simple proxies. For instance, in Chen and Beloborodov (2014), a mean free path $l = 0.2R_*$ is used for the one-photon process, and $l = 2R_*$ for the two-photon process. The rate of creation of pairs is not explicated as a function of the electron (or positron) momentum, neither of the local photon background. Instead, pair creations are supposed to be abundant enough to supply electric charges and current densities. The authors write that this approximation is somehow similar to the force-free approximation. In Harding et al. (2002), both one-photon and two-photon

processes are taken into account, and the two-photon process is controlled by a mean free path derived from Zhang and Yuan (1998), where anisotropy is partially taken into account : the energy integral has a lower limit that depends on the angular size of the hot cap providing the soft-photon background. Besides, these authors do not provide spectra for the created pairs although the energy distribution of the outgoing particles are important for the dynamics of pair cascades. A more complete model needs an integration over every local surface element with a threshold that depends on the location of each elementary emitter. This is what the results of the present paper allow to do within some approximation, together with angular and energy spectra of the outgoing pairs.

Pair creation by two photons is also important in high energy gamma-ray astrophysics. Many papers about gamma-ray bursts and active galactic nuclei refer to Svensson (1987) and the integrated mean free path in this paper is also based on Nikishov (1962). Actually, spectra of TeV radiation observed from distant (beyond 100 Mpc) extragalactic objects suffer essential deformation during the passage through the intergalactic medium, caused by energy-dependent absorption of gamma rays interacting with the diffuse extragalactic background light (Nikishov, 1962; Gould and Schröder, 1966). This effect drastically limits the horizon of the gamma-ray universe, and this has been taken into account in the science case of high-energy gamma ray observatories (Vassiliev, 2000).

In this paper, we revisit the computation of the two-photon pair-creation rate with the aim of dealing with arbitrarily anisotropic soft-photon background distribution. In addition, we give formulas for angle and energy spectra in order to be able to determine in which state pairs are created. After an introduction to the two-photon pair creation equations in section 4.3.2, the integral over the low-energy photons is defined in section 4.3.3. Practical expressions for spectra are derived in section 4.3.4, and applications to the cosmic microwave background and to a hot neutron star are developed in section 4.3.5.

4.3.2 The two-photon-quantum-electrodynamics reaction

When not specified, we use a unit system where the speed of light $c = 1$.

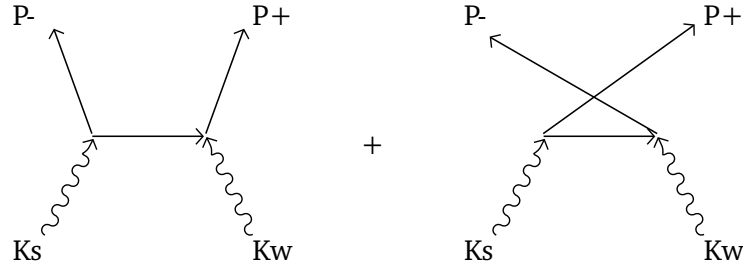


Fig. 4.2.: Reaction of electron-positron pair creation from a pair of photons represented to first order by Feynman diagrams. Photons have 4-momenta K_s and K_w while electron and positron have respectively P_- and P_+ .

General formalism

Any quantum-electrodynamics reaction from an initial quantum state $|i\rangle$ to an outgoing state $|o\rangle$ can be represented as the decomposition on a final states basis $\{|f_k\rangle\}$ of the evolved state $\hat{S}|i\rangle$, \hat{S} being the evolution operator,

$$|o\rangle = \sum_k \langle f_k | \hat{S} | i \rangle | f_k \rangle \quad (4.3)$$

From that starting point, if one is able to derive the appropriate evolution operator, one can then determine the probability of transition from a given state to any state of the final basis. We are interested in the reaction which yields an electron e_- and a positron e_+ from the encounter of two photons. Common applications take place in a frame where one is "strong", that is high-energy, and the other is "weak". Hence we call them γ_s and γ_w , and

$$\gamma_s + \gamma_w \rightarrow e_- + e_+ \quad (4.4)$$

The state of a free photon can be decomposed on a plane-wave basis parametrized by four-momentum and polarisation. The common assumption is that the effective state of a photon is very well approximated by one plane wave at the time of the encounter. Such a state is not physical in itself, because it cannot be normalized i.e. it does not belong to the L^2 space, or more physically because the Heisenberg inequality imposes to the wave function to be entirely spread through space as a consequence of the perfect determination of momentum. Though, this assumption should be valid over a local four-volume of space-time $V\delta t$ where the interaction through operator \hat{S} takes place.

Equivalently, free electrons and positrons live on a basis of plane-wave spinors parametrized by a four-momentum and a spin. From now on, the leptons are characterized by their charges and their four-momenta $P_+ = (P_+^0, \vec{p}_+)$ and $P_- =$

(P_-^0, \vec{p}_-) and photons by their four-momenta $K_s = (K_s^0, \vec{k}_s)$, and $K_w = (K_w^0, \vec{k}_w)$. We consider that their distributions are averaged over spin and polarization respectively. Following Berestetskii et al. (1982), the Lorentz-invariant cross-section equations are derived in terms of kinematic invariants (also called Mandelstam variables), defined as

$$\begin{aligned} s &= (P_- - K_s)^2 = (P_+ - K_w)^2, \\ t &= (K_w + K_s)^2 = (P_+ + P_-)^2, \\ u &= ((P_- - K_w)^2 = (P_+ - K_s)^2. \end{aligned} \quad (4.5)$$

The conservation of four-momentum writes

$$s + t + u = 2m^2, \quad (4.6)$$

where m is the mass of the electron.

The probability dw per unit time of making a pair is

$$dw = d^2\sigma \times j, \quad (4.7)$$

where $d\sigma$ is the Lorentz-invariant cross-section

$$\begin{aligned} d^2\sigma &= -ds 8\pi r_e^2 \frac{m^2}{t^2} \times \left[\left(\frac{m^2}{s - m^2} + \frac{m^2}{u - m^2} \right)^2 + \right. \\ &\quad \left. \left(\frac{m^2}{s - m^2} + \frac{m^2}{u - m^2} \right) - \frac{1}{4} \left(\frac{s - m^2}{u - m^2} + \frac{u - m^2}{s - m^2} \right) \right], \end{aligned} \quad (4.8)$$

where r_e is the classical radius of the electron ⁴, ds is the differential of the kinematic invariant s at P_-^0 and K_s^0 fixed,

$$ds = 2d(\vec{p}_- \cdot \vec{k}_s) = 2 \|\vec{p}_-\| \|\vec{k}_s\| \sin(\vec{p}_-, \vec{k}_s) d(\vec{p}_-, \vec{k}_s) \quad (4.9)$$

and j is the elementary two-particle flux of the reaction,

$$j = \frac{1}{V} \frac{K_s \cdot K_w}{K_s^0 K_w^0}, \quad (4.10)$$

and V is the interaction volume previously defined ⁵. Only the current j is frame-dependent. In particular it reads $j = 2/V$ in the center of mass (CM) of the reaction.

⁴In international units $r_e = \frac{e^2}{4\pi\epsilon_0 mc^2} \simeq 2.8179 \cdot 10^{-15}$ meters, with ϵ_0 the electric permittivity of vacuum.

⁵include a factor c in the definition of j when it is not assumed that $c = 1$.

Let us notice that a reaction is possible only if the energy of the two photons exceeds the mass energy of the electron and of the positron. One shows that the kinematic invariant t (4.5) is equal to the square of the energy in the CM. This allows to define the frame-invariant criterion

$$\sqrt{t} \geq 2m, \quad (4.11)$$

which turns into

$$K_s^0 K_w^0 (1 - \cos \xi) \geq 2m^2 \quad (4.12)$$

where ξ is the angle between the two photons.

A few important properties of dw can be evidenced by taking a look at cross-section(4.8) averaged over every possible direction of the outgoing lepton (Berestetskii et al., 1982). As a result, the averaged cross-section depends only on the kinematic invariant $\tau = t/(4m^2)$ the ratio between the CM energy and the threshold energy. Without loss of generality in the present discussion, we can assume that the reaction takes place in the CM frame, such that the elementary current $j = 2/V$. The ultra-relativistic limit (Berestetskii et al., 1982) shows that the cross-section vanishes like $\log \tau/\tau$. This kind of decrease with energy is a common feature of quantum mechanical cross-sections. Moreover, one can numerically estimate the CM energy corresponding to the maximum of the reaction rate to be $\sqrt{t} \simeq 1.4(2m)$.

Concerning the angular dependency, leptons are created almost isotropically when the reaction is near threshold while their momenta become aligned with those of the progenitor photons when going to higher energies (see e.g. Berestetskii et al. (1982)). In the observer's frame this translates in a larger angular dispersion for reactions close to threshold.

Equations (4.5-4.10) fully describe the interaction for a given pair of photons; but in a pulsar's magnetosphere, there is a huge amount of photon pairs. In a simulation, it is not possible to compute dw for each pair; we need a statistical approach and a kind of "collective" reaction rate dW . We define it in the next section.

The pair reactions that count in a pulsar magnetosphere

In a pulsar magnetosphere, the weak photons K_w are mostly caused by the black-body radiation of the neutron star, or possibly by synchrotron from secondary pair cascades. Their energies range in the X-ray domain. The strong photons are caused by the synchro-curvature radiation of energetic particles (electrons, positrons, and possibly ions). Their energies are in the gamma-ray domain. They are more scarce than weak photons. Let's follow a "rare" high-energy, strong photon taken from a phase-space distribution f_s . We assume that it flies through an abundant stream of

low-energy, weak photons with a distribution f_w . Strong photons negligibly interact with other strong photons because they are not abundant, and because the reaction would likely be far above threshold in Eq. (4.12), and therefore inefficient. Weak photons do not interact with other weak photons since their energies are under the reaction threshold. Thus, only weak/strong interactions remain, but weak photons are so numerous that a reaction negligibly changes their distribution. Because strong photons are less abundant, pair creations can change their distribution. Hence, for the simulation of a pulsar's magnetosphere, we need to compute the probability of interaction of a strong photon on the background distribution f_w of weak photons. Indeed, it does not matter which weak photon is annihilated but we want to update f_s as well as the lepton distributions with the outcome of the reactions. With our representation of the involved particles, this amounts to compute the probability dW of creating a lepton of four-momentum P from a photon K_s ,

$$dW = dW_{K_s \rightarrow P}. \quad (4.13)$$

For example, one could think of high-energy synchrotron or curvature photon emitted above the polar cap of a pulsar and flying through a stream of thermal photons emitted by the crust. Let us notice that the probabilities of making a positron or an electron are the same, and that a four-momentum has four components but only three are independent since $\|P\|^2 = m^2c^4$. These three free parameters can be parametrized by one direction (two parameters) and the energy of the particle.

4.3.3 Probability of reaction for a given photon distribution

Quite naturally, the desired probability is the sum over all the possible reactions involving a photon K_s from the background, that would produce an electron at P_- (respectively a positron at P_+),

$$dW_{f_w}(K_s, P_-) = \sum_{L_- = \{(K_w, P_+)/K_s \rightarrow P_-\}} dw(K_w, K_s, P) \times N_w \times N_s, \quad (4.14)$$

where N_w and N_s are the number of photons of four-momentums K_w and K_s respectively within the interaction volume V . In spite of greater simplicity in the CM frame, we must use Eq. (4.8) in the laboratory frame, because the CM frame would

be different for each of the summed pairs of photons. Since low energy photons are parametrized continuously, we must change our sum for an integral, which yields

$$\begin{aligned}
N_w &\rightarrow f_w(\vec{x}_w, \vec{k}_w) d^3\vec{x} d^3\vec{k}_w, \\
dW_{f_w}(K_s, P_-) &= N_s \int_{L_-} \frac{c}{V} \frac{K_s \cdot K_w}{K_s^0 K_w^0} f_w(\vec{x}, \vec{k}_w) d^6\Omega, \\
\text{where } d^6\Omega &= d^2\sigma d^3\vec{x} d^3\vec{k}_w.
\end{aligned} \tag{4.15}$$

We assume that strong photons are spread out in space such that their density does not vary on the interaction volume V such that their local density is $n_s = N_s/V$. Consequently the differential probability of interaction per unit time reads

$$\begin{aligned}
dW_{f_w}(K_s, P_-) &= n_s W_k, \\
W_k &= \int_{L_-} d^2\sigma \frac{c K_s \cdot K_w}{K_s^0 K_w^0} f_w(\vec{x}, \vec{k}_w) d^3\vec{k}_w,
\end{aligned} \tag{4.16}$$

where the volume element $dV = d^3\vec{x}$.

The domain of integration

Let us precisely define the domain L_- of integration. We note $\Pi_\alpha = \{P \in \mathbb{R}^4 : \|P\| = \alpha^2 c^4, P^0 \geq |\alpha|\}$ such that Π_m is the set of lepton four-momenta (m being the mass of the electron) and Π_0 is the set of photon four-momenta. Then,

$$L_-(P_-, K_s) = \{(P_+, K_w) \in \Pi_m \times \Pi_0 : K_w - P_+ = P_- - K_s\}. \tag{4.17}$$

Equivalently, L_- is the subset of $\mathbb{R}^4 \times \mathbb{R}^4$ parametrized by K_w with the following constraints:

$$\left\{ \begin{array}{ll}
P_+ = K_w - (P_- - K_s) & \text{(a),} \\
\|P_+\|^2 = m^2 c^4 & \text{(b),} \\
\|K_w\|^2 = 0 & \text{(c),} \\
K_w^0 \geq 0 & \text{(d),} \\
P_+^0 \geq m c^2 & \text{(e).}
\end{array} \right. \tag{4.18}$$

Condition (a) expresses the conservation of four-momentum. Conditions (b) and (e) come from $P_+^0 \in \Pi_m$, and conditions (c) and (d) come from $K_w \in \Pi_0$. We can compute the number of degrees of freedom in L_- . The set L_- is a subset of $\Pi_m \times \Pi_0$ of dimension 8. The condition (a) on quadrivectors subtracts 4 degrees of freedom.

The conditions (b) and (c) both subtract 1 degree of freedom. We are left with a set L_- of dimension 2.

Some of the conditions in Eq (4.18) are already incorporated in the solution of our problem. Condition (c) is already implicitly met in Eq. (4.16). Condition (a) is also implicitly met by the set of variables used. Only (b) is not straightforward, since P_+ is not directly part of the variables of integration. One can still convert it into a condition on the three other four-vectors by putting (a) into (b) and using (c), the three following equalities being equivalent:

$$\|P_+\|^2 = m^2 c^4$$

$$\|K_w - (P_- - K_s)\|^2 = m^2 c^4 \quad (4.19)$$

$$K_w^0(K_s^0 - P_-^0) - \|\vec{k}_s - \vec{p}_-\| K_w^0 \cos \xi = K_s \cdot P_-, \quad (4.20)$$

$$\xi = \text{angle}(\vec{k}_s - \vec{p}_-, \vec{k}_w) \quad (4.21)$$

where $\|\vec{k}_w\| = K_w^0$. The limit case where $\vec{k}_s = \vec{p}_-$, for which $\cos \xi$ is not defined, is physically impossible because Eq. (4.20) would imply $K_w^0 < 0$, in contradiction with condition (d). With some algebra, we can show that $K_s \cdot P_- \geq 0$ and that the condition $|\cos \xi| \leq 1$ imposes $K_w^0 > \epsilon_{min}$, where

$$\epsilon_{min} = \frac{K_s \cdot P_-}{\|\vec{k}_s - \vec{p}_-\| + K_s^0 - P_-^0} \quad (4.22)$$

More precisely $K_w^0 \in [-1, \cos \xi_0] = [\epsilon_{min}, +\infty[$ and $K_w^0(\cos \xi > \cos \xi_0) < 0$.

We can distinguish three regimes of approximation:

$$K_s^0 \gg p_- \quad : \quad \epsilon_{min} \sim \sqrt{m^2 + p_-^2} - p_- \cos \theta, \quad (4.23)$$

$$K_s^0 \sim p_- \quad : \quad \epsilon_{min} \sim K_s^0 \sqrt{\frac{1 - \cos \theta}{2}},$$

$$K_s^0 \ll p_- \quad : \quad \epsilon_{min} \sim p_-. \quad (4.24)$$

For further approximations, we consider that the weak-photon distribution has a cut-off at $\epsilon = \epsilon_{max} < m/4$.

$$k \gg m/4 > \epsilon_{max} = 128 \text{keV}. \quad (4.25)$$

Because the weak distribution function is in the most extreme case composed of thermal X-rays typically in the range 1 – 10 keV for a pulsar, this approximation is reasonable.

4.3.4 General solution

Energy spectrum

The probability of interaction depends on the integral W_k defined in Eq. (4.16). In this section, W_k is directly expressed as a multiple integral with explicit boundaries. The results exposed in this section can be used directly for applications. The path followed to compute them are described in appendix 4.A. A summary of the notations and useful relations is given in appendix 4.B. The new expression of W_k involves new variables that appear both in the integrand and in the boundaries of the integral. First, new notations are introduced, for shorter formulas,

$$K_s \equiv (k, \vec{k} = k\vec{z}), \quad (4.26)$$

$$P \equiv (P^0, \vec{p}), \quad (4.27)$$

$$K_w \equiv (\epsilon, \vec{x} = (x, y, z)), \quad (4.28)$$

$$\theta \equiv \text{angle}(\vec{k}, \vec{p}). \quad (4.29)$$

With the new notations related to P_- and to K_s , the integration set $L_-(P_-, K_s)$ can be rewritten $L_-(p, \cos \theta, k)$. Let Ω be the set of angular components of the electron P_- , we rewrite W_k as

$$W_{\vec{k}} = c \int_{\Omega} d\Omega \int_{L_-} \frac{d^2\sigma}{d\Omega} \frac{K_s \cdot K_w}{K_s^0 K_w^0} f_w(\vec{k}_w) d^3k_w. \quad (4.30)$$

We wish to compute the probability of making a pair of which the electron P_- is in a volume of phase space defined by

$$\begin{aligned} k/2 < p_1 < p < p_2 < k \\ (\cos \theta, \phi) \in \Omega &= [C_1, C_2] \times [0, 2\pi] \text{ with } C_{\min} \leq C_1 < C_2 < 1 \end{aligned}$$

where p_1, p_2, C_1 and C_2 can be set arbitrarily as long as the above inequalities are correct. After the computations exposed in section 4.A, W_k is transformed into a multiple integral with explicit boundaries. Before showing it, a new set of variables is introduced. The parameter μ parametrizes $\cos \theta$,

$$\cos \theta = 1 - \left(\frac{2(k-p)}{kp} \mu \epsilon_{\max} - \frac{m^2}{2p^2} \right). \quad (4.31)$$

It varies in an interval $\mu \in [\mu_{\min}, 1]$ where $\mu = 1$ corresponds to $\cos \theta = c_{\min}$ and μ_{\min} is such that $\cos \theta = 1$,

$$\mu_{\min} = \frac{1}{4} \frac{km}{p(k-p)} \frac{m}{\epsilon_{\max}} \quad (4.32)$$

We define the dimensionless coefficients $a_i(p)$,

$$a_1(p) = -\frac{m^2(k^2 - 2kp + 2p^2)}{8kp^2(k-p)}, \quad (4.33)$$

$$a_2(p) = -\frac{m^4(k^2 - 4kp + 2p^2)}{16\epsilon_{\max}kp^3(p-k)}, \quad (4.34)$$

$$a_3(p) = \frac{m^6(3k-2p)}{32\epsilon_{\max}^2p^3(k-p)^2}, \quad (4.35)$$

$$a_4(p) = -\frac{km^8}{64\epsilon_{\max}^3p^4(k-p)^2}, \quad (4.36)$$

and

$$R = 2\epsilon_{\max}\sqrt{\mu(1-\mu)}. \quad (4.37)$$

In the following we do not write the p dependence of the a_i coefficients except when otherwise stated. It is convenient to express the weak-photon three-momentum in cylindrical coordinates $\vec{x} = (r, \phi_w, z)$. Then, only the distribution function f_w depends on the angle ϕ_w , which allows a direct integration defining the function (see also (4.122))

$$F_w(r, \mu) = \int_{\phi_w=0}^{2\pi} f_w(r, \phi_w, z(r^2, \mu)) d\phi_w, \quad (4.38)$$

where $z(r^2, \mu)$ is defined in equation (4.119) by

$$z(r^2, \mu) = \frac{k}{4} \left(\frac{r^2}{\mu k \epsilon_{\max}} - 4\mu \frac{\epsilon_{\max}}{k} \right). \quad (4.39)$$

The integral $W_{\vec{k}}$ in (4.30) is approximated by

$$W_{\vec{k}} = c2\pi \int_{p_1}^{p_2} dp \int_{\mu_1}^{\mu_2} d\mu \sum_{i=1}^4 \frac{a_i}{\mu^i} \int_{r=0}^R 2F_w(r, \mu) r dr. \quad (4.40)$$

Here, the boundaries of the integration domain are left arbitrarily. The reaction probability integrated over every outgoing momenta can be computed as well. In this case the μ integral is taken from μ_{\min} to 1 and p ranges between $k/2$ and a maximum p_{\max} defined such as $\mu_{\min}(p = p_{\max}) = 1$. We find

$$p_{\max} = \frac{k}{2} \left(1 + \sqrt{1 - \frac{m^2}{k\epsilon_{\max}}} \right) \quad (4.41)$$

The spectrum of outgoing lepton energy is readily obtained as

$$\frac{dW_{\vec{k}}}{dp}(\max(p, k-p)) = c2\pi \int_{\mu_{\min}}^1 d\mu \sum_{i=1}^4 \frac{a_i}{\mu^i} \int_{r=0}^R 2F_w(r, p, \mu) r dr. \quad (4.42)$$

Angular spectrum

It is also possible to compute the angular spectrum of the outgoing leptons. The problem has to be split in two, whether one consider the higher-energy particle ($p > k/2$) or the lower-energy particle ($p < k/2$).

For the higher-energy particle, one takes equation (4.40) and changes variable μ to $c_\theta = 1 - \cos \theta$ using equation (4.31). One then obtains

$$\frac{dW_{\vec{k}}}{dc_\theta} = 2\pi c \int_{p_1}^{p_2} dp \sum_{i=1}^4 \frac{a'_i}{c^i} \int_{r=0}^R 2F_w(r, p, c_\theta) r dr \quad (4.43)$$

where

$$a'_i = a_i \frac{d\mu}{dc_\theta} = a_i \frac{kp}{2(k-p)\epsilon_{\max}}, \quad (4.44)$$

and the domain of integration has the following limits

$$p_{\min} = k/2 \leq p_1 \leq p_2 \leq p_{\max} \quad (4.45)$$

with

$$p_{\max} = \frac{\epsilon_{\max} k}{m} \frac{1 + \sqrt{1 - \frac{m^2}{\epsilon_{\max} k} - \frac{c_\theta m^2}{2\epsilon_{\max}^2}}}{2\epsilon_{\max}/m + c_\theta k/m}, \quad (4.46)$$

obtained by inverting eq. (4.32). The limits for c_θ are given by

$$0 \leq c_\theta \leq c_{\theta_{\max}} \quad (4.47)$$

with

$$c_{\theta_{\max}} = 2 \left(\frac{\epsilon_{\max}}{k} - \frac{m^2}{k^2} \right), \quad (4.48)$$

for which $p_{\max} = k/2 + \mathcal{O}(1)$.

In virtue of 37, F_w now depends explicitly on p , hence the dependence in (4.43).

For the lower-energy lepton, we need first to establish the kinematic relation between its outgoing angle defined by $\cos \theta' = 1 - c'_\theta$ and the higher-energy lepton variables. All primed quantities refer to the lower-energy lepton. Taking the strong-photon direction along the z axis we have the relation

$$1 - c'_\theta = \frac{p'_z}{p'}. \quad (4.49)$$

Using the conservation of momentum (4.18)a) one can express c'_θ to leading order

$$1 - c'_\theta = \frac{1 - \frac{\tilde{p}}{1-\tilde{p}} \frac{\tilde{m}^2}{\tilde{p}^2} - \tilde{p}}{\left(\left(1 - \tilde{p} - \frac{\tilde{m}^2}{2\tilde{p}}\right)^2 - \tilde{m}^2 \right)^{1/2}} + \mathcal{O}(1) \quad (4.50)$$

where every quantities tilded quantity is expressed in unit of k , $\tilde{a} = a/k$. Since there is no dependence on c_θ one can directly deduce that

$$\frac{dW_{\vec{k}}}{dc'_\theta} = \frac{dW_{\vec{k}}}{dp} \left| \frac{dp}{dc'_\theta} \right|, \quad (4.51)$$

which can be expressed using

$$\frac{dc'_\theta}{dp} = \frac{2\tilde{m}^2 (\tilde{m}^4 + 2(1 - \tilde{p})^2 \tilde{p}(3\tilde{p} - 1) + \tilde{m}^2(1 - \tilde{p}(\tilde{p}(5 - 2\tilde{p}) + 2))}{k(1 - \tilde{p})^2 (\tilde{m}^4 - 4\tilde{m}^2\tilde{p} + 4(1 - \tilde{p})^2 \tilde{p}^2)^{3/2}} \quad (4.52)$$

after numerical inversion of (4.50). One finds that c'_θ is a monotonously increasing function of p and that

$$c'_\theta(k/2) = 4 \frac{m^2}{k^2}, \quad (4.53)$$

$$c'_\theta(p_{\max}) = \frac{\epsilon_{\max}^2}{m^2} \left(1 + \sqrt{1 - \frac{m^2}{k\epsilon_{\max}}} \right). \quad (4.54)$$

With conic boundary conditions

We consider the case where the soft photon distribution is defined everywhere between two cones of axis \vec{k} and of half-apertures $0 \leq \xi_1 < \xi_2 \leq \pi$, and the distribution F_w (4.38) is given as a function of the coordinates ($\bar{\epsilon} = \epsilon/\epsilon_{\max}$, $C_\xi = \cos \xi$), where we deduce from (4.120) and (4.117)

$$\bar{\epsilon} = \frac{\bar{r}^2}{4\mu} + \mu, \quad (4.55)$$

$$C_\xi = 1 - \frac{2\mu}{\bar{\epsilon}}, \quad (4.56)$$

where $\bar{r} = r/\epsilon_{\max}$.

We are now looking for the appropriate boundary conditions to apply to integral (4.40). Using the fact that

$$\tan\left(\frac{\pi}{2} - \xi\right) = \frac{z(r^2, \mu)}{r} \quad (4.57)$$

where $z(r^2, \mu)$ is defined in eq. (4.39), one finds the new boundaries in r by inverting this relation. The resulting r boundaries are given by

$$r_{\xi_{1,2}} = 2\epsilon_{\max}\mu \left(\frac{1}{\tan \xi_{1,2}} + \frac{1}{\sin \xi_{1,2}} \right), \quad (4.58)$$

where one checks that $r_{\xi_2} < r_{\xi_1}$. We need the intersection $[r_{\xi_2}, r_{\xi_1}] \cap [0, R_{\max}]$ which implies solving for $R_{\max}(\mu_{\xi_{1,2}}) = r_{\xi_{1,2}}$, which gives us

$$\mu_{\xi_{1,2}} = \frac{1}{2} \frac{\sin^2 \xi_{1,2}}{1 + \cos \xi_{1,2}} \quad (4.59)$$

where one checks that $\mu_{\xi_2} > \mu_{\xi_1}$. We can rewrite the energy spectrum (4.42) as

$$\begin{aligned} \frac{dW_{\vec{k}}}{dp} (\max(p, k-p)) = & \quad (4.60) \\ 2\pi c r_e^2 \left(\int_{\mu_{\min}}^{\min(\max(\mu_{\min}, \mu_{\xi_1}), 1)} d\mu \int_{\max(0, r_{\xi_2})}^{r_{\xi_1}} dr + \right. & \\ \left. \int_{\min(\max(\mu_{\min}, \mu_{\xi_1}), 1)}^{\min(\mu_{\xi_2}, 1)} d\mu \int_{\max(0, r_{\xi_2})}^R dr \right) \sum_{i=1}^4 \frac{a_i}{\mu^i} 2F_w(r, \mu)r. & \end{aligned}$$

Concerning the angular spectrum, nothing more needs to be done for lower-energy leptons, and for higher-energy leptons we proceed similarly as for the energy spectrum above. Starting from (4.43) one needs to replace μ by its expression as a function of c_θ and p in R . This allows us to define the p analogs of $\mu_{\xi_{1,2}}$ by

$$p_{\xi_{1,2}} = k \frac{1 + \bar{r}_{\xi_{1,2}}^2 \frac{\epsilon_{\max}}{c_\theta k} + \sqrt{1 - \bar{r}_{\xi_{1,2}}^2}}{2 + c_\theta \frac{k}{\epsilon_{\max}} + \bar{r}_{\xi_{1,2}}^2 \frac{\epsilon_{\max}}{c_\theta k}}, \quad (4.61)$$

where one shows that $p_{\xi_1} < p_{\xi_2}$. The spectrum for higher-energy leptons is then obtained from (4.43)

$$\begin{aligned} \frac{dW_{\vec{k}}}{dc} = & \quad (4.62) \\ c2\pi \left(\int_{p_{\min}}^{\min(\max(p_{\min}, p_{\xi_1}), p_{\max})} dp \int_{\max(0, r_{\xi_2})}^{r_{\xi_1}} dr + \right. & \\ \left. \int_{\min(\max(p_{\min}, p_{\xi_1}), p_{\max})}^{\min(p_{\xi_2}, p_{\max})} dp \int_{\max(0, r_{\xi_2})}^R dr \right) \sum_{i=1}^4 \frac{a'_i}{\mu^i} 2F_w(r, \mu)r. & \end{aligned}$$

The weak-photon distribution (4.38) is defined by

$$F_w(\bar{\epsilon}, C_\xi) = \sum_{n,m} F_w^{(n,m)} \bar{\epsilon}^n C_\xi^m. \quad (4.63)$$

Integrations over r in (4.60) and (4.62) yield expressions of the type

$$\begin{aligned} & \sum_{i=1}^4 \frac{a_i}{\mu^i} \int_{r_1}^{r_2} 2F_w(r, \mu) r dr = \\ & 2\epsilon_{\max}^2 \sum_{i=1}^4 a_i \sum_{n,m} \sum_{l=0}^m \binom{m}{l} (-2)^l \mu^{l-i+1} \left[\bar{r} \bar{\epsilon}(\bar{r}, \mu)^{n-l} \right]_{r_1}^{r_2} \end{aligned} \quad (4.64)$$

where

$$\left[\bar{r} \bar{\epsilon}(\bar{r}, \mu)^{n-l} \right]_{r_1}^{r_2} = \begin{cases} 2\mu \frac{\bar{\epsilon}(\bar{r}_2, \mu)^{n-l+1} - \bar{\epsilon}(\bar{r}_1, \mu)^{n-l+1}}{n-l+1} & \text{if } n-l \neq -1 \\ 2\mu \log \left(\frac{\bar{\epsilon}(\bar{r}_2, \mu)}{\bar{\epsilon}(\bar{r}_1, \mu)} \right) & \text{if } n-l = 1 \end{cases}. \quad (4.65)$$

To obtain the final spectrum (4.60) (resp. (4.62)), integration over μ (resp. over p) is possible analytically : the first line of (4.65) is a rational fraction that can be integrated through partial fraction decomposition and the second line yields expressions of the type $\int x^k \log(\text{polynomial}(x)) dx$ (where k is integral) which values are given in most relevant textbooks such as (Gradshteyn and Ryzhik, 2007). However, the resulting expressions may be lengthy and a direct numerical integration might sometimes be more efficient.

4.3.5 Applications

Isotropic black-body background distribution

Here we propose to check our approximation eq. (4.40) against the exact isotropic case described in Nikishov (1962), Agaronyan et al. (1983), and Boettcher and Schlickeiser (1997). We assume a high-energy photon hitting on a thermal soft photon background given by

$$f_{\text{bb}}(\epsilon) = \frac{2}{(\hbar c 2\pi)^3} \frac{1}{e^{\epsilon/k_B T} - 1} \quad (4.66)$$

where T is the temperature of the body and k_B the Boltzmann constant. We choose a cutoff $\epsilon_{\max} = 20T$ (see Eq. 4.25) such that the neglected part of the black-body spectrum (4.66) represents less than $\sim e^{-20} \sim 10^{-9}$ the total amount of background photons. We perform a Chebyshev interpolation (see e.g. Grandclément

and Novak (2009)) of $\epsilon^2 f_{\text{bb}}(\epsilon)$ on the 25 first Chebyshev polynomials achieving a relative accuracy better than one thousandth everywhere and better than 10^{-6} for $0 \leq \epsilon/T \leq 10$, energies between which most of the photons are. This then allows us to derive the coefficients of the Laurent serie describing f_{bb} with poles of order one and two. Then, we produce the spectra of figure 4.4 and 4.3.

On the top panel of figure 4.3 we plot the total probability of absorbing a strong-photon of energy k as a function of

$$\zeta = \frac{kk_b T}{(mc^2)^2}. \quad (4.67)$$

This parametrization by ζ makes the temperature dependency simple

$$W_{\vec{k}} \propto \left(\frac{k_B T}{mc^2} \right)^3. \quad (4.68)$$

Here we choose to take $T = 2.7\text{K}$ which allows to reproduce the result of Gould and Schröder (1966) (dashed line) concerning absorption on the cosmic microwave background. The lower panel of figure 4.3 shows the ratio between our formula and the exact formula of Nikishov (1962). It shows that our result is fifty percent off at $\zeta < 1$ and asymptotically tends to the correct value for large ζ , the difference between the two curves is $\sim 10\%$ around the maximum of the curve located at $\zeta \sim 2$. On average on the range plotted on fig.4.3, our formula overestimates the reaction rate by 7%.

A toy model can help us understand the shape of this curve. The peak of a black-body spectrum is roughly at $\epsilon_{\text{bb}} \simeq 5k_b T$. The cross-section peaks when the center-of-mass energy is $1.4(2m)$, so if one approximates the black-body spectrum to its peak one gets

$$\epsilon_{\text{bb}} k (1 - \cos \xi) \simeq 3.9m^2. \quad (4.69)$$

For an isotropic distribution of soft photons, collisions take place at every angle $\xi \in [0, \pi]$. Taking the intermediate value $\xi = \pi/2$ one obtains from (4.69) an estimate of ζ for the peak of reactions

$$\zeta = \frac{kk_b T}{m^2} \simeq 0.8 \quad (4.70)$$

which is the right order of magnitude. One could argue that at such energies reactions would occur more face-on, meaning $\xi < \pi/2$ which is consistent with the higher peak position found on figure 4.3. We now proceed to the computation of pair energy spectra.

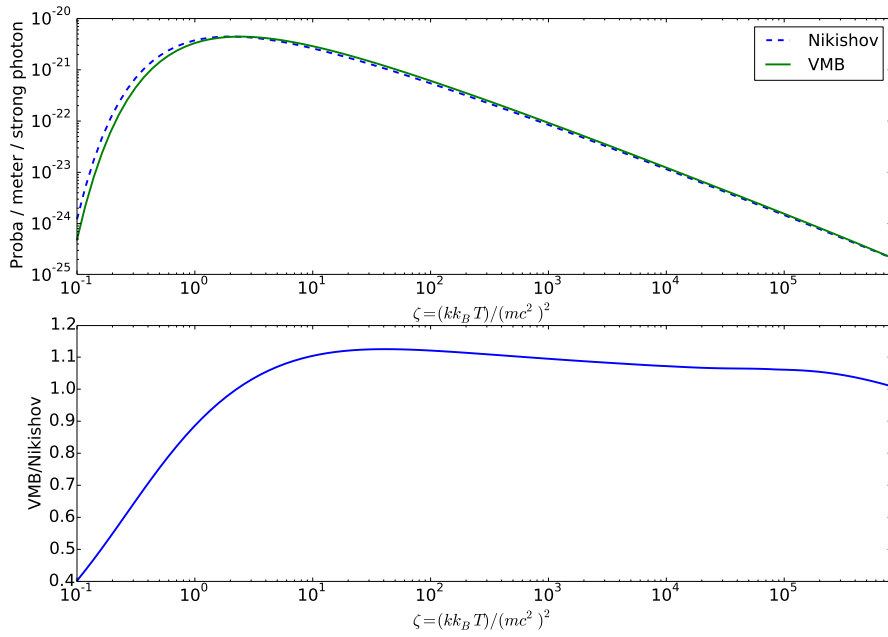


Fig. 4.3.: Comparison of absorption of high-energy photons on a black-body background with Nikishov's formula (dashed line) and with our's (VMB, plain line). The scaling (4.68) is that of a black-body at $T_{\text{bb}} = 2.7$ K (see formula (4.68)) to give an estimate of the effect of the cosmic-microwave background. In this case the energy of the strong photons ranges between $k \sim 100$ TeV and $k \sim 10^8$ TeV. The bottom panel shows the ratio between the two theories. The ratio of probabilities averaged over k is about 1.07. The peak of our curve occurs around $2.6m^2/T$ while Nikishov's is around $1.9m^2/T$. The ratio between the two curves at the position of our peak is approximately 1.01.

Figure 4.4 shows the pair-creation spectra for different values of ζ . Those spectra are directly computed using equation (4.40) and expressed as a function of p/k which allows the same scaling law as in equation (4.68), with p the momentum of one of the created leptons, and normalize each spectrum to unity such that the obtained spectral shape are universal i.e. do not depend on the temperature of the black-body or on the absolute value of k , but only on ζ . The shape and evolution of the spectra with the strong-photon energy is consistent with Agaronyan et al. (1983). In this paper, the authors consider spectra resulting from the reaction of two isotropic monoenergetic photon distributions with energies ϵ and k that are symmetrical with respect to $(k + \epsilon)/2$. Here, every spectrum is symmetrical with respect to $p/k = 0.5$ as result of neglecting $\mathcal{O}(\epsilon/k)$ terms. Besides the shape of these spectra is very reminiscing of pair-creation in the photon-plus-magnetic-field process that is well-known in the field of neutron-star magnetospheres (Daugherty and Harding, 1983). The analogy is not fortuitous since the latter process can in principle be seen as the interaction of a strong photon with an assembly of magnetic-field photons. We see on figure 4.4 that each spectrum is made of two peaks that move apart and become narrower and weaker as the reaction occurs farther above threshold. Notice that the narrowing is relative to the momentum span and not absolute.

The separation of the peaks at higher energies results from the fact that the cross-section favors alignment of ingoing and outgoing particles in the center-of-mass frame if the energy is much larger than the threshold energy. It follows that a Lorentz boost to the observer's frame along this axis results in a low-energy and a high-energy particle. The intensity of the peaks of course depends on the background distribution, but also on the cross-section which decays as $\log(\tau)/\tau$ (see section 4.3.2). The latter dependency explains the above-threshold decrease of the peak intensity and the former explains the below-threshold decrease, as shown on the lower panel of figure 4.4. One notices that spectra are not smooth in their center, which is naturally explained by our approximations that ensure continuity at the center but not continuity of derivatives.

Above a hot neutron star

In this section, we consider a homogeneously hot neutron star at temperature T and two kinds of photons : the down photons and the up photons. Down photons are going radially toward the center of the star while up photons are going in the opposite direction, away from the star. This configuration aims at approximating a pulsar magnetic pole. Indeed, in a pulsar magnetosphere high-energy photons are expected to be mostly created by curvature radiation of electrons and positrons flowing along magnetic field lines that can be considered radial at low altitudes

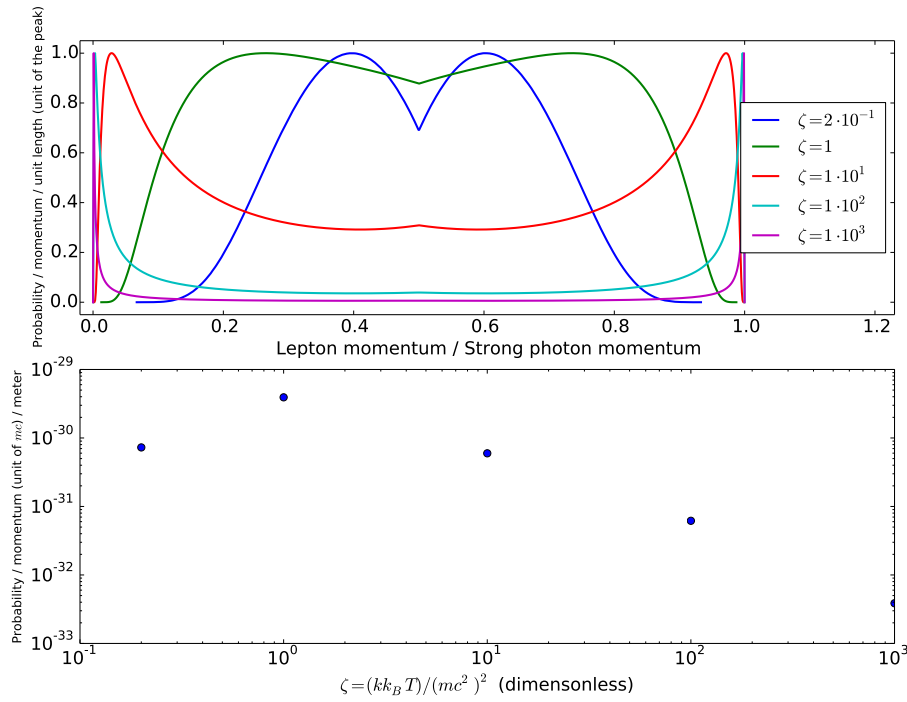


Fig. 4.4.: Spectra of outgoing leptons (electron or positron) for different strong-photon momenta k on a black-body background at temperature T_{bb} (top panel). m is the mass of the electron, the speed of light and the Boltzmann constant are taken to be unity. The amplitudes are normalized to the amplitude of the peaks of each spectrum, and these amplitudes are reported on the lower panel. As in figure 4.3 these amplitudes are normalized to correspond to the cosmic-microwave background. The most intense peaks arise around a momentum k such that its reaction with a background photon at T_{bb} is at threshold, i.e. $kT_{\text{bb}} \sim m^2$. The more above threshold, the more separated, narrow and low the peaks are. The separation of the peaks can be understood as a mere relativistic-frame effect, by analogy with a two-photon collision.

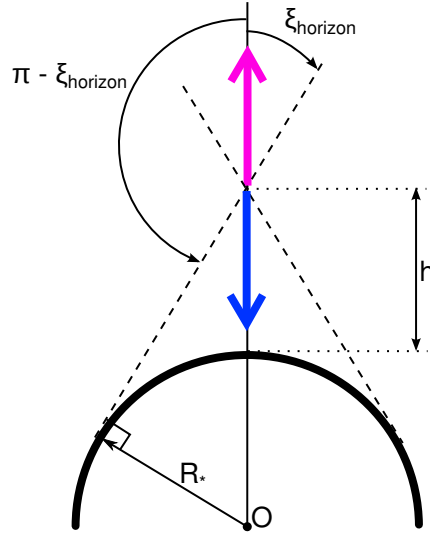


Fig. 4.5.: A neutron star of center O and radius R_* above which a up photon and a down photon are represented by radial arrows of opposite directions. Both photons are represented at an height h above the surface of the star. From this height, they can interact with soft photons coming from the surface of the star within a cone of aperture ξ_{horizon} , eq. (4.71), represented by dashed lines. The incidence angle between the strong photon and soft photons therefore lies between 0 and ξ_{horizon} for the up photon (purple upward arrow), and between $\pi - \xi_{\text{horizon}}$ and π for the down photon (blue downward arrow).

above the poles. Note that we do not consider only a hot cap here but the full star, as means of geometrical simplification.

The case of pair production from photon-photon collisions in pulsar magnetospheres was studied by authors such as Zhang and Qiao (1998) and Harding et al. (2002). In these papers, the authors generalize the formula of Nikishov (1962) with a minimum energy threshold for the background distribution corrected by a factor $(1 - \cos \theta_c)^{-1}$ where θ_c is the maximum viewing angle on the hot polar cap of the star. In other words, they consider an isotropic black-body distribution where only photons within the viewing angle of the cap contribute, however with a threshold energy that corresponds to the largest incidence angle only since the threshold does not depend on the location of the emitter on the cap. Therefore, this approximation overestimates the threshold which generally translates in underestimating the reaction rate. This has little consequences when the viewing angle is wide, which is the case very close to the cap. However, one expects a faster decrease as one goes away from the cap and the factor $(1 - \cos \theta_c)^{-1}$ grows larger. As an example, the authors of Zhang and Qiao (1998) compute a maximum reaction probability of $5.7 \cdot 10^{-5} \text{ m}^{-1}$ at a viewing angle of 90° when we get $6.7 \cdot 10^{-5} \text{ m}^{-1}$ (see peak of the down-photon $h = 10^{-3}$ curve on figure 4.6 for an estimate), but they obtain only $6.3 \cdot 10^{-6} \text{ m}^{-1}$ at 45° when we still have a probability of $4.3 \cdot 10^{-5} \text{ m}^{-1}$ (see their equation 9, for $T = 10^6$ Kelvins)).

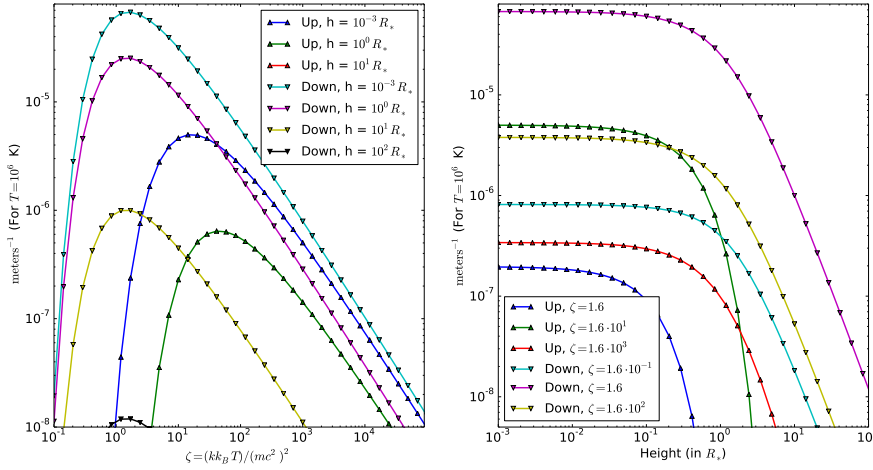


Fig. 4.6.: Probability of reaction per meter of a strong photon of momentum k as a function of $\zeta = (kk_B T)/(mc^2)^2$ and height h above a star of radius R_* . Up-triangle markers represent photons going radially up from the star. Down-triangle markers represent photons going down to the star. The probability scales like T^3 , according to equation (4.68), and is here represented using a fiducial $T = 10^6$ K. Left-hand-side panel : probability as a function of ζ at various heights. Right-hand-side panel : probability as a function of height h at various ζ .

Besides, an interest of our formalism is that it can in principle deal with any other orientation of the strong photon with respect to the star, and in particular the up photons.

In this configuration, the distribution of soft photons is still given by eq. (4.66) except that it is now zero when the angle ξ between the soft and the strong photon is beyond the horizon of the star as seen from the strong photon (see figure 4.5). For a photon going upward, the horizon is defined by

$$\sin \xi < \frac{R_*}{R_* + h} = \sin \xi_{\text{horizon}} \quad (4.71)$$

where R_* is the radius of the star (typically 10km) and h is the height above its surface. Consequently, we use eqs. (4.60) and (4.62) with angles $\xi_1 = 0, \xi_2 = \xi_{\text{horizon}}$ for a up photon and $\xi_1 = \pi - \xi_{\text{horizon}}, \xi_2 = \pi$ for a down photon.

Figure 4.6 shows the probability of reaction per unit length (we will sometimes say "reaction rate") as a function of ζ at various heights h above the cap (left panel), and as a function of h at various ζ (right panel). As in the previous subsection, the temperature dependance is T^3 for a given value of ζ . All the figures in this section are made with a fiducial temperature of 10^6 K. With this value the conversion from ζ to k is : $k \simeq 5.9 \cdot 10^3 \zeta mc^2$. At the lowest altitude we computed, $h = 10^{-3}R_*$, the peak of the reaction rate is around $\zeta = 1.6$ for down photons and about an order

of magnitude higher for up photons $\zeta \simeq 16$. This is a direct consequence of the threshold eq. (4.69) given the less favorable incidence angles of up photons. Another point is that the position of the maximum shifts to lower ζ as height increases for down photons, but to larger ζ s for up photons. As can be seen on the right-hand-side panel, the reaction probability per unit length is fairly stable (within a factor of two) until $\sim 1R_*$, after which it decays very sharply. The decay is sharper as ζ increases for down photons and smoother for up photons, which explains the crossing between some curves on the right-hand-side panel.

A qualitative reasoning explains these behaviors. For a low-energy down photon (i.e. $\zeta \lesssim 1$), most of the soft photons most likely to react are in a narrow cone almost face-on with the strong photon. The aperture of the cone defines the limit beyond which the reaction is below threshold. When the strong photon is higher, the almost face-on soft photons are the last to disappear because of the shrinking of the viewing angle. As energy rises, this cone becomes wider since soft photons provoking a near-threshold reaction are located at a wider angle according to formula (4.69). Inside the first cone also appears a co-axial cone with a narrower aperture inside which photons are not contributing significantly anymore, since reactions are too far above threshold (and therefore the cross-section is too small) because of small incidence angles. At large strong-photon energies ($\zeta \gg 1$), the soft photons close to the outer cone are the first to disappear when the viewing angle shrinks because of a larger height. This explains the faster decay of the reaction probability with h for larger ζ s of down-photon curves on figure 4.6. The same kind of reasoning applies for up photons. Because soft photons are arriving "from behind", there is always an inner cone inside which the reactions are below threshold, and an outer cone limited by the angle beyond which the cross-section is too small if $\zeta \gg 1$ or the viewing angle if the strong-photon energy is small enough. The lower the energy of the strong photon the wider the outer cone and the most sensitive to viewing angle the reaction rate is. That explains why, contrary to down photons, the reaction rate decays slower with altitude when ζ is larger on figure 4.6. With this reasoning, one also understands why the energy of the reaction-rate peak (left panel) is quite stable at low altitudes and becomes smaller for down photons at high altitudes ($\gtrsim 1R_*$) or larger for up photons.

Figure 4.7 shows the optical depth of strong photons as a function of ζ through $10R_*$ from the surface. The optical depth is defined by

$$\tau_\zeta(10R_*) = \int_0^{10R_*} W_\zeta(h) dh. \quad (4.72)$$

Because of the effects mentioned above the peak for down photons is slightly shifted downward at $\zeta \simeq 1.4$ while upward for up photons at $\zeta \simeq 30$. The corresponding typical Lorentz factors of the created particles are $8 \cdot 10^3$ and $2 \cdot 10^5$ respectively.

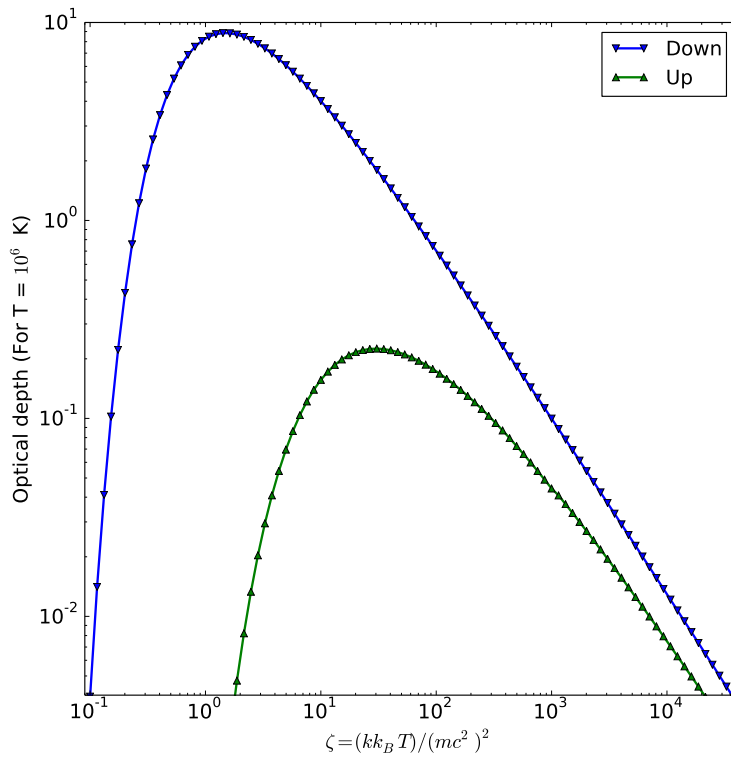


Fig. 4.7.: Reaction rate in equation (4.30) integrated from 0 to $10R_*$ for up and down photons as a function ζ . The amplitudes are valid for a homogeneously hot star of temperature $T = 10^6\text{K}$, and can be converted to other temperatures using the T^3 scaling law (4.68). For photons going down toward the star, the peak is at $\zeta \simeq 1.4$ with an amplitude of $\simeq 8.8$. For photons going up away from the star, the peak is at $\zeta \simeq 30$ with an amplitude of $\simeq 0.23$.

The peak optical depths are respectively $\tau \simeq 8.8$ and $\tau \simeq 0.23$ at a temperature of 10^6 Kelvins. One concludes that at this temperature more than three out of four up photons at the peak energy escape the magnetosphere if no other reaction or source of soft photons opacifies it. The magnetosphere may become opaque if the star is hotter than $\sim 1.6 \cdot 10^6$ K, temperature for which the maximum optical depth reaches 1 owing to the T^3 dependence of the reaction rate. Down photons with ζ between ~ 0.25 and ~ 64 have optical depths larger than unity and therefore are absorbed before they hit the star except if they are emitted at very low altitudes $h \ll R_*$. The maximum optical depth of down photons is below one, namely the magnetosphere is transparent, for a temperature below $0.5 \cdot 10^6$ K. Let's notice that our approximation of a uniformly hot star obviously leads to overestimating the optical depth on distances larger than the size of an actual hotspot.

Figure 4.8 shows the energy spectra of the created leptons (left panel) and the evolution of the position and widths of the peaks as a function of ζ at various heights (right panel). The spectra have the same double-peaked structure as in the isotropic case (figure 4.4) but evolve differently depending on the orientation of the strong photon. The general principle is the same : the more above threshold the more separated peaks, with the consequence that they narrow when they get close to the limits of $p/k \in [0, 1]$. For down photons, the width of the peaks w_p (in unit of k) has very little dependence on altitudes which is due to the fact that for the range of $\zeta \lesssim 20$ visible on this plot (right panel), the efficient soft photons are mostly face-on and suffer no effect of viewing angle. The same thing applies for the position of the most energetic peak p_p (and the least energetic at $k - p_p$). Down-photon peaks are wide $w_p \sim 0.45$ for $\zeta \lesssim 2$ and then sharply narrow while their position smoothly goes from $p_p/k \sim 0.8$ to $p_p/k \lesssim 1$ at large ζ s. On the contrary, up photons are very sensitive to altitude, which is explained by the fact that the higher above the star, the narrower the viewing angle and therefore the incidence angle, and the more energetic up photons need to be for the reaction to be at or above threshold. As a consequence up-photons peaks are very centered at low values of ζ s, with $p_p/k \sim 0.6$, and are even more centered at higher altitudes. With ζ rising, the energy distribution becomes increasingly asymmetric as $p_p/k \rightarrow 1^-$, although it takes a larger ζ at higher altitude. Similarly, peak widths are growing with ζ until a maximum $w_p \sim 0.45$ at a ζ all the more large that altitude is high, after which w_p drops sharply. This sharp change of slope happens because the two peaks separate (see comment of figure 4.8).

Figure 4.9 shows the normalized angular spectra for both up and down photons, and both higher-energy ($p > k/2$) and lower-energy ($p < k/2$) outgoing leptons at various values of ζ . It is remarkable that apart from their amplitudes (not visible on this normalized plot), these spectra do not change much with height apart at large and very unlikely angles, and therefore we limit ourselves to only one height. These

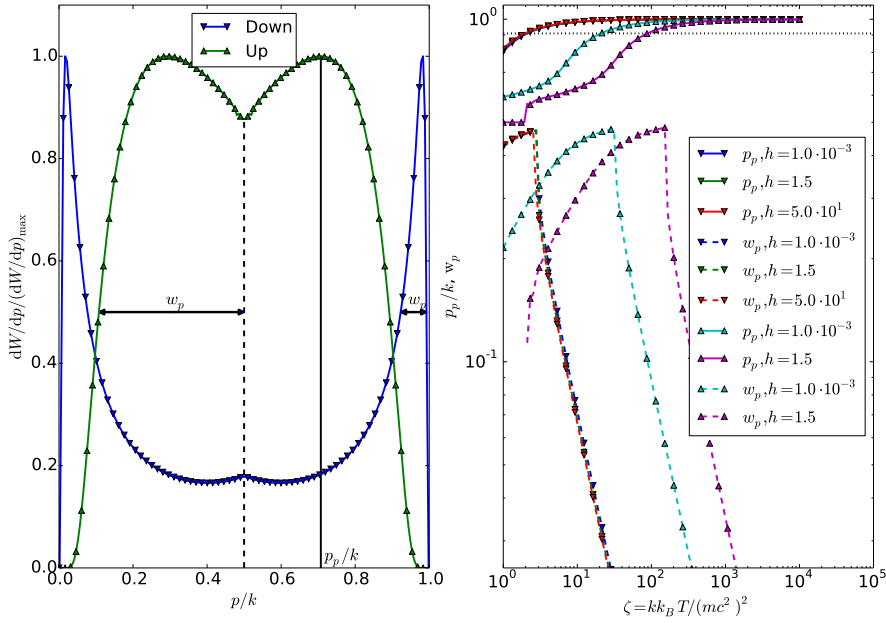


Fig. 4.8.: Left-hand-side panel : example of two normalized spectra of energy of created particles. These spectra are normalized to the amplitude of the largest peak, and energy is given in units of the incident strong photon k . In both cases, k corresponds to $\zeta = 10$ at an altitude $h = 0.5R_*$, and the only difference resides in the up or down orientation of the strong photon. As in the isotropic case 4.4, spectra are generally made of two peaks more or less thin and separated. The width at half maximum of peaks w_p is defined in the two possible cases : if one side of a peak never reaches its half before rising again to another peak in which case the width is taken to be half of the double-peak width, or if the peak is well defined on both sides in which case the definition is straightforward. The position of the most energetic peak p_p/k is defined as well. Right-hand-side panel : Evolution with ζ of positions p_p/k of the higher-energy peak (curves on the higher part of the plot), and widths at half maximum w_p (curves on the lower part of the plot) for up and down photons at various heights h (in units of R_*). Positions are ranging from 0.5 at low ζ s which corresponds to a perfectly centered peak or to a null spectrum when a reaction is below threshold (lowest energies of up photons), to $\simeq 0.98$ at large ζ s. The horizontal dotted line shows the positions at which the ratios between the two peaks is 10. Widths at half maximum are rising to ~ 0.45 until the two peaks separate and drop sharply to $\simeq 0.029$.

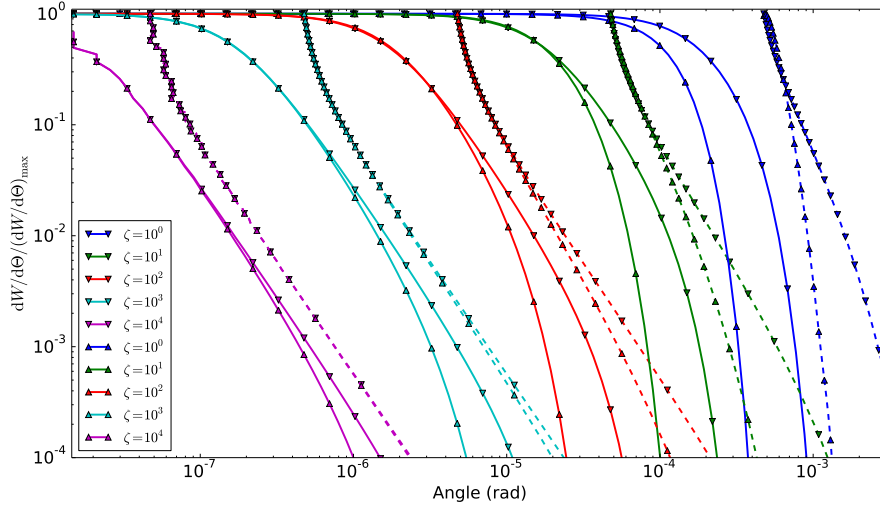


Fig. 4.9.: Angular spectra for various values of $\zeta = \frac{kk_b T}{(mc^2)^2}$ and both up and down orientations (respectively up-triangle and down-triangle markers) normalized to their maximum values. Solid lines correspond to angular spectra of the higher energy leptons ($p > k/2$) and dashed-line spectra to their lower-energy counterparts ($p < k/2$). All these spectra correspond to a height above the star $h = 0.001R_*$ which is representative for all other heights. Indeed their amplitudes significantly change with height but their shapes (and therefore the shown normalized spectra) barely change.

spectra are monotonously decreasing as the angle becomes larger, and the larger ζ the larger the outgoing angle. Lower-energy leptons have larger outgoing angles than their higher-energy counterpart and are not created below a minimum angle defined in equation (4.53). For a given ζ , leptons created from down photons are always going out at larger angles, and the difference is growing at larger angles of the spectrum. In a pulsar magnetosphere the outgoing may be important because the pairs will radiate more or less synchrotron radiation depending on their momentum perpendicular to the local magnetic field. We see here that the angles with respect to the progenitor strong photon are overall very small, which is expected from relativistic collimation. If one assumes that strong photons are produced through curvature radiation along the magnetic-field lines, then the angle distributions presented on figure 4.9 matter only if the mean free path is much shorter than the radius of curvature of the field line. This is not the case with the parameters presented in this section, and would probably require an extra source of photons.

4.3.6 Discussion

Recent simulations of aligned millisecond-pulsar magnetospheres indicate that significant pair production may occur near the so-called separatrix gap and y point

(see Cerutti and Beloborodov (2016) and references therein) near the light cylinder. This implies that the source of pairs be photon-photon collisions. However, in the most detailed modeling of pair creation realized by Chen and Beloborodov (2014), photon-photon pairs are created with a constant and uniform mean free path of $2R_*$. If one assumes that the source of soft photons is only provided by the star, this assumption seems reasonable close to the star, $h < 2R_*$, but greatly overestimated beyond owing to the exponential cutoff of the reaction rate with altitude (figure 4.6). This issue can be overcome if another source of soft photons can be found, resulting for example from synchrotron radiation near the light cylinder. Moreover, in these simulations, the direction of strong photons relative to the soft-photon sources is not taken into account, which can have an effect of several orders of magnitude on reaction rates with a strong dependence on strong-photon energies (see figure 4.7). The energy separation of the two outgoing leptons (figure 4.8) may also have an important impact on the subsequent synchrotron radiated by the pair. Indeed, the synchrotron peak frequency scales like γ^2 , where γ is the Lorentz factor of the particle around the magnetic field. Therefore, a typical situation in which the higher-energy lepton takes 10 times more energy than the other (dotted line on figure 4.6) results in two synchrotron peaks radiated two orders of magnitude apart. This situation is reached at values of ζ for which the optical depth on figure 4.7 is still high i.e. more than half the peak value. Notice that we implicitly assume here that both particles share the same angle with respect to the local magnetic field, which is justified by small outgoing angles shown on figure 4.9.

4.3.7 Conclusion

We propose a formalism to analyze photon-photon pair creations with an arbitrarily anisotropic soft-photon background. This formalism allows to calculate energy and angle spectra of outgoing pairs, as given by formulas (4.60) and (4.62) respectively.

Calculations are carried using two approximations : the first being that the strong photon is much more energetic than the soft-photon cutoff energy ϵ_{\max} , and the second that the outgoing higher-energy lepton of momentum \vec{p} be very aligned with the progenitor strong photon of momentum \vec{k} in the sense that $(\vec{k} - \vec{p})_{\perp} / (\vec{k} - \vec{p})_{\parallel} \ll 1$, (4.94), where perpendicular and parallel components are taken with respect to \vec{k} . This latter approximation is the most stringent one. Indeed, one can show that the inequality itself (< 1) is always true within the frame of our first approximation, but its large validity ($\ll 1$) comes if the reaction is far above threshold i.e. $k\epsilon_{\max}/m^2 \gg 1$.

In section 4.3.5, we compare our formalism with the exact formula that can be found in the literature (Nikishov (1962), or Agaronyan et al. (1983) eq. 4 and 5 for a more detailed formulation), and show that our approximated formulation gives results accurate at $\sim 7\%$ on average, with $\sim 10\%$ near the peak and asymptotically tend to the exact value at high energies. However, the difference can be as large as $\sim 50\%$ at low energies. We show pair spectra that are consistent with those of Agaronyan et al. (1983) in the isotropic case.

In section 4.3.5 we show that the differences created by the strong anisotropy of radiation near a hot neutron star are much more important than a few percent, potentially reaching several orders of magnitude depending on energy, direction of the strong photon, and altitude above the star. We consider two directions for strong photons : radially toward the star (down photons) and away from the star (up photons). In both cases reaction rates are stable until $1R_*$, before undergoing an exponential cutoff. However, the peak of strong-photon absorption occurs at an energy ~ 10 times larger for up photons. Energy pair spectra show two peaks symmetric with respect to $k/2$, similarly to the isotropic case. These peaks separate as the energy of the reaction rises. We show that such a difference in energy between the two outgoing leptons can importantly affect the synchrotron emission of the pairs for a large range of strong-photon energy compared to a simple model in which both components of a pair take away the same energy.

These findings are meant to contribute to a better modeling of pair creation from photon-photon collisions in pulsar magnetospheres. Recent millisecond-pulsar-magnetosphere simulations gave an important role to this pair-production mechanism (Cerutti and Beloborodov, 2016). However, the current state of modeling leaves an important uncertainty on the amount of soft photons needed to sustain such pair discharges. The results of this work provide means to estimate the mean free path on a soft-photon background resulting from a homogeneously hot neutron star. Moreover it provides formulas to obtain results with virtually any soft photon distribution, in particular resulting from secondary synchrotron close to the light cylinder. The possibility to generate energy spectra allows to differentiate between the two components of a pair and therefore to differentiate their synchrotron emissions.

4.A Derivation of the general result

We show that the domain of integration can be approximated by an hyperboloid of revolution. Then, we compute the integral W_k over this surface assuming that the distribution function of weak photons is given by a polynomial (e.g. Taylor expansion). A variety of notations and relations is used, we summarize them in appendix 4.B.

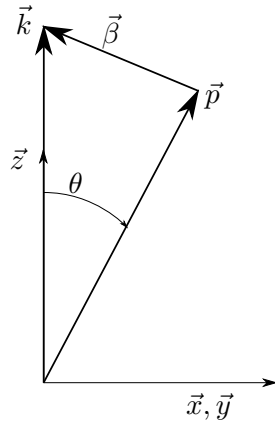


Fig. 4.10.: Coordinate system. In our approximation, \vec{k} is a quasi symmetry axis.

4.A.1 Parametrization of L_- by the three-momentum of the weak photons

The spectrum of pair creation is the density of probability of making a pair as a function of the energy of one of the particles. By definition, it is symmetric with respect to half of the total energy $k + \epsilon \simeq k$: if one of the particles has an energy p then the other has $k - p$ as a result of energy conservation. Therefore we consider only the upper half of the spectrum, for $p > k/2$ and

$$\frac{dW}{dp}(p) = \frac{dW}{dp}(k - p) \quad (4.73)$$

Therefore, we are left with the very helpful ordering

$$k \gtrsim p \gg m, \epsilon_{\max}, \quad (4.74)$$

which allows to write :

$$P^0 = p + \frac{m^2}{2p} + \mathcal{O}\left(\frac{m^2}{p^2}\right). \quad (4.75)$$

Further, we learn from the angle-averaged cross-section (Berestetskii et al., 1982) that when the reaction is way above threshold, one of the particles of the pair takes most of the energy while the other takes almost nothing (section 4.3.2), which reinforces our assumption. In the following calculation we note $\mathcal{O}(n)$ a development up to a bounded function of

$$\left(\frac{m}{k}\right)^n \sim \left(\frac{m}{p}\right)^n \sim \left(\frac{\epsilon_{\max}}{k}\right)^n \sim \left(\frac{\epsilon_{\max}}{p}\right)^n. \quad (4.76)$$

This leads to the conclusion that \vec{p} is almost aligned with \vec{k} . Indeed, we can show

that $\epsilon_{min} < \epsilon_{max}$ implies that momentum can be conserved only if $\cos \theta > C_{min}$, where

$$C_{min} = \frac{k + \epsilon_{max}}{kp} (P^0 - \epsilon_{max}) - \frac{\epsilon_{max}}{kp} \sqrt{k^2 + p^2 - 2kP^0 + 2k\epsilon_{max} - 2P^0\epsilon_{max} + \epsilon_{max}^2}. \quad (4.77)$$

This is approximated as

$$C_{min} = 1 + \frac{m^2}{2p^2} - 2\frac{\epsilon_{max}(k-p)}{kp} + \mathcal{O}(3). \quad (4.78)$$

Therefore we set \vec{k} as the main axis of our coordinate system (Figure 4.10), parallel to the unit vector \vec{z} of the direct triad $(\vec{x}, \vec{y}, \vec{z})$. For a weak photon of energy ϵ :

$$1 - \cos \theta \leq 2\frac{\epsilon(k-p)}{kp} - \frac{m^2}{2p^2} + \mathcal{O}(3) \quad (4.79)$$

By squaring relevantly the mass-shell constrain 4.18b) one obtains the following quadratic constrain :

$$\left(\epsilon(P^0 - k)\right)^2 = \left(\vec{x} \cdot (\vec{k} - \vec{p}) + K \cdot P\right)^2 \quad (4.80)$$

which can be rewritten as

$$\vec{x}(\alpha^2 1 - \bar{\beta})\vec{x} - 2A\bar{\beta} \cdot \vec{x} = A^2, \quad (4.81)$$

where

$$A = K \cdot P \quad (4.82)$$

$$\bar{\beta} = \vec{k} - \vec{p}, \quad (4.83)$$

$$\alpha = k - P^0, \quad (4.84)$$

and $\bar{\beta}$ is defined by

$$\vec{x}\bar{\beta}\vec{x} = \left(\bar{\beta} \cdot \vec{x}\right)^2. \quad (4.85)$$

We find

$$\bar{\beta} = \begin{pmatrix} \beta_x^2 & 0 & 0 \\ 2\beta_x\beta_y & \beta_y^2 & 0 \\ 2\beta_x\beta_z & 2\beta_y\beta_z & \beta_z^2 \end{pmatrix}. \quad (4.86)$$

Let's rewrite Eq. (4.81) in a dimensionless form,

$$\vec{x}\left(\frac{\alpha^2}{A^2}1 - \frac{\vec{\beta}}{A^2}\right)\vec{x} - 2\frac{\vec{\beta}}{A} \cdot \vec{x} = 1. \quad (4.87)$$

The three proper values of this quadratic form are

$$\left(\frac{\alpha^2}{A^2} - \frac{\beta_x^2}{A^2}, \frac{\alpha^2}{A^2} - \frac{\beta_y^2}{A^2}, \frac{\alpha^2}{A^2} - \frac{\beta_z^2}{A^2}\right). \quad (4.88)$$

The geometrical type of this quadratic form is determined by the signs of its proper values. For this we express the different quantities using the approximation defined in Eq. (4.74),

$$A = m^2 \left(\frac{1}{2} \frac{k}{p} + \frac{kp}{m^2} (1 - \cos \theta) \right) + \mathcal{O}(1) \quad (4.89)$$

$$= 2m^2 \frac{k-p}{m} \frac{\epsilon_{\max}}{m} \mu$$

$$\alpha = m \left(\frac{k}{m} - \frac{p}{m} - \frac{m}{2p} \right) + \mathcal{O}(2) \quad (4.90)$$

$$\sqrt{\beta_x^2 + \beta_y^2} = \beta_{\perp} = p \sqrt{2(1 - \cos \theta)} + \mathcal{O}(3) \quad (4.91)$$

$$\beta_z = \beta_{\parallel} = p \left(\frac{k}{p} - \cos \theta \right) \quad (4.92)$$

It can be shown that, provided that $\epsilon_{\max} < \frac{3}{8}m$ and for any relevant θ or p ,

$$\alpha > \beta_{\perp} \quad (4.93)$$

Similarly, provided that $\epsilon_{\max} < \frac{1}{4}m$ (see Eq. (4.25)),

$$\frac{\beta_{\perp}}{\beta_{\parallel}} < 1 \quad (4.94)$$

The smaller ϵ_{\max} with respect to m the more effective these constraints will be. (Notice that the functions are monotonous on the appropriate range.) Moreover, the maximum value of $1 - \cos \theta$ is the limiting factor for ϵ_{\max} , and therefore these limits are less stringent if one considers creation of particles at smaller angles. Besides, $\sqrt{k\epsilon_{\max}}$ ⁶ is the higher bound of the energy of the two photons in the center of mass frame, and given our condition $k \gg m$, ϵ_{\max} close to m leads to an energy way above threshold in Eq. (4.12), and therefore very unlikely to happen (section 4.3.2), although it depends on the angle of incidence of the weak photon on the strong one as well. For these reasons, we should consider that the higher limit for ϵ_{\max} is a "smooth" one meaning that most photons of the weak distribution should actually not be close to ϵ_{\max} , even when ϵ_{\max} is close to the limit $m/4$, except if one has a

⁶The energy of one photon in the center of mass of two photons, one at energy k and another at energy ϵ , is $\sqrt{k\epsilon(1 - \cos \omega)}$ where ω is the angle between the two photons 3-momenta

very peculiar photon distribution. This discussion a posteriori justifies condition 4.25. The proper vectors associated to the proper values in Eq. (4.88) are

$$\begin{aligned}\vec{v}_1 &= (0, 0, 1), \\ \vec{v}_2 &= (0, 1, v_{2z}), \\ \vec{v}_3 &= \left(1, \frac{2\beta_x\beta_y}{\beta_y^2 - \beta_x^2}, v_{3z}\right),\end{aligned}$$

with

$$v_{2z} = \frac{2\beta_y\beta_z}{\beta_z^2 - \beta_y^2} \ll 1, \quad (4.95)$$

$$v_{3z} = \left[2\beta_x\beta_z - 4\frac{\beta_x\beta_z\beta_y}{\beta_z^2 - \beta_y^2}\right] \frac{1}{\beta_z^2 - \beta_x^2} \ll 1. \quad (4.96)$$

The above components are negligible in virtue of Eqs. (4.93) and (4.94). Therefore, any vector parallel to the z axis has its image parallel to the z axis, and any vector perpendicular to the z axis has its image roughly perpendicular to the z axis.

We can simplify the orthogonal proper values in Eq (4.88), which are now both equal to :

$$\frac{\alpha^2}{A^2} \quad (4.97)$$

It can be shown that

$$\alpha < \beta_{\parallel}, \quad (4.98)$$

$$\frac{\beta_{\parallel} - \alpha}{m} = \mathcal{O}(1). \quad (4.99)$$

This implies that the parallel proper value (the third one in Eq. (4.88)) is negative. Because the parallel proper value is negative while the two orthogonal values are positive, the quadratic form in Eq.(4.81) describes a paraboloid of revolution.

The above remarks and Eqs. (4.93) and (4.94) allow to simplify the quadratic form in Eq. (4.81). We are left with

$$-\left(\frac{\beta_z^2}{A^2} - \frac{\alpha^2}{A^2}\right) (z + z_0)^2 + \frac{\alpha^2}{A^2} (y^2 + z^2) = 1 - z_0^2 \left(\frac{\beta_z^2}{A^2} - \frac{\alpha^2}{A^2}\right), \quad (4.100)$$

where

$$z_0 = \frac{A\beta_{\parallel}}{\beta_{\parallel}^2 - \alpha^2}. \quad (4.101)$$

Dividing everything by $\left(\frac{\beta_z^2}{A^2} - \frac{\alpha^2}{A^2}\right)$ we get our final, although not fully standard, form of Eq. (4.81):

$$\frac{(z + z_0)^2}{z_0^2} - \frac{x^2 + y^2}{L^2} = 1 - \delta^2, \quad (4.102)$$

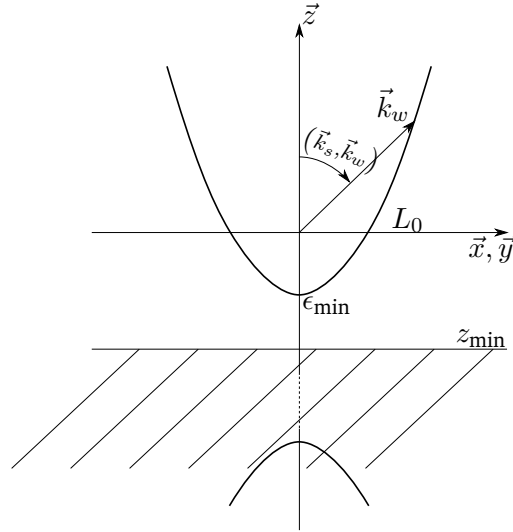


Fig. 4.11.: Representation of the mass shell (4.18)b) within approximation (4.25).

where the characteristic orthogonal radius L and the displacement δ are

$$L^2 = \frac{A^2}{\alpha^2} \frac{\beta_{\parallel}^2}{\beta_{\parallel}^2 - \alpha^2}, \quad (4.103)$$

$$\delta^2 = \frac{\beta_{\parallel}^2 - \alpha^2}{\beta_{\parallel}^2}. \quad (4.104)$$

Equation 4.100 describes a paraboloid of revolution of axis \vec{z} , i.e. parallel to the strong photon 3-momentum \vec{k} . We notice that $L^2/z_0^2 = \mathcal{O}(1)$ meaning that the hyperboloid is very steep around the parallel axis. Besides, the small displacement δ , $\delta^2 = \mathcal{O}(1)$, is responsible for a shift of the bottom of the paraboloid under the plane of zero parallel momentum. This corresponds to reactions with head-on weak photons that are in general of smaller energies, as shown on figure 4.11.

We must remember that the inclusion of L_- into the paraboloid defined in Eq. (4.102) is derived from the condition in Eq. (4.18b). It must be completed with the condition in Eq. (4.18e) that reads

$$\vec{x} \cdot \vec{\beta} + A \geq 0. \quad (4.105)$$

From a geometrical point of view, this means that the relevant photons are those with momenta above the plane of normal vector $\vec{\beta}$ of equation $\vec{x} \cdot \vec{\beta} = -A$. Using relation (4.94), this approximates to the plane orthogonal to the parallel direction, \vec{z} , at position :

$$z_{\min} = -\frac{A}{\beta_{\parallel}} \simeq -2\epsilon_{\min} \quad (4.106)$$

As a consequence, only the upper sheet of the hyperboloid defined in Eq. (4.102) corresponds to the physical mass shell. Indeed this hyperboloid crosses the parallel axis \vec{z} at abscissa z_δ^\pm such that :

$$z_\delta^\pm = -z_0 \left(1 \pm \sqrt{1 - \delta^2} \right) \quad (4.107)$$

This relation takes into account the fact that $z_0 \gg |z_{\min}|$. Because $\delta \ll 1$,

$$z_\delta = -z_0 \left(1 - \sqrt{1 - \delta^2} \right) \simeq -\frac{1}{2} z_0 \delta^2 \quad (4.108)$$

Further, one may show that $z_\delta = \min \|\vec{x}\|^7$ which corresponds to the physical idea that the smallest weak photon that can produce a pair is the one that hits the strong photon head-on. How does it compare to ϵ_{\min} determined in the previous section ? With the notations used in this section,

$$\epsilon_{\min} = \frac{A}{\|\vec{\beta}\| + \alpha}. \quad (4.109)$$

Using the approximation in Eq. ((4.94)), $\|\vec{\beta}\| = \beta_\parallel + \mathcal{O}(\beta_\perp/\beta_\parallel)$, we get

$$\epsilon_{\min} = z_\delta + \mathcal{O}(\beta_\perp/\beta_\parallel). \quad (4.110)$$

This is consistent with the definition of ϵ_{\min} in Eq. (4.22) as the minimum energy allowed in L_- .

4.A.2 Integration

We now compute the integral W_k defined in Eq. (4.16). Within the frame of our approximations, Eq. (4.102) shows that the probability of making a pair is symmetric around \vec{k} . This leads to a first angular integration of ϕ that yields a 2π factor. The differential element $d^3\vec{k}_w = dx dy dz$ is constrained by Eq. (4.102) that defines L_- . Thus we write $z = z(x, y, p)$ through the constrain $L_-(p, \cos \theta, k)$ and

$$dz = \left| \frac{\partial z}{\partial p} \right| dp. \quad (4.111)$$

⁷Then one shows easily from (4.102) that $x^2 + y^2$ has a minimum for $z_m = -z_0 \frac{L/z_0}{1 + L^2/z_0^2} = -z_0 L/z_0 + \mathcal{O}(L^2/z_0^2)$ ($\mathcal{O}(L^2/z_0^2) = \mathcal{O}(1)$). Hence $z_m \simeq -\frac{A}{\alpha} \frac{\beta_\parallel}{\alpha}$ while $z_\delta = \frac{A}{\beta_\parallel}$. Using the fact that $\alpha \lesssim \beta_\parallel$ one gets that $z_m \lesssim z_\delta$, which means z_m is slightly under the bottom of the hyperboloid. Since $x^2 + z^2$ can be easily shown to be a growing function of z , its smallest value can only be z_δ .

We can now write (4.30) as follows

$$W_{\vec{k}} = c \ 2\pi \int_{C_1}^{C_2} d \cos \theta \int_{p_1}^{p_2} dp \times \int_{L_-(x,y)} \frac{d^2 \sigma}{d\Omega} \frac{K_s \cdot K_w}{K_s^0 K_w^0} f_w(\vec{k}_w) \left| \frac{\partial z}{\partial p} \right| dx dy, \quad (4.112)$$

where $L_-(x, y)$ is the projection of L_- onto the (x, y) plane. We need to expand the different quantities appearing in (4.112). Let us start with an explicit projection of the upper hyperboloid on the plane (\vec{x}, \vec{y}) . This projection is a disc of radius

$$R = 2\epsilon_{\max} \sqrt{\mu(1-\mu)}, \quad (4.113)$$

where μ is defined in Eq. (4.31). For the change of variable $\theta \rightarrow \mu$, we need to switch the integration on p with the integration on $\cos \theta$ in (4.112), with

$$d \cos \theta = 2 \frac{(k-p)}{p} \frac{\epsilon_{\max}}{k} d\mu \quad (4.114)$$

Moreover, the shape of the domain naturally suggests to use polar coordinates in the plane (\vec{x}, \vec{y}) , with radius $r = \sqrt{x^2 + y^2}$, angle ϕ_w and $dx dy = r dr d\phi_w$. The differential cross-section is

$$\frac{d^2 \sigma}{d\Omega} = -\frac{r_e^2}{4} \frac{pm^2}{k\epsilon_{\max}^2 \mu^2} \left[\left(\frac{m^2}{4\epsilon_{\max} p \mu} + \frac{m^2}{4\epsilon_{\max} (k-p) \mu} \right)^2 - \frac{m^2}{4\epsilon_{\max} p \mu} - \frac{m^2}{4\epsilon_{\max} (k-p) \mu} - \frac{1}{4} \frac{p}{k-p} - \frac{1}{4} \frac{k-p}{p} \right]. \quad (4.115)$$

The elementary current in Eq. (4.10) is

$$\frac{K_s \cdot K_w}{K_s^0 K_w^0} = 1 - \cos \xi + \mathcal{O}(\beta_{\perp}/\beta_{\parallel}), \quad (4.116)$$

where

$$\cos \xi = 1 - 2\mu \frac{\epsilon_{\max}}{\epsilon} + \mathcal{O}(1). \quad (4.117)$$

The expression of $\epsilon = \sqrt{x^2 + y^2 + z^2}$ needs as well to be developed as a function of x, y and p , which implies to write a clear expression for $z(p)$. From Eq. (4.102),

$$z = -z_0 + z_0 \sqrt{1 + \frac{x^2 + y^2}{L^2} - \delta^2}. \quad (4.118)$$

One can show that under approximations in Eq. (4.25), $\frac{x^2 + y^2}{L^2} < 1/16$ and should be in practice much smaller. Therefore,

$$z \simeq \frac{z_0}{2} \left(\frac{x^2 + y^2}{L^2} - \delta^2 \right) \quad (4.119)$$

This allows to make ϵ explicit,

$$\epsilon = \frac{1}{4\mu\epsilon_{\max}} \left(x^2 + y^2 + 4\mu^2\epsilon_{\max}^2 \right), \quad (4.120)$$

as well as the derivative of z :

$$\frac{\partial z}{\partial p} = \frac{k^2}{2(k-p)p} \left(\frac{m^2}{kp} - \frac{2\epsilon_{\max}\mu}{k} \right) \left(1 + \frac{r^2}{4\epsilon_{\max}^2\mu^2} \right). \quad (4.121)$$

We note

$$\begin{aligned} \left(\frac{\partial z}{\partial p} \right)_{\text{left}} &= \frac{k^2}{2(k-p)p} \left(\frac{m^2}{kp} - \frac{2\epsilon_{\max}\mu}{k} \right), \\ \left(\frac{\partial z}{\partial p} \right)_{\text{right}} &= \left(1 + \frac{r^2}{4\epsilon_{\max}^2\mu^2} \right). \end{aligned}$$

We need the absolute value of $\partial z/\partial p$, and one can show from (4.121) that it is always negative, so that we shall always take the opposite of Eq. (4.121) and remove the absolute value in the following developments. The distribution function f_w is the only element that depends on ϕ_w . Moreover, the integration over the hyperboloid L_- leads to get rid of z through Eq. (4.119). For further developments, we explicitly keep track of the fact that $L_- = L_-(p, \cos \theta) = L_-(p, \mu)$

$$F_w(r, p, \mu) = \int_{\phi_w=0}^{2\pi} f_w(r, \phi_w, z(r^2, \mu)) d\phi_w. \quad (4.122)$$

We can separate the integration of (4.30) in several parts. The parts with a dependance on r are to be found in the Jacobian $|\partial z/\partial p|$ (see Eq. (4.121)) of which we take only the rightmost factor, the current in Eq. (4.116), the distribution function, and the differential element rdr . Parts that depend only on μ or p are the differential cross section in Eq. (4.115), the two first factors in the Jacobian $\left| \frac{\partial z}{\partial p} \right|$ in Eq. (4.121), and the Jacobian in Eq. (4.114). The dependance of the integrated distribution function F_w is not known a priori. We obtain

$$\begin{aligned} W_{\vec{k}} &= c2\pi \int_{p_1}^{p_2} dp \int_{\mu_1}^{\mu_2} d\mu \frac{\partial \cos \theta}{\partial \mu} \frac{d^2\sigma}{d\Omega} \left| \frac{\partial z}{\partial p} \right|_{\text{left}} \times \\ &\int_{r=0}^R \frac{\partial z}{\partial p} \Big|_{\text{right}} \frac{K_s \cdot K_w}{K_s^0 K_w^0} F_w(r, p, \mu) r dr. \end{aligned} \quad (4.123)$$

The boundary conditions on the p integral, $(p_i)_{i=1,2}$ must be understood as $p_i = \max(p_i, k - p_i)$ in virtue of symmetry (4.73). At lowest order, one can show that the r part of the integrand is merely equal to $2F_w(r, p, \mu)rdr$ and that the μ part can be reduced after a partial fraction decomposition to

$$\sum_{i=1}^4 \frac{a_i(p)}{\mu^i}, \quad (4.124)$$

where the dimensionless coefficients $a_i(p)$ are given by Eq. (4.33). Then Eq. (4.123) can be formally reduced to Eq. (4.40).

4.B Formula Compendium

The cosine of the angle θ between the strong photon \vec{k} and the outgoing lepton \vec{p} is parametrized below by

$$\cos \theta = 1 - c \quad (4.125)$$

and the following parametrization by μ can lead to significant simplifications

$$c = 2 \frac{k-p}{p} \frac{\epsilon_{\max}}{k} \mu - \frac{m^2}{2p^2}. \quad (4.126)$$

The following quantities are used are intermediates in the derivation of the hyperboloid of integration,

$$A = K \cdot P \quad (4.127)$$

$$\vec{\beta} = \vec{k} - \vec{p} \quad (4.128)$$

$$\alpha = k - P^0 \quad (4.129)$$

$$\bar{\beta} = \begin{pmatrix} \beta_x^2 & 0 & 0 \\ 2\beta_x\beta_y & \beta_y^2 & 0 \\ 2\beta_x\beta_z & 2\beta_y\beta_z & \beta_z^2 \end{pmatrix} \quad (4.130)$$

and can be explicitated to relevant order (see (4.76)) as

$$\begin{aligned} A &= m^2 \left(\frac{1}{2} \frac{k}{p} + \frac{kp}{m^2} c \right) + \mathcal{O}(1) = 2m^2 \frac{k-p}{m} \frac{\epsilon_{\max}}{m} \mu \\ \alpha &= m \left(\frac{k}{m} - \frac{p}{m} - \frac{m}{2p} \right) + \mathcal{O}(2) \\ |\beta_x| \sim |\beta_y| &\sim \sqrt{\beta_x^2 + \beta_y^2} = \beta_{\perp} = p\sqrt{2c} + \mathcal{O}(3) \\ \beta_z &= \beta_{\parallel} = p \left(\frac{k}{p} - 1 + c \right) \end{aligned} \quad (4.131)$$

The characteristics of the hyperboloid (4.102), are then related to the previous quantities by

$$\begin{aligned}
 z_0 &= \frac{A\beta_{\parallel}}{\beta_{\parallel}^2 - \alpha^2} = \frac{k}{2(k-p)}(k-p+pc) = \frac{k}{2} + \mathcal{O}(1) \\
 L^2 &= \frac{A^2}{\alpha^2} \frac{\beta_{\parallel}^2}{\beta_{\parallel}^2 - \alpha^2} = \frac{pk^2}{4(k-p)} \left(2c + \frac{m^2}{p^2}\right) = \mu k \epsilon_{\max} \quad , \quad (4.132) \\
 \delta^2 &= \frac{\beta_{\parallel}^2 - \alpha^2}{\beta_{\parallel}^2} = \frac{p}{k-p+2cp} \left(2c + \frac{m^2}{p^2}\right) = 4\mu \frac{\epsilon_{\max}}{k} + \mathcal{O}(2)
 \end{aligned}$$

where $c = 1 - \cos\theta$.

From this one finds the derivative of z :

$$\frac{\partial z}{\partial p} = \frac{k^2}{2(k-p)p} \left(\frac{m^2}{kp} - \frac{2\epsilon_{\max}\mu}{k} \right) \left(1 + \frac{r^2}{4\epsilon_{\max}^2\mu^2} \right) \quad (4.133)$$

Pulsar timing model of J0337+1715

5.1 Introduction

5.1.1 Pulsar timing

Pulsar timing takes advantage of the very high average regularity of pulsars to detect even small variations of the signal and interpret them as effects coming from the environment of the pulsar, like one or more companion, or along the path of light between the pulsar and the observer, like the variation of the density of electrons along the line of sight. The pulse-to-pulse signal is usually quite noisy, however once pulses have been piled up on a large number of cycles, the resulting average pulse profile is very stable and the times of arrival can be estimated with uncertainties as low as ~ 100 ns.

In this chapter, we try to account for the variations in the timing data of the millisecond pulsar J0337 + 1715 observed at the radiotelescope of Nançay (France)¹ by developing an adapted timing model. The observations used include 3014 times of arrival observed at the Nançay radiotelescope and span from MJD 56492 to MJD 57523. The frequency of observation is around 1.4GHz, for a bandwidth of 512MHz. Each time of arrival results from the stacking of 10min of observation (so more than 200,000 pulses stacked per time of arrival). The uncertainty on each time of arrival is $\lesssim 2\mu\text{s}$, and we seek a model providing a numerical accuracy of a few nanoseconds. This means, in particular, that the motion of the pulsar due to its companions must be resolved with an accuracy $\lesssim 1$ meter.

5.1.2 On the triple system J0337 + 1715

The discovery of the system J0337 + 1715 was initially published in Ransom et al. (2014). It consists of a radio millisecond pulsar of mass $m_p \sim 1.4M_\odot$ with a spin frequency of ~ 366 Hz orbiting with two white-dwarf stars in hierarchical order. The pulsar orbits the inner white dwarf of mass $m_i \sim 0.2M_\odot$ with a semi-major

¹This work is undertaken in collaboration with Ismaël Cognard, Lucas Guillemot and Gilles Theureau, (LPC2E Orléans, France) who carried out (and keep going!) all the timing observations.

axis $a_p \sim 2$ ls (light second), an eccentricity $e_I \sim 7 \cdot 10^{-4}$, and an orbital period of $P_I \sim 1.6$ days, forming an inner binary system. This inner binary, approximated to its barycenter, orbits the outer white dwarf of mass $m_o \sim 0.4M_\odot$ with a semimajor axis of $a_b \sim 118$ ls, an eccentricity $e_O \sim 4 \cdot 10^{-2}$, and an orbital period $P_O \sim 327$ days (see Ransom et al. (2014) or below for accurate values).

Thus, this system is fairly compact : the distance between the inner white dwarf and the pulsar is ~ 10 times smaller than the radius of the orbit of Mercury, while the entire system would roughly fit inside the orbit of Venus. Above all, their mutual interactions are strong enough for the bi-Keplerian model sketched above (see also section 5.3.1) to fail fitting the timing even on short time scales (months) (Ransom et al., 2014). From a dynamical point of view, this is what makes this system unique. Indeed, the previous pulsars with more than one companion were surrounded by planetary-mass companions at somewhat larger distances, such as B1257+12 (Wolszczan and Frail, 1992; Konacki and Wolszczan, 2003) or B1620-26 (Sigurdsson and Thorsett, 2005), and only needed small corrections on longer time scales to account for deviations from Keplerian orbits.

Therefore, the three-body motion need to be solved to model accurately the timing data. Although an analytical solution of the three-body problem was found by Sundman under the form of an infinite serie (Sundman, 1913; Henkel, 2001), its very slow convergence makes it unpractical compared to a direct numerical integration, to which we resort in the following.

In this chapter we present our work on a timing model based on a numerical integration of the three-body equations of motion. Anticipating the conclusions of this chapter, figure 5.1 shows the timing residuals of the model presented in this chapter fitted on the Nançay data presented above. We see that these residuals look compatible with noise, suggesting our model is complete and accurate. The parameters found for this model are compatible with Ransom et al. (2014), and will serve as a reference in the discussion of the different delays composing the timing formula (section 5.2).

5.2 The pulsar timing formula

The aim of the pulsar timing formula is to model the link between the integer number of turns of the pulsar made from an arbitrary reference time and the times of arrival measured at the telescope on Earth. This integer number is the keystone of pulsar timing. Since the pulsar spin period is much larger than the pulse itself, once the turn numbers are determined they provide a model independent reference of the phase of the pulsar. Said differently, any set of calculated times of arrival falling

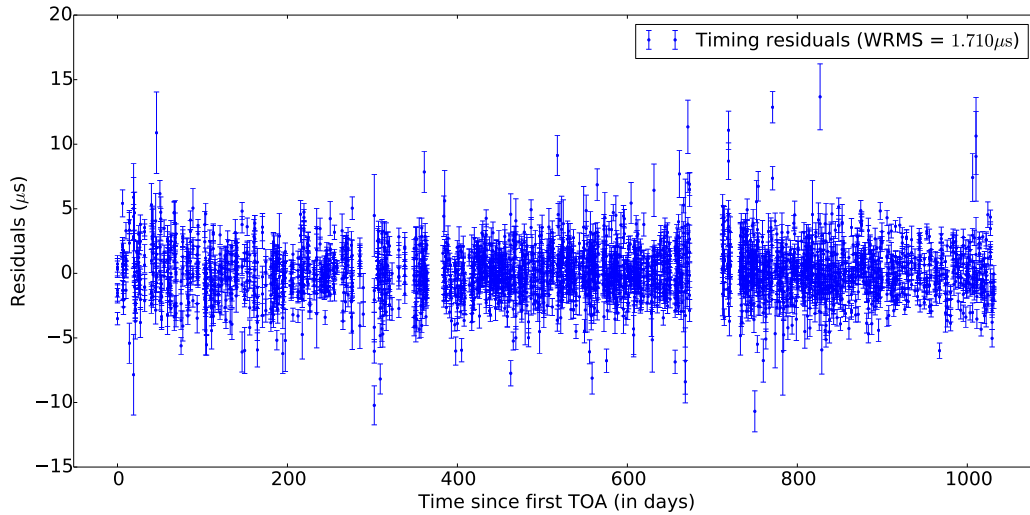


Fig. 5.1.: Timing residuals of a fit of timing data of PSR J0337+1715 with the model presented in the current chapter. There are 3014 times of arrival that were observed at the Nançay radiotelescope and span from MJD 5692 (0 on the plot) to MJD 57523. The frequency of observation is around 1.4GHz, for a bandwidth of 512MHz. Each time of arrival results from the stacking of 10min of observation.

within one spin period of a set of observed times of arrival share the same turn numbers. Fitting a particular model then amounts to compute the phase of the pulsar at each time of arrival according to the model, and fit it to the « data » made of the set of integer turns. Of course, the turns are not directly observed, but they can be determined iteratively, first by finding the common denominator of a set of close-by times of arrival, the spin period, then fitting a more complex model thanks to the turns that could be determined with this purely periodic model, which allows to extrapolate further the turns, and so on.

Four reference frames have to be considered when establishing the pulsar timing formula :

- The proper time of the observer on Earth II.
- The Solar-system-barycenter (SSB) reference frame of coordinates $(c\tau, \vec{\rho})$. The space coordinates are that of the Barycenter Coordinate Reference System (BCRS) and the time coordinate is the Time Coordinate Barycenter (TCB) defined in McCarthy and Petit (2004). The origin of spatial coordinates are at the barycenter of the system, and the time coordinate corresponds to that of an observer at infinity from (the gravitational field of) the Solar system.
- The pulsar-system-barycenter (PSB) reference frame with coordinate system (ct, \vec{r}) in which the center of mass of the system is at rest. The coordinate

system has its origin at the center of mass of the system and the proper time is that of an observer at infinity from (the gravitational field of) the pulsar system. Assuming all other sources of gravitational field are negligible in the Universe, and that the pulsar system and the Solar system are too far to influence each other gravitational field, the PSB reference frame and the SSB reference frame differ by their spatial origin and a relative velocity \vec{v}_\odot .

- The « proper » frame of the neutron star with coordinate system (cT, \vec{X}) in which the emission of the pulsar can be described as if the star was isolated (no companions) (Damour and Deruelle, 1986).

It is to be noted that we use Greek letters for coordinates in Solar-system reference frames, Latin letters for coordinates in pulsar-system reference frames, capital letters for proper times and lowercase letters for coordinate times.

5.2.1 The timing formula in the PSB reference frame

In the « proper » frame of the neutron star, the « proper » rotational phase of the star $\phi(T)$ is assumed to be given by the first three terms of its Taylor expansion,

$$\phi(T) = 2\pi fT + \frac{1}{2}2\pi f'T^2 + \phi_0, \quad (5.1)$$

where f and f' are the frequency and frequency derivative of the rotation at a time $T_0 = 0$ at which the phase is ϕ_0 . These last two quantities are unknown and inconsequential and will therefore be ignored as well as other constant terms in the following.

Then, the number of turns N corresponds to times T_N

$$N = fT_N + \frac{1}{2}f'T_N^2. \quad (5.2)$$

If the beam was emitted radially from the pulsar, T_N would correspond to the time of emission T_e of the pulse in the frame of the star. However, the transverse velocity of the region of emission is responsible for relativistic aberration, which arises from the relativistic transformation between the frame of the star and the frame of the center of mass which depends essentially on the orbital velocity of the star (see section 5.4.4). The phase of the star at the time of emission of the pulse seen by the observer $\phi(T_e)$ is then shifted from $2\pi N$ by a small amount $\delta_A\phi(T_e)$,

$$\phi(T_e) = 2\pi N + \delta_A\phi(T_e). \quad (5.3)$$

Inserting equation (5.2) into (5.3) and replacing $\phi(T_e)$ by its expression (5.1), one obtains the time of emission in the « proper » reference frame of the star,

$$T_e = T_N + \underbrace{\frac{\delta_A \phi(T_e)}{2\pi f}}_{\Delta_A(T_e)} + \mathcal{O}\left(\frac{\delta_A \phi(T_e)}{2\pi f} f' T_e\right), \quad (5.4)$$

where it is understood that for any reasonable observation span and pulsar parameters $f' T_e / f \ll 1$ and $\delta_A \phi(T_e) \ll 1$ (see section 5.4.4).

The time of emission in the PSB reference frame is obtained by adding the so-called Einstein delay $\Delta_E(t_e)$ which accounts for time dilation between the two frames due to the gravitational field of the companion(s) and the orbital velocity of the pulsar,

$$t_e = T_e + \Delta E(t_e). \quad (5.5)$$

(see section 5.4.2 for details) The signal is now on its way to the radiotelescope. We first describe the rest of the trip of the photon in the coordinate system of the PSB reference frame.

In flat spacetime, the time of travel of the photon amounts to a purely geometrical delay $\Delta_G(t_a^{\text{obs}}, t_e)$ which depends on the position of the pulsar at t_e and on the position of the observer at the arrival time t_a^{obs} (see section 5.4.1). However, spacetime is deformed on the path of the light by the gravitational field of the companion(s), and this deformation varies over the orbital period. This results in the so-called Shapiro delay $\Delta_S(t_e)$. A similar delay $\Delta_S^\odot(t_a^{\text{obs}})$ is due to the Sun and the planets in the Solar system. The Earth and the neutron star contribute as well, but by a constant amount that can be dropped.

One last kind of delay arises from the fact the radio waves do not propagate in vacuum but rather in the interstellar medium Δ_{DM} , then in the Solar wind in the surrounding of the Sun Δ_{SW} , and finally in the atmosphere of the Earth Δ_{atm} . These delays can be time dependent: Δ_{SW} depends on the orbital position of the Earth, Δ_{DM} may have a secular drift, Δ_{atm} depends on the local humidity and pressure as well as the Solar activity for the ionospheric part (Edwards et al., 2006). These delays are also frequency dependent and vanish at high frequencies. We group them in a single propagation-medium delay

$$\Delta_M = \Delta_{\text{DM}} + \Delta_{\text{SW}} + \Delta_{\text{atm}}. \quad (5.6)$$

In our model, these delays are computed by a call to the Tempo2 library (Hobbs et al., 2006; Edwards et al., 2006).

Finally, the time of arrival at the observer reads

$$t_a^{\text{obs}} = t_e + \Delta_G(t_a^{\text{obs}}, t_e) + \Delta_S(t_e) + \left[\Delta_S^\odot(t_a^{\text{obs}}) + \Delta_M \right]. \quad (5.7)$$

The square brackets emphasize that the delays that are naturally expressed in SSB coordinate time are formally converted to the PSB coordinate time.

5.2.2 Connection between the PSB and the SSB reference frames

The above expression (5.7) is fully described in the PSB reference frame. However, this is not practical for two reasons : Solar-system ephemeris are commonly given in the BCRS (our SSB reference frame) and the observer measures the times of arrival with his own proper time Π . Moreover, the SSB is generally moving with respect to the PSB at a constant velocity \vec{v}_\odot (see section 5.4.1), so that the two reference frames differ not only by their origins but also by a Lorentz boost. One solution could consist in converting everything to one frame or another (which was formally done with the square brackets above). However, the connection between the PSB, the SSB and the observer's reference frames is most conveniently made by introducing the time of arrival of an “infinite-frequency” radio pulse at the SSB. It is denoted t_a^{SSB} in the PSB coordinate time, and τ_a in the SSB coordinate time. This time of arrival corresponds to the hypothetical time of arrival of the signal at the location of the SSB were the Solar system not present and the propagation in pure vacuum: said differently the arrival time does not depend on Solar-system Shapiro delays, and neither on propagation-medium delays as would be the case for an infinite-frequency wave. The geometrical propagation delay has to be split,

$$\Delta_G = \left[\Delta_G^\odot \right] + \bar{\Delta}_G + \frac{\vec{v}_\odot \cdot \vec{n}_\odot}{c} (t_a^{\text{SSB}} - t_{\text{pos}}), \quad (5.8)$$

where $\left[\Delta_G^\odot \right]$ is the difference between the geometric path to the observer and the path to the SSB in PSB coordinate time (the square brackets have the same meaning as in equation (5.7)), and $\bar{\Delta}_G$ is the path to the SSB minus the leading parallel proper motion term, most conveniently expressed in the PSB coordinate time. The last term puts aside the leading parallel proper motion term for reasons that are explained below. The SSB is moving with respect to the PSB at a constant velocity \vec{v}_\odot from a position of reference at time t_{pos} (see section 5.4.1). The unit vector \vec{n}_\odot points from the SSB to the PSB at time t_{pos} .

Introducing the above equation (5.8) into (5.7), it results from the definition of t_a^{SSB} that

$$t_a^{\text{obs}} - \left[\Delta_G^\odot - \Delta_S^\odot - \Delta_M \right] = t_a^{\text{SSB}} = t_e + \bar{\Delta}_G + \frac{\vec{v}_\odot \cdot \vec{n}_\odot}{c} (t_a^{\text{SSB}} - t_{\text{pos}}) + \Delta_S. \quad (5.9)$$

As mentioned above, the SSB and the PSB differ only by a speed \vec{v}_\odot (if one neglects the gravitational potential of the rest of the galaxy). Therefore,

$$\tau_a = t_a^{\text{SSB}} \sqrt{1 - \vec{v}_\odot^2/c^2}. \quad (5.10)$$

The right-hand part of equation (5.9) can then be written

$$D\tau_a = t_e + \bar{\Delta}_G + \Delta_S - \frac{\vec{v}_\odot \cdot \vec{n}_\odot}{c} t_{\text{pos}}, \quad (5.11)$$

where D is the Doppler factor obtained by combining the factor in equation (5.10) with the proper motion term in equation (5.8). It is defined by

$$D = \frac{1 - \vec{v}_\odot \cdot \vec{n}_\odot}{\sqrt{1 - \vec{v}_\odot^2/c^2}}. \quad (5.12)$$

The last term in equation (5.11) is constant, but it can in principle be arbitrarily large since t_{pos} is arbitrary. We therefore choose to keep track of it, although omitting it would at worse result in a redefinition of the frequency f .

The left-hand part of equation (5.9) can be immediately transposed in the SSB coordinate time by formally removing the square brackets and operating the replacements $t_a^{\text{SSB}} \rightarrow \tau_a$, $t_a^{\text{obs}} \rightarrow \tau_a^{\text{obs}}$,

$$\tau_a^{\text{obs}} - \Delta_G^\odot - \Delta_S^\odot - \Delta_M = \tau_a. \quad (5.13)$$

The proper time of arrival of the observer is related to the coordinate time of the SSB by an Einstein delay $\Delta_E^\odot(\tau_a^{\text{obs}})$,

$$\Pi_a^{\text{obs}} = \tau_a^{\text{obs}} + \Delta_E^\odot(\tau_a^{\text{obs}}). \quad (5.14)$$

This delay is similar to that occurring between the reference frame of the star and the PSB reference frame, except that it accounts for the frame transformation arising from the velocity of the Earth and the gravitational field of the Sun and the planets.

Combining equation (5.14) with (5.13), using (5.11) combined with the pulsar system Einstein delay (5.5), and using the time of integer turns (5.4), equation (5.7) becomes

$$\tau_a = \Pi_a^{\text{obs}} - \Delta_E^{\odot}(\tau_a^{\text{obs}}) - \Delta_G^{\odot}(\tau_a) - \Delta_S^{\odot}(\tau_a^{\text{obs}}) - \Delta_M \quad (5.15)$$

$$D\tau_a = T_N + \Delta_A(T_e) + \Delta_E(t_e) + \bar{\Delta}_G(t_e) + \Delta_S(t_e) - \frac{\vec{v}_{\odot} \cdot \vec{n}_{\odot}}{c} t_{\text{pos}}. \quad (5.16)$$

Thus, we connect the number of turns N given in equation (5.2) to the time of arrival measured by the observer Π_a^{obs} .

Equation (5.15) contains only Solar-system quantities that can be expressed in the SSB frame of reference. Note that even Δ_M is defined only by Solar-system related measurements. Indeed, the interstellar dispersion term Δ_{DM} related to Δ_M by equation (5.6) is directly deduced from the spectrum of the signal measured by the observer. The two other terms are obviously most conveniently expressed on the SSB reference frame. Equation (5.16) contains mostly (but not only, see section 5.4.1) quantities related to the pulsar system that can be expressed in the PSB frame of reference.

The connection between the two τ_a equations (5.15) and (5.16) is simply made by a constant Doppler factor D (equation (5.12)). In practice, the Doppler factor cannot be measured as it is not separable from a redefinition of various parameters (Damour and Taylor, 1992), and it is common to leave it to $D = 1$.

In our model, the Solar system part (5.15) is computed by the Tempo2 library (Hobbs et al., 2006; Edwards et al., 2006), while the pulsar system part (5.16) is specific to the model developed for PSR J0337 + 1715 which we introduce in sections 5.3 and 5.4

5.3 The three-body orbits

5.3.1 Bi-Keplerian model and parametrization of the orbits

Description of the bi-Keplerian model

The simplest three-body model possible is the bi-Keplerian model. It takes advantage of the proximity of the inner white dwarf with the neutron star relative to the outer white dwarf to approximate the inner binary (the neutron star + inner white dwarf) as a pointlike particle located at its barycenter.

Therefore, the system is broken in two two-body systems (see figure 5.2). The outer system, in which positions and velocities are defined relative to the center of mass of the whole system, is composed of

- the outer white dwarf characterized by $(m_o, \vec{r}_o, \vec{v}_o)$ (mass, position and velocity relative to the center of mass of the whole system),
- the inner binary as a pointlike particle characterized by the total mass of the pulsar and the inner white dwarf $m_b = m_i + m_p$ and by the position and velocity of the barycenter of the inner binary (\vec{r}_b, \vec{v}_b) .

The inner-binary system, in which positions and velocities are defined relative to the center of mass of the binary \vec{r}_b, \vec{v}_b , is composed of

- the pulsar itself of mass m_p and position and velocity $(\vec{r}_{p/b}, \vec{v}_{p/b})$,
- the inner binary of mass m_i and position and velocity $(\vec{r}_{i/b}, \vec{v}_{i/b})$,

such that the positions and velocities of the inner-binary components relative to the whole system are defined by

$$\vec{r}_k = \vec{r}_{k/b} + \vec{r}_b, \quad (5.17)$$

$$\vec{v}_k = \vec{v}_{k/b} + \vec{v}_b, \quad (5.18)$$

where $k \in \{p, i\}$.

Description in terms of orbital elements

Each two-body orbit is solution of the independent two-body Newtonian equation of motion and the two systems are only connected by equations (5.17)-(5.18). These so-called Keplerian solutions are the well-known elliptical orbits centered on the barycenter of the two bodies. They can be entirely described by six time-invariant quantities called the orbital elements of the system, namely the semi-major axis a and the eccentricity e of the ellipse, the time of passage at periastron t_{per} , and the angles giving the orientation of the ellipse in space :

- the longitude of ascending node Ω defined by the direction in the plane of the sky, called the line of ascending node, where one of the two objects of the system (arbitrarily chosen) crosses the plane in the outward direction from the observer;

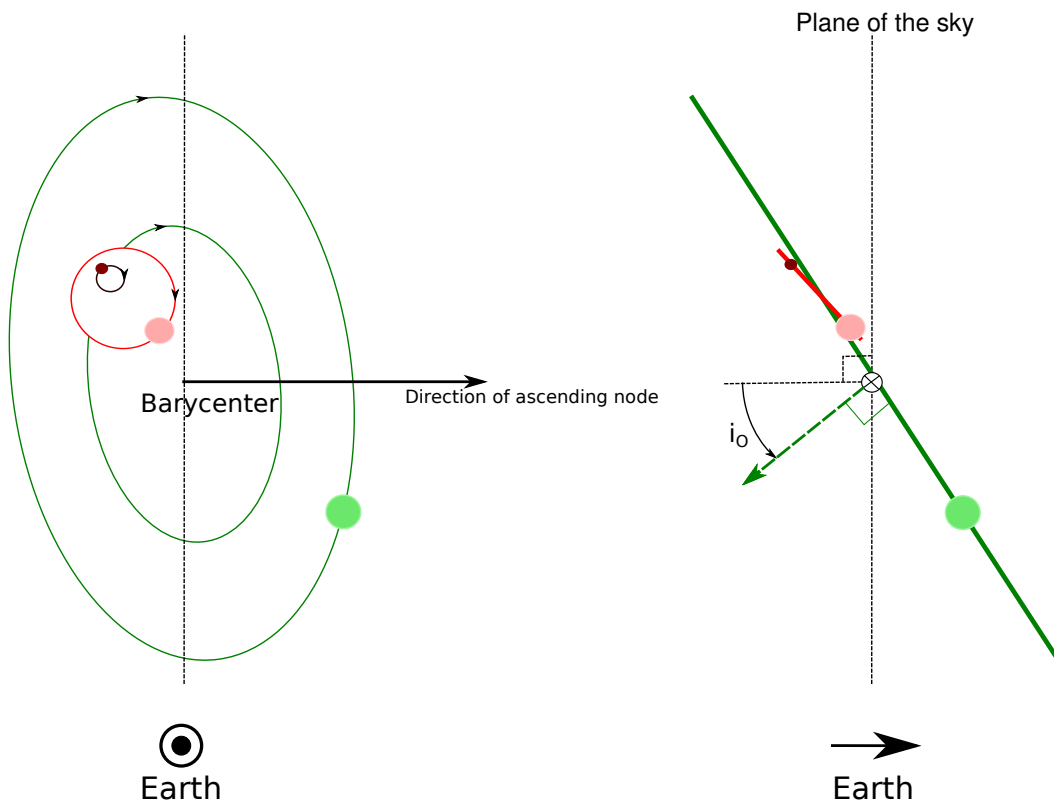


Fig. 5.2.: Sketch of the orbits of the system J0337 + 1715 assuming a bi-Keplerian model (not to scale) such as given by the osculating orbits of the initial conditions (see text). The neutron star (red) is the heaviest and has the smallest orbit. Together with the inner white dwarf (pink) it forms the inner-binary system. To a good approximation, this inner binary can be approximated to its barycenter to orbit with the outer white dwarf (green). The angle i_0 is the angle between the normal to the plane of the sky \vec{n}_\odot and the normal to the outer orbit (right-handed with the direction of travel of the orbit).

- the inclination angle defined by the angle between the normal direction to the plane of the sky and the normal direction to the plane of the orbit in the plane normal to the direction of ascending node;
- the argument of periastron ω defined by the angle between the line of ascending node and the direction of the periastron in the plane of the orbit.

The plane of the sky is defined as the plane normal to the direction of the barycenter of the whole system (see figure 5.2) seen from the barycenter of the Solar system in the Barycentric Coordinate reference System (BCRS, McCarthy and Petit (2004) and section 5.2). The direction of the line of ascending node cannot be constrained and is set arbitrarily since the pulsar cannot be angularly separated from the barycenter for such small orbits at such large distances.

Together, these parameters define the position and velocity of one of the bodies at the time of passage at periastron, and even the locus of the orbit (the ellipse), but not the speed at which the orbit is traveled at times posterior to t_{per} . This depends on the period P of the orbit, or equivalently on the reduced mass of the equivalent one-body problem (see e.g. (Beutler, 2004)). Indeed, these two parameters are connected by the so-called mass function². Taking the orbital elements for one of the bodies labeled by the subscript 1, the mass function reads

$$f(a_1, P, i) = \frac{4\pi^2 (a_1 \sin i)^3}{G P^2} = \frac{m_2^3}{\underbrace{(m_1 + m_2)^2}_{\text{Reduced mass}}} \sin^3 i, \quad (5.19)$$

where m_2 is the mass of the second body, and P is common to the two bodies so does not have a subscript. The function $\sin i$ is kept on both sides of the equality since often only $a_1 \sin i$ and P are measurable (in true binary systems) (see e.g. Blandford and Teukolsky (1976) and Damour and Deruelle (1986)).

If, additionally to the orbital elements for body one, the period (or equivalently the mass function) is known, then the positions and velocities of body one are known at every time t . Eventually, if one of the masses is known, then the other mass is deduced from the mass function, and the positions and velocities of the second body can be deduced from those of the first body using the center-of-mass and momentum conservation laws (see also section 5.3.2). The system is entirely determined, and the following biunivoque relation holds

$$(a_1, e, t_{\text{per}}, i, \omega, \Omega_1, P, m_1) \leftrightarrow (\vec{r}_1(t), \vec{v}_1(t), \vec{r}_2(t), \vec{v}_2(t), m_1, m_2), \quad (5.20)$$

²The mass function is a particular formulation of Kepler's third law commonly used in the timing of binary pulsars.

where a subscript has been added only when the quantity is not identical for both bodies.

Parametrization of the orbits in the triple system

In this section, we call orbital elements the set of the previous section completed with periods and masses, $(a_k, e_s, t_{\text{per}_s}, i_s, \omega_s, \Omega_s, P_s, m_k)$. They are either specific to one body, subscript k , or common to the two bodies in the system, subscript s . We note $k \in \{p, i\}$ in the inner binary or $k \in \{b, o\}$ in the outer system, and $s \in \{I, O\}$ for the inner-binary and the outer binary respectively.

In a non-Keplerian system the orbital elements are no longer constants of motion, however they still provide a set of quantities parametrizing the phase space as a function of time. In particular in a hierarchical system like J0337 + 1715, the orbital elements vary on a secular time scale and describe at each instant the so-called osculating orbit: the Keplerian orbit tangent to the actual orbit. They are therefore very useful to describe the initial conditions of the equations of motion at a time of reference t_0 , and we have a relation similar to (5.20) but specifically at t_0 ,

$$(a_k(t_0), e_s(t_0), P_s(t_0), t_{\text{per}_s}(t_0), i_s(t_0), \omega_s(t_0), \Omega_k(t_0), m_1) \quad (5.21)$$

$$\leftrightarrow (\vec{r}_1(t_0), \vec{v}_1(t_0), \vec{r}_2(t_0), \vec{v}_2(t_0), m_1, m_2).$$

In the following we will keep the t_0 dependency implicit.

The system J0337 + 1715 includes three bodies treated like pointlike masses. Therefore, one counts 3×6 position-and-velocity degrees of freedom, and 3 masses for a total 21 degrees of freedom. For now, we assume that the position and velocity of the center of mass are set to 0, which gives 6 relations, taking the number of degrees of freedom down to 15. This can be covered by taking the initial state vectors (at t_0) of the inner-binary barycenter (\vec{r}_b, \vec{v}_b) , and of the pulsar within the binary $(\vec{r}_{p/b}, \vec{v}_{p/b})$ and the three masses (m_p, m_i, m_o) . The three-body conservation laws for the center of mass and momentum (see also (5.29)-(5.28)) then give the other vectors,

$$m_p \vec{r}_{p/b} + m_i \vec{r}_{i/b} = \vec{0} \quad \text{and} \quad (m_p + m_i) \vec{r}_b + m_o \vec{r}_o = \vec{0}, \quad (5.22)$$

$$m_p \vec{v}_{p/b} + m_i \vec{v}_{i/b} = \vec{0} \quad \text{and} \quad (m_p + m_i) \vec{v}_b + m_o \vec{v}_o = \vec{0}. \quad (5.23)$$

In terms of orbital elements, a possible parametrization consists in

$$\begin{pmatrix} \vec{r}_{p/b}, \vec{v}_{p/b}, m_p, m_i, \\ \vec{r}_b, \vec{v}_b, m_o \end{pmatrix} \leftrightarrow \begin{pmatrix} a_p, e_I, t_{\text{per}_I}, i_I, \omega_I, \Omega_I, P_I, m_p \\ a_b, e_o, t_{\text{per}_O}, i_O, \omega_O, \Omega_O, P_O \end{pmatrix}. \quad (5.24)$$

The vectors and orbital elements on the first line are univoquely related. On the second line, m_o can be deduced from the mass function (5.19) and $m_b = m_i + m_o$ already obtained from the first line. Hence, we defined the osculating bi-Keplerian system at time t_0 (see also figure 5.2).

In practice, the data does not allow to determine both Ω_I and Ω_O (which determine the rotation of the system in the plane of the sky), however their difference matters: thus, we only have one parameter $\delta\Omega = \Omega_I - \Omega_O$. Moreover, the orbits have low eccentricities and it is known for two-body systems that a parametrization in terms of the Laplace-Lagrange parameters $e_k \cos \omega_s, e_k \sin \omega_s$ and the time of passage at the line of ascending node $t_{asc_k} = t_{per_s} - \omega_s P_s / 2\pi$ is preferable in this case (Lange et al., 2001). Finally, we use the classical binary Rømer delay parameter $a_k \sin i_s$ (see e.g. Edwards et al. (2006)) which must be completed with $a_k \cos i_s$. Our final set of initial-condition parameters is defined by

$$\begin{pmatrix} a_p \sin i_I, a_p \cos i_I, e_I \cos \omega_I, e_I \sin \omega_I, t_{asc I}, P_I, m_p \\ a_b \sin i_O, a_b \cos i_O, e_O \cos \omega_O, e_O \sin \omega_O, t_{asc O}, \delta\Omega, P_O \end{pmatrix} \quad (5.25)$$

We described here the procedure to obtain initial state vectors from orbital elements based on the Newtonian conservation laws. The procedure is very similar at the post-Newtonian (PN) level but with the use of the corresponding conservations laws (see also section 5.3.3). The algebra is made much more cumbersome, and truncations at first PN order have to be made, resulting in additional systematic errors when integrating the equations of motion (see also section 5.3.4).

5.3.2 Equations of motion at Newtonian order

At Newtonian order, the equations of motion for n-body gravitational systems are well known,

$$\frac{d\vec{v}_a}{dt} = \sum_a \sum_{b \neq a} \frac{m_b \delta \vec{x}_{ab}}{r_{ab}^3}, \quad (5.26)$$

where the m_a are the masses of each body, \vec{x}_a their positions, \vec{v}_a their velocities, $\delta \vec{x}_{ab} = \vec{x}_b - \vec{x}_a$ and $r_{ab} = \|\vec{x}_a - \vec{x}_b\|$. They satisfy conservation laws for the energy

H , the total momentum \vec{P} and the center-of-mass position \vec{X} (one could add the angular momentum),

$$H = \sum_a \left(m_a c^2 + \frac{1}{2} m_a v_a^2 \right), \quad (5.27)$$

$$\vec{P} = \sum_a m_a \vec{v}_a, \quad (5.28)$$

$$\vec{X} = \frac{1}{M} \sum_a m_a \vec{x}_a, \quad (5.29)$$

where $M = \sum_a m_a$ is the total mass of the system. We use the notation $v_a = \|\vec{v}_a\|$.

5.3.3 Equations of motion at first post-Newtonian order (1PN)

Post-Newtonian dynamics corresponds to the development of theories of gravity (general relativity but not only, see Will (2014) for a review) in powers of the small parameter $Gm/rc^2 \sim v^2/c^2 \sim \epsilon$, where m and v are masses and velocities in the system. In the case of the system J0337 + 1715, the most relativistic part is the inner binary for which $v^2/c^2 \sim 10^{-8}$, and $Gm/rc^2 \sim 10^{-6}$ so that we consider $\epsilon \sim 10^{-6}$. Given that the size of the orbit is about 2 light seconds a modification of order ϵ of the orbit can result in several microseconds of timing delay. Therefore it may be necessary to take into account leading post-Newtonian corrections up to $\mathcal{O}(\epsilon)$.

From the two-body exact analytical calculations, it is known that the main effect is the precession of periastron. Estimating this for the inner binary one gets $\delta\phi = Gm/(c^2 a(1 - e^2)) \sim 2\pi\epsilon \sim 6 \cdot 10^{-5}$ rad/revolution (see e.g. Misner et al. (1973)). However, owing to the small eccentricity of the orbit, $e_I \simeq 7 \cdot 10^{-4}$ (Ransom et al., 2014), such a precession can be partially or even entirely absorbed in a redefinition of the orbital period. This depends on the time span and the quality of the data. In the case of J0337 + 1715, the difference is not yet very significant.

We start from the Lagrangian of (Damour and Taylor, 1992) for a n-body gravitational system at first post-Newtonian order (1PN),

$$\begin{aligned} \mathcal{L} = & \sum_{a=1}^n \left[-m_a c^2 + m_a \frac{v_a^2}{2} + \frac{1}{2} \sum_{b \neq a} \left(\frac{Gm_a m_b}{r_{ab}} \right) + m_a \frac{v_a^4}{8c^2} \right. \\ & \left. + \frac{1}{2} \sum_{b \neq a} \left\{ \frac{Gm_a m_b}{r_{ab}} \left(-\frac{(\vec{v}_a \cdot \vec{n}_{ab})(\vec{v}_b \cdot \vec{n}_{ab})}{2c^2} - \frac{(4\gamma+3)\vec{v}_a \cdot \vec{v}_b}{2c^2} + \frac{1}{2}(2\gamma+1) \left(\frac{v_a^2}{c^2} + \frac{v_b^2}{c^2} \right) \right) \right. \right. \\ & \left. \left. - (2\beta - 1) \sum_{c \neq a} \frac{G^2 m_a m_b m_c}{c^2 r_{ab} r_{ac}} \right\} \right] \end{aligned}$$

where γ and β are two post-Newtonian parameters. In the following, we assume that the correct theory of gravitation is general relativity for which $\gamma = \beta = 1$.

Using the Euler-Lagrange equations, one derives the equations of motion (Soffel, 1989; Will, 1993)

$$\begin{aligned}
\frac{d\vec{v}_a}{d(ct)} = & \sum_{b \neq a} \frac{m_b \delta \vec{x}_{ab}}{r_{ab}^3} \left[1 - 4\vec{v}_a \cdot \vec{v}_b + v_a^2 + 2v_b^2 - \frac{3}{2} \frac{(\vec{v}_b \cdot \delta \vec{x}_{ab})^2}{r_{ab}^2} - \frac{5m_a}{r_{ab}} - \right. \\
& \left. 4 \sum_{c \neq a} \frac{m_c}{r_{ac}} + \sum_{c \neq a, c \neq b} m_c \left(\frac{1}{2} \frac{\delta \vec{x}_{ab} \cdot \delta \vec{x}_{bc}}{r_{bc}^3} - \frac{1}{r_{bc}} \right) \right] + \\
& \sum_{b \neq a} m_b \frac{\delta \vec{x}_{ab} \cdot (4\vec{v}_a - 3\vec{v}_b)}{r_{ab}^3} (\vec{v}_b - \vec{v}_a) + \\
& \frac{7}{2} \sum_{b \neq a} \sum_{c \neq a, c \neq b} m_b m_c \frac{\delta \vec{x}_{bc}}{r_{ab} r_{bc}^3}, \tag{5.30}
\end{aligned}$$

where $\delta \vec{x}_{ab} = \vec{x}_b - \vec{x}_a$, $r_{ab} = \|\vec{x}_a - \vec{x}_b\|$, $v_a = \|\vec{v}_a\|$ and $\vec{n}_{ab} = \delta \vec{x}_{ab}/r_{ab}$. This equation is simplified using the fact that the gravitational constant G or the speed of light c do not come separately from a mass or a velocity, except in the time derivative on the left-hand side. The complete expression is obtained by replacing masses by the corresponding Schwarzschild radius $m_{\{a,b,c\}} \rightarrow Gm_{\{a,b,c\}}/c^2$ and the velocities by the corresponding fraction of the speed of light $\vec{v}_{\{a,b,c\}} \rightarrow \vec{v}_{\{a,b,c\}}/c$.

We derived the n-body 1PN Hamiltonian using the Legendre transform $H = \sum_a \vec{v}_a \cdot \frac{\partial L}{\partial \vec{x}_a} - L$,

$$\begin{aligned}
H = & \sum_a \left\{ m_a c^2 + \frac{1}{2} m_a v_a^2 + \frac{3}{8} m_a \frac{v_a^4}{c^2} + \right. \\
& \sum_{b \neq a} \left[-\frac{Gm_a m_b}{r_{ab}} \left(1 + \frac{7}{2} \frac{\vec{v}_a \cdot \vec{v}_b}{c^2} + \frac{1}{2c^2} (\vec{v}_a \cdot \vec{n}_{ab})(\vec{v}_b \cdot \vec{n}_{ab}) - 3 \frac{v_a^2}{c^2} \right) + \right. \\
& \left. \left. \sum_{c \neq a} \frac{Gm_a m_b}{r_{ab}} \frac{Gm_c}{r_{ac} c^2} \right] \right\}. \tag{5.31}
\end{aligned}$$

Similarly, we derived the total momentum of the system $P = \sum_a \frac{\partial L}{\partial \vec{v}_a}$,

$$\vec{P} = \sum_a \left[m_a \vec{v}_a \left(1 + \frac{v_a^2}{2c^2} - \frac{1}{2} \sum_{b \neq a} \frac{Gm_b}{c^2 r_{ab}} \right) - \frac{1}{2} \sum_{b \neq a} \frac{Gm_b}{c^2 r_{ab}} (\vec{v}_a \cdot \vec{n}_{ab}) \vec{n}_{ab} \right] \tag{5.32}$$

And finally the center-of-mass \vec{X} satisfies $H/c^2 \frac{d\vec{X}}{dt} = \vec{P}$. One integrates ³ (5.32) to first order in v^2/c^2 ,

$$\frac{H}{c^2} \vec{X} = \sum_a m_a \vec{x}_a \left(1 + \frac{v_a^2}{2c^2} - \frac{1}{2} \sum_{b \neq a} \frac{Gm_b}{c^2 r_{ab}} \right). \quad (5.34)$$

The energy needs only be taken at first order (sometimes one calls it the post-Newtonian mass),

$$\frac{H}{c^2} = \sum_a \left(m_a + \frac{1}{2} m_a \frac{v_a^2}{c^2} - \sum_{b \neq a} \frac{Gm_a m_b}{c^2 r_{ab}} \right) \quad (5.35)$$

It is important to note that, although the Lagrangian (5.30) possesses exact conserved quantities and equations of motion, the consistency of calculations does not require to develop expressions further than $\circ(\epsilon)$. Consequently, the equations of motion (5.30) and the center of mass (5.34) only approximately correspond to the Lagrangian (5.30). This has the important consequence of lowering the accuracy of conservation of the conserved quantities to $\circ(\epsilon)$, which is seen to dominate over the numerical noise on figure 5.3.

5.3.4 Numerical integration of the equations of motion

The numerical integration of the Newtonian equations of motion (5.26) or 1PN equations of motion (5.30) are carried out using a Burlish-Stoer scheme with adaptive step from the Boost C++ library ⁴. The uncertainty on the times of arrival is $\sim 1\mu\text{s}$. Such a delay in the time of arrival corresponds to a displacement of the source of $1\mu\text{s} \times c \sim 300\text{m}$. Therefore we want to enforce an accuracy in the solution $\ll 300\text{m}$ and possibly lower than 1 m to reach a nanosecond level accuracy. This requires going beyond the standard 64 bits of *double* floating point precision. Instead, we use the C *long double* type which with our compiler allows encoding numbers on 80 bits, which proves sufficient to compute the position of the pulsar with an accuracy of about 1m.

³It is useful to show that, to leading order in v^2/c^2 ,

$$\sum_a m_a \vec{x}_a \frac{d}{dt} \left(v_a^2 - \sum_{a \neq b} \frac{Gm_b}{r_{ab}} \right) = - \sum_a \sum_{a \neq b} \frac{Gm_a m_b}{r_{ab}} (\vec{v}_a \cdot \vec{n}_{ab}) \vec{n}_{ab}. \quad (5.33)$$

One uses the equation of motion at Newtonian order (5.30) to express the derivative of \vec{v}_a .

⁴<http://www.boost.org/>

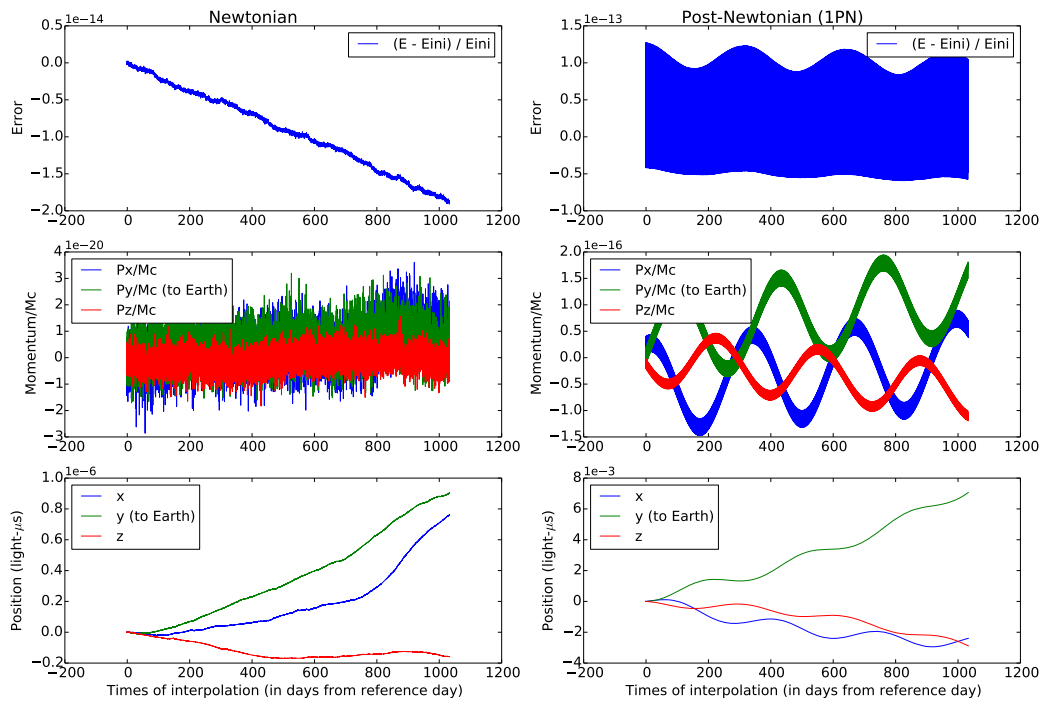


Fig. 5.3.: Conservation of energy (top), momentum (middle) and center of mass (bottom) in the purely Newtonian case (left-hand-side column) and at first post-Newtonian order (right-hand-side column). Momentum is normalized to Mc such that the plots show approximately the velocity of the center of mass as a fraction of the speed of light. The center of mass position is expressed in light microseconds ($1\mu s$), such that a value of 1 corresponds to a delay of one microsecond in a timing observation. Newtonian conservation laws are respected at machine precision level, but clear oscillations dominate in the post-Newtonian quantities that correspond to the fact that expressions are accurate only to first post-Newtonian order (see text).

The principal means of control are the conserved quantities both at Newtonian and post-Newtonian levels. Figure 5.3 shows the relative variation of the energy (equations (5.27) and (5.31)), the evolution of the momentum (equations (5.28) and (5.32)) and of the position of the center of mass (equations (5.29) and (5.34)) in the Newtonian and 1PN case on the entire time span of the data treated in this chapter. In the energy and momentum expressions the rest-mass terms have been removed to emphasize the role of the terms depending on positions and velocities.

In the Newtonian case the energy is conserved with an accuracy better than $2 \cdot 10^{-14}$ during all the integration. The velocity of the center of mass (deduced from the momentum) is about $\sim 10^{-20} Mc$ where M is the total mass of the system. This translates in a drift of the position of the center of mass of less than 10^{-6} light microseconds (μs), or $3 \cdot 10^{-4} m$.

In the 1PN case the energy is conserved with an accuracy better than $2 \cdot 10^{-13}$ during all the integration. The velocity of the center of mass (deduced from the momentum) is about $\sim 10^{-16} Mc$ where M is the total mass of the system. This translates in a drift of the position of the center of mass of less than $8 \cdot 10^{-3} \mu s$ ($\lesssim 3m$). It is clear that the accuracy is much deteriorated in this case compared to the Newtonian integration. This is negligibly due to larger round-off errors owing to the larger number of operations necessary to evaluate the 1PN equations of motion, but rather to the fact that the equations of motion are only conservative at the $\epsilon \sim 10^{-6}$ level owing to truncations in their derivation from the Lagrangian (5.30). Therefore, systematic relative errors at $\epsilon^2 \sim 10^{-12}$ occur, which is visible at the clear oscillation patterns on all the post-Newtonian panels on figure 5.3. It is also plausible that the velocity of the center of mass is enhanced because of post-Newtonian truncation error in the calculation of the initial conditions (see section 5.3.1). This has dramatic consequences on the drift of the center of mass which reaches almost 10 ns in the direction of the Earth (and is therefore detectable). However it is to be noted that this drift is mostly at constant speed plus a quasiperiodic oscillation of lower amplitude (1ns). Fortunately, the constant-velocity drift is exactly equivalent to proper motion parallel to the direction of the pulsar system (see section 5.2), and therefore will be completely absorbed when fitting for proper motion.

Overall, the goal of a few nanoseconds precision is reached in both Newtonian and post-Newtonian regimes on the present time span. However, it is to be noted that some improvements may be needed on larger time spans for the post-Newtonian motion.

5.4 The components of the timing formula : the timing delays

5.4.1 The geometric delay Δ_G

Let us assume a light signal emitted at the PSB coordinate time t_e and received at time t_a^{obs} . The purely geometrical distance between the observer at t_a^{obs} , $\vec{O}(t_a^{\text{obs}})$, and the pulsar at t_e , $\vec{P}(t_e)$, divided by the speed of light gives the geometric delay in PSB coordinate time,

$$\Delta_G = \frac{1}{c} \left\| \vec{P}(t_e) - \vec{O}(t_a^{\text{obs}}) \right\|. \quad (5.36)$$

The geometric path can be decomposed into

$$\vec{P}(t_e) - \vec{O}(t_a^{\text{obs}}) = \vec{r}_p(t_e) + \vec{R}_{\text{BB}}(t_a^{\text{SSB}}) - \vec{r}_o(t_a^{\text{obs}}) \quad (5.37)$$

where \vec{r}_o is the position of the observer with respect to the solar-system barycenter in PSB coordinates, \vec{R}_{BB} is the vector from the solar-system barycenter to the pulsar-system barycenter, and \vec{r}_p is the position of the pulsar with respect to the PSB. The vector \vec{R}_{BB} is defined by

$$\vec{R}_{\text{BB}} = d\vec{n}_{\odot} + \underbrace{\vec{v}_{\odot}(t_a^{\text{SSB}} - t_{\text{pos}})}_{\vec{k}}, \quad (5.38)$$

where d is the distance between the barycenters of the Solar and pulsar systems at a reference time t_{pos} , \vec{k} is the displacement of the PSB relative to the SSB relative to t_{pos} , and \vec{n}_{\odot} is the unit vector pointing from the SSB to the PSB at t_{pos} . We assume that the relative motion is purely inertial, and no significant extra source of acceleration is present (in particular the gravitational potential of the galaxy is negligible, see e.g. Edwards et al. (2006)).

The unit vector pointing to the pulsar barycenter from the Solar-system barycenter \vec{n}_{\odot} at t_{pos} can be expressed as a function of the right ascension α and declination δ (in the BCRS),

$$\vec{n}_{\odot}(t) = \begin{pmatrix} \cos \alpha \cos \delta \\ \sin \alpha \cos \delta \\ \sin \delta \end{pmatrix}. \quad (5.39)$$

The motion of the PSB relative to the SSB is decomposed onto the right-handed orthonormal vector basis $(\vec{u}_\alpha, \vec{u}_\delta, \vec{n}_\odot)$ where (in the BCRS),

$$\vec{u}_\alpha = \begin{pmatrix} -\sin \alpha \\ \cos \alpha \\ 0 \end{pmatrix}, \vec{u}_\delta = \begin{pmatrix} -\cos \alpha \sin \delta \\ -\sin \alpha \sin \delta \\ \cos \delta \end{pmatrix}. \quad (5.40)$$

Proper motion can then be expressed in this base by $\vec{k} = \vec{\mu}d(t_a^{\text{SSB}} - t_{\text{pos}})$. The proper motion motion vector $\vec{\mu} = (\mu_\alpha, \mu_\delta, \mu_\parallel) = (\alpha' \cos \alpha, \delta', d'/d)$, where α', δ', d' are the derivative with respect to the time in the SSB τ at t_{pos} of the right ascension, declination and distance of the PSB.

Taking the Euclidian norm of (5.37) and inserting (5.38), the geometric delay can be expressed

$$\Delta_G = c^{-1} \left(d^2 + 2d\vec{n}_\odot \cdot (\vec{r}_p + \vec{k} - \vec{r}_o) + (\vec{r}_p + \vec{k} - \vec{r}_o)^2 \right)^{1/2}, \quad (5.41)$$

where it is understood that the position of the pulsar \vec{r}_p is taken at the time of emission t_e and the position of the observer \vec{r}_o at the time of arrival at the observer t_a^{obs} .

The distance d being overwhelmingly larger than the other terms it is numerically unfit, and we need to expand (5.41) to second order in $\frac{\|\vec{r}_p + \vec{k} - \vec{r}_o\|}{d}$ to be able to put aside the constant, and therefore inessential, d/c term,

$$\begin{aligned} \Delta_G = & \frac{d}{c} \left(1 + \frac{\vec{r}_p + \vec{k} - \vec{r}_o}{d} \cdot \vec{n}_\odot + \right. \\ & \frac{\|\vec{r}_p + \vec{k} - \vec{r}_o\|^2}{2d^2} - \frac{((\vec{r}_p + \vec{k} - \vec{r}_o) \cdot \vec{n}_\odot)^2}{2d^2} + \\ & \left. \frac{((\vec{r}_p + \vec{k} - \vec{r}_o) \cdot \vec{n}_\odot)^3}{2d^3} - \frac{((\vec{r}_p + \vec{k} - \vec{r}_o) \cdot \vec{n}_\odot) \|\vec{r}_p + \vec{k} - \vec{r}_o\|^2}{2d^3} \right). \end{aligned} \quad (5.42)$$

We shall keep only one term from the third order correction in the following, the Shklovskii correction, as it is potentially much larger than the others (see discussion below).

After dropping the d/c term in (5.42), we separate Δ_G into the three parts of equation (5.8), which we recall,

$$\Delta_G = [\Delta_G^\odot] + \bar{\Delta}_G + \frac{\vec{v}_\odot \cdot \vec{n}_\odot}{c} (t_a^{\text{SSB}} - t_{\text{pos}}). \quad (5.43)$$

The extra-Solar part of the geometric delay can be developed into

$$\Delta_G^- = \frac{1}{c} \left(\underbrace{\vec{r}_p \cdot \vec{n}_\odot}_{\text{Roemer}} + \underbrace{\frac{k_\perp^2}{2d}}_{\text{Shklovskii}} + \underbrace{\frac{\vec{r}_{p\perp}^2}{2d} - \frac{\vec{r}_{p\perp} \cdot \vec{r}_{o\perp}}{d} + \frac{\vec{k}_\perp \cdot \vec{r}_{p\perp}}{d}}_{\text{Kopeikin}} - \underbrace{\frac{k_\parallel k_\perp^2}{2d^2}}_{\text{Shklovskii correction}} \right), \quad (5.44)$$

where the component of a vector \vec{x} parallel to the unit vector \vec{n}_\odot is denoted $x_\parallel = \vec{x} \cdot \vec{n}_\odot$, and the perpendicular component is denoted

The first term in (5.44) is the so-called Rømer delay (see e.g Blandford and Teukolsky (1976)), the second term was introduced in Shklovskii (1970), the following three terms are collectively called the « Kopeikin terms » and the last term is the only second-order term we keep which can be interpreted as a correction to the Shklovskii term. The first two terms are respectively called the annual-orbital parallax and the orbital parallax (Kopeikin, 1995), the third is the apparent viewing-geometry term (Kopeikin, 1996). The Rømer delay component of the timing solution of PSR J0337 + 1715 is shown on figure 5.4. The projection of the orbital motion is essentially sinusoidal, with the particularity of the triple system that two quasisinusoidal components are superimposed, one for each companion.

Assuming a biperian model of the orbits (see section 5.3.1), one can estimate the order of magnitude of each term. Recalling that the position of the pulsar $\vec{r}_p = \vec{r}_{p/B} + \vec{r}_B$, the amplitude of the Rømer delay is

$$\begin{aligned} \frac{\vec{r}_p \cdot \vec{n}_\odot}{c} &= \frac{\vec{r}_{p/B} \cdot \vec{n}_\odot + \vec{r}_B \cdot \vec{n}_\odot}{c}, \\ &\sim \frac{2a_p \sin i_i}{c} + \frac{2a_B \sin i_o}{c}, \\ &\sim 2.4\text{s} + 1.5 \cdot 10^2\text{s}, \end{aligned} \quad (5.45)$$

where the two last lines give the order of magnitude of the amplitude (between a minimum and a maximum) of the leading quasiperiodic terms of periods P_I and P_O for the first and second term respectively. These two components are visible on figure 5.4.

Assuming a pulsar proper motion $\vec{v}_\odot \sim 100\text{km/s}$ during 10 years and parameters of PSR J0337 + 1715 the Shklovskii term weights $k_\perp^2/2d \lesssim 0.08\text{s}$, and the Kopeikin terms $\vec{r}_{p\perp}^2/2d \lesssim 5 \cdot 10^{-2}\mu\text{s}$, $\vec{r}_{p\perp} r_o/d \lesssim 1\mu\text{s}$, and $k_\perp \vec{r}_{p\perp}/d \lesssim 100\mu\text{s}$. Although the Shklovskii term is large, it cannot usually be distinguished from a redefinition of the frequency derivative f' owing to its t_a^2 dependence. The order of magnitude of the largest second order terms, in $1/d^2$, can be estimated by multiplying the present estimates of the first-order terms by $\|\vec{k}\|/d \lesssim 10^{-6}$ on a ten-year time scale. Only the Shklovskii term is large enough to yield a contribution larger than 1ns in second

order terms, which is the reason why we included the Shklovskii correction term in equation(5.44) and nothing else.

The Solar-system part of the geometric delay contains all the remaining terms. Further, Δ_G^\odot is obtained from $[\Delta_G^\odot]$ by operating the replacement $\vec{r}_o \rightarrow \vec{\rho}_o$ where $\vec{\rho}_o$ is the position of the observer in SSB coordinates. Ideally the displacement \vec{k} and the distance d should also be replaced by their value in SSB coordinates, however the difference between the two frames is of order $\vec{v}_\odot^2/c^2 \ll 1$ and these two quantities only occur at order $1/d$ terms. We therefore neglect this difference and keep the PSB coordinate \vec{k} and d for convenience. We obtain

$$\Delta_G^\odot = \frac{1}{c} \left(-\vec{\rho}_o \cdot \vec{n}_\odot - \frac{k_\perp \rho_{o\perp}}{d} + \frac{\rho_{o\perp}^2}{d} \right), \quad (5.46)$$

where the component of a vector \vec{x} perpendicular to the unit vector \vec{n}_\odot is denoted $x_\perp = \vec{x} - \vec{x} \cdot \vec{n}_\odot$. Note that we did not keep any second order term here as they are all negligible for our purpose (see estimates above).

Note that from our definition of Δ_G^\odot (equation (5.8) and the discussion around), this delay accounts for the difference between the geometric path from the pulsar to the observer and the from the pulsar to the SSB. As a result, Δ_G^\odot is strictly-speaking made of all the terms containing ρ_o . However, Δ_G^\odot contains one r_o term, namely the annual-orbital Kopeikin term. This discrepancy is explained by the fact that we are tied to the computation of Δ_G^\odot by the Tempo2 library, which associates all Kopeikin terms to the pulsar-system part of the geometric delay (equation (50) of Edwards et al. (2006)). Nevertheless, this difference is negligible. Let us recall that the separation of Δ_G in two terms aims only at defining the time of arrival at the SSB in SSB coordinate time τ_a (equation (5.9) and (5.13)) in order to connect it with its equivalent in PSB coordinate time t_a^{SSB} through equation (5.10). The difference between the two times is $t_a^{\text{SSB}} - \tau_a = \mathcal{O}(\vec{v}_\odot^2/c^2)$ and therefore the error made on the emission time is of negligible order $\sim 1/d \mathcal{O}(\vec{v}_\odot^2/c^2)$. Besides, as explained at the end of section 5.2 the Doppler factor D (equation (5.12)) is not separately measurable and often in practice $D = 1$, in which case the PSB and SSB time coordinate are equal and the problem does not effectively exist.

5.4.2 The Einstein delay Δ_E

The Einstein delay accounts for the redshift between the « proper » reference frame of the pulsar and the PSB reference frame. It can be shown (Will, 1984) that taking into account the strong field contribution of the neutron star itself changes the result only by an inessential constant. Moreover, the extent of the star compared to the scale of variation of the gravitational field of the companions is very small. Therefore,

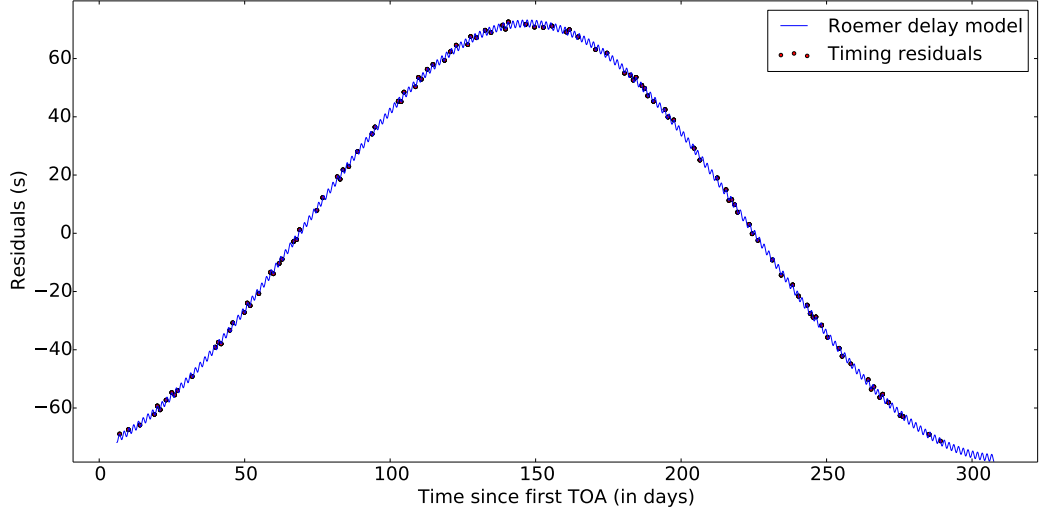


Fig. 5.4.: Roemer delay component of the timing solution of PSR J0337 + 1715 shown on figure 5.1. The computed value of equation (5.44) (blue line) has been removed from the residuals (red dots). One clearly sees one period between ~ 0 and ~ 300 days of amplitude ~ 150 s due to the orbit with the outer white dwarf, and a modulation at the inner binary period of amplitude ~ 2 s.

in the following, the neutron star is formally approximated to a pointlike massless particle of proper time T .

At first post-Newtonian order, i.e. neglecting terms of order smaller than $Gm/r \sim v^2/c^2 = \epsilon$ where m, r, v are characteristic masses, orbital distances, and velocities of the system, the metric in PSB coordinates reads

$$ds^2 = \left(1 - 2\frac{U}{c^2}\right)c^2 dt^2 - \left(1 + 2\frac{U}{c^2}\right)d\vec{r}^2 + o(\epsilon), \quad (5.47)$$

where ds is the elementary length element, and any other gravitational field than those of the pulsar system is neglected. The gravitational potential at Newtonian order is given by

$$U(\vec{r}) = \sum_{k \in \{i, o\}} \frac{Gm_k}{|\vec{r}_k - \vec{r}|}, \quad (5.48)$$

where the sum runs over all the companions of the system, m_k and \vec{r}_k being the mass and the position of each of them. The subscripts $k \in n\{i, o\}$ respectively stand for inner companion and outer companion. The pulsar has coordinates (\vec{r}_p, \vec{v}_p) .

The proper time of the pulsar is defined from the metric by

$$dT^2 = dt^2 \left(1 - 2\frac{U(\vec{r}_p)}{c^2} - \frac{\vec{v}_p^2}{c^2} + o(\epsilon)\right), \quad (5.49)$$

where $\vec{v}_p = d\vec{r}_p/dt$ is the velocity of the pulsar in the PSB reference frame.

Taking the square-root of equation (5.49), developing it to relevant order in ϵ , and integrating,

$$T - t_0 = t - T_0 - \int_{t_0}^t dt \left(\frac{U(\vec{r}_p)}{c^2} + \frac{\vec{v}_p^2}{2c^2} \right), \quad (5.50)$$

where t_0 is the (arbitrary) time at which the proper time T coincides with the PSB coordinate time.

Eventually, the Einstein delay of equation (5.5) is given by

$$\Delta_E(t_e) = t_e - T_e = \int_{t_0}^{t_e} dt \left(\frac{U(\vec{r}_p)}{c^2} + \frac{\vec{v}_p^2}{2c^2} \right) \quad (5.51)$$

In the two-body case, the above integral grows linearly with time on average, to which adds up a sinusoidal component. Since the linear component cannot be distinguished from a redefinition of the pulsar frequency f , analytical timing models usually drop it (see e.g. Blandford and Teukolsky (1976), Damour and Deruelle (1986)). With three bodies, the orbital motion is only quasi-periodic (in the case of PSR J0337 + 1715) and there is no rigorous exact definition of a linear component possible. Therefore in our numerical model, the Einstein delay is computed through direct integration of the integral in (5.51). However, to emphasize the oscillatory behavior of the delay, we approximately removed the linear component on figure 5.5 by showing $\Delta_E(t_e) - (\Delta_E(t_e^{\text{last}}) - \Delta_E(t_e^{\text{first}}))/(t_e^{\text{last}} - t_e^{\text{first}})t_e$.

Orders of magnitude of the quasiperiodic terms can be estimated. We assume a bi-Keplerian model (see section 5.3.1). Recalling that the barycenter b of the inner binary is in orbit with the outer companion, one decomposes the position and the speed of the pulsar in $\vec{r}_p = \vec{r}_{p/b} + \vec{r}_b$, $\vec{v}_p = \vec{v}_{p/b} + \vec{v}_b$. It follows that the amplitude of the oscillatory components of the velocity term in equation (5.51) are estimated to

$$\begin{aligned} \int dt \frac{\vec{v}_p^2}{c^2} &= \frac{1}{c^2} \int dt \left(\vec{v}_{p/b}^2 + \vec{v}_b^2 + 2\vec{v}_{p/b} \cdot \vec{v}_b \right), \\ &\sim \frac{e_I^2 a_p^2}{c^2 P_I} + \frac{e_O^2 a_b^2}{c^2 P_O} + \frac{8\pi a_b a_p}{c^2 P_O}, \\ &\sim 10^{-5} \mu\text{s} + 1 \mu\text{s} + 100 \mu\text{s}, \end{aligned} \quad (5.52)$$

and for the gravitational potential term,

$$\begin{aligned} \int dt \frac{U(\vec{r}_p)}{c^2} &= \int dt \frac{Gm_i}{c^2 \|\vec{r}_{p/b}\| \left(1 + \frac{m_p}{m_i}\right)} + \frac{Gm_o}{c^2 \|\vec{r}_b + \vec{r}_{p/b}\| \left(1 + \frac{m_p+m_i}{m_o}\right)} \\ &\sim \frac{e_p Gm_i}{c^2 (a_p + a_b) 2\pi} \frac{P_I}{c^2 a_b \left(1 + \frac{m_p+m_i}{m_o}\right) 2\pi} + \frac{e_o Gm_o}{c^2 a_b^3 \left(1 + \frac{m_p+m_i}{m_o}\right)^3 2\pi} \frac{P_I}{c^2 a_b^3 \left(1 + \frac{m_p+m_i}{m_o}\right)^3 2\pi}, \\ &\sim 1 \mu\text{s} + 1000 \mu\text{s} + 0.1 \mu\text{s}, \end{aligned} \quad (5.53)$$

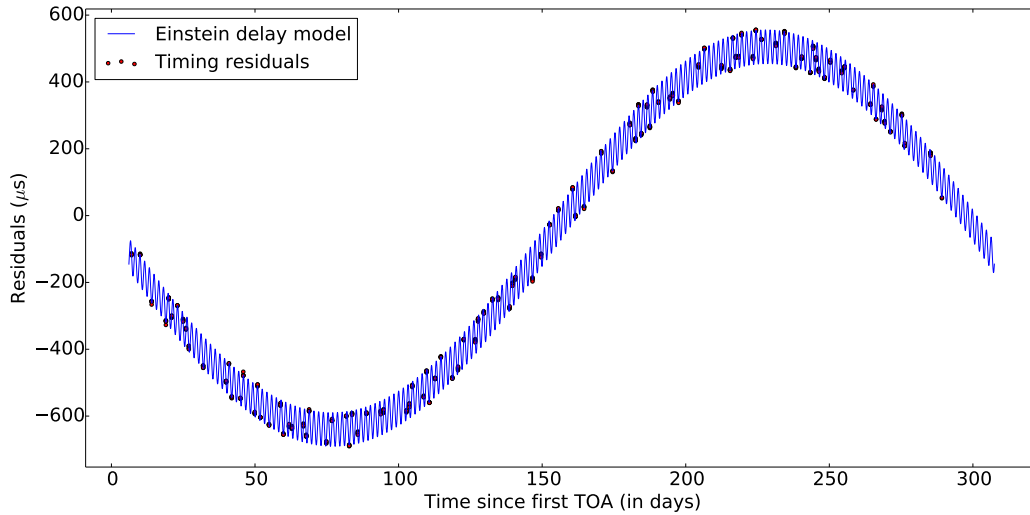


Fig. 5.5.: Einstein delay component of the timing solution of PSR J0337 + 1715 shown on figure 5.1. The computed value of equation (5.51) (blue line) has been removed from the residuals (red dots). The linear component of the Einstein delay has been removed for clarity (see text). One clearly sees one period between ~ 0 and ~ 300 days of amplitude ~ 1.1 ms due to the gravitational field and the eccentricity of the outer white dwarf, and a modulation at the inner binary period of amplitude ~ 0.1 ms due to the cross velocity term (see text).

where the last two lines of equations (5.52) and (5.53) show the amplitude (between a minimum and a maximum) of each quasiperiodic term. The last term on the first line gives the last two terms on the last two lines. The integral goes over one quasiperiod P_I or P_O for eccentricity terms, and in cross terms the outer component is assumed to be approximately constant over one inner period P_I .

As in the two-body case, the oscillatory part is created by the eccentricities of the orbits. Indeed, in a circular two-body motion, U and \vec{v}_p^2 are constants. However, the presence of a third body creates new terms corresponding to the coupling between the orbits in $\vec{r}_{p/b} \cdot \vec{r}_b$ and $\vec{v}_{p/b} \cdot \vec{v}_b$. This cross term largely dominates the otherwise quasinegligible velocity terms and is weak in the potential terms (third term of (5.52) and (5.53)). Overall, the Einstein delay for PSR J0337 + 1715 is dominated by the outer companion orbit and by the velocity coupling term, the latter being specific to three-body systems.

5.4.3 The Shapiro delay Δ_S

The so-called Shapiro delay (Shapiro, 1964) accounts for the first order correction to the light travel time due to general relativity. As for the Einstein delay, the contribution of the neutron star amounts to an inessential constant (Damour and

Deruelle, 1986). We therefore focus on the perturbation from the companions, using the first-post-Newtonian-order metric (5.47).

Let us consider a photon emitted by the pulsar and traveling in vacuum. The line element (5.47) is null along the trajectory of the photon such that

$$dt^2 = d\vec{r}^2 \left(1 + 4 \frac{U(\vec{r})}{c^2} \circ (\epsilon) \right), \quad (5.54)$$

where \vec{r} is the position of the photon at time t in PSB coordinates.

Taking the square-root of equation (5.54), developing it to relevant order in ϵ , and integrating,

$$t_a^{\text{obs}} - t_e = \Delta_G + 2 \int_{\vec{r}=\vec{r}_p(t_e)}^{\vec{r}_o(t_a^{\text{obs}})} d \|\vec{r}\| \frac{U(\vec{r})}{c^2}, \quad (5.55)$$

where Δ_G is the geometric delay (including the distance d) as defined in equation (5.36) and corresponds to the integration of the first term in equation (5.54).

Given the very large distance between the pulsar and the observer the integral in equation (5.55) can be split in two, namely $\int_{\vec{r}=\vec{r}_p(t_e)}^{\vec{r}_o(t_a^{\text{obs}})} = \int_{\vec{r}=\vec{r}_p(t_e)}^{\infty} + \int_{\infty}^{\vec{r}_o(t_a^{\text{obs}})}$, which gives rise to the two Shapiro delays in the pulsar system Δ_S and in the Solar system Δ_S^\odot . We focus here on the former.

To compute the integral, the assumption is made that the position of the companions is fixed to their positions at t_e . Since the companions move at speeds $\sim v \ll c$, the displacement of the companions during the passage of light in their zone of gravitational influence amounts to a correction of order $\sim v/c$. The amplitude of the Shapiro delay in the case of PSR J0337 + 1715 is of only a few microseconds and such a correction can safely be neglected (see figure 5.6). The Shapiro delay is then given by (Backer and Hellings, 1986)

$$\begin{aligned} \Delta_S(t_e) &= \int_{\vec{r}=\vec{r}_p(t_e)}^{\infty} d \|\vec{r}\| \frac{U(\vec{r})}{c^2} \\ &= - \sum_{k \in \{i, o\}} \frac{2Gm_k}{c^3} \ln \left(\frac{\|\vec{r}_k - \vec{r}_p\| + (\vec{r}_k - \vec{r}_p) \cdot \vec{n}_\odot}{\text{constant}} \right), \end{aligned} \quad (5.56)$$

where it is understood that $\vec{r}_p = \vec{r}_p(t_e)$ and $\vec{r}_k = \vec{r}_k(t_e)$.

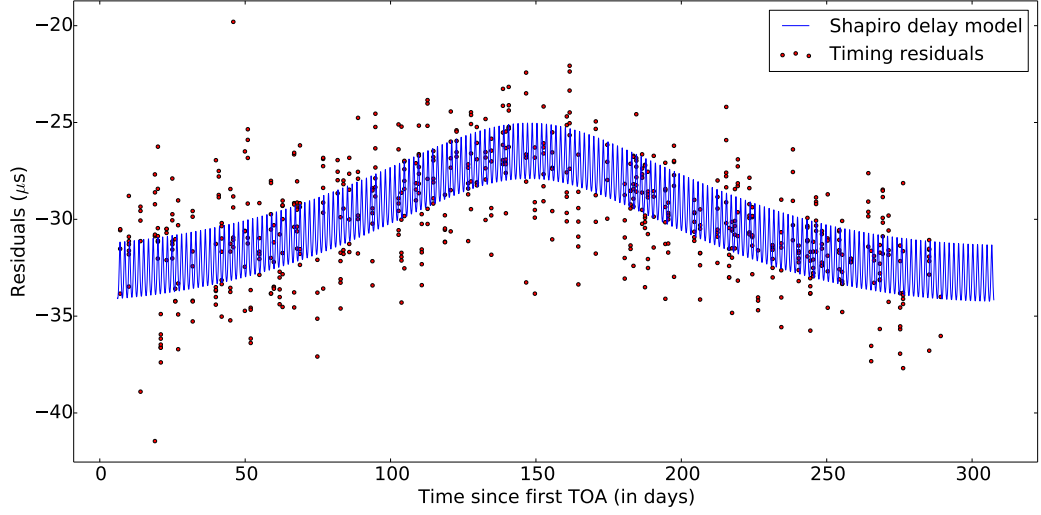


Fig. 5.6.: Shapiro delay component of the timing solution of PSR J0337 + 1715 shown on figure 5.1. The computed value of equation (5.56) (blue line) has been removed from the residuals (red dots). One clearly sees one period between ~ 0 and ~ 300 days of amplitude $\sim 7\mu\text{s}$ due to the orbit with the outer white dwarf, and a modulation at the inner binary period of amplitude $\sim 3\mu\text{s}$. The amplitude of the latter Shapiro delay is comparable to the timing noise.

Assuming a bikeplerian model (section 5.3.1), one sees that the amplitude between the maximum and the minimum of the Shapiro delay depends essentially on the masses and on the inclinations of the planes of the orbits,

$$\begin{aligned} \max(|\Delta_S|) - \min(|\Delta_S|) &= \sum_{k \in \{i, o\}} \frac{2Gm_k}{c^3} \ln \left(\frac{\max(\|\vec{r}_k - \vec{r}_p\| + (\vec{r}_k - \vec{r}_p) \cdot \vec{n}_{\odot})}{\min(\|\vec{r}_k - \vec{r}_p\| + (\vec{r}_k - \vec{r}_p) \cdot \vec{n}_{\odot})} \right), \\ &\sim \sum_{k \in \{i, o\}} \frac{2Gm_k}{c^3} \ln \left(\frac{1 + \sin i_k}{1 - \sin i_k} \right), \end{aligned} \quad (5.57)$$

$$(5.58)$$

Since the orbits are almost coplanar $i_o \simeq i_i$, and the difference between the two bodies is explained by their masses, $m_i \sim 0.2$, $m_o \sim 0.4$.

Figure 5.6 shows the Shapiro delay component calculated for PSR J0337 + 1715. One clearly sees the two components, although only the outer-companion component is sensitively larger than the noise level.

5.4.4 The aberration delay Δ_A

The aberration delay of equation (5.3) accounts for the fact that the emission from the pulsar is radial only in the proper frame of the emission mechanism, somewhere in the close magnetosphere presumably corotating with the star. Like the Einstein

and Shapiro delays, in can be treated without regard for the strong gravitational field of the neutron star, which only amounts to a constant shift (Damour and Deruelle, 1986). Therefore, the problem can be treated as that of a purely special relativistic source.

Let us consider three reference frames : the emission reference frame \hat{E} which is the « proper » frame of the emission mechanism, the « proper » reference frame of the pulsar \hat{P} , and the PSB reference frame $\hat{P}\hat{S}\hat{B}$. Here « proper » applies to a virtual massless neutron star. The emission frame \hat{E} is moving at a speed $2\pi f(T)R_e$ relatively to \hat{P} , where R_e is the radius of emission from the center of the star, and $f(T)$ is the spin frequency at the instant T . Given the smallness of the aberration delay (see below), the time variation of the spin frequency can be neglected on observational time scales and $f(T) = f$ is constant. Therefore, the Lorentz transformation between \hat{E} and \hat{P} amounts to a small constant angular shift of the direction of emission. If the pulsar orbits with companions, however, the transformation from \hat{P} to $\hat{P}\hat{S}\hat{B}$ depends on the instantaneous pulsar velocity \vec{v} with respect to the PSB. This transformation leads to a phase shift at the time of emission compared to a radial emission of

$$\delta_A\phi(T_e) = 2\pi f \frac{\vec{\omega} \times \vec{n}_\odot}{\|\vec{\omega} \times \vec{n}_\odot\|^2} \cdot \frac{\vec{v}(t_e)}{c} + \mathcal{O}\left(\frac{v^2}{c^2}\right), \quad (5.59)$$

where $\vec{\omega}$ is the spin vector of the pulsar (right-hand orientation) with norm $\|\vec{\omega}\| = 2\pi f$.

Following equation (5.4), we obtain the corresponding aberration delay (Smarr and Blandford, 1976; Damour and Deruelle, 1986),

$$\Delta_A(t_e) = \frac{\delta_A\phi(T_e)}{2\pi f} = \frac{\vec{\omega} \wedge \vec{n}_\odot}{\|\vec{\omega} \wedge \vec{n}_\odot\|^2} \cdot \frac{\vec{v}(t_e)}{c} + \mathcal{O}\left(\frac{v^2}{c^2}\right). \quad (5.60)$$

The amplitude of this delay depends on the direction of the spin axis. This delay could in principle be a way to determine it, however its amplitude is so small, as we will see, that it is not possible with the present data for PSR J0337 + 1715 to fit for it. Besides, it is known to be highly correlated with other parameters in binary systems (Damour and Deruelle, 1986) so that it is generally not measured. In the timing model for PSR J0337 + 1715, we therefore include it assuming that the spin angular momentum of the pulsar is aligned with the orbital angular momentum

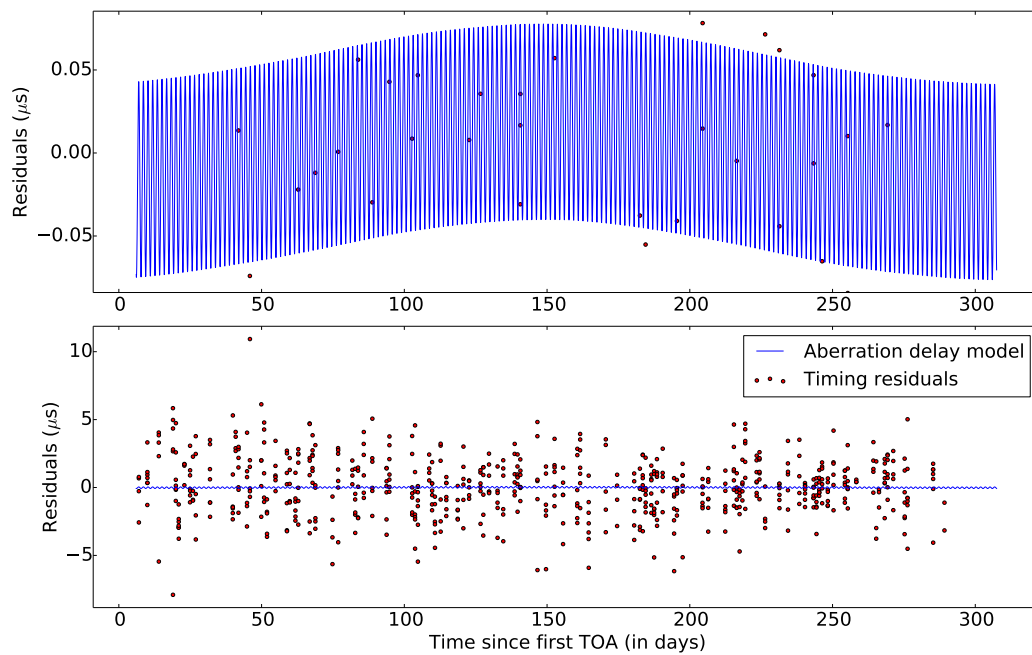


Fig. 5.7.: Aberration delay component of the timing solution of PSR J0337 + 1715 shown on figure 5.1. The computed value of equation (5.60) (blue line) has been removed from the residuals (red dots). The amplitude is much smaller than the noise as can be seen on the bottom panel. On the top panel, one clearly sees one period between ~ 0 and ~ 300 days of amplitude $\sim 0.04 \mu\text{s}$ due to the orbit with the outer white dwarf, and a modulation at the inner binary period of amplitude $\sim 0.1 \mu\text{s}$.

of the system, which is reasonable in view of the formation processes. With this assumption, and using the decomposition $\vec{v}_p = \vec{v}_{p/b} + \vec{v}_b$, we can write

$$\begin{aligned}\Delta_A &= \frac{1}{2\pi f c} \left(\vec{v}_{p/b} + \vec{v}_b \right) \cdot \frac{\vec{\omega} \times \vec{n}_\odot}{\|\vec{\omega} \times \vec{n}_\odot\|} \\ &\sim \frac{2a_p}{f P_I c} + \frac{2a_b}{f P_O c} \\ &\sim 8 \cdot 10^{-2} \mu\text{s} + 2 \cdot 10^{-2} \mu\text{s}\end{aligned}\tag{5.61}$$

where as before the last two lines show the amplitudes (between a minimum and a maximum) of quasiperiodic components estimated using a bi-Keplerian model (see also section 5.3.1).

Figure 5.7 shows the aberration-delay component of the timing model of PSR J0337 + 1715. It is clear that this delay is well below the noise level with the current data.

5.5 Validation and preliminary results

We implemented our model in a C++ code that solves the equations of motion in the pulsar system at the Newtonian or post-Newtonian order, computes all the pulsar-system specific delays, and resorts to the Tempo 2 software⁵ (Hobbs et al., 2006; Edwards et al., 2006) for the computation of propagation (dispersion measure in particular) and Solar-system delays. The code outputs a χ^2 , that is the log of the posterior probability that the model corresponds to this data,

$$\chi^2 = \sum_i \frac{\left(\Pi_a^{\text{obs}}{}_i - \Pi_a^{\text{obs}}(i, \{\text{parameters}\}) \right)^2}{\sigma_i^2},\tag{5.62}$$

where the σ_i are the uncertainties on each time of arrival. The fit to the data then consists in minimizing the χ^2 , or equivalently to find the most likely parameters.

For this purpose with resort to the software Minuit⁶ (James and Roos, 1975; James and Winkler, 2004) developed at CERN for multidimensional minimizations. The solution corresponding to the data presented in this chapter is given in table 5.1.

Once a solution is found, we developed a python interface using Cython⁷ in order to be able to study the timing solution interactively. All the plots in this chapter were made using this interface.

⁵<http://www.atnf.csiro.au/research/pulsar/tempo2/>

⁶<http://lcgapp.cern.ch/project/cls/work-packages/mathlibs/minuit/index.html>

⁷Cython is a language somewhat half-way between python and C/C++ that allows to interface python modules with C/C++ codes in a relatively easy way. See <http://cython.org/>.

Parameter	Symbol	Value
Fixed values		
Distance	d	$4.2400 \cdot 10^3$ ly
Distance proper motion	μ_d	0.00000 mas/yr
Dispersion measure	DM	$2.1316 \cdot 10^1$ pc \cdot cm $^{-3}$
Dispersion measure variation	DM'	0.0 pc \cdot cm $^{-3}$ yr $^{-1}$
Fitted values		
Spin frequency	f	$3.6595 \cdot 10^2$ s $^{-1}$
Spin frequency derivative	f'	$-2.3552 \cdot 10^{-15}$ s $^{-2}$
Laplace-Lagrange sin	$e_I \sin \omega_I$	$6.8948 \cdot 10^{-4}$
Laplace-Lagrange cos	$e_I \cos \omega_I$	$-7.5354 \cdot 10^{-5}$
Semimajor axis line of sight	$a_p \sin i_I$	-1.2175 ls
Semimajor axis plane of sky	$a_p \cos i_I$	1.4900 ls
Time of ascending node	t_{ascI}	$-5.7516 \cdot 10^2$ days
Orbital period	P_I	1.6294 days
Pulsar mass	m_p	$1.4378 M_\odot$
Laplace-Lagrange sin	$e_O \sin \omega_O$	$3.5079 \cdot 10^{-2}$
Laplace-Lagrange cos	$e_O \cos \omega_O$	$-3.5135 \cdot 10^{-3}$
Semimajor axis line of sight	$a_b \sin i_O$	$-7.4675 \cdot 10^1$ ls
Semimajor axis plane of sky	$a_b \cos i_O$	$9.1412 \cdot 10^1$ ls
Time of ascending node	t_{ascO}	$-2.6212 \cdot 10^2$ days
Orbital period	P_O	$3.2728 \cdot 10^2$ days
Difference in long. of asc. nodes	$\delta\Omega$	$2.5586 \cdot 10^{-3}$ °
Right ascension	α	$3h37m43.8227s$
Declination	δ	$17^\circ 15' 15.0636''$
Right-ascension proper motion	μ_α	$-2.0365 \cdot 10^{-1}$ mas/yr
Declination proper motion	μ_δ	5.1807 mas/yr

Tab. 5.1.: Parameters of the model fitted on the data from PSR J0337 + 1715 presented in this chapter. The times of ascending node shown are the difference with the reference date MJD 56492.297192640595. The position reference date is $t_{\text{pos}} = \text{MJD } 56337$. No error bars are given here and the number of the digits given is somewhat arbitrary.

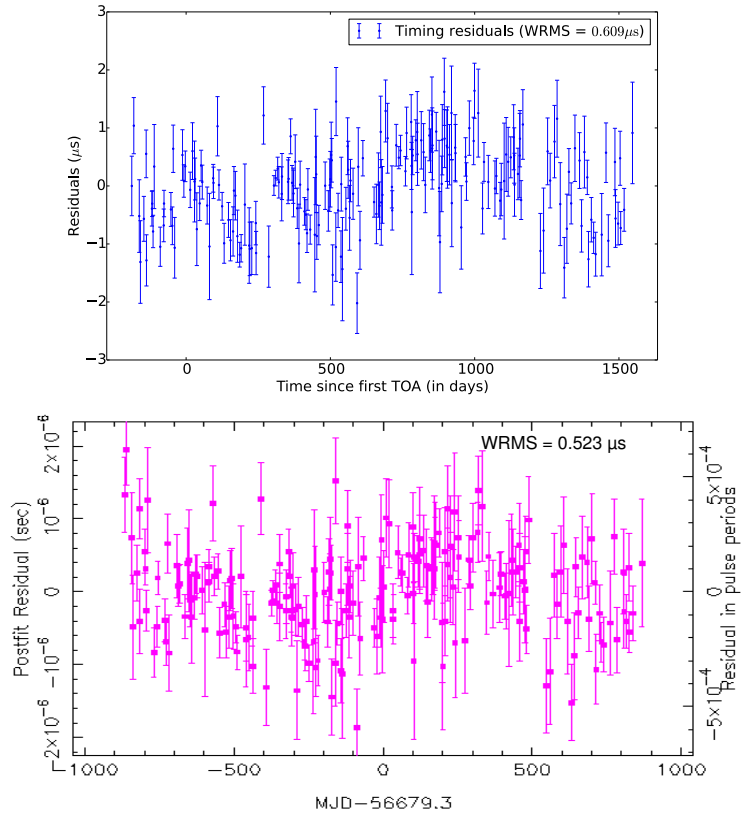


Fig. 5.8.: Comparison of the timing residuals obtained with the model of the present chapter (top panel) and with Tempo2 (bottom panel). The weighted root mean square (WRMS) of the residuals are respectively $0.609\mu\text{s}$ and $0.523\mu\text{s}$. The data come from the Nançay radiotelescope.

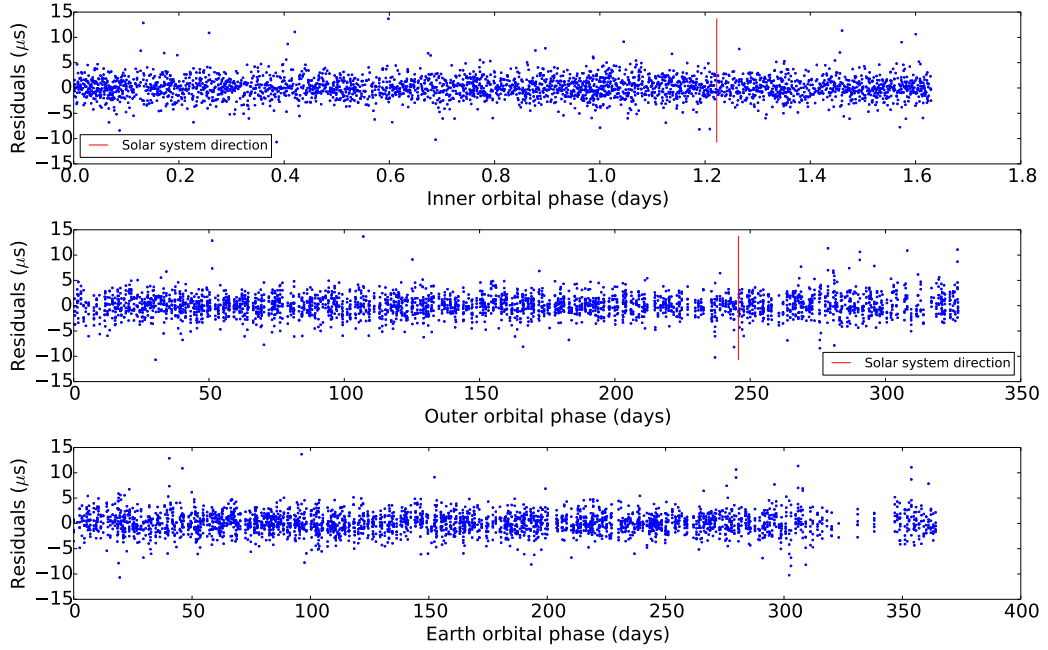


Fig. 5.9.: Same residuals of J0337 + 1715as in figure 5.1, but folded according to the (osculating) period of the inner binary (top panel), the (osculating) period of the outer system (middle panel) and the period of the Earth around the Sun (bottom panel).

Our code also supports the timing of binary pulsars with equations of motion solved numerically. This allows us to compare the results of our code with the results of the analytical binary model implemented in Tempo2. We show the example of PSR J1614 – 2230 on figure 5.8. This is a millisecond pulsar with a $\sim 0.5M_{\odot}$ white-dwarf companion in an almost edge-on ~ 9 -day orbit. The main relativistic delay is the Shapiro delay, owing to the grazing inclination angle. This allows a good determination of the mass of the companion. It also has a detectable and fairly large proper motion of a few hundred km/s. Its distance, about 1 kpc, is similar to that of J0337 + 1715. The data set from the Nançay radiotelescope spans over ~ 1800 days which is comparable but larger than the data set available for J0337 + 1715. Above all, this pulsar is timed with a very good accuracy of $\sim 0.5\mu\text{s}$ which, altogether, makes it a good binary system to test our code. We obtain a result very similar to that of Tempo2, however with a slightly larger weighted root mean square of the residuals of the fit, the difference being $\lesssim 0.1\mu\text{s}$. This discrepancy is still under investigation.

One way to make clearly appear nonrandom structure in the residuals is to fold the residuals with a period that plays a role in the model. Figure 5.9 shows a folding of the residuals of J0337 + 1715 according to the period of the inner binary, of the outer system, and of the Earth. No visible structure appears with the current data.

5.6 Outlook

We developed a C++ Markov-Chain-Monte-Carlo code using the algorithm of Goodman and Weare (2010) and following the implementation of Foreman-Mackey et al. (2013), to assess the error bars on each parameter using Bayesian probabilities. This code is parallelized using the MPI library⁸ to provide the computing power necessary to sample the posterior probability of the parameters. Indeed, each call to the model takes a few seconds on a contemporary processor, mostly to compute the orbits, and millions of calls will probably be necessary for the MCMC algorithm to converge.

With this tool in hand, it will be eventually possible to proceed to a test of the strong equivalence principle (SEP)⁹. The conjecture that the SEP implies that the theory of gravitation is indeed general relativity is commonly accepted (Will, 2014). This principle is a generalization of the weak equivalence principle, that includes self-gravitating bodies to the principle as well as local Lorentz invariance and local position invariance. The weak equivalence principle states that a freely falling test mass (non self-gravitating unlike a planet or a star) follows a trajectory independent from its structure or composition. It was demonstrated by the astronaut Dave Scott during the Apollo 15 mission, when he dropped simultaneously a hammer and a feather that reached the ground at the same time¹⁰.

Although this was of course simply an outreach experiment, the Apollo missions (and in particular Apollo 15) played a key role in the measurement of the current best limits on the validity of the weak equivalence principle by laying on the Moon's surface reflectors and allowing the so-called Lunar Laser Ranging (LLR) experiment. The LLR experiment measures the distance between the Earth and the Moon with an accuracy of about 10 cm (Murphy, 2013) by measuring the flying time of a laser pulse reflected by the reflectors. This allows to measure with exquisite accuracy the Earth-Moon orbits. These orbits are not isolated, rather both bodies are falling within the gravitational field of the Sun. Thus, any violation of the weak equivalence principle would result in different accelerations in the field of the Sun of the Moon and the Earth owing to their different compositions and masses, and modify their orbits compared to what general relativity predicts. Since these bodies are also self-gravitating (although weakly, the ratio gravitational energy over total mass is $\epsilon_g \sim 5 \cdot 10^{-10}$ for the Earth), this allows a test of the SEP as well. These tests were proposed by Nordtvedt (1968). The current limit corresponds to a relative differential acceleration of $\Delta a/a \leq 1.3 \cdot 10^{-13}$ at a 95% confidence level, which

⁸Message Passing Interface (MPI), <http://mpi-forum.org/docs/docs.html>

⁹In this perspective, a collaboration with Paulo Freire and Norbert Wex (Max Planck Institute for Radioastronomy, Bonn, Germany) was started.

¹⁰The video of this experiment is available on *the dedicated NASA webpage*.

corresponds to a SEP test in term of the Nordvedt parameter $|\eta| \sim \Delta a/a/\epsilon_g \leq 3 \cdot 10^{-4}$ (Murphy, 2013).

One sees the potential of the system J0337 + 1715: taking the outer white dwarf to play the role of the Sun, the inner binary plays the role of the Earth-Moon system and, instead of laser ranging, one uses pulsar timing. The accuracy of pulsar timing is not as good as laser ranging : the relative position of the pulsar in the system can be determined with a few-hundred-meter accuracy. However, the bodies are much more self-gravitating, in particular the neutron star which gravitational energy contribution to the inertial mass amounts to 0.15. Therefore, although the uncertainty on the acceleration of the bodies would be larger, the much larger gravitational mass fraction compensates largely (Freire et al., 2012) and would in principle allow an unprecedented test of the SEP. This would not be the first test of the strong equivalence principle using pulsars. Indeed, it is possible to perform a statistical test to see if the orbits of pulsar-white-dwarf systems are on average modified by the gravitational potential of the galaxy, the so-called Damour-Schäfer test. The most stringent limit obtained this way is $|\eta| \leq 2.3 \cdot 10^{-3}$ (Gonzalez et al., 2011).

Conclusion

During these three years, I discovered several aspects of the rich world of pulsars: original radiative processes, complex plasma physics, diversity of observations, timing... Pulsars are a chance offered by nature to scientists : being the siege of some of the most complex and inaccessible phenomena they also provide means to probe their physics sometimes with a precision, in particular with timing, that even some Earth-bound experiments may envy. The numerous faces, the complexity of these objects, and the associated wealth of observations keep fascinating me and I intend to continue in this way, notably with a post-doctoral position at the Jodrell Bank center for astrophysics.

The large scale transfers of energy and momentum in pulsars are globally understood: the spindown power of the star is sent away under the form of a large amplitude electromagnetic wave and/or an ultrarelativistic wind. However, the processes and mechanisms converting this energy are the ground of an intense theoretical work of which chapter 2 gives an overview, and of which this thesis aims at being a piece. Observational constraints have multiplied in the recent years with the advent of always more powerful high-energy observatories, from XMM-Newton and Chandra in x rays to MAGIC, HESS and VERITAS at very high energies ($> 100\text{GeV}$), without forgetting the breakthrough that represents the Large Area Telescope (LAT) mounted on the Fermi observatory. It is now clear that, at least for gamma-ray pulsars, a large part of the spindown energy is sent away under the form of gamma rays, much more than in any other wavelength.

This thesis aims at gaining insight in the processes able to produce gamma rays in pulsar magnetospheres, as well as the necessary underlying distribution of ultrarelativistic particles, in view of weaving the photon and matter creation and destruction processes into a consistent cascade of particles able to provide the necessary matter and radiation fields to the theory of pulsar magnetospheres. Eventually, cascades must be embedded in global simulations of the magnetospheres, only able to account for the complexity and the multiple physical scales involved in the pulsar machinery. Undoubtedly, the ultimate goal of pulsar modeling is to be able to provide accurate phase-resolved spectra from radio to gamma rays with a theory able to account for the great diversity of objects observed.

Curvature and synchrocurvature radiation

Luckily, if high-energy radiations take away most of the energy, the basic processes producing them are also somewhat simpler to model than the puzzling coherent radio emissions from which pulsars were first discovered. Mostly, they are believed to result from the incoherent radiation of the accelerated charges, which basic theory in classical electrodynamics is well understood. However, curvature radiation, one of the most important, if not the most important, case of radiation by an accelerated charge in pulsar magnetospheres is specific to these environments and escapes any experimental study. Indeed, it results from the fact that in very intense magnetic fields, any relativistic cyclotron motion is rapidly quenched by emission of photons, and the only motion remaining is along the field.

To study curvature radiation, the radiation of an electron or positron on its fundamental Landau level traveling at ultrarelativistic speed in a curved magnetic field, one then relies on theory. The first and most followed approach consists in replacing in the well-known classical theory of synchrotron radiation the radius of curvature of the synchrotron trajectory by the radius of the curvature of a magnetic field line, or possibly of the drift trajectory of the particle in the magnetic field. Mathematically more complicated, but physically similar, is the approach that consists in developing the so-called synchrocurvature radiation theory, in which the particle spirals in the field. Curvature radiation is then the limit of zero-pitch angle of this theory. Although straightforward, the two approaches suffer from extending the classical theory of motion and radiation of a lepton to a domain where the orbital motion is so small that quantum effects can no longer be neglected, owing to the intense magnetic fields assumed.

In chapter 3, we present a quantum theory of curvature and synchrocurvature radiation. We give, for the first time, the state of an electron in a curved magnetic field within the approximation that it lies on low orbital (Landau) levels of energy. The state of the particle is quantified by the angular momentum around the curvature axis and the main orbital quantum number of the synchrotronlike orbit around the magnetic field. The radiation is then obtained as transitions at first quantum-electrodynamics order, in the continuum limit for the angular momentum around the curvature axis but between discrete numbers for the main quantum number. Additionally, the particles are assumed to be ultrarelativistic, although in the limit that the coupling between the longitudinal motion and the perpendicular motion (with respect to the direction of the field) are negligibly coupled, which in pulsars is valid for Lorentz factors up to $\sim 10^6 - 10^7$ depending on the intensity of the magnetic field. The classical theory of curvature radiation is expanded to second order in the fraction of the energy of the particle taken away by the photon. Classical curvature radiation then arises as the leading order of the expansion while the extra terms, in

particular related to the fact that the particle can no longer be considered pointlike, can become dominant at high energies thus changing importantly the shape and intensity of the spectrum at the highest energies.

These findings may have significant consequences on the production of high-energy photons which are the progenitors of pair cascades, in particular in the inner magnetosphere where the magnetic field is stronger. In the outer magnetosphere, the lower magnetic fields allow the particles to be on higher Landau levels and our scheme of approximation would need to be expanded in two directions to consistently account for all the regimes of radiation expected :

- the coupling between longitudinal and orbital motion must be accounted for to allow for a solution of the state of the electron consistent with large Lorentz factors and lower magnetic fields,
- the radiation must be expanded to larger orders in the fraction of particle energy taken by the photon, to allow for higher Landau levels and large Lorentz factors.

The first point is challenging, since Dirac's equation is no longer separable in the coordinate system we use if the coupling terms are taken into account. It is therefore uncertain that rapid progress can be made in this direction. However, it is to be noted that the classical theory of synchrocurvature radiation often suffers from the same caveat, with the notable exception of the work of Kelner et al. (2015) in which the correction amounts on average to an effective radius of curvature. The second point is more straightforward, as this expansion arises from the direct Taylor expansion of integrals which can therefore be expanded further, although with cumbersome developments, or even integrated numerically.

Two-photon pair creation

As global simulations of pulsar magnetospheres develop, it becomes clear the required plasma densities in the outer parts of the magnetosphere requires abundant pair cascades in these regions. These cannot be provided by the main mechanism invoked close to the star, where a gamma ray converts in a pair on the strong background magnetic field, since the magnetic field is too small at these distances. Therefore the likely process responsible for these cascades is the creation of pairs by the collisions of two photons.

The two-photon process requires a somewhat large density of photons to be efficient, and gamma rays are scarce. Therefore, most of the reactions result from the collision

of a gamma ray with the soft photon from a dense background which may be provided by thermal x-ray photons from the star, or synchrotron and synchrocurvature photons from the magnetosphere. Either way, the sources are expected to be localized and photon distributions fairly or very anisotropic, this being even amplified by the effect of relativistic collimation.

We present in chapter 4 a formalism that allows to compute the reaction rate of a gamma ray on an arbitrary background of soft photons, within the approximation of a large ratio of the energy of the gamma ray over the energy of the soft photons. This formalism also provides the spectrum of outgoing leptons, thus giving all the necessary input for pair-cascade simulations. Further developments will require to put together this formalism with particle dynamics and radiation processes in order to see to what extent pair cascades can develop with the two-photon mechanism with various kinds of soft-photon backgrounds.

The triple system J0337 + 1715

This thesis was also the opportunity to continue a project that was begun during my master's final internship in Orléans with Ismaël Cognard and Lucas Guillemot, and was continued notably thanks to Paulo Freire's encouragement. This project, presented in chapter 5, consists in the realization of a complete timing model for the triple system J0337 + 1715, whose three-body mutual interactions challenge the analytical models. The main element different from existing timing softwares, such as Tempo and Tempo2, is the use of a numerical solution of the equations of motion, and the adaptation of all the steps of the timing model to this constrain, with the goal of keeping a very high accuracy at all stages. Further developments are on the way to determine consistently the uncertainties on the parameters of the model. Once this work is completed, the system J0337 + 1715 offers a unique test bench for the strong equivalence principle.

Transverse skills

To complete this work, I needed to acquire a variety of skills and techniques, in particular :

- Mathematical physics tools: perturbation theory, Chebyshev interpolation, special functions...
- Formal calculus softwares were used on a regular basis, in particular Mathematica, and occasionally Sage.

- Bayesian statistics, and in particular Markov Chain Monte Carlo methods.
- High-performance computing : Fortran, C and C++ languages were broadly used, with resort to the multiprocessing libraries MPI and occasionally to OPENMP. The local computer cluster of Paris Observatory, Tycho, was used as well as the larger PSL cluster MESOPSL.
- Fast-development programming languages, Python and Cython were used, either on their own or to interface Fortran and C++ codes into interactive command-line programs.

I also enjoyed teaching general astronomy during these three years, as well as participating in various outreach events such as the SpaceBus Sénégal 2015 and Morocco in 2016, or the tutoring of primary school classes.

Bibliography

- Agaronyan, F. A., A. M. Atoyan, and A. M. Nagapetyan (Apr. 1983). « Photoproduction of electron-positron pairs in compact x-ray sources ». en. In: *Astrophysics* 19.2, pp. 187–194 (cit. on pp. 191, 204, 207, 217).
- Aleksić, J., E. A. Alvarez, L. A. Antonelli, et al. (Nov. 2011). « Observations of the Crab Pulsar between 25 and 100 GeV with the MAGIC I Telescope ». In: *The Astrophysical Journal* 742, p. 43 (cit. on pp. 90, 91).
- Aleksić, J., E. A. Alvarez, L. A. Antonelli, et al. (Apr. 2012). « Phase-resolved energy spectra of the Crab pulsar in the range of 50-400 GeV measured with the MAGIC telescopes ». In: *Astronomy and Astrophysics* 540, A69 (cit. on p. 22).
- Aleksić, J., S. Ansoldi, L. A. Antonelli, et al. (May 2014). « Detection of bridge emission above 50 GeV from the Crab pulsar with the MAGIC telescopes ». en. In: *Astronomy & Astrophysics* 565, p. L12 (cit. on p. 21).
- Ansoldi, S., L. A. Antonelli, P. Antoranz, et al. (Jan. 2016). « Teraelectronvolt pulsed emission from the Crab Pulsar detected by MAGIC ». In: *Astronomy & Astrophysics* 585, A133 (cit. on pp. 21, 22).
- Arendt, Jr and J. A. Eilek (Jan. 1998). « The Shape of Pulsar Polar Caps ». In: *arXiv:astro-ph/9801257*. arXiv: astro-ph/9801257 (cit. on p. 33).
- Arons, J. (Sept. 1981). « Pair creation above pulsar polar caps - Steady flow in the surface acceleration zone and polar CAP X-ray emission ». In: *The Astrophysical Journal* 248, pp. 1099–1116 (cit. on pp. 79, 80).
- (Mar. 1983). « Pair creation above pulsar polar caps - Geometrical structure and energetics of slot gaps ». In: *The Astrophysical Journal* 266, pp. 215–241 (cit. on pp. 80, 86, 87).
- (Nov. 1996). « Pulsars as gamma ray sources. » In: *Astronomy and Astrophysics Supplement Series* 120, pp. 49–60 (cit. on p. 86).
- Arons, J. and E. T. Scharlemann (1979). « Pair formation above pulsar polar caps - Structure of the low altitude acceleration zone ». In: *The Astrophysical Journal* 231, pp. 854–879 (cit. on pp. 80, 82, 86, 87).
- Arons, Jonathan (2009). « Pulsar Emission: Where to Go ». en. In: *Neutron Stars and Pulsars*. Ed. by Werner Becker. Astrophysics and Space Science Library 357. Springer Berlin Heidelberg, pp. 373–420 (cit. on pp. 109, 118, 140, 147, 159).
- Baade, W. and F. Zwicky (May 1934). « On Super-Novae ». en. In: *Proceedings of the National Academy of Sciences* 20.5, pp. 254–259 (cit. on p. 22).

- Backer, D. C. and R. W. Hellings (1986). « Pulsar timing and general relativity ». In: *Annual review of astronomy and astrophysics* 24, pp. 537–575 (cit. on p. 254).
- Bai, Xue-Ning and Anatoly Spitkovsky (June 2010). « Modeling of Gamma-ray Pulsar Light Curves Using the Force-free Magnetic Field ». In: *The Astrophysical Journal* 715, pp. 1282–1301 (cit. on pp. 84, 103).
- Baring, Matthew G. (Nov. 1988). « Synchrotron emission, pair production and annihilation in strongly magnetized relativistic plasmas ». In: *Monthly Notices of the Royal Astronomical Society* 235, pp. 51–78 (cit. on pp. 52, 53).
- Baring, Matthew G., Peter L. Gonthier, and Alice K. Harding (Sept. 2005). « Spin-dependent Cyclotron Decay Rates in Strong Magnetic Fields ». In: *The Astrophysical Journal* 630, pp. 430–440 (cit. on p. 44).
- Becker, Werner (2009). « X-Ray Emission from Pulsars and Neutron Stars ». en. In: *Neutron Stars and Pulsars*. Ed. by Werner Becker. Astrophysics and Space Science Library 357. Springer Berlin Heidelberg, pp. 91–140 (cit. on pp. 12, 14, 15).
- Bellac, Michel Le (2003). *Physique quantique*. Français. Les Ulis; Paris: EDP Sciences (cit. on pp. 115, 116, 142).
- Beloborodov, Andrei M. (Aug. 2008). « Polar-Cap Accelerator and Radio Emission from Pulsars ». In: *The Astrophysical Journal Letters* 683, p. L41 (cit. on p. 83).
- Berestetskii, V. B., Evgenii Mikhailovich Lifshits, and Lev Petrovitch Pitaevski (1982). *Quantum electrodynamics*. anglais. Trans. by John Bradbury Sykes and John Stewart Bell. Oxford, Royaume-Uni (cit. on pp. 46, 53, 54, 113, 115, 121, 123, 130, 142, 166, 188, 190, 194, 195, 218, 288).
- Beskin, V. S., S. V. Chernov, C. R. Gwinn, and A. A. Tchekhovskoy (June 2015). « Radio Pulsars ». en. In: *Space Science Reviews* 191.1-4, pp. 207–237 (cit. on p. 11).
- Beutler, Gerhard (Dec. 2004). *Methods of Celestial Mechanics: Volume I: Physical, Mathematical, and Numerical Principles*. English. 1st Softcover Edition without CD-ROM of original Hardcover Edition. edition. Berlin ; New York: Springer (cit. on p. 239).
- Blandford, R. and S. A. Teukolsky (Apr. 1976). « Arrival-time analysis for a pulsar in a binary system. » In: *The Astrophysical Journal* 205, pp. 580–591 (cit. on pp. 239, 249, 252).
- Boettcher, M. and R. Schlickeiser (Sept. 1997). « The pair production spectrum from photon-photon annihilation. » In: *Astronomy and Astrophysics* 325, pp. 866–870 (cit. on pp. 191, 204).
- Bonazzola, S., F. Mottez, and J. Heyvaerts (Jan. 2015). « General solution for the vacuum electromagnetic field in the surroundings of a rotating star ». In: *Astronomy and Astrophysics* 573, A51 (cit. on pp. 33, 93).
- Bonomatto, S. and M. J. Rees (1971). « On possible observable effects of electron pair-production in QSOs ». In: *Monthly Notices of the Royal Astronomical Society* 152, p. 21 (cit. on p. 191).
- Burns, M. L. and A. K. Harding (Oct. 1984). « Pair production rates in mildly relativistic magnetized plasmas ». In: *The Astrophysical Journal* 285, pp. 747–757 (cit. on p. 191).
- Bussard, R. W., S. B. Alexander, and P. Mészáros (1986). « One-and two-photon Compton scattering in strong magnetic fields ». In: *Physical Review D* 34.2, p. 440 (cit. on p. 47).

- Caballero, I. and J. Wilms (2012). « X-ray pulsars: a review. » In: *Memorie della Societa Astronomica Italiana* 83, p. 230 (cit. on p. 141).
- Caraveo, P. A., A. De Luca, S. Mereghetti, A. Pellizzoni, and G. F. Bignami (July 2004). « Phase-Resolved Spectroscopy of Geminga Shows Rotating Hot Spot(s) ». In: *Science* 305, pp. 376–380 (cit. on p. 16).
- Cerutti, Benoît and Andrei M. Beloborodov (Dec. 2016). « Electrodynamics of Pulsar Magnetospheres ». en. In: *Space Science Reviews*, pp. 1–26 (cit. on pp. 101, 103, 216, 217).
- Cerutti, Benoît, Alexander Philippov, Kyle Parfrey, and Anatoly Spitkovsky (Mar. 2015). « Particle acceleration in axisymmetric pulsar current sheets ». In: *Monthly Notices of the Royal Astronomical Society* 448, pp. 606–619 (cit. on p. 103).
- Cerutti, Benoît, Alexander A. Philippov, and Anatoly Spitkovsky (Apr. 2016). « Modelling high-energy pulsar light curves from first principles ». In: *Monthly Notices of the Royal Astronomical Society* 457.3, pp. 2401–2414 (cit. on pp. 103, 106).
- Chen, Alexander Y. and Andrei M. Beloborodov (Nov. 2014). « Electrodynamics of Axisymmetric Pulsar Magnetosphere with Electron-Positron Discharge: A Numerical Experiment ». In: *The Astrophysical Journal Letters* 795, p. L22 (cit. on pp. 102, 103, 191, 216).
- Cheng, A., M. Ruderman, and P. Sutherland (Jan. 1976). « Current flow in pulsar magnetospheres ». In: *The Astrophysical Journal* 203, pp. 209–212 (cit. on p. 91).
- Cheng, A. F. and M. A. Ruderman (1977). « Pair-production discharges above pulsar polar caps ». In: *The Astrophysical Journal* 214, pp. 598–606 (cit. on p. 50).
- Cheng, K. S. and J. L. Zhang (1996). « General Radiation Formulae for a Relativistic Charged Particle Moving in Curved Magnetic Field Lines: The Synchrocurvature Radiation Mechanism ». In: *The Astrophysical Journal* 463, p. 271 (cit. on pp. 110, 119, 138–140, 174, 176, 180).
- Cheng, K. S., C. Ho, and M. Ruderman (Jan. 1986a). « Energetic radiation from rapidly spinning pulsars. I - Outer magnetosphere gaps. II - VELA and Crab ». In: *The Astrophysical Journal* 300, pp. 500–539 (cit. on p. 91).
- (Jan. 1986b). « Energetic Radiation from Rapidly Spinning Pulsars. II. VELA and Crab ». In: *The Astrophysical Journal* 300, p. 522 (cit. on pp. 91, 93, 94, 96).
- Cheng, K. S., M. Ruderman, and L. Zhang (July 2000). « A Three-dimensional Outer Magnetospheric Gap Model for Gamma-Ray Pulsars: Geometry, Pair Production, Emission Morphologies, and Phase-resolved Spectra ». In: *The Astrophysical Journal* 537, pp. 964–976 (cit. on pp. 33, 93, 94).
- Cognard, I., L. Guillemot, T. J. Johnson, et al. (2011). « Discovery of Two Millisecond Pulsars in Fermi Sources with the Nançay Radio Telescope ». en. In: *The Astrophysical Journal* 732.1, p. 47 (cit. on pp. 19, 20).
- Contopoulos, Ioannis, Demosthenes Kazanas, and Christian Fendt (Jan. 1999). « The Axisymmetric Pulsar Magnetosphere ». In: *The Astrophysical Journal* 511, pp. 351–358 (cit. on pp. 98, 99).
- Cordes, J. M. (June 1978). « Observational limits on the location of pulsar emission regions ». In: *The Astrophysical Journal* 222, pp. 1006–1011 (cit. on p. 11).

- Damour, Thibault and Nathalie Deruelle (1986). « General relativistic celestial mechanics of binary systems. II. The post-newtonian timing formula ». In: *Annales de l'institut Henri Poincaré (A) Physique théorique* 44.3, pp. 263–292 (cit. on pp. 232, 239, 252, 253, 256).
- Damour, Thibault and J. H. Taylor (Mar. 1992). « Strong-field tests of relativistic gravity and binary pulsars ». In: *Physical Review D* 45, pp. 1840–1868 (cit. on pp. 236, 242).
- Daugherty, J. K. and A. K. Harding (Jan. 1982). « Electromagnetic cascades in pulsars ». In: *The Astrophysical Journal* 252, pp. 337–347 (cit. on pp. 68, 82, 83, 85).
- (Oct. 1983). « Pair production in superstrong magnetic fields ». In: *The Astrophysical Journal* 273, pp. 761–773 (cit. on pp. 50–53, 207).
- Daugherty, J. K. and I. Lerche (1976). « Theory of pair production in strong electric and magnetic fields and its applicability to pulsars ». In: *Physical Review D* 14.2, p. 340 (cit. on p. 53).
- Daugherty, Joseph K. and Alice K. Harding (Oct. 1986). « Compton scattering in strong magnetic fields ». In: *The Astrophysical Journal* 309, pp. 362–371 (cit. on p. 47).
- Davidson, Ronald C. (2001). *Physics of nonneutral plasmas*. anglais. London, Royaume-Uni de Grande-Bretagne et d'Irlande du Nord, Pays multiples: Imperial College Press (cit. on p. 75).
- Dermer, Charles D. (Sept. 1990). « Compton scattering in strong magnetic fields and the continuum spectra of gamma-ray bursts - Basic theory ». In: *The Astrophysical Journal* 360, pp. 197–214 (cit. on pp. 47–49).
- Deutsch, Arnim J. (Jan. 1955). « The electromagnetic field of an idealized star in rigid rotation in vacuo ». In: *Annales d'Astrophysique* 18, p. 1 (cit. on p. 93).
- Dyks, J. and B. Rudak (Dec. 2003). « Two-Pole Caustic Model for High-Energy Light Curves of Pulsars ». In: *The Astrophysical Journal* 598, pp. 1201–1206 (cit. on pp. 86, 88, 89, 93, 95).
- Edwards, R. T., G. B. Hobbs, and R. N. Manchester (Nov. 2006). « TEMPO2, a new pulsar timing package - II. The timing model and precision estimates ». en. In: *Monthly Notices of the Royal Astronomical Society* 372.4, pp. 1549–1574 (cit. on pp. 233, 236, 241, 247, 250, 258).
- Eilek, Jean A. and Timothy H. Hankins (June 2016). « Radio emission physics in the Crab pulsar ». In: *Journal of Plasma Physics* 82, p. 635820302 (cit. on p. 11).
- Fawley, W. M., J. Arons, and E. T. Scharlemann (Oct. 1977). « Potential drops above pulsar polar caps - Acceleration of nonneutral beams from the stellar surface ». In: *The Astrophysical Journal* 217, pp. 227–243 (cit. on pp. 59, 75, 77).
- Fishman, Gerald J. (June 1992). « Gamma ray observations of the Crab pulsar - Past, present, future ». In: *Annals of the New York Academy of Sciences* 655, pp. 309–318 (cit. on p. 95).
- Foreman-Mackey, Daniel, David W. Hogg, Dustin Lang, and Jonathan Goodman (2013). « emcee: the MCMC hammer ». In: *Publications of the Astronomical Society of the Pacific* 125.925, p. 306 (cit. on p. 262).
- Frank M, I and I Tamm E (1937). In: *Dokl. Akad. Nauk.* 14, p. 107 (cit. on p. 44).

- Freire, Paulo C. C., Michael Kramer, and Norbert Wex (Sept. 2012). « Tests of the universality of free fall for strongly self-gravitating bodies with radio pulsars ». en. In: *Classical and Quantum Gravity* 29.18, p. 184007 (cit. on p. 263).
- Friedman, H., S. W. Lichtman, and E. T. Byram (Sept. 1951). « Photon Counter Measurements of Solar X-Rays and Extreme Ultraviolet Light ». In: *Physical Review* 83, pp. 1025–1030 (cit. on p. 12).
- Ginzburg, Vitalij Lazarevič and Vadim Nikolaevič (1929-) Cytovič (1990). *Transition radiation and transition scattering*. eng. The Adam Hilger series on plasma physics. Bristol New York: A. Hilger (cit. on p. 44).
- Goldreich, Peter and William H. Julian (Aug. 1969). « Pulsar Electrodynamics ». In: *The Astrophysical Journal* 157, p. 869 (cit. on pp. 5, 6, 28, 32, 56–59, 102, 191).
- Goldstein, Herbert (1980). *Classical mechanics*. anglais. Reading (Mass.), Etats-Unis d'Amérique, Pays-Bas (cit. on p. 170).
- Gonthier, P. L. and A. K. Harding (Apr. 1994). « General relativistic corrections in the gamma-ray emission from pulsars ». In: *The Astrophysical Journal* 425, pp. 767–775 (cit. on p. 79).
- Gonzalez, M. E., I. H. Stairs, R. D. Ferdman, et al. (2011). « High-precision Timing of Five Millisecond Pulsars: Space Velocities, Binary Evolution, and Equivalence Principles ». en. In: *The Astrophysical Journal* 743.2, p. 102 (cit. on p. 263).
- Goodman, Jonathan and Jonathan Weare (Jan. 2010). « Ensemble samplers with affine invariance ». en. In: *Communications in Applied Mathematics and Computational Science* 5.1, pp. 65–80 (cit. on p. 262).
- Gould, D. M. and A. G. Lyne (Nov. 1998). « Multifrequency polarimetry of 300 radio pulsars ». In: *Monthly Notices of the Royal Astronomical Society* 301, pp. 235–260 (cit. on p. 10).
- Gould, Robert J. and Gerald Schröder (Feb. 1966). « Opacity of the Universe to High-Energy Photons ». In: *Physical Review Letters* 16.6, pp. 252–254 (cit. on pp. 192, 205).
- Gourgoulhon, Éric (2013). *Special Relativity in General Frames*. Graduate Texts in Physics. Berlin, Heidelberg: Springer Berlin Heidelberg (cit. on p. 165).
- Gradshteyn, Izrail' Solomonovich and Iosif Moiseevich Ryzhik (2007). *Table of integrals, series and products*. anglais. Ed. by Alan Jeffrey and Daniel Zwillinger. Trans. by Scripta technica. Pays-Bas, Etats-Unis d'Amérique, Allemagne (cit. on pp. 179, 204).
- Grandclément, Philippe and Jérôme Novak (Jan. 2009). « Spectral Methods for Numerical Relativity ». In: *Living Reviews in Relativity* 12, p. 1 (cit. on p. 204).
- Gruzinov, Andrei (Apr. 2006). « Force-Free Electrodynamics of Pulsars ». In: *arXiv:astro-ph/0604364*. arXiv: astro-ph/0604364 (cit. on p. 97).
- Harding, Alice K. and Constantinos Kalapotharakos (Sept. 2015). « Synchrotron Self-Compton Emission from the Crab and Other Pulsars ». In: *The Astrophysical Journal* 811, p. 63 (cit. on pp. 90, 103).
- Harding, Alice K and Dong Lai (Sept. 2006). « Physics of strongly magnetized neutron stars ». In: *Reports on Progress in Physics* 69.9, pp. 2631–2708 (cit. on pp. 53, 56).

- Harding, Alice K. and Alex G. Muslimov (Nov. 2011). « Pulsar Pair Cascades in Magnetic Fields with Offset Polar Caps ». In: *arXiv:1111.1668 [astro-ph]*. arXiv: 1111.1668 (cit. on p. 84).
- Harding, Alice K. and Alexander G. Muslimov (Nov. 1998). « Particle Acceleration Zones above Pulsar Polar Caps: Electron and Positron Pair Formation Fronts ». In: *The Astrophysical Journal* 508, pp. 328–346 (cit. on pp. 47, 49, 77, 80–82, 85, 86).
- Harding, Alice K. and Robert Preece (1987). « Quantized synchrotron radiation in strong magnetic fields ». In: *The Astrophysical Journal* 319, pp. 939–950 (cit. on pp. 43, 44, 119, 141).
- Harding, Alice K., Matthew G. Baring, and Peter L. Gonthier (Feb. 1997). « Photon-Splitting Cascades in Gamma-Ray Pulsars and the Spectrum of PSR 1509-58 ». In: *The Astrophysical Journal* 476, pp. 246–260 (cit. on p. 37).
- Harding, Alice K., Alexander G. Muslimov, and Bing Zhang (2002). « Regimes of Pulsar Pair Formation and Particle Energetics ». en. In: *The Astrophysical Journal* 576.1, p. 366 (cit. on pp. 191, 209).
- Harko, T. and K. S. Cheng (Sept. 2002). « Unified classical and quantum radiation mechanism for ultrarelativistic electrons in curved and inhomogeneous magnetic fields ». In: *Monthly Notices of the Royal Astronomical Society* 335, pp. 99–113 (cit. on pp. 110, 119, 138, 140).
- Henkel, Malte (2001). « Sur la solution de Sundman du problème des trois corps ». fra. In: *Philosophia Scientiae* 5.2, pp. 161–184 (cit. on p. 230).
- Hewish, A., S. J. Bell, J. D. H. Pilkington, P. F. Scott, and R. A. Collins (Feb. 1968). « Observation of a Rapidly Pulsating Radio Source ». In: *Nature* 217.5130, pp. 709–713 (cit. on pp. 2, 7, 9, 107, 118).
- Hibschman, Johann A. and Jonathan Arons (June 2001). « Pair Multiplicities and Pulsar Death ». In: *The Astrophysical Journal* 554, pp. 624–635 (cit. on pp. 67, 70, 79–81, 85).
- Hobbs, G. B., R. T. Edwards, and R. N. Manchester (June 2006). « tempo2, a new pulsar-timing package - I. An overview: tempo2, a new pulsar-timing package - I. Overview ». en. In: *Monthly Notices of the Royal Astronomical Society* 369.2, pp. 655–672 (cit. on pp. 233, 236, 258).
- Hoensbroech, A. von and K. M. Xilouris (Nov. 1997). « Effelsberg multifrequency pulsar polarimetry ». In: *Astronomy and Astrophysics Supplement Series* 126 (cit. on p. 12).
- Holloway, N J (May 1973). « P-N Junction in Pulsar Magnetospheres ». In: *Nature Physical Science* 246, pp. 6–9 (cit. on p. 91).
- Huff, L. D. (1931). « The Motion of a Dirac Electron in a Magnetic Field ». In: *Physical Review* 38.3, pp. 501–512 (cit. on pp. 110, 119, 287).
- Jackson, E. Atlee (Jan. 1976). « Pulsar atmospheric current loops ». en. In: *Nature* 259.5538, pp. 25–26 (cit. on p. 100).
- Jackson, John David (1998). *Classical Electrodynamics, 3rd Edition* (cit. on pp. 38, 44, 63, 108, 117, 145–147, 149).
- Jager, O. C. de, B. C. Raubenheimer, and J. W. H. Swanepoel (Aug. 1989). « A powerful test for weak periodic signals with unknown light curve shape in sparse data ». In: *Astronomy and Astrophysics* 221, pp. 180–190 (cit. on p. 19).

- Jager, O. C. de, A. K. Harding, P. F. Michelson, et al. (Jan. 1996). « Gamma-Ray Observations of the Crab Nebula: A Study of the Synchro-Compton Spectrum ». In: *The Astrophysical Journal* 457, p. 253 (cit. on p. 85).
- James, Fred and MINUIT Roos (1975). « Minuit-a system for function minimization and analysis of the parameter errors and correlations ». In: *Computer Physics Communications* 10.6, pp. 343–367 (cit. on p. 258).
- James, Fred and Matthias Winkler (2004). « Minuit user's guide ». In: *CERN, Geneva* (cit. on p. 258).
- Johnson, M. H. and B. A. Lippmann (1949). « Motion in a constant magnetic field ». In: *Physical Review* 76.6, p. 828 (cit. on pp. 110, 119, 287).
- Kalapotharakos, Constantinos, Demosthenes Kazanas, Alice Harding, and Ioannis Contopoulos (Apr. 2012). « Toward a Realistic Pulsar Magnetosphere ». In: *The Astrophysical Journal* 749, p. 2 (cit. on p. 103).
- Kanbach, G. (1999). « Temporal and Spectral Details of Bright EGRET Pulsars ». In: *Astrophysical Letters and Communications* 38, p. 17 (cit. on p. 88).
- Karuppusamy, R., B. W. Stappers, and W. van Straten (June 2010). « Giant pulses from the Crab pulsar: A wide-band study ». In: *Astronomy and Astrophysics* 515, A36 (cit. on p. 11).
- Kelner, S. R., A. Yu Prosekin, and F. A. Aharonian (Jan. 2015). « Synchro-curvature radiation of charged particles in the strong curved magnetic fields ». In: *The Astronomical Journal* 149.1. arXiv: 1501.04994, p. 33 (cit. on pp. 41, 110, 119, 138, 141, 159, 160, 267).
- Kijak, J. and J. Gil (Jan. 2003). « Radio emission altitude in pulsars ». In: *Astronomy and Astrophysics* 397, pp. 969–972 (cit. on pp. 10, 11).
- Kirk, John G., Yuri Lyubarsky, and Jerome Petri (2009). « The Theory of Pulsar Winds and Nebulae ». en. In: *Neutron Stars and Pulsars*. Ed. by Werner Becker. Astrophysics and Space Science Library 357. Springer Berlin Heidelberg, pp. 421–450 (cit. on p. 56).
- Konacki, Maciej and Alex Wolszczan (2003). « Masses and orbital inclinations of planets in the PSR B1257+ 12 system ». In: *The Astrophysical Journal Letters* 591.2, p. L147 (cit. on p. 230).
- Kopeikin, S. M. (Jan. 1995). « On possible implications of orbital parallaxes of wide orbit binary pulsars and their measurability ». In: *The Astrophysical Journal Letters* 439, pp. L5–L8 (cit. on p. 249).
- (Aug. 1996). « Proper Motion of Binary Pulsars as a Source of Secular Variations of Orbital Parameters ». In: *The Astrophysical Journal Letters* 467, p. L93 (cit. on p. 249).
- Kozlenkov, A. A. and I. G. Mitrofanov (1986). « Two-photon production of e^* pairs in a strong magnetic field ». In: *Zh. Eksp. Teor. Fiz* 91, pp. 1978–1989 (cit. on p. 53).
- Krause-Polstorff, J. and F. C. Michel (Mar. 1985). « Electrosphere of an aligned magnetized neutron star ». In: *Monthly Notices of the Royal Astronomical Society* 213.1, 43P–49P (cit. on p. 100).
- Kuiper, L., W. Hermsen, G. Cusumano, et al. (Nov. 2001). « The Crab pulsar in the 0.75-30 MeV range as seen by CGRO COMPTEL. A coherent high-energy picture from soft X-rays up to high-energy gamma-rays ». In: *Astronomy and Astrophysics* 378, pp. 918–935 (cit. on p. 90).

- Lai, Dong (July 2001). « Matter in strong magnetic fields ». In: *Reviews of Modern Physics* 73 (cit. on p. 36).
- Landau, L., E. Lifshitz, and Edouard Gloukhian (1966). *Physique théorique - Théorie du Champ*. fre. 2e édition revue. Moscou: Mir (cit. on p. 63).
- Lange, Ch., F. Camilo, N. Wex, et al. (Sept. 2001). « Precision timing measurements of PSR J1012+5307 ». In: *Monthly Notices of the Royal Astronomical Society* 326, pp. 274–282 (cit. on p. 241).
- Latal, H. G. (Oct. 1986). « Cyclotron radiation in strong magnetic fields ». In: *The Astrophysical Journal* 309, pp. 372–382 (cit. on pp. 43, 44, 141).
- Lattimer, J. M. and M. Prakash (Apr. 2004). « The Physics of Neutron Stars ». en. In: *Science* 304.5670, pp. 536–542 (cit. on pp. 22, 24).
- Luca, De (2005). « On the Polar Caps of the Three Musketeers ». In: *ApJ* 623, pp. 1051–1069 (cit. on p. 16).
- Lyne, Andrew and Francis Graham-Smith (Apr. 2012). *Pulsar Astronomy*. English. 4 edition. Cambridge ; New York: Cambridge University Press (cit. on p. 10).
- Lyubarskii, Y. E. and S. A. Petrova (Sept. 1998). « Synchrotron absorption in pulsar magnetospheres ». In: *Astronomy and Astrophysics* 337, pp. 433–440 (cit. on pp. 44, 91).
- Manchester, R. N., G. B. Hobbs, A. Teoh, and M. Hobbs (Apr. 2005). « The Australia Telescope National Facility Pulsar Catalogue ». In: *The Astronomical Journal* 129, pp. 1993–2006 (cit. on pp. 2, 3, 10).
- Marshall, F. E., L. Guillemot, A. K. Harding, P. Martin, and D. A. Smith (2016). « A New, Low Braking Index for the LMC Pulsar B0540–69 ». en. In: *The Astrophysical Journal Letters* 827.2, p. L39 (cit. on p. 2).
- McCarthy, Dennis D. and Gérard Petit (2004). *IERS Conventions (2003)*. English. OCLC: 746001655. Frankfurt am Main: Bundesamt für Kartographie und Geodäsie (cit. on pp. 231, 239).
- Medin, Zach and Dong Lai (Dec. 2007). « Condensed surfaces of magnetic neutron stars, thermal surface emission, and particle acceleration above pulsar polar caps ». In: *Monthly Notices of the Royal Astronomical Society* 382.4, pp. 1833–1852 (cit. on pp. 35–37).
- Melrose, D. B. and A. J. Parle (1983). « Quantum electrodynamics in strong magnetic fields. I Electron states ». In: *Australian Journal of Physics* 36, pp. 755–774 (cit. on pp. 110, 136, 287).
- Melrose, Don, Amir Levinson, Alex Judge, and Qinghuan Luo (Sept. 2005). « Oscillating pair creation in pulsar magnetospheres ». In: vol. 784, pp. 274–286 (cit. on p. 83).
- Michel, F. Curtis (Feb. 1973a). « Rotating Magnetosphere: a Simple Relativistic Model ». In: *The Astrophysical Journal* 180, pp. 207–226 (cit. on p. 99).
- (Mar. 1973b). « Rotating Magnetospheres: an Exact 3-D Solution ». In: *The Astrophysical Journal Letters* 180, p. L133 (cit. on pp. 97–99).
- (Sept. 1974). « Rotating Magnetosphere: Acceleration of Plasma from the Surface ». In: *The Astrophysical Journal* 192, pp. 713–718 (cit. on pp. 75, 77).
- (1982). *Theory of pulsar magnetospheres*. English. OCLC: 39828148. New York, NY: American Physical Society (cit. on p. 45).

- Michel, F. Curtis and Hui Li (Sept. 1999). « Electrodynamics of neutron stars ». In: *Physics Reports* 318.6, pp. 227–297 (cit. on pp. 27, 28).
- Misner, Charles W., Kip S. Thorne, and John Archibald Wheeler (1973). *Gravitation*. anglais. San Francisco, Etats-Unis d'Amérique: W. H. Freeman and company (cit. on p. 242).
- Mohr, Peter J., David B. Newell, and Barry N. Taylor (Sept. 2016). « CODATA recommended values of the fundamental physical constants: 2014 ». en. In: *Reviews of Modern Physics* 88.3 (cit. on p. 285).
- Murphy, T. W. (2013). « Lunar laser ranging: the millimeter challenge ». en. In: *Reports on Progress in Physics* 76.7, p. 076901 (cit. on pp. 262, 263).
- Muslimov, A. G. and A. I. Tsygan (Mar. 1992). « General relativistic electric potential drops above pulsar polar caps ». In: *Monthly Notices of the Royal Astronomical Society* 255, pp. 61–70 (cit. on pp. 78, 87).
- Muslimov, Alex G. and Alice K. Harding (May 2003). « Extended Acceleration in Slot Gaps and Pulsar High-Energy Emission ». In: *The Astrophysical Journal* 588, pp. 430–440 (cit. on pp. 87, 89, 90).
- (May 2004). « High-Altitude Particle Acceleration and Radiation in Pulsar Slot Gaps ». In: *The Astrophysical Journal* 606, pp. 1143–1153 (cit. on pp. 89, 90).
- Nikishov, A I (Feb. 1962). « Absorption of High-energy photons in the universe ». In: *Soviet physics JETP* 14.2 (cit. on pp. 190, 192, 204, 205, 209, 217).
- Nordtvedt, K. (June 1968). « Testing Relativity with Laser Ranging to the Moon ». In: *Physical Review* 170.5, pp. 1186–1187 (cit. on p. 262).
- Olver, Frank W. J. and National Institute of Standards and Technology (U.S.), eds. (2010). *NIST handbook of mathematical functions*. Cambridge ; New York: Cambridge University Press : NIST (cit. on pp. 39–41, 128, 131, 133, 148, 152, 168, 174, 175, 179, 289).
- Oppenheimer, J. Robert and George M. Volkoff (1939). « On massive neutron cores ». In: *Physical Review* 55.4, p. 374 (cit. on p. 23).
- Ostriker, J. P. and J. E. Gunn (Sept. 1969). « On the Nature of Pulsars. I. Theory ». In: *The Astrophysical Journal* 157, p. 1395 (cit. on p. 28).
- Özel, Feryal and Paulo Freire (Sept. 2016). « Masses, Radii, and the Equation of State of Neutron Stars ». en. In: *Annual Review of Astronomy and Astrophysics* 54.1, pp. 401–440 (cit. on pp. 4, 22–25).
- Pacini, F. (Nov. 1967). « Energy Emission from a Neutron Star ». en. In: *Nature* 216.5115, pp. 567–568 (cit. on pp. 1, 27).
- Pétri, J. (July 2007). « Relativistic stabilisation of the diocotron instability in a pulsar “cylindrical” electrosphere ». In: *Astronomy and Astrophysics* 469, pp. 843–855 (cit. on p. 102).
- (June 2015). « Multipolar electromagnetic fields around neutron stars: exact vacuum solutions and related properties ». In: *Monthly Notices of the Royal Astronomical Society* 450, pp. 714–742 (cit. on pp. 33, 93).
- Pétri, J., J. Heyvaerts, and S. Bonazzola (May 2002a). « Diocotron instability in pulsar electrospheres. I. Linear analysis ». In: *Astronomy and Astrophysics* 387, pp. 520–530 (cit. on p. 102).

- Pétri, J., J. Heyvaerts, and S. Bonazzola (Mar. 2002b). « Global static electrospheres of charged pulsars ». In: *Astronomy and Astrophysics* 384, pp. 414–432 (cit. on p. 100).
- Philippov, Alexander A. and Anatoly Spitkovsky (Apr. 2014). « Ab Initio Pulsar Magnetosphere: Three-dimensional Particle-in-cell Simulations of Axisymmetric Pulsars ». In: *The Astrophysical Journal Letters* 785, p. L33 (cit. on p. 102).
- Philippov, Alexander A., Anatoly Spitkovsky, and Benoit Cerutti (Mar. 2015). « Ab Initio Pulsar Magnetosphere: Three-dimensional Particle-in-cell Simulations of Oblique Pulsars ». In: *The Astrophysical Journal Letters* 801, p. L19 (cit. on p. 104).
- Pierbattista, M., I. A. Grenier, A. K. Harding, and P. L. Gonthier (Sept. 2012). « Constraining γ -ray pulsar gap models with a simulated pulsar population ». In: *Astronomy and Astrophysics* 545, A42 (cit. on p. 93).
- Pilia, M., J. W. T. Hessels, B. W. Stappers, et al. (Feb. 2016). « Wide-band, low-frequency pulse profiles of 100 radio pulsars with LOFAR ». In: *Astronomy and Astrophysics* 586, A92 (cit. on p. 12).
- Radhakrishnan, V. and D. J. Cooke (1969). « Magnetic Poles and the Polarization Structure of Pulsar Radiation ». In: *Astrophysical Letters* 3, p. 225 (cit. on p. 11).
- Rankin, J. M. (Nov. 1983). « Toward an empirical theory of pulsar emission. I Morphological taxonomy. » In: *The Astrophysical Journal* 274, pp. 333–368 (cit. on pp. 11, 12).
- Rankin, Joanna M. (Mar. 1990). « Toward an empirical theory of pulsar emission. IV - Geometry of the core emission region ». In: *The Astrophysical Journal* 352, pp. 247–257 (cit. on pp. 10, 11).
- (Mar. 1993). « Toward an empirical theory of pulsar emission. VI - The geometry of the conal emission region ». In: *The Astrophysical Journal* 405, pp. 285–297 (cit. on p. 11).
- Ransom, S. M., I. H. Stairs, A. M. Archibald, et al. (Jan. 2014). « A millisecond pulsar in a stellar triple system ». In: *Nature* 505, pp. 520–524 (cit. on pp. 7, 229, 230, 242).
- Ritter, H. and U. Kolb (June 2003). « Catalogue of cataclysmic binaries, low-mass X-ray binaries and related objects (Seventh edition) ». In: *Astronomy and Astrophysics* 404, pp. 301–303. eprint: astro-ph/0301444 (cit. on p. 5).
- (Mar. 2004). « VizieR Online Data Catalog: Cataclysmic Binaries, LMXBs, and related objects (Ritter+, 2003) ». In: *VizieR Online Data Catalog* 5113 (cit. on p. 5).
- Roberts, Mallory SE (2012). « Surrounded by spiders! New black widows and redbacks in the Galactic field ». In: *Proceedings of the International Astronomical Union* 8.S291, pp. 127–132 (cit. on p. 4).
- Romani, Roger W. (Oct. 1996). « Gamma-Ray Pulsars: Radiation Processes in the Outer Magnetosphere ». In: *The Astrophysical Journal* 470, p. 469 (cit. on pp. 93, 94).
- Romani, Roger W. and I.-A. Yadigaroglu (Jan. 1995). « Gamma-ray pulsars: Emission zones and viewing geometries ». In: *The Astrophysical Journal* 438, pp. 314–321 (cit. on pp. 87, 93, 95).
- Ruderman, M. (1974). « Matter in Superstrong Magnetic Fields ». In: vol. 53, p. 117 (cit. on pp. 35, 36).

- Ruderman, M. A. and P. G. Sutherland (1975). « Theory of pulsars - Polar caps, sparks, and coherent microwave radiation ». In: *The Astrophysical Journal* 196, pp. 51–72 (cit. on pp. 66, 71, 72, 74, 75, 82, 107, 119, 140).
- Ruffini, Remo, Gregory Vereshchagin, and She-Sheng Xue (Feb. 2010). « Electron–positron pairs in physics and astrophysics: From heavy nuclei to black holes ». en. In: *Physics Reports* 487.1-4, pp. 1–140 (cit. on p. 190).
- Scharlemann, E. T., J. Arons, and W. M. Fawley (1978). « Potential drops above pulsar polar caps - Ultrarelativistic particle acceleration along the curved magnetic field ». In: *The Astrophysical Journal* 222, pp. 297–316 (cit. on pp. 77, 78, 90).
- Scharlemann, Ernst T. and Robert V. Wagoner (June 1973). « Aligned Rotating Magnetospheres. General Analysis ». en. In: *The Astrophysical Journal* 182, pp. 951–960 (cit. on p. 97).
- Schiff, L. I. (July 1939). « A Question in General Relativity ». In: *Proceedings of the National Academy of Science* 25, pp. 391–395 (cit. on p. 59).
- Schwinger, Julian (1949). « On the Classical Radiation of Accelerated Electrons ». In: *Physical Review* 75.12, pp. 1912–1925 (cit. on pp. 38, 147, 179, 180).
- (Feb. 1954). « The Quantum Correction in the Radiation by Energetic Accelerated Electrons ». en. In: *Proceedings of the National Academy of Sciences* 40.2, pp. 132–136 (cit. on pp. 40, 141).
- Schwinger, Julian and Wu-yang Tsai (Jan. 1978). « New approach to quantum corrections in synchrotron radiation ». In: *Annals of Physics* 110.1, pp. 63–84 (cit. on p. 141).
- Shapiro, Irwin I. (Dec. 1964). « Fourth Test of General Relativity ». In: *Physical Review Letters* 13, pp. 789–791 (cit. on p. 253).
- Shklovskii, I. S. (Feb. 1970). « Possible Causes of the Secular Increase in Pulsar Periods. » In: *Soviet Astronomy* 13, p. 562 (cit. on pp. 27, 249).
- Sigurdsson, S. and S. E. Thorsett (July 2005). « Update on Pulsar B1620-26 in M4: Observations, Models, and Implications ». In: vol. 328. eprint: arXiv:astro-ph/0404538, p. 213 (cit. on p. 230).
- Smarr, L. L. and R. Blandford (July 1976). « The binary pulsar - Physical processes, possible companions, and evolutionary histories ». In: *The Astrophysical Journal* 207, pp. 574–588 (cit. on p. 256).
- Smith, F. G., D. H. P. Jones, J. S. B. Dick, and C. D. Pike (July 1988). « The optical polarization of the Crab Pulsar ». In: *Monthly Notices of the Royal Astronomical Society* 233, pp. 305–319 (cit. on p. 95).
- Smith, I. A., F. C. Michel, and P. D. Thacker (Apr. 2001). « Numerical simulations of aligned neutron star magnetospheres ». In: *Monthly Notices of the Royal Astronomical Society* 322, pp. 209–217 (cit. on pp. 59, 102).
- Soffel, Michael M. (1989). *Relativity in astrometry, celestial mechanics, and geodesy*. anglais. Berlin, Allemagne (cit. on p. 243).
- Sokolov, Arsenii Aleksandrovich and Igor' Mikhaïlovich Ternov (1968). *Synchrotron radiation*. anglais. Berlin, Allemagne: Akademie (cit. on pp. 40, 41, 44, 110, 115, 119, 124–126, 128, 134, 136, 141, 142, 287).

- Spitkovsky, A. and J. Arons (2002). « Simulations of Pulsar Wind Formation ». In: vol. 271, p. 81 (cit. on p. 102).
- Spitkovsky, Anatoly (Sept. 2006). « Time-dependent Force-free Pulsar Magnetospheres: Axisymmetric and Oblique Rotators ». In: *The Astrophysical Journal Letters* 648, pp. L51–L54 (cit. on pp. 98, 99, 103, 104).
- Sturmer, Steven J. (June 1995). « Electron Energy Losses near Pulsar Polar Caps ». In: *The Astrophysical Journal* 446, p. 292 (cit. on p. 47).
- Sturrock, P. A. (Mar. 1971). « A Model of Pulsars ». In: *The Astrophysical Journal* 164, p. 529 (cit. on pp. 68, 71, 83, 191).
- Sundman, Karl F. (Dec. 1913). « Mémoire sur le problème des trois corps ». fr. In: *Acta Mathematica* 36.1, pp. 105–179 (cit. on p. 230).
- Svensson, Roland (1987). « Non-thermal pair production in compact X-ray sources - First-order Compton cascades in soft radiation fields ». In: *Monthly Notices of the Royal Astronomical Society* 227, pp. 403–451 (cit. on p. 192).
- Tademaru, E. (July 1973). « On the Energy Spectrum of Relativistic Electrons in the Crab Nebula ». In: *The Astrophysical Journal* 183, pp. 625–636 (cit. on p. 83).
- The Fermi-LAT collaboration, 2013 (Oct. 2013). « The Second Fermi Large Area Telescope Catalog of Gamma-ray Pulsars ». In: *The Astrophysical Journal Supplement Series* 208.2. arXiv: 1305.4385, p. 17 (cit. on pp. 18, 20, 22, 90).
- Timokhin, A. N. (May 2006). « On the force-free magnetosphere of an aligned rotator ». In: *Monthly Notices of the Royal Astronomical Society* 368, pp. 1055–1072 (cit. on pp. 98, 99).
- (Nov. 2010). « Time-dependent pair cascades in magnetospheres of neutron stars - I. Dynamics of the polar cap cascade with no particle supply from the neutron star surface ». In: *Monthly Notices of the Royal Astronomical Society* 408, pp. 2092–2114 (cit. on pp. 62, 83, 85).
- Timokhin, A. N. and J. Arons (Feb. 2013). « Current flow and pair creation at low altitude in rotation-powered pulsars' force-free magnetospheres: space charge limited flow ». In: *Monthly Notices of the Royal Astronomical Society* 429, pp. 20–54 (cit. on pp. 83, 84).
- Timokhin, A. N. and A. K. Harding (Sept. 2015). « On the Polar Cap Cascade Pair Multiplicity of Young Pulsars ». In: *The Astrophysical Journal* 810, p. 144 (cit. on pp. 66–68, 85, 90, 191).
- Tolman, Richard C. (Feb. 1939). « Static Solutions of Einstein's Field Equations for Spheres of Fluid ». In: *Physical Review* 55, pp. 364–373 (cit. on p. 23).
- Truemper, J., W. Pietsch, C. Reppin, et al. (1978). « Evidence for strong cyclotron line emission in the hard X-ray spectrum of Hercules X-1 ». In: *The Astrophysical Journal Letters* 219, pp. L105–L110 (cit. on pp. 13, 14).
- Tsai, Wu-yang and Thomas Erber (1975). « Propagation of photons in homogeneous magnetic fields: Index of refraction ». In: *Physical Review D* 12.4, pp. 1132–1137 (cit. on p. 52).
- Usov, V. V. and D. B. Melrose (1995). « Pulsars with Strong Magnetic Fields - Polar Gaps Bound Pair Creation and Nonthermal Luminosities ». In: *Australian Journal of Physics* 48, p. 571 (cit. on p. 50).

- Vassiliev, V. V. (Jan. 2000). « Extragalactic background light absorption signal in the TeV γ -ray spectra of blazars ». In: *Astroparticle Physics* 12, pp. 217–238 (cit. on p. 192).
- VERITAS Collaboration, E. Aliu, T. Arlen, et al. (Oct. 2011). « Detection of Pulsed Gamma Rays Above 100 GeV from the Crab Pulsar ». In: *Science* 334, p. 69 (cit. on p. 90).
- Viganò, D., J. A. Pons, J. A. Miralles, and N. Rea (May 2015a). « Magnetic fields in Neutron Stars ». In: eprint: arXiv:1501.06735, pp. 90–101 (cit. on pp. 107, 118).
- Viganò, Daniele, Diego F. Torres, Kouichi Hirotani, and Martín E. Pessah (Dec. 2015b). « Compact formulae, dynamics and radiation of charged particles under synchro-curvature losses ». In: *Monthly Notices of the Royal Astronomical Society* 447.2. arXiv: 1411.5836, pp. 1164–1172 (cit. on pp. 63, 109, 110, 119, 138, 141, 158, 159).
- Voisin, G., S. Bonazzola, and F. Mottez (Dec. 2016). « Why curvature radiation in neutron-star magnetospheres should be treated in the framework of quantum electrodynamics ». In: *SF2A-2016: Proceedings of the Annual meeting of the French Society of Astronomy and Astrophysics*. Ed. by C. Reylé, J. Richard, L. Cambrésy, et al., pp. 45–49 (cit. on pp. 107, 140, 157).
- Voisin, Guillaume, Silvano Bonazzola, and Fabrice Mottez (Jan. 2017a). « Curvature radiation from a quantum-electrodynamics point of view ». In: *AIP Conference Proceedings* 1792.1, p. 090002 (cit. on p. 161).
- (Apr. 2017b). « Dirac states of an electron in a circular intense magnetic field ». In: *Physical Review D* 95, p. 085002 (cit. on pp. 112, 118, 140, 143).
 - (May 2017c). « Quantum theory of curvature and synchro-curvature radiation in a strong and curved magnetic field, and applications to neutron star magnetospheres ». In: *Physical Review D* 95, p. 105008 (cit. on pp. 112, 139).
- Watson, George Neville (1966). *A treatise on the theory of Bessel functions*. anglais. Cambridge, Royaume-Uni de Grande-Bretagne et d'Irlande du Nord: Cambridge University Press (cit. on p. 179).
- Will, Clifford M. (1984). « Gravitational redshift of gravitational clocks ». In: *Annals of Physics* 155.1, pp. 133–157 (cit. on p. 250).
- (1993). *Theory and experiment in gravitational physics*. anglais. Cambridge England, Royaume-Uni (cit. on p. 243).
 - (2014). « The Confrontation between General Relativity and Experiment ». en. In: *Living Reviews in Relativity* 17 (cit. on pp. 242, 262).
- Wolszczan, A. and D. A. Frail (Jan. 1992). « A planetary system around the millisecond pulsar PSR1257 + 12 ». In: *Nature* 355, pp. 145–147 (cit. on p. 230).
- Zhang, Bing and G. J. Qiao (Oct. 1998). « Two-photon annihilation in the pair formation cascades in pulsar polar caps ». In: *Astronomy and Astrophysics* 338, pp. 62–68 (cit. on p. 209).
- Zhang, J. L. and Y. F. Yuan (Jan. 1998). « The Quantum Radiation Formulae of a New Radiation Mechanism in Curved Magnetic Fields ». In: *The Astrophysical Journal* 493, pp. 826–833 (cit. on pp. 119, 138, 140, 192).
- Zhang, L., K. S. Cheng, Z. J. Jiang, and P. Leung (Mar. 2004). « Gamma-Ray Luminosity and Death Lines of Pulsars with Outer Gaps ». In: *The Astrophysical Journal* 604, pp. 317–327 (cit. on pp. 93, 94, 96).



Constants and notations

All quantities are expressed in the international unit system (SI). The values of the fundamental constants below are taken from the CODATA (Mohr et al., 2016).

Symbol	Value	Unit	Expression	Definition
c	299792458	m/s		Speed of light in vacuum
ϵ_0	$\frac{10^7}{4\pi c^2}$	F/m		Electric permittivity of vacuum
μ_0	$4\pi \cdot 10^{-7}$	H/m	$\frac{1}{\epsilon_0 c^2}$	Magnetic permeability of vacuum
\hbar	$1.054571800(13) \cdot 10^{-34}$	J s		Planck constant divided by 2π
m	$9.10938356(11) \cdot 10^{-31}$	kg		Mass of the electron
e	$1.6021766208(98) \cdot 10^{-19}$	C		Absolute value of the electron charge
α_{fs}	$7.2973525664(17) \cdot 10^{-3}$		$\frac{e^2}{4\pi\epsilon_0\hbar c}$	Fine structure constant
r_e	$2.8179 \cdot 10^{-15}$	m	$\frac{e^2}{4\pi\epsilon_0 m c^2}$	Classical radius of the electron
λ_C	$\simeq 3.86 \cdot 10^{-13}$	m	$\frac{\hbar}{mc}$	Reduced Compton wavelength
B_c	$\simeq 4.4 \cdot 10^9$	Teslas	$\frac{m^2 c^2}{e\hbar}$	Critical magnetic field
M_\odot	$1.988435 \cdot 10^{30}$	kg		Mass of the Sun
γ				Lorentz factor
\vec{E}		V/m		Electric field
\vec{B}		T		Magnetic field
\vec{m}		A m ²		Magnetic dipole moment
ρ		C m ⁻³		Charge density
ρ		m		Radius of curvature
ω_B		rad/s	$\frac{eB}{\gamma m}$	Synchrotron pulsation
Ω_C		rad/s	$\frac{c}{\rho}$	Curvature-radiation pulsation
ϵ_B		J	$mc^2 \frac{B}{B_c}$	Energy step between Landau levels

If there is no ambiguity, the norm of a vector \vec{A} is noted by merely dropping the vector sign (arrow) :

$$\|\vec{A}\| = A. \quad (\text{A.1})$$

For a quantity A ,

$$A_n = \frac{A}{10^n}. \quad (\text{A.2})$$

Landau levels as a solution of the Klein-Gordon equation

The derivation of the states of an electron in a uniform magnetic field can be found in many textbooks in the nonrelativistic case, and several derivations exist in the literature in the relativistic case (e.g. Huff (1931), Johnson and Lippmann (1949), Melrose and Parle (1983), Sokolov and Ternov (1968)). The result is that the electron behaves like a free particle in the direction along the magnetic field, while its cyclotron orbit is quantified, much like the orbit of an electron in an atom.

Here we recall some basics of quantum mechanics followed by the main steps of the derivation of Landau levels using the relativistic Klein-Gordon equation : this equation does not embody the spin of the electron, but the resulting proper energies turn out to be very close to the Dirac-equation solution, and the algebra is simpler. To obtain the exact same proper energies (B.14) as with Dirac's Hamiltonian we add an ad hoc spin term to the regular Klein-Gordon equation, which gives the modified equation (B.7).

In quantum mechanics, the Hamiltonian plays the role of the operator of translation in time. The recipe to obtain the operator consists in taking the classical Hamiltonian and replace the momenta $\vec{p} = (p_x, p_y, p_z)$, the energy H (or E), and positions x, y, z by operators acting on states $|\phi\rangle : (x, y, z) \rightarrow \phi(t, x, y, z)$ which belong to the L^2 function space. Taking the example of the x variable, and of the energy,

$$x \rightarrow \hat{x}|\phi\rangle = x\phi(t, x, y, z) \quad (\text{B.1})$$

$$p \rightarrow \hat{p}_x|\phi\rangle = -i\hbar\partial_x\phi(t, x, y, z), \quad (\text{B.2})$$

$$H \rightarrow \hat{H}|\phi\rangle = i\frac{\hbar}{c}\partial_t\phi(t, x, y, z), \quad (\text{B.3})$$

where hats designate the operators, and the equality gives the representation of the operator in the (x, y, z) space (another representation could be in Fourier space).

The measurable states of a particle are then the proper states of the Hamiltonian

$$\hat{H}|\phi_E\rangle = E|\phi_E\rangle, \quad (\text{B.4})$$

where E is the proper value and the energy of the corresponding proper state $|\phi_E\rangle$.

Based on the success of the Schrödinger Hamiltonian

$$\hat{H}_S = \frac{\hat{p}^2}{2m}, \quad (\text{B.5})$$

which is merely the translation of the kinetic energy of a particle of mass m into an operator, it was natural to seek a relativistic equivalent. However, the translation of the square root in the relativistic energy into an operator proved difficult. A first approach then consisted in taking the square of the energy with the well-known formula $E^2 - c^2\vec{p}^2 = m^2c^4$, where E is the time component of the four-momentum of a particle of mass m . After translation in operators, this gives the so-called Klein-Gordon equation

$$\hat{H}_{KG} = m^2c^4 + c^2\hat{p}^2, \quad (\text{B.6})$$

where $\hat{H}_{KG} = -\hbar^2/c^2\partial_t^2$ is not a Hamiltonian, since it is homogeneous to an energy squared. The proper electron Hamiltonian was introduced by Dirac and is related to Klein-Gordon's equation by a form of squaring.

To obtain the states of a particle in a magnetic field one includes the field through its potential vector \vec{A} as in classical mechanics by the replacement $\hat{\vec{p}} \rightarrow \hat{\vec{p}} + e\vec{A}$ where $-e$ is the charge of the electron. We add an ad hoc spin operator $-eB\hbar\hat{\Sigma}$, where B is the magnetic-field intensity, which presence can be justified from Dirac's equation (Berestetskii et al., 1982),

$$\hat{H}_{KG} = m^2c^4 + c^2(\hat{\vec{p}} + e\vec{A})^2 - eB\hbar c^2\hat{\Sigma}. \quad (\text{B.7})$$

In the rest of this demonstration we use a unit system with $\hbar = c = 1$.

We seek the proper states of equation B.7. We assume an electron in a uniform magnetic field of intensity B along the z axis such that a convenient potential vector is

$$\vec{A} = (0, xB, 0). \quad (\text{B.8})$$

Note that \vec{A} could be chosen differently owing to the gauge freedom.

We further assume proper states $|\phi\rangle$ that are also proper functions of \hat{p}_y and \hat{p}_z with of proper values p_y and p_z defined by $\hat{p}_{y,z}|\phi\rangle = p_{y,z}|\phi\rangle$. We anticipate here on the fact that the equation can be solved by separation of variables which gives these proper-state properties for variables x and y . This can also be seen as the expression of the two symmetries of the problem (rotation around the magnetic field, translation along it) in the particular gauge used here. We assume that the states are also proper states of the operator $\hat{\Sigma}$ with proper values $\sigma = \pm 1$.

A proper state of B.7 ϕ with proper value E^2 satisfies

$$\left[-\partial_x^2 + (p_y + eBx)^2 + p_z^2 - eB\sigma + m^2\right] \phi = E^2 \phi. \quad (\text{B.9})$$

This equation can be put in the form of the Weber differential equation

$$\left(\partial_{x'}^2 + \left(\nu + \frac{1}{2} - \frac{x'^2}{4}\right)\right) \phi = 0, \quad (\text{B.10})$$

where

$$x' = \sqrt{2} \sqrt[4]{eB} \left(x - \frac{p_y}{eB}\right), \quad (\text{B.11})$$

$$\nu = \frac{E^2 + eB\sigma - p_z^2 - m^2}{2eB} - \frac{1}{2}. \quad (\text{B.12})$$

Equation B.10 has two independent solutions under the form of parabolic cylinder functions $D_\nu(x')$ (Olver and National Institute of Standards and Technology (U.S.), 2010).

Wave functions must vanish at infinity. This condition implies that ν be a positive integer $k = \nu$ such that

$$E^2 = 2eB \left(k + \frac{1 - \sigma}{2}\right) + p_z^2 + m^2. \quad (\text{B.13})$$

Except for the ground state $\sigma = -1, k = 0$ there are always two values of each number that determine the same state. This allows to simplify by introducing the main quantum number $n = k + (1 - \sigma)/2$. Putting back c and \hbar and writing $p_z = p^\parallel$, we obtain the so-called Landau levels of energies for the modified Klein-Gordon equation

$$E = \pm \sqrt{m^2 c^4 + 2m c^2 \epsilon_B n + c^2 p^\parallel{}^2}. \quad (\text{B.14})$$

The first term in the square root is the rest-mass energy, the second corresponds to the quantification of the cyclotron orbits by the quantum number $n \geq 0$, and the third one corresponds to the kinetic energy along the direction parallel to the magnetic field. Note that without taking the spin into account i.e. in the pure Klein-Gordon case where $\sigma = 0$, the ground state would be above the rest mass energy : $\sqrt{m^2 c^4 + 2m c^2 \epsilon_B (0 + 1/2)}$.

The energy

$$\epsilon_B = \hbar \frac{eB}{m}, \quad (\text{B.15})$$

where eB/m is the cyclotron frequency, corresponds to the step between two Landau levels in the nonrelativistic limit. Indeed, assuming $mc^2 \gg \epsilon_B, cp^{\parallel}$, equation (B.14) becomes,

$$E = \pm \left(mc^2 + n\epsilon_B + \frac{p^{\parallel 2}}{m} \right). \quad (\text{B.16})$$

One can also write the Landau levels as a function of the critical field

$$B_c = \frac{m^2 c^2}{e\hbar} \simeq 4.4 \cdot 10^9 \text{T}, \quad (\text{B.17})$$

which gives

$$\epsilon_B = mc^2 \frac{B}{B_c}. \quad (\text{B.18})$$

The critical magnetic field thus sets the magnetic-intensity limit above which the difference between Landau levels is larger than the rest-mass-energy of the electron.

Colophon

This thesis was typeset with $\text{\LaTeX} 2_{\epsilon}$. It uses a modified version of the *Clean Thesis* style developed by Ricardo Langner. The design of the *Clean Thesis* style is inspired by user guide documents from Apple Inc.

Download the *Clean Thesis* style at <http://cleanthesis.der-ric.de/>.

Résumé

Les pulsars sont des étoiles à neutron hautement magnétisées en rotation rapide produisant un rayonnement pulsé. Cette thèse est dédiée à leur magnétosphère, c'est à dire la zone proche de l'étoile à neutron, remplie d'un plasma entraîné par la rotation rapide de celle-ci. Il a été montré dès 1969 que la magnétosphère doit avoir des zones très peu denses arborant des champs électriques intenses capables d'accélérer le plasma raréfié de ces régions à des énergies très élevées le long du champ magnétique. La courbure des lignes de champ, couplée avec la rotation d'une particule autour du champ, cause un rayonnement dit de « synchro-courbure ». L'énergie est rayonnée essentiellement en photons gamma (γ). Ces photons peuvent ensuite être convertis par interaction quantique photon γ -champ magnétique ou γ - γ en une paire électron-positron $e+e^-$ dont chaque composante rayonne à son tour, résultant en une cascade qui alimente la magnétosphère en plasma. Cette thèse traite particulièrement de deux phénomènes clés de ces cascades : le rayonnement de synchro-courbure et la création de paires par interaction γ - γ .

Cette thèse traite aussi du modèle de chronométrage du pulsar milliseconde dans un système triple J0337+1715.

Mots Clés

Pulsar, synchrotron, chronométrage

Abstract

Pulsars are highly magnetized fast rotating neutron stars producing a pulsed radiation. This thesis is dedicated to their magnetosphere, namely the zone surrounding the star and filled with a plasma dragged by the rotation of the star. It was shown as soon as 1969 that the magnetosphere must have vacuum gaps, where intense electric fields develop that are capable of accelerating the rarefied plasma to very high energies along the magnetic field. The curvature of the field lines, together with the rotation around the magnetic field, results in the so-called « synchrocurvature » radiation. The energy is mostly radiated in gamma photons (γ). These photons may then be converted by the γ -photon-magnetic-field or γ - γ quantum processes in an electron-positron pair $e+e^-$, each component of which then radiates at its turn which results in a cascade that provides plasma to the magnetosphere. This thesis particularly deals with two key phenomena of these cascades : synchrocurvature radiation and γ - γ pairs.

This thesis also concerns the timing model of the millisecond pulsar in a triple system J0337+1715.

Keywords

Pulsar, neutron star, radiative processes, synchrotron, timing